

Mixing, Hydrography, and Flow in the eastern Channel of the Lucky Strike Segment

Dissertation

zur Erlangung des Doktorgrades
der Mathematisch-Naturwissenschaftlichen Fakultät
der Christian-Albrechts-Universität zu Kiel

vorgelegt von
Sandra Tippenhauer

Kiel 2015



Referenten

Referent: Prof. Dr. Torsten Kanzow

Alfred-Wegener-Institut
Helmholtz-Zentrum für Polar- und Meeresforschung
Bussestraße 24
27570 Bremerhaven

Universität Bremen

Koreferent: Prof. Dr. Inga M. Koszalka

GEOMAR Helmholtz-Zentrum für Ozeanforschung Kiel
Düsternbrooker Weg 20
24105 Kiel

Universität zu Kiel

Tag der mündlichen Prüfung: 10.07.2015

Zum Druck genehmigt: 10.07.2015

gez. _____

Prof. Dr. Wolfgang J. Duschl, Dekan

Abstract

Diapycnal mixing in the deep ocean is known to be much stronger in the vicinity of rough topography of mid-ocean ridges than over abyssal plains. In this thesis a microstructure probe attached to an autonomous underwater vehicle (AUV) was used to infer the spatial distribution of the dissipation rate of turbulent kinetic energy (ϵ) in the central valley of the Mid-Atlantic Ridge. This represents the first successful realization of a horizontal, AUV-based, deep-ocean microstructure survey. The study focused on a channel with unidirectional, partially supercritical sill overflow. The density was found to decrease along the channel following the mean flow of 3 to 8 cm/s. The magnitude of the dissipation rate was distributed asymmetrically relative to the position of the sill. Elevated dissipation rates were present in a segment 1 to 4 km downstream of the sill, reaching $1 \cdot 10^{-7}$ W/kg. Flow speeds of more than 20 cm/s and elevated density finestructure were observed within this segment.

The average along-channel flow was found to be strongly modulated by the semi-diurnal M_2 tidal flow. Supercritical flow down the lee slope of the sill was observed during strong flow velocity conditions, and a hydraulic jump is expected to occur downstream of the sill during these phases. Consistently, upward displacement of isopycnals was observed in the area where the velocity distribution suggested the presence of a hydraulic jump. Indications for upstream propagating hydraulic jumps were found during phases of decreasing flow velocities. Upstream propagating hydraulic jumps offer a possibility of inducing turbulent mixing closer to the sill or even upstream of it.

The distributions of the flow, density and mixing rate provide a consistent picture of the fundamental physical mechanisms controlling the mixing in this deep ocean channel, i.e. tidally modulated, jet unidirectional sill overflow with a hydraulic jump inducing turbulent mixing downstream.

These results indicate deep-ocean mixing to depend heavily on the local bottom topography and flow conditions. Although one particular channel was studied, the fundamental physical mechanisms identified in this thesis are expected to be applicable to other, similar channels. Furthermore, the results nicely illustrate that horizontally-profiling AUV-based observations may be an efficient tool to study deep-ocean turbulence over complex terrain where free-falling and lowered turbulence measurements are inefficient and time-consuming.

Zusammenfassung

Die Verteilung der diapkyknischen Vermischung im tiefen Ozean ist nicht homogen. In der Nähe von rauer Topographie, wie zum Beispiel an Mittelozeanischen Rücken, ist die Vermischung stark erhöht. Im Rahmen dieser Doktorarbeit wurde eine an einem autonomen Unterwasserfahrzeug (AUV) befestigte Mikrostruktur-Sonde verwendet, um die Dissipation turbulenter kinetischer Energie im Zentralgraben des Mittelatlantischen Rückens zu bestimmen. Dies sind die ersten erfolgreichen Mikrostrukturmessungen mit einem horizontal profilierenden AUV im tiefen Ozean. Im Fokus dieser Studie stand ein kontinuierlich durchströmter Kanal, der teilweise von einer Schwelle blockiert wird. Stromabwärts der Schwelle war die Strömung teilweise superkritisch. Im Mittel betrug die Strömungsgeschwindigkeit 3 bis 8 cm/s und die Dichte des Wassers nahm in Richtung der Strömung ab. Relativ zur Position der Schwelle wurde eine asymmetrische Verteilung der Vermischung beobachtet. In dem Abschnitt von 1 bis 4 km stromabwärts der Schwelle wurde die stärkste Vermischung gefunden, mit einem Maximalwert von $1 \cdot 10^{-7}$ W/kg. In dem gleichen Abschnitt wurden zudem erhöhte Strömungsgeschwindigkeiten und Dichteveriabilitäten beobachtet.

Die mittlere Strömung wurde stark von den halbtägigen Gezeiten, wie der M_2 -Gezeit moduliert. Während der Phasen mit hoher Strömungsgeschwindigkeit wurde superkritische Strömung auf der Leeseite der Schwelle beobachtet, wodurch stromabwärts ein hydraulischer Sprung zu erwarten ist. In dem Bereich, in dem der hydraulische Sprung aufgrund der Verteilung der Strömungsgeschwindigkeiten erwartet wird, waren die Isopyknen stark nach oben ausgelenkt. Diese Auslenkung stellt ein charakteristisches Zeichen für einen hydraulischen Sprung da. Während der Phasen mit geringer Strömungsgeschwindigkeit wurden Anzeichen stromaufwärts propagierender hydraulischer Sprünge beobachtet. Propagierende hydraulische Sprünge erhöhen die Vermischung in der Nähe oder sogar stromaufwärts der Schwelle.

Die Verteilungen von Dichte, Strömung und Vermischung zeigte ein konsistentes Bild der fundamentalen physikalischen Prozesse, die die Vermischung in diesem Tiefsee-Kanal kontrollieren, nämlich, die durch die halbtägige Gezeit moduliert, aber unidirektionale Strömung über die Schwelle einschließlich eines hydraulischen Sprungs, sowie starke Vermischung stromabwärts der Schwelle. Die Ergebnisse zeigen, dass die Vermischung im tiefen Ozean stark von der lokalen Strömung und der Topographie abhängt. Auch wenn hier ein bestimmter Kanal untersucht wur-

de, wird davon ausgegangen, dass die somit identifizierten physikalischen Prozesse auf ähnliche Tiefsee-Kanäle übertragbar sind.

Die Ergebnisse zeigen, dass horizontale, AUV-basierte Messungen geeignet sind, Turbulenz im tiefen Ozean in der Nähe komplexer Topographie zu untersuchen, insbesondere in Gegenden, in denen frei-fallende oder gefierte Messungen ineffizient und zeitraubend sind.

Contents

1	Introduction	1
1.1	Ocean Circulation, Heat Transport and Mixing	1
1.2	The Aim of this Thesis	7
1.3	The Study Site	9
1.3.1	Hydrography and Flow at the Mid-Atlantic Ridge south of the Azores Islands	9
1.3.2	The Lucky Strike Segments Topography, Flow and Mixing as well their Impact on the greater North Atlantic	15
1.4	Hydraulic Jump and Froude Number	17
2	Data and Instruments	25
2.1	Shipboard Observations	25
2.2	Moored Observations	26
2.3	Autonomous Observations	28
2.3.1	The AUV <i>Abys</i> s	28
2.3.2	Microstructure Profiler, Mounting and Vibrations	29
2.3.3	Processing and Calibration of Shear Sensor Data	32
2.3.4	AUV Missions	32
2.4	AUV Speed, Flow Velocity and Calibration	33
3	Processing Dissipation Rates obtained aboard AUV <i>Abys</i>s	37
3.1	Inferring Dissipation Rates from Velocity Shear Microstructure	37
3.2	Two Methods to compute the Dissipation Rate	40
3.3	Noise and Error Estimate	41
4	Turbulence, Density and Flow Distribution along the Channel	45
4.1	Dissipation Rate along the Channel	45
4.1.1	High Resolution Dissipation of Turbulent Kinetic Energy	45
4.1.2	Average Dissipation Rate	49
4.2	Average Velocity and Density Field	50
4.2.1	Horizontal Distribution of the Flow inside the Channel	51
4.2.2	Vertical along-Channel Flow and Density Distribution	53
4.2.3	Vertical across-Channel Section of the along-Channel Flow and Density Distribution	57
4.2.4	Summary	58
4.3	Averaged Diffusivity	59
4.3.1	Turbulent Diffusivity Distribution along the Channel	59

4.3.2	Advection Diffusion Balance	61
4.4	Density and Temperature fine-Structure	63
4.4.1	Horizontal Density Anomalies	64
4.4.2	Horizontal Temperature Variability and Scales of Turbulence	65
4.4.3	One Example of the Variability of Turbulence, Density and Temperature	70
4.5	Summary and Discussion	73
5	Tidal Influence on the Flow, the Density, and the Dissipation Rate Distribution	77
5.1	Tides and short term Variability	77
5.1.1	Tidal Variability in along-Channel Velocity	78
5.1.2	Tidal Variability in Temperature Time-Series	83
5.1.3	Summary	92
5.2	Evolution of the Flow and Density Field on short Time Scales . . .	93
5.2.1	Evolution of the Flow and Density Field at one Location just downstream of the Sill	93
5.2.2	Temporal Variability in along-Channel Density Field	98
5.3	Tidal Variability of the Flow and Density Field	101
5.3.1	Along-channel Flow and Density Distribution	102
5.3.2	Across-Channel Distribution of Flow and Density	108
5.3.3	Summary	111
5.4	Dissipation in tidally varying Flow	111
5.5	Summary and Discussion	118
6	Signal Propagation	125
6.1	Internal Waves	125
6.2	Vertical Velocities and their High-Frequency Variability	130
6.3	Upstream propagating Hydraulic Jump?	135
6.4	Summary and Discussion	139
7	Synthesis	141
A	Additional material	147
	References	I
	List of Figures	IX
	List of Tables	XIII
	Acknowledgments	XV
	Erklärung	XVII

Publications

This thesis contains the manuscript: **Tippenhauer, S.**; Dengler, M.; Fischer, T.; Kanzwo, T. 2015. Turbulence and finestructure in a deep ocean channel with sill overflow on the Mid-Atlantic Ridge. Deep Sea Research Part I: Oceanographic Research Papers 99, 10-22.

S. Tippenhauer conducted the data processing and analysis, developed and applied the methodology, and wrote the manuscript. The co-authors contributed to the scientific content of the manuscript with designing the experiments at sea, discussions of the methodology and results, and comments on the manuscript.

1 Introduction

1.1 Ocean Circulation, Heat Transport and Mixing

The ocean plays an important role in the meridional redistribution of heat which is introduced by the energy input at low latitudes via solar radiation. Up to 22% of the total meridional, poleward heat transport of about 5 PW (1 PW = 10^{15} W) is accomplished by the ocean currents (*Trenberth and Caron, 2001*), which bring warm surface waters to high latitudes where they lose energy to the atmosphere and cool (*Warren (1981); Wunsch and Ferrari (2004)*). Subsequently the cold, dense water masses sink via open-ocean or shelf convection and form the deep waters which spread equatorward along deep isopycnals (*Dickson and Brown, 1994*). The amount of downwelled water has to be balanced by an equal amount of water rising elsewhere in the ocean in order to close the circulation (*Munk, 1966; Munk and Wunsch, 1998; Kanzow et al., 2007*). This flow pattern is referred to as the meridional overturning circulation (MOC, Fig. 1.1) and provides the most impor-

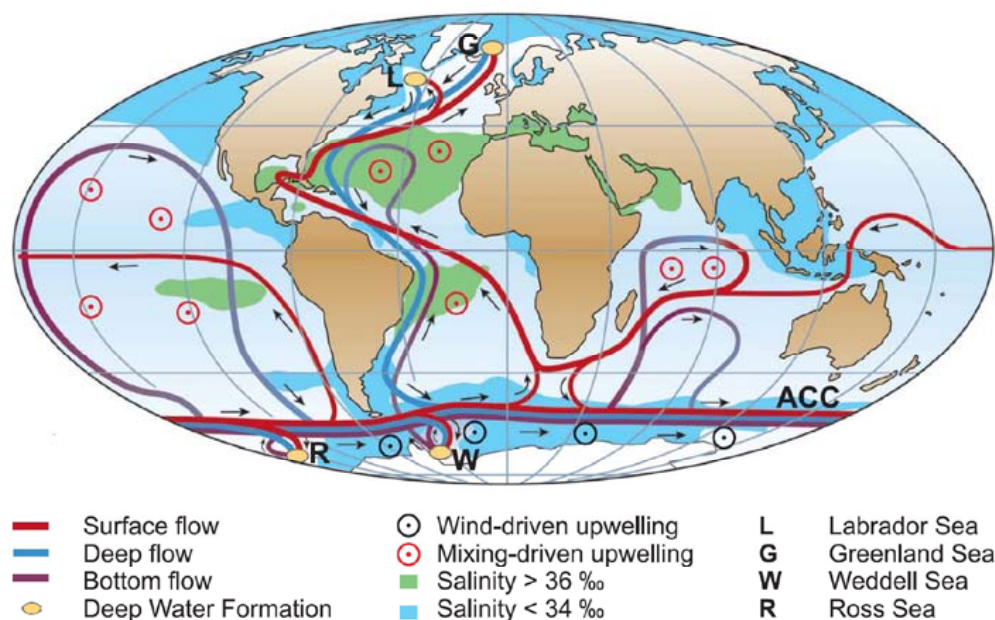


Figure 1.1: Sketch of the global meridional overturning circulation (MOC) (*Rahmstorf, 2002; Kuhlbrodt et al., 2007*). Surface heat transport (red) towards deep convection sites at high latitudes where deep waters are formed (indicated with G, L, W, and R) as well as the pathways of deep return flow (blue) and mixing sites.

1 Introduction

tant oceanic contribution to the meridional transport of heat. In the subtropical North Atlantic more than 60% of the northward ocean heat transport are associated to the MOC (e.g. *Bryden and Imawaki (2001)*) resulting in the moderate climate over the northern Atlantic sector compared to the northern Pacific sector (*Rahmstorf, 2003*).

In order to close the MOC energy is required to achieve upwelling which is primarily provided as mechanical energy input by tides and the global wind field (*Wunsch and Ferrari, 2004*). That energy is transferred to potential energy and heat by diapycnal mixing and irreversible dissipation of turbulent kinetic energy, respectively (*Wunsch and Ferrari, 2004*). Before the energy budget and the circulation scheme are discussed the turbulent kinetic energy equation and the concept of the turbulent eddy diffusivity are shortly introduced.

The turbulent kinetic energy (TKE) in the ocean is expressed by the ‘turbulent kinetic energy equation’ which describes the local change of TKE in time as well as the advection by the mean flow (*Olbers et al., 2012*). In steady state the TKE is usually estimated by the terms describing the production of TKE from the mean shear (first term in Equation 1.1), the transfer from kinetic to potential energy achieved by work done against gravity (second term in Equation 1.1), and the dissipation rate of TKE ϵ which can be expressed as:

$$- \overline{u'w'} \frac{\partial U}{\partial z} = \frac{g}{\bar{\rho}} \overline{w'\rho'} + \epsilon \quad (1.1)$$

for one-dimensional sheared flow U , the density ρ , the acceleration due to gravity g , and the fluctuations of the horizontal and vertical velocity u' and w' , respectively (*Osborn, 1980; Ferron et al., 1998; Olbers et al., 2012*).

It is commonly assumed that the buoyancy flux $\overline{w'\rho'}$ can be expressed as down-gradient diffusion using a turbulent eddy diffusivity K [m^2/s] multiplied by the density gradient $\partial\bar{\rho}/\partial z$ in analogy to the molecular diffusion of a tracer. Based on this assumption and the TKE Equation 1.1, *Osborn (1980)* derived the following expression for the turbulent eddy diffusivity K :

$$K = \frac{\Gamma\epsilon}{N^2}. \quad (1.2)$$

where N is the buoyancy frequency, ϵ is the dissipation rate of TKE, and the parameter Γ is related to the mixing efficiency which is usually approximated to equal 0.2 (*Osborn, 1980; Ferron et al., 1998*).

Although several studies were conducted quantifying the deep ocean mixing it is still under debate where and how deep and bottom waters are returned to the surface. According to *Munk and Wunsch (1998)* an energy input of 2.1 TW (1 TW = 10^{12} W) is required to upwell the 30 Sv (1 Sv = $1 \cdot 10^6$ m^3/s) of deep and bottom water formation, if mixing would be distributed uniformly in the oceans. This would require an average diapycnal diffusivity of $K \sim 10^{-4}$ m^2/s

1.1 Ocean Circulation, Heat Transport and Mixing

which exceeds the observed mixing rates by one order of magnitude (*Munk and Wunsch, 1998*). From a tracer release experiment as part of the World Ocean Circulation Experiment (WOCE) *Ledwell et al. (1993)* find a diapycnal diffusivity of $K \sim 1.1 \cdot 10^{-5} \text{ m}^2/\text{s}$ for the upper ocean below the winter mixed layer. *Toole et al. (1994)* report a similar diapycnal diffusivity of $K \sim 1 \cdot 10^{-5} \text{ m}^2/\text{s}$ to $K \sim 5 \cdot 10^{-5} \text{ m}^2/\text{s}$ derived from deep reaching vertical profiles of velocity and temperature microstructure obtained in the Northeast Pacific and Northeast Atlantic which they find representative for ocean interior conditions. In contrast, *Toole et al. (1994)* report downward increasing diffusivities close to a sea-mount of up to $K \sim 5 \cdot 10^{-4} \text{ m}^2/\text{s}$ at 3000 m depth (water depth approximately 3500 m) in the Northeast Pacific. Also *Polzin et al. (1997)* report elevated diffusivities in the South Atlantic above the Mid-Atlantic Ridge (MAR) exceeding $K \sim 5 \cdot 10^{-4} \text{ m}^2/\text{s}$ in the bottom-most 150 m, while they confirmed the level of $K \sim 1 \cdot 10^{-5} \text{ m}^2/\text{s}$ for all depths above abyssal plains in the Brasil Basin and above the South American Continental Rise. Elevated diffusivities are also found near the Equator at the MAR in the Romanche and Chain Fracture Zone (RFZ and CFZ), where the cold and fresh Antarctic Bottom Water (AABW) and the warmer and more saline Lower North Atlantic Deep Water (LNADW) in the layer above, pass through the MAR and enter the Sierra Leone and Guinea abyssal plains in the eastern Atlantic basin *Mantyla and Reid (1983)*. Diffusivities of $(100 - 1000) \cdot 10^{-4} \text{ m}^2/\text{s}$ were found at the northern exit of the RFZ in the bottom-most 1000 m where the AABW exhibit an abrupt warming and salinification from vertical mixing with the warmer and more saline LNADW above (*Mantyla and Reid, 1983; Polzin et al., 1996; Ferron et al., 1998*). The widely accepted interpretation was, that mixing is low above abyssal plains but the missing buoyancy flux would be compensated for by elevated mixing in the proximity of rough topography.

In a global study *Kunze et al. (2006)* confirm the low diffusivities of $O(10^{-5}) \text{ m}^2/\text{s}$ in the upper ocean for all ocean basins, and elevated diffusivities up to $O(10^{-4}) \text{ m}^2/\text{s}$ in the bottom 1000 m in the North Atlantic and Southern Ocean. They also report high diffusivities to extent into the pycnocline over rough topography accompanied by strong near-bottom flow. The findings of *Kunze et al. (2006)* suggest an average diffusivity which is smaller than $10^{-4} \text{ m}^2/\text{s}$ by a factor of 2 – 3. They argue that their data include observations near rough topography and thus elevated topography induced mixing cannot provide the missing abyssal mixing. *Kunze et al. (2006)* furthermore note, that hydraulic flow through narrow passages could dominate abyssal mixing which was suggested by *Bryden and Nurser (2003)* although it would contradict the concept of kinetic energy driving the mixing rather than potential energy established by *Munk and Wunsch (1998)*.

Another wind-driven contribution to close the circulation is the upwelling in the Southern Ocean by Ekman suction and subsequent mixing near the surface (*Döös and Webb, 1994; Toggweiler and Samuels, 1998; Webb and Sugimoto, 2001*). *Marshall and Speer (2012)* present a revised circulation scheme with an upper and lower MOC cell (Fig. 1.2). According to this revised circulation scheme North

1 Introduction

Atlantic Deep Water (NADW), being less dense than AABW, flows southward in intermediate depth and is fueled by AABW from below. These studies argue that near-surface waters around Antarctica have the same densities as NADW such that it would not be necessary to bring the bottom waters up through the whole water column via mixing but only to the level of the deep waters at intermediate depth (Fig. 1.2). Based on this argumentation *Webb and Sugimoto* (2001) estimate an average ocean wide diffusivity $O(5 \cdot 10^{-5}) \text{ m}^2/\text{s}$ corresponding to 0.6 TW to be sufficient to close the circulation.

Although the circulation is apparently closed by adiabatic upwelling in the Southern Ocean, mixing associated to rough topography which occurs at depth levels of NADW as well as AABW, is not fully understood. It was commonly explained by topography-induced breaking of internal waves which are generated by (tidal) currents interacting with the topography. More recent findings support the view that the strongest mixing does not occur above rough topography but inside deep ocean channels (*St. Laurent et al.*, 2001; *Thurnherr et al.*, 2005; *Thurnherr*, 2006; *St. Laurent and Thurnherr*, 2007). The observations that exist to date in the vicinity of or inside channels on mid-ocean ridges suggest that the bottom-intensified along-channel currents are directed uphill (*Ledwell et al.*, 2000; *Thurnherr and Speer*, 2003; *Thurnherr et al.*, 2005; *St. Laurent and Thurnherr*, 2007; *MacKinnon et al.*, 2008). All of these studies show an along-channel decrease of density in the direction of the flow indicating strong mixing. Such a setting is reported by

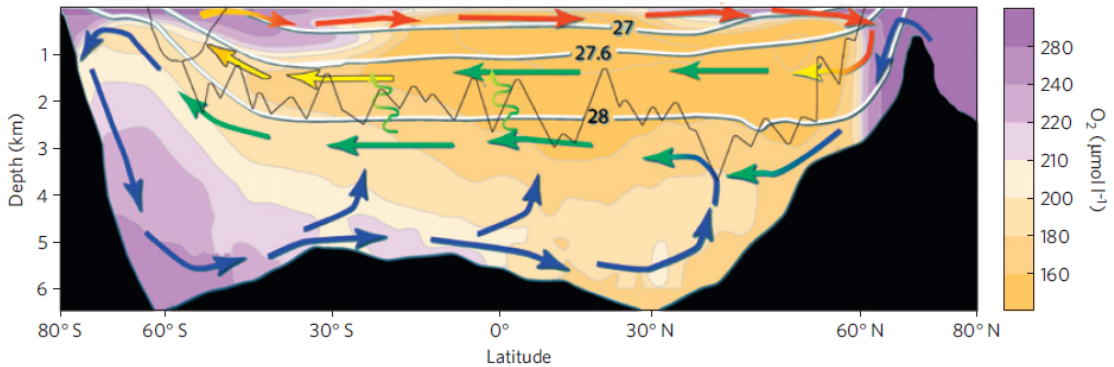


Figure 1.2: Schematic diagram by *Marshall and Speer* (2012) of the upper and lower cell of the global MOC emanating from the northern and southern polar seas, respectively. Colored arrows indicate lighter mode and thermocline water (red), upper deep water (yellow), deep water including NADW (green) and bottom waters (blue). Squiggly arrows indicate topography induced mixing. Density surface 1027.6 kg/m^3 roughly separates the two cells (blue-white line, natural density, *Marshall and Speer* (2012)). Colored contour-plot indicates the zonally averaged oxygen distribution. The jagged, black line indicates the depth of the MAR and the Scotia Ridge (just downstream of Drake Passage) in the Southern Ocean. Black indicates the depths of the ocean basins and of the overflows in the North Atlantic.

1.1 Ocean Circulation, Heat Transport and Mixing

Thurnherr et al. (2005) for a zonal channel on the western flank of the MAR near 22° S in the Brazil Basin (Fig. 1.3). They show 80% of the dissipation of turbulent kinetic energy below 2000 m to occur inside the channel below the channel-wall crest. Particularly elevated mixing is observed downstream of one cross-channel

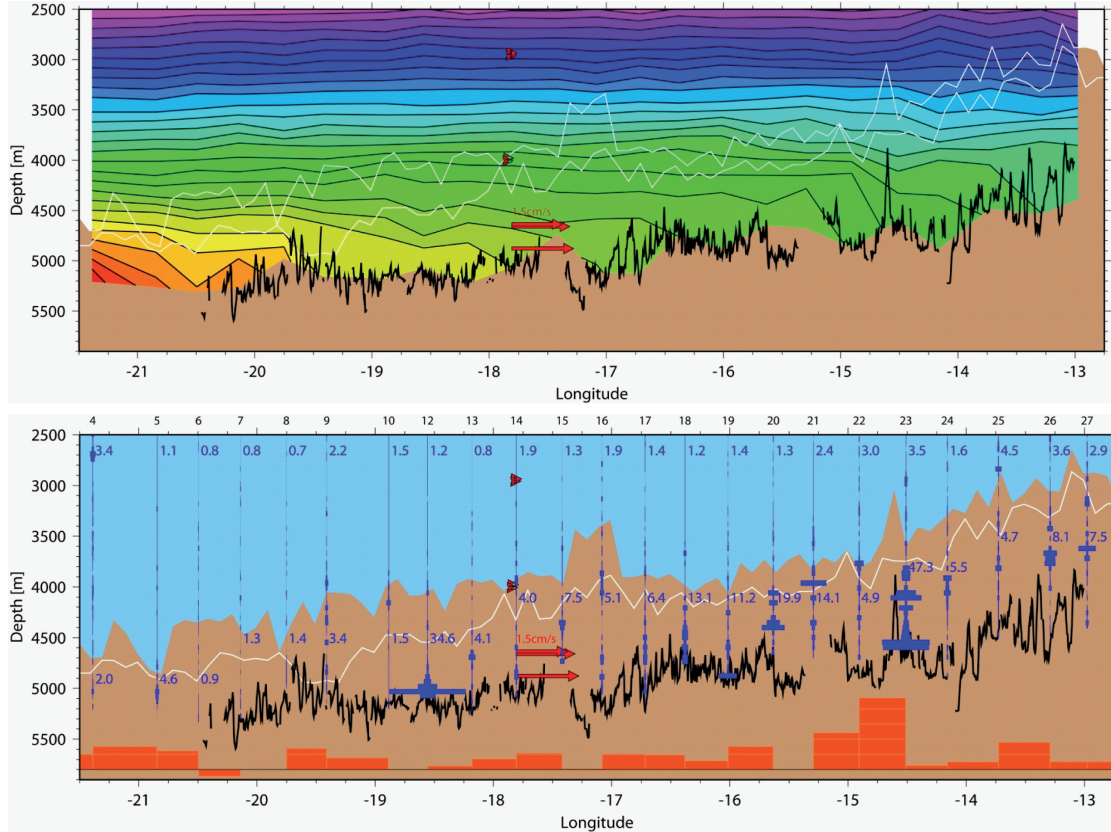


Figure 1.3: Flow, density (upper panel), and dissipation distribution (lower panel) in a ridge-flank channel on the western flank of the MAR in the south Atlantic near 22° S from *Thurnherr et al.* (2005). Dissipation profiles with station numbers above the panel show the 50-dbar-averaged dissipation rate displayed as horizontal bars with a peak value at station 12 of $3.2 \cdot 10^{-8}$ W/kg. Depth-averaged dissipation rates between 2000 m and the mean depth of the two channel walls are printed next to the profiles near 2700 m in units of $1 \cdot 10^{-10}$ W/kg. The numbers printed inside the channel correspond to the mean dissipations below the channel-wall crests. Red arrows near $17^\circ 45'$ W shows the along-channel flow from a two year current-meter record-mean. Horizontal density gradients above the blocking topography indicated by blocks below the channel floor. Each density-gradient block represents a value of $1 \cdot 10^{-7}$ kg/($\text{m}^3 \cdot \text{m}$), twice the temporal variability; blocks above the zero line (at 5800 m) indicate eastward-decreasing densities. The jagged solid line shows the axial depth of the channel between the stations. Upper panel: The topography is shaded up to the channel depth. The white line show the levels of the lower and upper channel wall. Contours denote density. Lower panel: The channel-wall topography is shaded up to the peak of the higher of the two lateral walls; the white line shows the level of the lower wall.

1 Introduction

sill which blocks the along-channel flow up to a depth of 1000 m above the channel floor. Several sills are observed in the channel but dissipation measurements are available only close the one sill. The magnitude of the along-channel density gradient with a maximum of $4.7 \cdot 10^{-7} \text{ kg}/(\text{m}^3 \cdot \text{m})$ is reported to be correlated with the flow across such sills (*Thurnherr et al.*, 2005). Processes leading to elevated mixing associated with flows across sills in the channel could be e.g. shear instabilities, topographic lee waves or hydraulic jumps (*Thorpe*, 2005). These sill related processes can be modulated in strength by the tides (*Helfrich*, 1995; *Dale and Inall*, 2015) such that the modulation of the dissipation rates in the tidal cycle as observed by *Ledwell et al.* (2000) and *St. Laurent et al.* (2001) is not necessarily confined to the breaking of tidally-induced internal waves. High dissipation rates downstream of sills might, even if modulated by tides, also be sustained by the mean flow. *Thurnherr et al.* (2005) showed that much more energy was found in the low-frequency flow along the channel than in the tidal band. Similar settings with along-channel density gradients have been observed in most of the channels on the MAR flank in the south Atlantic and it has been shown that they can be maintained by a balance of horizontal advection towards the ridge crest and vertical eddy diffusivity (*Thurnherr and Speer*, 2003). Based on topographic data *Thurnherr et al.* (2005) estimate that about 1000 channels exist on slow spreading ridges with $O(10^4)$ sills. If they all show similar flow and hydrographic conditions, sill overflow with associated mixing might be present in all of them. At least nine such channels are found in a 2° stretch of the MAR rift valley near 37° N . Indications for sill overflow was observed in four of these channels but probably occurs in all of them (*St. Laurent and Thurnherr*, 2007). Using dissipation rate estimates observed in one of these channels *St. Laurent and Thurnherr* (2007) estimate the buoyancy flux occurring in this 2° stretch to equal a tenth of that occurring at RFZ. Scaled over the MAR in the greater North Atlantic this deep ocean channel overflow induced buoyancy flux equals that occurring at RFZ (*St. Laurent and Thurnherr*, 2007). This suggests the buoyancy flux associated to mixing in deep ocean channels at mid-ocean ridges to be important for the global ocean energy budget (*St. Laurent and Thurnherr*, 2007). Furthermore this suggests mixing at mid-ocean ridges to depend heavily on the local bottom topography arrangement.

However, the dynamics underlying the circulation and mixing processes in such channels are still subject of research. In contrast to studies in channels with sills which report of particularly elevated mixing rates and large horizontal density gradients associated with the flow over the sills (*Polzin et al.*, 1996; *Ferron et al.*, 1998; *St. Laurent and Thurnherr*, 2007; *Alford et al.*, 2013), the study by *MacKinnon et al.* (2008) report strong mixing in a channel without sills but with a strong along channel flow. They argue that the elevated mixing is the result of the interaction between the mean current and small-scale internal gravity waves and internal tides.

In a regime where mixing is the result of strong, possibly hydraulically controlled flow across a sill, mixing would be expected to be elevated downstream of the

sill (e.g. *Alford et al. (2013)*). *St. Laurent and Thurnherr (2007)* present evidence for hydraulically controlled sill-overflow but failed to show clear evidence for a downstream maximum of the dissipation rate. They used a vertically profiling technique (deep microstructure profiler, DMP) to infer the dissipation rate inside a deep ocean channel in the rift valley of the MAR near 37° N (rift valley denoted the hydrothermally active along-ridge channel in the middle of mid-ocean ridges). *St. Laurent and Thurnherr (2007)* report increasing dissipation rates towards larger depths, reaching values of nearly 10^{-6} W/kg close to the sea floor. The absence of a downstream maximum of the dissipation rate may be either caused by the limited horizontal/temporal coverage of the data or by other processes involved in the dynamics of the overflow leading to elevated mixing upstream. As described above, similar along-channel flow across blocking sills associated with elevated mixing is present in several channels covering depths levels influencing the AABW (*Thurnherr et al., 2005; Alford et al., 2013*) to shallower sites with depths of only 2000 m (*St. Laurent and Thurnherr, 2007; Dale and Inall, 2015*). Processes in such channels thus control a large fraction of the mixing associated with rough topography in the bottom waters as well as in the deep waters (Fig. 1.2). Understanding the physics behind these processes is vital in understanding topography associated mixing which in turn is crucial in improving climate models by better parameterization of mixing processes.

1.2 The Aim of this Thesis

This thesis concentrates on physical processes associated with mixing close to a sill blocking the along-channel flow. The cross-sill structure of the mixing is in the focus of the considerations. The same channel is studied here as was investigated by *St. Laurent and Thurnherr (2007)*. Physical processes leading to mixing up- and/or downstream are investigated to identify the regime controlling the mixing. In this context the presence of hydraulic jumps and internal waves is studied as well as their respective importance. Furthermore, the mean flow and the variability induced by tides is analyzed.

These objectives demand a data set of high resolution, both temporal as well as spatial, above rough topography in the deep ocean. In order to acquire a data set which meets these criteria, a near-sea-floor circulation and mixing experiment was undertaken containing classical lowered and moored observations as well as temporal and spatial high resolving, horizontal mapping of several oceanographic parameters. The key instrument of this study is a horizontally operated microstructure probe (MicroRider, MR) attached to a deep diving autonomous underwater vehicle (AUV). This is the first successful realization of horizontal, deep ocean, AUV based, dissipation measurements. The MR is used the first time on the AUV *Abyss* so that data processing software had to be developed.

The targets and open questions addressed in the course of this thesis can be subdivided into a scientific-technological part including the development of the software

1 Introduction

for data processing for the MR deployed aboard AUV *Abyss* and a pure scientific part concerning the open questions regarding the physical processes in the deep ocean channel in the rift valley of the MAR near 37° N.

In the context of the scientific-technological part

- processing software for the MR-AUV system was developed,
- the potential of horizontal deep ocean velocity microstructure profiling was assessed.

In the context of the pure scientific part open questions concerning the deep ocean channel at the MAR near 37° N were investigated:

- Is the mixing distributed uniformly along the channel with respect to the position of the sill?
- What underlying physical processes control the mixing inside the deep ocean channel?
- Do tides influence the flow, density and mixing distribution throughout the channel?
- Is there evidence for internal waves and/or hydraulic jumps?
- Is there evidence for upstream propagating signals which could induce mixing at the sill or further upstream?

After an introduction of the data set underlying this study, the AUV, the MR as well as the arising challenges in operating these two instruments is given in Section 2. The method of inferring the dissipation rate of turbulent kinetic energy from the MR aboard the AUV *Abyss* is reported in Section 3. The findings regarding the above mentioned scientific questions are reported in Section 4, 5, and 6. Section 7 synthesis the results.

1.3 The Study Site

In the following two sections the study site at the Lucky Strike segment (LS) will be introduced. Firstly, the water masses and the topography influencing the region around the LS segment will be described and secondly, the LS segment will be introduced in more detail.

1.3.1 Hydrography and Flow at the Mid-Atlantic Ridge south of the Azores Islands

The Lucky Strike segment is located in the subtropical North Atlantic at the MAR near 37° N. In this region the MAR is sloping upwards approaching the Azores Island about 400 km northeast of the Lucky Strike segment (Figs. 1.4, 1.5, 1.7). Several studies have been conducted in this area describing hydrothermal activities and water mass properties which are summarized below (*Keller et al.*, 1975; *Wilson et al.*, 1995, 1996; *Thurnherr et al.*, 2008).

The upper water column south of the Azores Islands is dominated by the south-eastward flowing, meandering Azores current (AC in Fig. 1.5) which is reported to extend to a depth of 1700 m with a sharp front at about 34° N, south of the Lucky

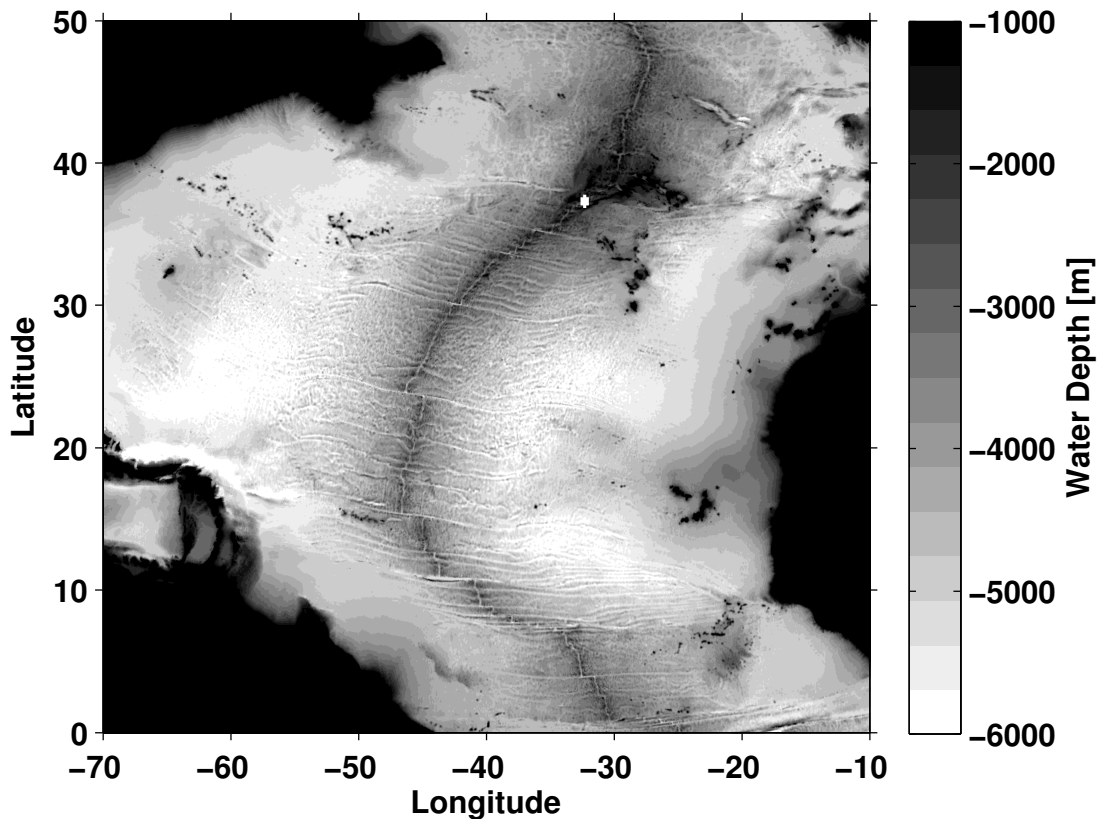


Figure 1.4: Topography of the North Atlantic (Etopo 1 (NOAA)). The Lucky Strike segment is marked by a white dot.

1 Introduction

Strike segment (*Wilson et al.*, 1995). North of the front the surface salinity is below 36.4 (standardly expressed without units) and the 15°C isotherm is found in shallower depth than 300 m with typical values of 100 m (*Gould, 1985; Thurnherr and Richards, 2001; Thurnherr et al., 2008*). Sea surface salinities were below 36.4 (Fig. 1.6a) and the 15°C isotherm was found between 100 and 200 m depth also in the data set underlying this study (Fig. 1.6a, for data set see Section 2).

The AC front apparently is the southern limit of the Mediterranean Water (MW) which exits the Gibraltar sill at 36° N and spreads towards the west between 700 m and 1200 m. Also in this study MW with salinities of up to 35.5 between 700 and 1000 m was found at the LS segment (Fig. 1.6a). The topography of the MAR

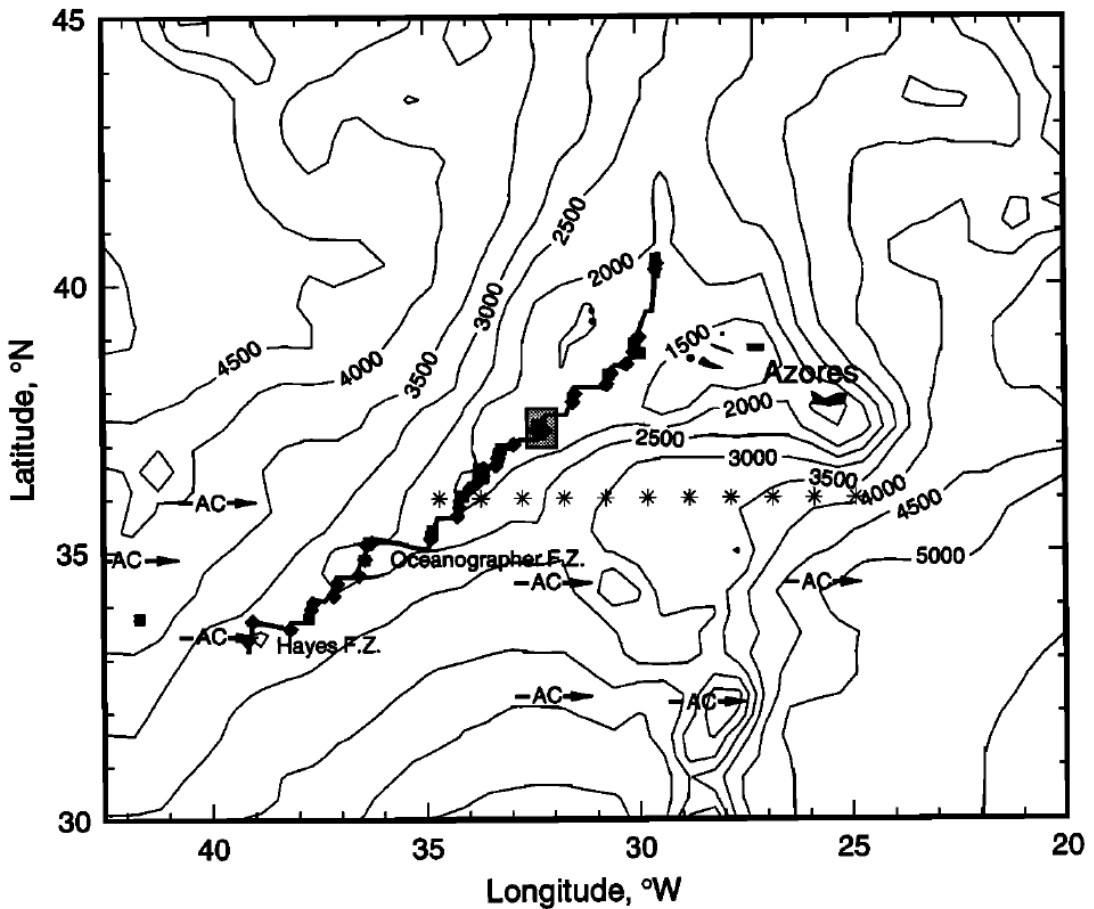


Figure 1.5: Map by *Wilson et al.* (1995) of the French-American Zero-Angle Photon Spectrometer and Rocks (FAZAR) cruise study region. The Lucky Strike segment is boxed. The bottom topography is given in meters. The thick solid line represents the ridge axis segmentation with stations marked by squares (sled) or diamonds (hydrocasts) (*Wilson et al.*, 1995). Positions of the Azores Current previously described in the literature (*Gould, 1985; Harvey and Arhan, 1988; Sy, 1988*) are marked AC. The region of the transitional water type described in the text is marked by asterisks. FZ stands for ‘Fracture Zone’. Topography with higher resolution is shown in Fig. 1.7.

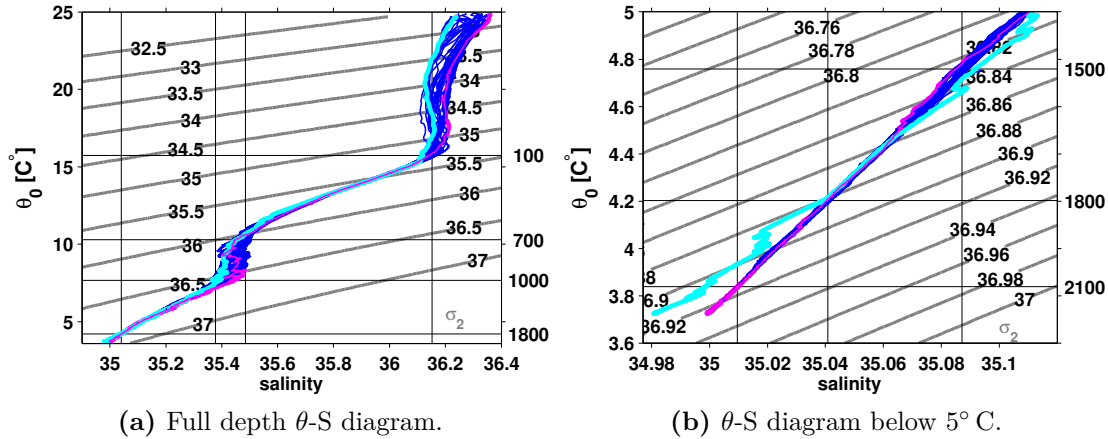


Figure 1.6: θ -S diagram from all CTD profiles (blue) obtained during the cruise P403 in the eastern channel of the Lucky Strike segment together with one profile from the southern (magenta) and one from the northern basin (cyan). Contour lines indicate potential density σ_2 (i.e. referred to 2000 dbar). Vertical and horizontal lines indicate specific depth levels given at the right [dbar].

inhibits zonal exchange in the region of the LS segment between the eastern and western basin of the north Atlantic up to a depth of 700 m as indicated by θ -S properties (Wilson *et al.*, 1995). They report increased temporal variability of the salinity above the topographic confinement which they attribute to pulses of cold subpolar water and MW water as was already suggested by Käse and Zenk (1987). The hydrographic properties below the topographic confinement of the MAR are reported to show differences between the water inside the rift valley and on the MAR flanks (Thurnherr *et al.* (2008), their Fig. 3, and Fig. 1.12a in this thesis). The density and buoyancy frequency inside the rift valley are reported to be smaller compared to the density and buoyancy frequency obtained at the outer rift valley walls in the same water depth. Thurnherr *et al.* (2008) concluded that this is the result of dense water being blocked at the inflow sills and diapycnal mixing inside the rift valley. Already Wilson *et al.* (1996) stated that they expect enhanced mixing in the rift valley as they found a variable background density field as well as homogeneous hydrothermal signals over a larger depth range than expected from the known hydrothermal vent field. Wilson *et al.* (1995) stated that a chemical tracer based study would be needed in this region to resolve hydrothermally induced anomalies, as the variations of temperature and salinity on isopycnals were too large to detect hydrothermal plumes.

In summary, the water inside the rift valley is reported to be less dense than the water outside the rift valley (Thurnherr *et al.*, 2008). There are indications for strong mixing inside the rift valley (St. Laurent and Thurnherr, 2007; Thurnherr *et al.*, 2008) and the water mass properties inside the rift valley are determined by blocking of dense water at the inflow sills and subsequent mixing inside the valley (Thurnherr *et al.*, 2008).

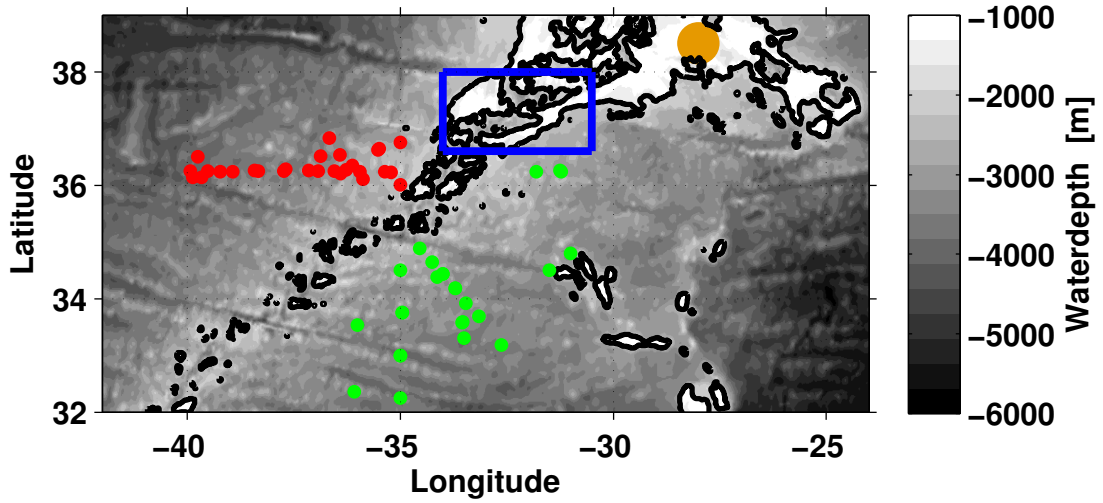


Figure 1.7: Topography (Etopo 1 (NOAA)) of the MAR from 33° N to 40° N with the 1800m isobath marked by a thick black line. The region including the Lucky Strike segment is marked by a blue box and expanded in Figure 1.8. Stations from the World Ocean Database from the eastern and western North Atlantic are marked by green and red dots, respectively. The Azores Islands are marked by an orange dot.

The near bottom flow inside the rift valley was directly observed by *Keller et al.* (1975) for 46 d in October 1973 at a sill south of the LS segment (lower left box Fig. 1.8). For two of their three current meters (red dots lower left box Fig. 1.8) average velocities of 2.6 cm/s and 8.2 cm/s with maximum values of 14.4 cm/s and 24.2 cm/s are reported. The instruments recorded predominantly north to north-eastward flow, following the orientation of the rift valley, while one current meter showed episodic return flow on semi-diurnal time scales. The return flow was ob-

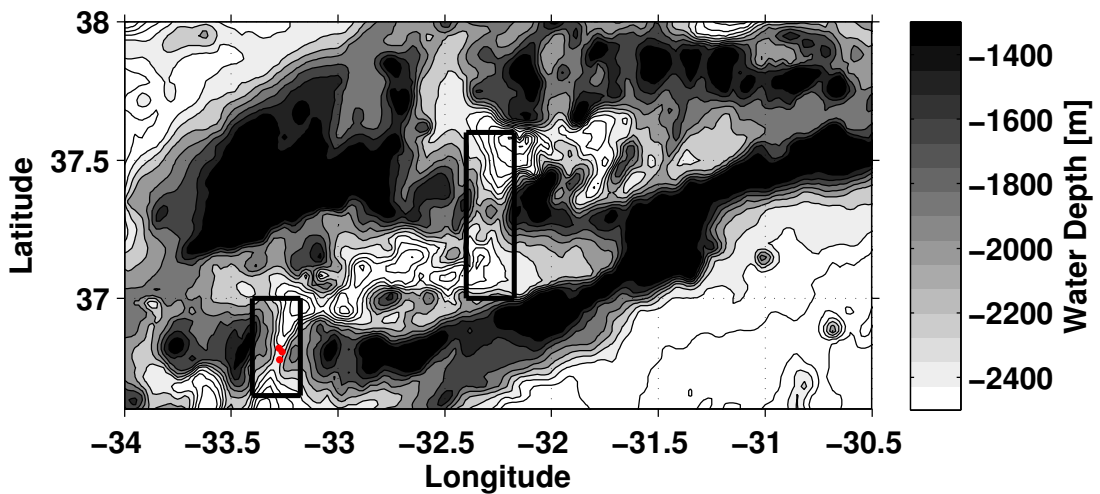


Figure 1.8: Topography of the rift valley 400 km south of the Azores (Etopo 1 (NOAA)). The Lucky Strike segment (center of the plot) and the FAMOUS study site reported in *Keller et al.* (1975) (lower left corner) are marked by a box.

served at the site with the weakest mean flow on the western edge of the 4 to 5 km wide channel in the rift valley (*Keller et al.*, 1975). The unidirectional northward flow was observed at the center of the channel. Furthermore, the velocity records showed pronounced semi-diurnal variability superimposed on variations on longer time scales (their Fig. 2). Based on spectral analyses *Keller et al.* (1975) showed the semi-diurnal frequencies to be the most energetic signal, followed by their first harmonic. A weak signal at the inertial period (20 h) was also found. *Keller et al.* (1975) concluded that a mean northward current is superimposed on the tidally varying flow regime and speculated that this flow pattern is topographically controlled. Additionally *Keller et al.* (1975) reported on measurements from November 1972 also showing northeastward flow with a similar magnitude. They cautiously stated that this flow pattern seems to be persistent at least during October-December and subsequent studies indicate that this ‘rift valley circulation’ is persistent over time-scales of years to decades (*Thurnherr and Richards*, 2001; *Thurnherr et al.*, 2005; *Thurnherr*, 2006; *Thurnherr et al.*, 2008).

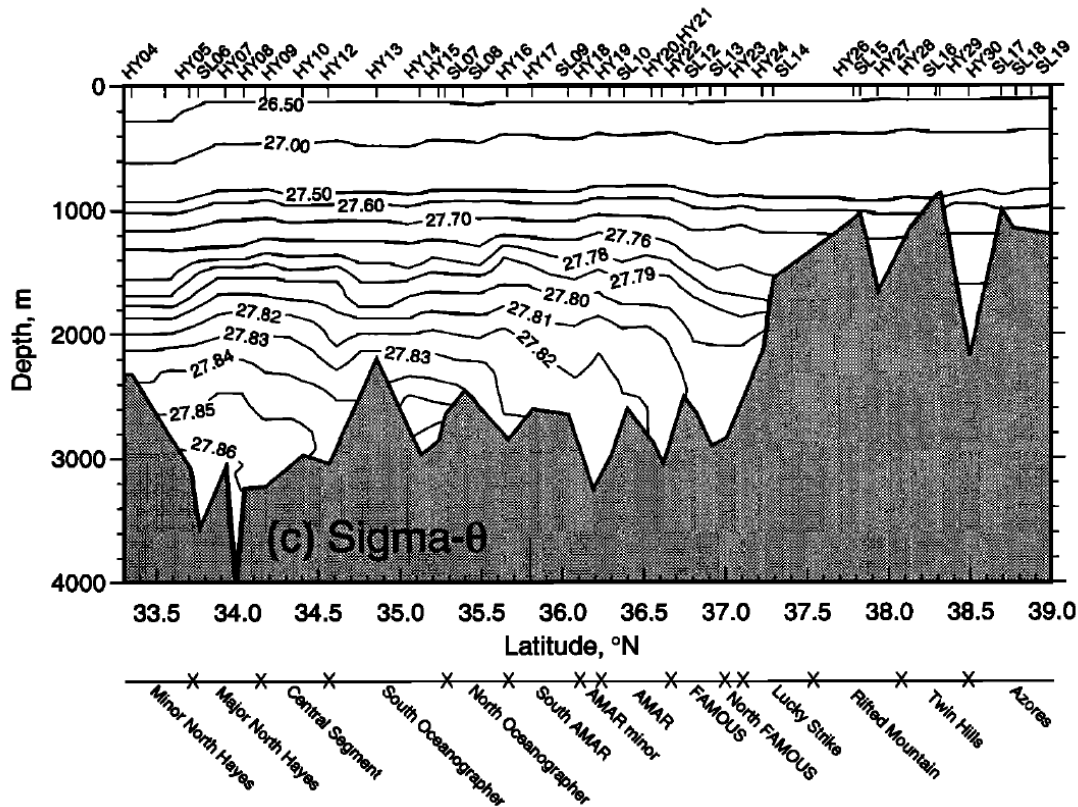


Figure 1.9: Section of potential density σ_θ for the FAZAR study region by *Wilson et al.* (1995) (their Fig. 3c). Stations are plotted along latitude, although they follow a line along the axis of the MAR (Station map in Fig. 1.5). The longitude changes from $39^\circ 10'$ W in the south (near Station hydrocast HY04) to $30^\circ 04'$ W in the north (near Station sled deployment SL19). The boundaries of the ridge segments are shown along the bottom. Station locations are designated by ticks at the top.

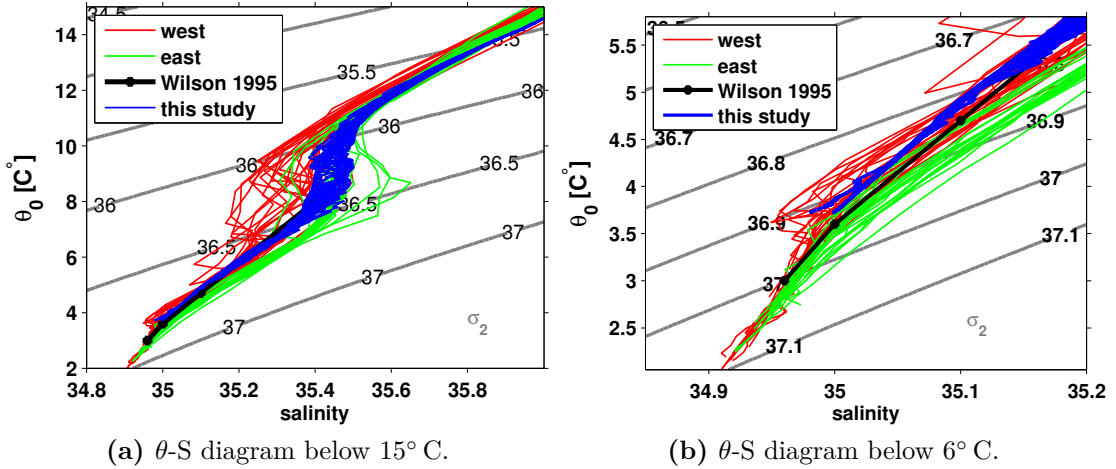


Figure 1.10: θ -S diagram from World Ocean Database profiles east (green) and west (red) of the MAR together with all CTD profiles obtained during the cruise P403 in the eastern channel of the Lucky Strike segment. The position of the World Ocean Database profiles is indicated in Figure 1.7. The θ -S properties reported by *Wilson et al.* (1995) is very roughly indicated as black line. Contour lines indicate potential density σ_2 (i.e. referred to 2000 dbar).

In such a setting with the water mass in a channel being determined at the inflow sills, with unidirectional flow inside a restricted channel as the rift valley, with strong mixing inside the channel, the density of the water is expected to decrease along the flow as observed in a zonal channel on the western flank of the MAR near 22°S in the Brazil Basin (*Thurnherr et al.*, 2005). For the MAR south of the Azores Islands between 33.5° N and 39° N the same was observed. *Wilson et al.* (1995) report decreasing densities in northward direction below 1700 m (Fig. 1.9). At the southern tip of their study region the densest water had a density of $\sigma_\theta = 27.86^i$ corresponding to $\sigma_2 \sim 37^{ii}$ with a salinity of less than 34.96 and a potential temperature below 3° C. This water mass properties indicate that the water entering the rift valley is LNADW (*Lherminier et al.*, 2010), which is a composite of Denmark Strait Overflow Water (DSOW) and Island Scotland Overflow Water (ISOW). The study by *Thurnherr et al.* (2002) reported the water inside the rift valley to originate from the eastern North Atlantic but the more recent study by *Thurnherr et al.* (2008) based on a larger data set does not show clear evidence for eastern or western origin. The comparison of the data underlying this thesis with data from the World Ocean Database did also not show clearly whether the water in the rift valley originates from the eastern or western North Atlantic (Fig. 1.10). The freshening of LNADW over the past decades which has been reported by *Curry et al.* (2003); *Thurnherr et al.* (2008) further increases the uncertainty.

ⁱ σ_θ – potential density $\rho - 1000 \text{ kg/m}^3$ referred to the sea surface. σ_θ is standardly expressed without units.

ⁱⁱ σ_2 – potential density $\rho - 1000 \text{ kg/m}^3$ referred to 2000 dbar. σ_2 is standardly expressed without units.

The density of the LNADW however, which enters the ridge valley decreases along the northward flow inside the ridge valley (Fig. 1.9). The mechanism causing the density decrease might be comparable to the one causing the lightening of the water in the zonal channel near 22° S in the Brazil Basin, although both channels seem rather different. The one channel being a zonal channel on the MAR flank near 22° S in depth of 4000 to 5500 m and the other being the meridional rift valley of the MAR between 33.5° N and 39° N. Despite these differences similar phenomena of along channel flow down the density gradients and sills blocking the along-channel flow associated with increased mixing point to potential similarities of physical mechanisms in both channels. Since the physical mechanisms controlling the mixing could not clearly be identified in previous studies, this thesis concentrates on such processes at the example of the Lucky Strike segment.

1.3.2 The Lucky Strike Segments Topography, Flow and Mixing as well their Impact on the greater North Atlantic

As pointed out in the previous paragraph the Lucky Strike segment is located in a region of strong density gradients at the MAR near 37° N. It consists of two deep basins, both approximately 2700 m deep and separated by the Lucky Strike volcano (upper right box in Fig. 1.8 and expanded in Fig. 1.11). Two meridional channels connect the two basins at the eastern and western side of the volcano, respectively. The volcano is hydrothermally active and has a minimum depth of 1540 m. The two channels are approximately equally deep with a sill depth of 2075 m and a width of 3 km in the eastern channel and a sill depth of 2060 m with a width of 5 km in the western channel (Fig. 1.11). Both channels have very steep walls with a mean rise over run of ≈ 0.5 (Thurnherr *et al.*, 2008). The southward inflow into

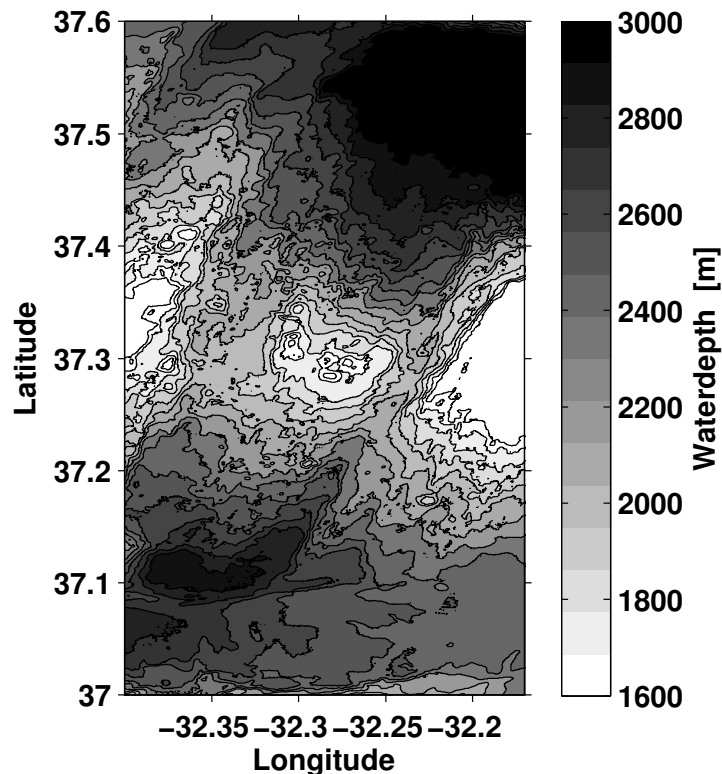


Figure 1.11: Topography of the Lucky Strike segment. The Lucky Strike volcano is located in the middle of the figure with meridional channels connecting the deep southern and northern basin east and west of the volcano.

1 Introduction

the LS segment occurs via the sill where the current observations by *Keller et al.* (1975) were conducted showing northward, along-valley flow (lower left box Fig. 1.8). As discussed in the previous paragraphs, there is evidence for longterm persistent northward flow along the rift valley of the MAR between 33.5° N and 39° N (*Keller et al.*, 1975; *Thurnherr and Richards*, 2001; *Thurnherr et al.*, 2005; *Thurnherr*, 2006; *Thurnherr et al.*, 2008) indicating that the water entering the LS segment originates from the inflow into the rift valley a few hundred kilometer further south (*Thurnherr et al.*, 2008). The deepest water mass observed in the LS segment during the course of this study revealed a density range of $\sigma_\theta = 27.804$ (northern basin) to $\sigma_\theta = 27.818$ (southern basin) which is in good agreement with the results reported by *Wilson et al.* (1995) (Fig. 1.9).

Both basins of the LS segment are connected to the western North Atlantic via sills with depths of about 1800 m (*Thurnherr et al.*, 2008). Below this depth level *Thurnherr et al.* (2008) observed a separation in density of the water inside from the water outside of the rift valley. From the eastern North Atlantic the LS segment is separated by the eastern rift-valley wall below 1300 m.

The flow at the LS segment is directed predominantly to the north along the channel with peak velocities of 20 cm/s and a mean of 10 cm/s observed in the eastern channel of the LS segment (*Thurnherr et al.*, 2008). In the western channel similar but weaker northward flow is reported. *Thurnherr et al.* (2008) estimate a transport of about 0.1 Sv below 1800 m into the northern Basin where it can only upwell as the basin is enclosed below 1800 m.

Studying the density difference between the southern and the northern basin *Thurnherr et al.* (2008) found a dipole structure with decreasing densities towards the north below 1900 m and increasing densities above. Here, in this thesis, the density gradient was also observed but with northward decreasing densities up to 1700 m (Fig. 1.12b). A similar structure was found 200 km to the south together with northward sill-overflow with a transport of 0.1 Sv and diapycnal diffusivities of 10^{-2} m²/s (*Thurnherr*, 2006; *Thurnherr et al.*, 2008). Such a dipole structure is typical for bottom intensified mixing and was also observed in the zonal channel near 22° S reported by *Thurnherr et al.* (2002).

As mentioned before *St. Laurent and Thurnherr* (2007) report on strong mixing in the LS segment near the sill close to the bottom. They estimate diapycnal diffusivities of $3 \cdot 10^{-3}$ m²/s in the bottom boundary layer reaching $3 \cdot 10^{-2}$ m²/s just downstream of the sill. With a water mass conversion of $2 \cdot 10^3$ kg/s at Lucky Strike alone and nine similar sills within 250 km at the rift valley *St. Laurent and Thurnherr* (2007) estimate the buoyancy flux in this area to equal a tenth of that occurring at Romanche fracture zone. They state that scaled over the MAR in the North Atlantic the buoyancy flux is as large as at the Romanche fracture zone. From analyses of the topography of the North Atlantic *St. Laurent and Thurnherr* (2007) assume 3% of the basin area to be occupied by ridges with similar deep channel. They further assume a diffusivity of $1 \cdot 10^{-5}$ m²/s for the region away from this ridges and a diffusivity of $3 \cdot 10^{-4}$ m²/s in and above deep channels. Based on this assumption they estimate the area-integrated diapycnal diffusive

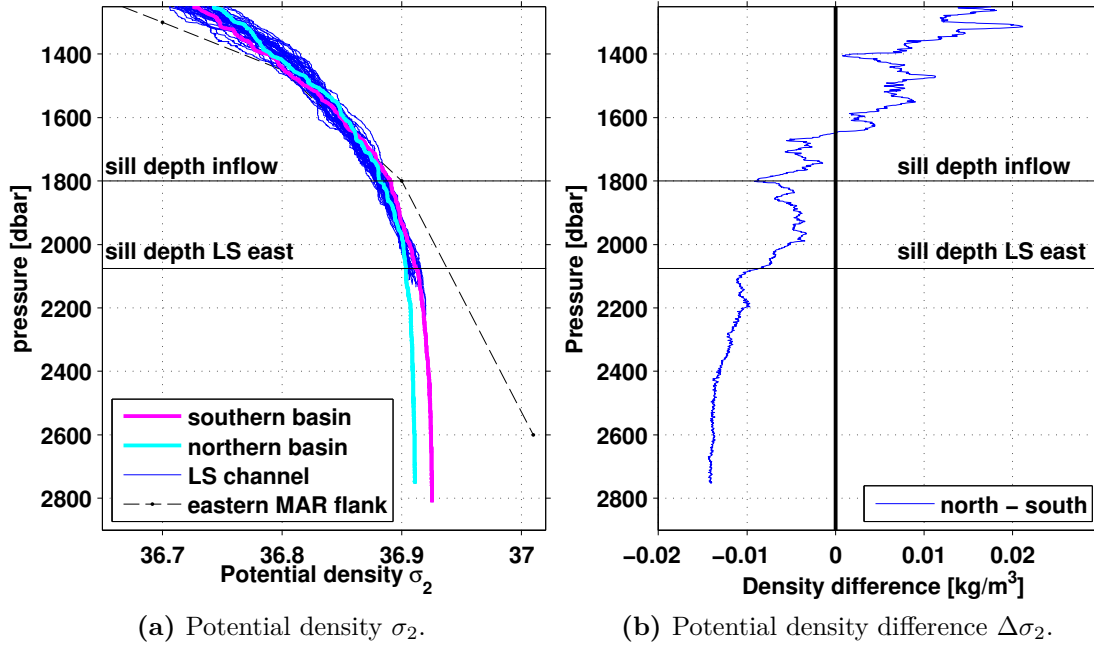


Figure 1.12: Potential density σ_2 (a) from all CTD profiles obtained in the eastern channel of the Lucky Strike segment together with one profile from the southern (magenta), one from the northern basin (cyan), and one profile with the approximate density-depth distribution found on the eastern MAR flank reported by *Thurnherr et al.* (2008). b: Density difference from southern to northern basin.

flux associated with these channels to equal the diffusivity of the rest of the basin. Understanding the deep mixing processes at sites as the LS segment thus might be very important in understanding mixing of deep water masses.

1.4 Hydraulic Jump and Froude Number

In the next paragraphs hydraulic jumps and the Froude Number are introduced as they are one of the central aspects for the dynamics examined throughout this thesis. Since hydraulic jumps have been studied for more than 150a only recent studies are mentioned below.

A hydraulic jump is a phenomenon of rapidly varying flow where the flow speed and flow depth of the flow change (e.g. *Whitehead* (1998); *Thorpe* (2010); *Olbers et al.* (2012)). Hydraulic jumps occur in e.g. man made channels, spillways and rivers. A common example of a hydraulic jump is the circular hydraulic jump which occurs in a horizontal sink.

The hydraulic jump is the transition region where the flow regime changes from ‘supercritical’ flow associated with large flow speed (u_1 in Fig. 1.13) and small flow

1 Introduction

depth (h_1 in Fig. 1.13) to ‘sub-critical’ flow associated with low flow speed (u_2 in Fig. 1.13) and large flow depth (h_2 in Fig. 1.13). The transition may occur due to deceleration of the flow originating from e.g. friction or a change of the steepness of the underlying slope.

Across the hydraulic jump mass, volume and momentum have to be conserved if no entrainment occurs. Furthermore energy cannot be gained over the jump i.e. energy is either constant or transformed by mixing (*Thorpe, 2010*).

A dimensionless parameter used to describe the flow regime of a given flow is the Froude Number Fr . It is defined as the relation of the flow speed to the speed of long gravity waves $c = \sqrt{gH}$. For uniform flow u of depth H the Froude Number can be given as (*Olbers et al., 2012*):

$$Fr = \frac{u}{\sqrt{gH}}. \quad (1.3)$$

For a two layer system consisting of a bottom layer of thickness h and density $\rho + \Delta\rho$ flowing at an average velocity \bar{u} below a motionless layer ($u = 0$) of density ρ the reduced gravity $g' = g\Delta\rho/\rho$ has to be used such that:

$$Fr = \frac{\bar{u}}{\sqrt{g'h}}. \quad (1.4)$$

In supercritical flow the Froude number is $Fr > 1$ indicating the flow speed to exceed the speed of long waves i.e. no wave propagation is possible in upstream direction. In sub-critical flow the Froude Number is $Fr < 1$, the speed of the waves is larger as the speed of the flow i.e. waves can propagate in upstream direction.

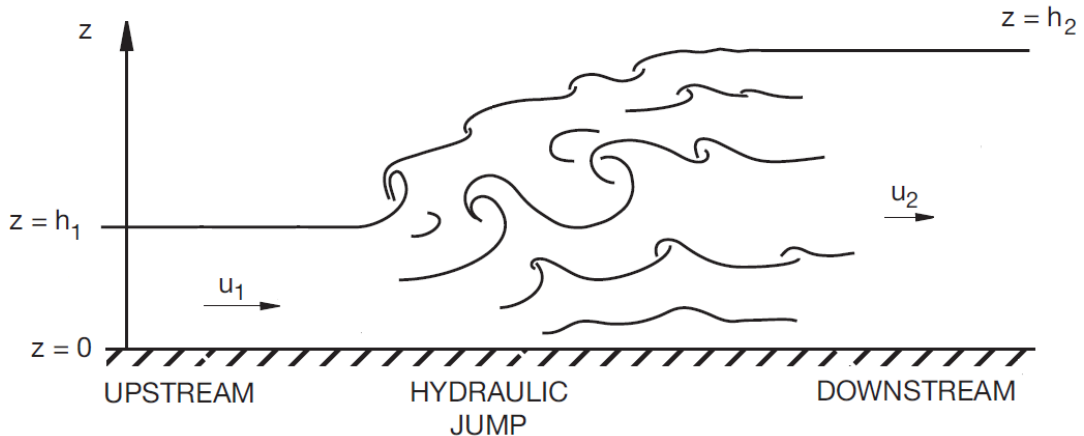


Figure 1.13: Sketch of a hydraulic jump in uniform flow from left to right over a flat surface at $z = 0$ based on *Thorpe (2007)*. The water velocity and depth upstream is u_1 and h_1 , while it is u_2 and h_2 downstream, respectively with $u_1 > u_2$ and $h_1 < h_2$.

1.4 Hydraulic Jump and Froude Number

A hydraulic jump can have different amplitudes depending on the initial flow velocity (u_1 in Fig. 1.13) upstream of the jump. A rough definition is given by *Chow* (1959) for different ranges of Froude Numbers (the ranges are not to be understood as clear-cut but as overlapping depending on local conditions (*Chow*, 1959)). *Chow* (1959) define a hydraulic jump with Froude Numbers of $Fr = 1 - 1.7$ as a ‘Undular jump’ which shows undulations at the surface (Fig. 1.14). Most of the jumps energy is carried downstream by the undular waves and only little dissipation occurs at the jump location (*Thorpe*, 2010). The range of $Fr = 1.7 - 2.5$ is called a ‘weak jump’. A weak jump apparently is associated with small rollers at the surface, low energy loss and a relatively smooth surface downstream (Fig. 1.14). In an ‘Oscillating jump’ more energy is lost to dissipation of turbulent kinetic energy and an oscillating jet of irregular period is formed ($Fr = 2.5 - 4.5$). Such a jump damages the bottom due to erosion. For a hydraulic jump with Froude Numbers in the range of $Fr = 4.5 - 9$ the location of the jump is relatively independent from the downstream water depth. It is associated with dissipation rates of 45 to 70 % of the jump energy. This jump is called a ‘steady jump’. A stronger jump with Froude Number $Fr > 9$ is called a ‘strong jump’. It shows a rough surface and generates waves downstream originating from water rollers generated by the jet. Up to 80 % of the energy may be dissipated (*Chow*, 1959).

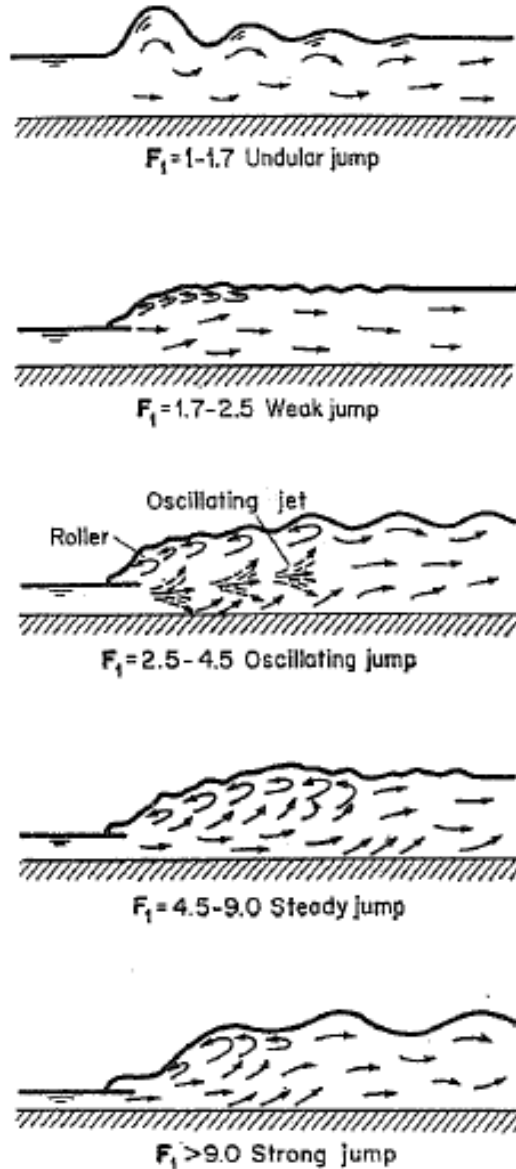


Figure 1.14: Sketch of hydraulic jumps of different amplitude by *Chow* (1959) (their Fig. 15-2).

The hydraulic jumps and Froude Number ranges mentioned above apply for a flow of uniform density and velocity in a rectangular channel. The situation is more complex in stratified and sheared flow as it occurs in the ocean (*Thorpe*, 2010). Mixing in the transition region and entrainment from the layer above change the density and velocity profiles downstream of the jump.

1 Introduction

In a model study conducted by *Thorpe* (2010) the conditions under which a stationary hydraulic jump can exist in a system of stratified and sheared flow, are evaluated. In the model a lower layer of stratified and sheared flow is situated below a motionless layer of uniform density. A Froude Number is defined depending on the vertical structure of the flow and density which, according to *Thorpe* (2010), is similar but not equal to the Froude Number defined in Equation 1.3 or 1.4. Using the conservation of mass, volume, and momentum flux across the hydraulic jump without entrainment or a change in isopycnal levels, he finds a Froude Number range ($Fr_* < Fr < Fr_c$) where a transient, i.e. a non-stationary hydraulic jump can form. Fr_* is the smallest Froude Number where an unstable hydraulic jump can form while Fr_c is the smallest Froude Number where a stable (stationary) hydraulic jump can form. In a hydraulic jump with the Froude Number in the range $Fr_* < Fr < Fr_c$, upstream wave propagation is possible, modifying the upstream flow, subsequently leading to disintegration of the hydraulic jump (i.e. the jump exists only temporarily).

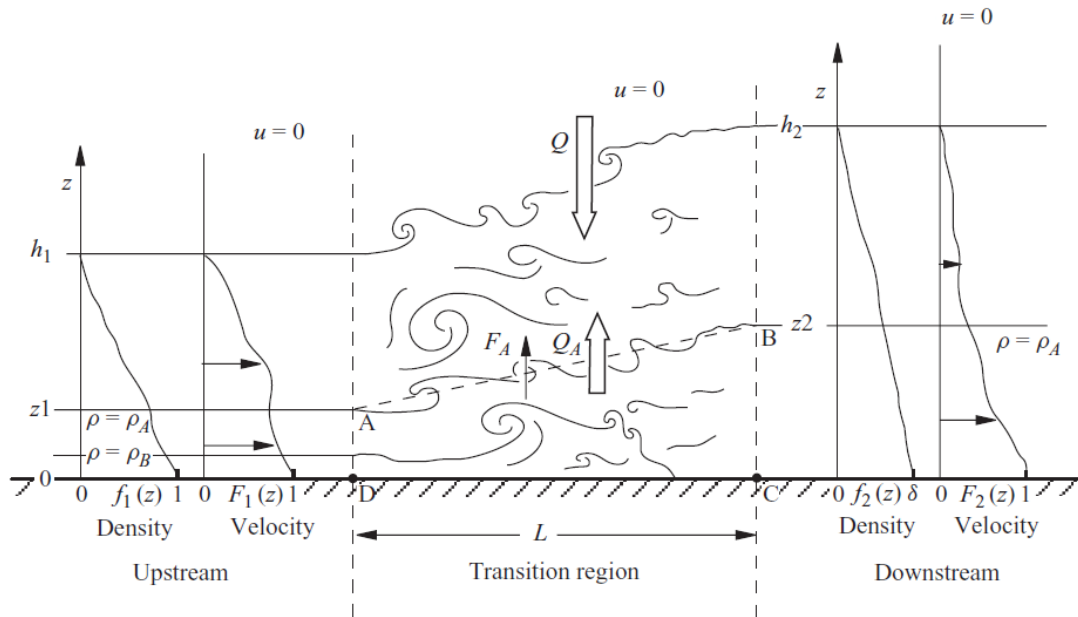


Figure 1.15: Sketch of a hydraulic jump in a stratified shear flow from left to right over a flat surface at $z = 0$ by *Thorpe* (2010). Example profiles of density (f) and velocity (F) up (f_1 and F_1) and downstream (f_2 and F_2) of the turbulent region denoted as ‘hydraulic jump’. The hydraulic jump is located in the transition region where volume may be entrained from the layer above (volume flux Q). Q_A and F_A denote the upward advective and diffusive flux. The isopycnal with the density $\rho = \rho_A$ enters the transition region at the depth $z = z_1$ while it leaves the transition region at the depth $z = z_2$. The dashed line AB denotes the theoretical mean location of the isopycnal surface within the turbulent transition region.

In the model study both, density $f_i(z)$ and velocity $F_i(z)$ are functions of the vertical coordinate z , where $i = 1$ describes the upstream, and $i = 2$ describes the downstream profile (Fig. 1.15, *Thorpe* (2010)). The parameter η describes the shape of the profiles ($0 < \eta < 1$, Fig. 1.16). The flow and density are constant at the bottom up to a depth of $z \leq \eta h$. Above, in the range of $\eta h \leq z \leq h$ the flow velocity and density decreasing linearly. The upper layer for $z \geq h$ is assumed to be stationary ($u(z) = 0$) and of uniform density. The two extreme cases $\eta = 0$ and $\eta = 1$ are, firstly $\eta = 0$ where the density decreases linearly over the lower layer (upper panel in Fig. 1.16) and secondly $\eta = 1$ where the density is constant over the lower layer, i.e. the case of $\eta = 1$ equals the ‘usual two layer case’ where both layer have uniform density.

In the model the parameter Q (Fig. 1.15) describes the downward volume flux entrained in the hydraulic jump, while Q_A and F_A denote the upward advective and diffusive flux of mass across the isopycnal within the hydraulic jump (Fig. 1.15). *Thorpe* (2010) examines the dependence of the entrainment, the energy flux and the jump amplitude (q , i.e. change in layer thickness across the jump $q = h_2/h_1$). He shows the entrainment, the energy flux and the jump amplitude to increase with increasing Froude Numbers. While hydraulic jumps with large Froude Numbers can exist only with entrainment, small hydraulic jumps can also occur without entrainment. In small hydraulic jump where the Froude Number Fr is only slightly greater than the minimum Froude Number Fr_* , turbulence is mostly carried downstream by the waves of the undular jump. In a hydraulic jump of larger amplitude a larger amount of energy is lost to turbulence at the location of the jump (*Thorpe*, 2010). The exact value of the critical Froude Number Fr_c and the minimum Froude Num-

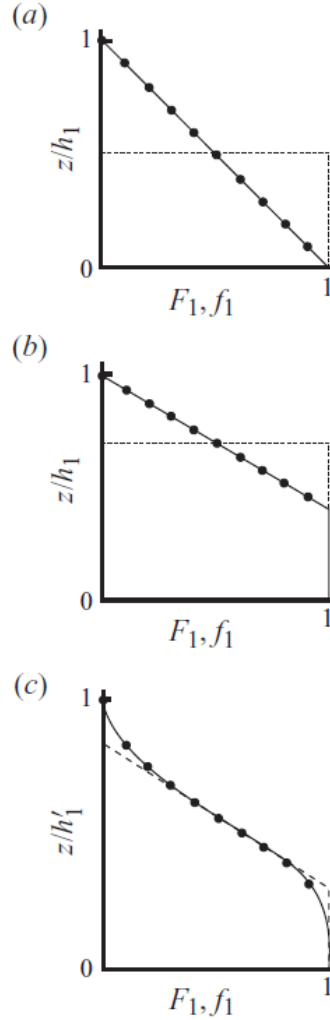


Figure 1.16: The dependence of the flow and density profile from the parameter η and the corresponding two-layer profiles (dotted) by *Thorpe* (2010). Profiles in (a) with $\eta = 0$, in (b) with $\eta = 0.4$, and in (c) the cosine profile given by the dashed line corresponding to $\eta = 0.4$.

1 Introduction

ber Fr_* depend on the exact shape of the flow and density profile upstream and downstream of the hydraulic jump (Fig. 1.17). The situation for $\eta = 1$ equals the two layer case where the density is constant over the lower layer. In that case the minimum and the critical Froude Number are even $Fr_* = Fr_c$ (Fig. 1.17). Note, that the Froude Number used by *Thorpe* (2010) is not necessarily equal to the definition given in 1.3 or 1.4 for which the critical Froude Number is about unity (*Lighthill*, 1967; *Whitehead*, 1998; *Thorpe*, 2010).

Throughout this thesis, Froude Numbers are computed following *Alford et al.* (2013) the same definition already given in Equation 1.4:

$$Fr = \bar{u} / \sqrt{g'H}, \quad (1.5)$$

where \bar{u} denotes the average flow speed, H the layer thickness and g' the reduced gravity $g' = g\Delta\rho/\rho$. The average flow speed, the layer thickness and the density were taken from the layer below the isopycnal $\sigma_2 = 36.893 \hat{=} \rho_1$ (Fig. 4.6) which was the isopycnal showing the most pronounced upward displacement as is shown in later paragraphs. For $\Delta\rho = \rho_1 - \rho_2$ for the reduced gravity, the difference of the before mentioned density ρ_1 and ρ_2 was used. For ρ_2 the average density of the layer between the isopycnals $\sigma_2 = 36.893$ and $\sigma_2 = 36.877$, the lowest nearly horizontal isopycnal, was used. Froude numbers were computed from station-averaged profiles to represent time average conditions, and from single stations. Whenever Froude Numbers are discussed in the following paragraphs they are given at the top of the corresponding figure.

For comparison of Froude Numbers computed here in this thesis with those reported by *St. Laurent and Thurnherr* (2007) for the same channel at the Lucky Strike segment, it should be noted that the study of *St. Laurent and Thurnherr* (2007) computed Froude Numbers from:

$$Fr_p = \frac{U}{NH}, \quad (1.6)$$

which can be inferred from Equation 1.5 using the reduced gravity $g' = g(\rho_2 - \rho_1)/\rho_1$ and the buoyancy frequency $N = -g/\rho \, d\rho/dz$ for a two layer system (*Ollbers et al.*, 2012). N and U are the depth averaged buoyancy frequency and flow speed of the lower layer of thickness H . Following *Thorpe* (2010) this definition is named the ‘pseudo Froude Number’ Fr_p and the critical value for Fr_p is assumed to be about unity (*Thorpe*, 2010).

Using Equation 1.6 *St. Laurent and Thurnherr* (2007) computed Froude Numbers over the layer below 1800 m. The situation observed by *St. Laurent and Thurnherr* (2007) might be comparable to the situation examined in the model study by *Thorpe* (2010) using $\eta = 0 - 0.4$ as parameter for the profile shape (*Thorpe*, 2010). The largest Fr_p found by *St. Laurent and Thurnherr* (2007) upstream of the sill was 0.92 which according to *Thorpe* (2010) is in the range of Fr_* and Fr_c ,

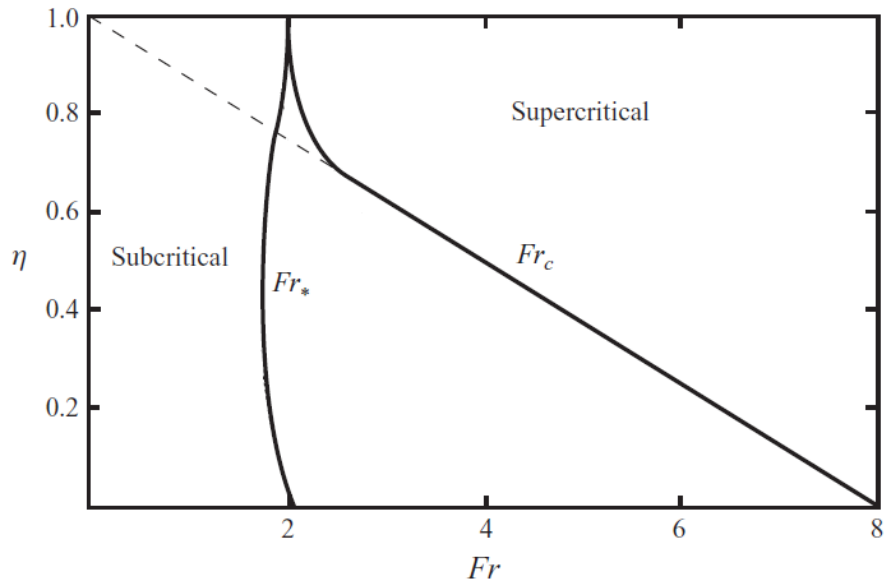


Figure 1.17: The Froude Number Fr_* and Fr_c as function of the parameter η following *Thorpe* (2010). The situation at $\eta = 1$ equals the two layer case where $Fr_* = Fr_c$.

thus indicating the existence of a undular hydraulic jump, which might decay due to upstream wave propagation.

In this thesis the Froude Numbers are used to characterize the flow regime and to indicate whether a hydraulic jump is likely to occur. The exact values of Fr_* and Fr_c are unknown as they depend on the flow and density profiles up- and downstream but they might be determinable with the model by *Thorpe* (2010) in future studies. The values will be referred to as near critical if they exceed unity as introduced by *Thorpe* (2010). Indications whether a hydraulic jump was observed can also be drawn from density contours as they ‘jump’ upwards in a hydraulic jump.

2 Data and Instruments

The data set underlying this thesis was obtained during the cruise P403 in August 2010 aboard *R/V Poseidon*. Different observational strategies were used to sample the deep ocean channel at Lucky Strike. With the autonomous underwater vehicle *Abyss* spatially and temporally high resolving shear and temperature microstructure data, as well as density data, were acquired in the horizontal, while the background hydrographic and flow conditions were monitored with classical lowered and moored platforms. The instruments, measurements, as well as processing methods and resulting data sets from lowered, moored, and AUV-based density observations are introduced in the following. The method of inferring dissipation rates from velocity shear obtained with the AUV *Abyss* derived in the course of this thesis will be introduced in Section 3. The reference time of all measurements throughout this thesis is the Universal Time Coordinated (UTC).

2.1 Shipboard Observations

Lowered conductivity, temperature, depth (CTD) and lowered acoustic Doppler current profiler (LADCP) measurements were carried out from *R/V Poseidon*. A *SeaBird SBE 9 plus* CTD was used mounted on a rosette together with one or two *Teledyne/RDI Workhorse* 300 kHz ADCPs (downlooking for casts 2 – 45 and additionally an upward looking unit for casts 46 – 51).

The CTD profiles were processed with standard GEOMAR software, have a resolution of 1 dbar and an accuracy of 0.002°C for temperature and 0.002 for salinity (standardly expressed without units, PSS-78). The density accuracy was estimated to be 0.0016 kg/m³ using Gaussian error propagation.

LADCP data were processed using the LADCP-processing software from *Lamont-Doherty Earth Observatory* (LDEO, processing software *Thurnherr*). Processed LADCP profiles have a resolution of 10 m.

The CTD/LADCP measurements were conducted mostly in the eastern channel of the LS segment (Fig. 2.1). They were grouped according to their position along the channel in eight grouped-stations: three upstream of the sill (U3-U1), one at the sill (S) and four downstream of the sill (D1-D4) (Table 2.1). The few stations in the western channel were not considered in this thesis. A map of all single stations with numbering can be found in the Appendix A.1.

The stations upstream of the sill were located in the center of the channel while the stations D2 and D3 downstream of the sill were distributed over a wider range such that they were subdivided into a western, a center, and an eastern station respectively. All LADCP derived velocities used throughout this study were converted

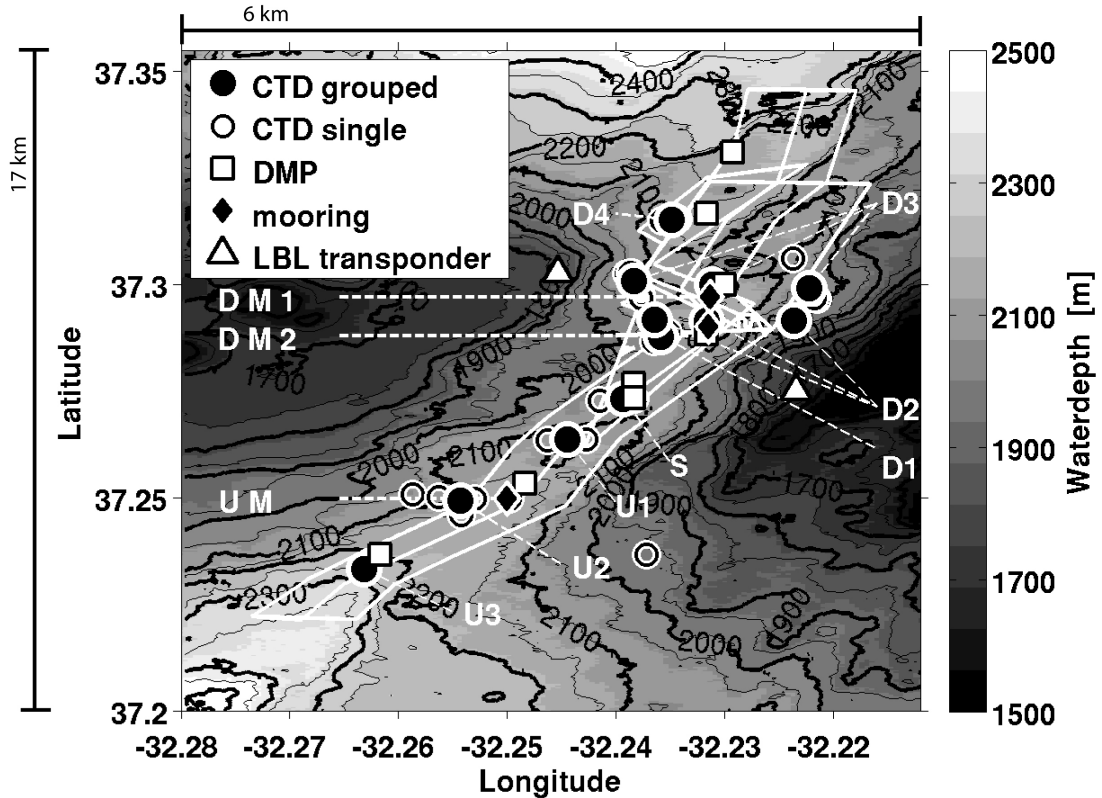


Figure 2.1: Eastern channel of the LS segment: position of lowered CTD/LADCP observations (full and empty circles), positions of the Deep Microstructure Profiler casts (DMP, empty squares) of the study by *St. Laurent and Thurnherr* (2007), the mooring positions upstream (UM) and downstream of the sill (DM1 and DM2, diamonds), the tracks of the successful AUV dives (white lines) as well as the positions of the long baseline positioning system transponders (LBL, empty triangles) for AUV navigation.

to channel following coordinates Section 2.2).

2.2 Moored Observations

Two moorings were deployed for the duration of the cruise (9 d), one upstream (UM) and one downstream (DM) of the sill (Fig. 2.1, for details regarding the mooring deployments see Table 2.2). The northern or downstream mooring (DM) was recovered after five days and immediately redeployed about 800 m further upstream. The first deployment period is referred to as DM1 and the second period as DM2. Both moorings were equipped with two *Seabird SBE 37* CTD recorders each (MicroCAT). One recorder was deployed at 24 m above the seafloor in each mooring and the second recorder was deployed at 110 m in the DM1 mooring and at 130 m in both, the DM2, and the UM mooring. Above the upper CTD recorder one downward-looking 300 kHz ADCP was deployed in each moor-

Group	Latitude [° N]	Longitude [° W]	Station #	Comment
U3	37.233	32.263	10, 14, 43	Upstream 3
U2	37.249	32.254	2, 11, 30, 31, 32, 41	Upstream 2
- e	37.237	32.237	45	east
U1	37.264	32.245	3, 42	Upstream 1
S	37.273	32.239	4, 16, 17, 18	Sill
D1	37.288	32.236	5, 15	Downstream 1
D2	37.293	32.233	33 - 36, 38 - 40	Downstream 2
- w	37.294	32.237	33, 36, 40	west
- c	37.292	32.232	34, 38	center
- e	37.291	32.224	35, 39	east
D3	37.300	32.231	6, 9, 19 - 29, 46	Downstream 3
- w	37.303	32.239	6, 9, 19, 22, 25, 28	west
- c	37.230	32.231	20, 23, 26, 29	center
- e	37.299	32.222	21, 24, 27, 46	east
D4	37.315	32.235	7, 12, 44	Downstream 4
western channel			47 - 51	

Table 2.1: Group- and single-station names and positions of shipboard lowered CTD and LADCP measurements.

ing (122 m, 142 m, and 134 m above the sea floor in the DM1, the DM2, and the UM mooring, respectively). The upstream mooring additionally contained one current meter (*Aanderaa RCM8*, RCM) at 25 m above the sea floor. The RCM can detect velocities larger than 2 cm/s and recorded the velocity with a sampling rate of 5 min.

The MicroCATs were operated with 45 s sampling interval. The data was calibrated using one calibration cast prior to the deployment. The error for the temperature was estimated to below 0.004 K while the error for the salinity was below 0.005.

The ADCPs were run with 8 m bin length and 10 pings per ensemble resulting in an accuracy of 0.6 cm/s per bin (*Datasheet*).

The ADCP deployed in mooring DM1 and DM2 was operated with 40 s per ensemble for most of the time. Only the first 1.6 h of the deployment the time per ensemble of the ADCP in mooring DM1 was set to 5.6 s. It was remotely changed and set to 60 s per ensemble for the next 48.2 h. Then it was changed again and set to 40 s time per ensemble for the rest of the deployment (DM1 2.8 d, DM2 3.8 d). The ADCP in the mooring UM was set to 20 s time per ensemble. All DM1 and DM2 ADCP data were interpolated to 20 s for consistency reasons.

Due to weak backscatter only bins 2 – 6 at the DM1 and the DM2 mooring were used, which corresponded to a depth range above the sea floor of 74 – 114 m at DM1 and 94 – 134 m at DM2. From the UM mooring only bins 2 – 5 were used. This corresponded a depth range of to 94 – 126 m above the sea floor. As only

2 Data and Instruments

4 – 5 bins were used, which cannot necessarily be assumed as independent, the accuracy of 0.6 cm/s per bin can be interpreted as upper bound of the accuracy of the bin-averaged velocity. The accuracy for the time-averages (Tables 4.1, 4.2, and 6.1) was estimated using the corresponding degrees of freedom (25 for DM and 59 for UM) to be 0.12 cm/s for the short time-series of the downstream moorings and 0.08 cm/s for the upstream mooring. The degrees of freedom were computed using the time-lag for zero autocorrelation. For most purposes the data were low-pass filtered with a cutoff frequency of 1/6 1/min to eliminate high-frequency noise without eliminating internal waves. The buoyancy frequency estimated from lowered CTD observations was about 1/100 1/min.

To compute the along-channel flow, the moored ADCP-derived meridional and zonal velocities were rotated in along-channel direction by 41°, 47° and 30° for the DM1, the DM2, and the UM mooring, respectively.

Mooring	Lat [° N]	Lon [° W]	Deployment [UTC]		Recovery [UTC]	
			Day	Time	Day	Time
UM	37.250	32.263	16/08/2010	18:10	25/08/2010	10:48
DM1	37.297	32.231	16/08/2010	11:00	21/08/2010	10:00
DM2	37.290	32.232	21/08/2010	17:40	25/08/2010	12:24

Table 2.2: Positions (latitude (Lat) and longitude (Lon)), deployment and recovery times of the upstream (UM) and downstream (DM1, DM2) moorings, respectively.

2.3 Autonomous Observations

A microstructure package, *MicroRider* (MR), attached to the autonomous underwater vehicle (AUV) *Abyss* from *GEOMAR* used for horizontal profiling, was the key instrument of this study. The AUV and MR as well as the mounting of the MR at the AUV, data processing, calibration, and the sampling strategy will be introduced in the following.

2.3.1 The AUV *Abyss*

The AUV *Abyss* is a Remote Environmental Measuring UnitS (REMUS) vehicle manufactured by *Hydroid Inc.* that can be operated in water depths up to 6000 m. It is 4 m long and has a maximum diameter of 0.66 m. A pumped CTD (*Seabird SBE 49 FastCat*) is mounted to the side of the AUV. The CTD was operated at a sampling rate of 5 Hz.

For navigation at the surface the AUV is equipped with a Global Positioning System (GPS) receiver while the AUV can be operated using a Wireless Local Area Network (WLAN) from the ship. When submerged the Inertial Navigation System (INS, *Kearfott*) determines the position via dead reckoning. A Doppler Velocity

Log (DVL, *Teledyne RDI Workhorse Navigator 300 kHz*) for bottom tracking and altitude measurements allows to determine the speed and distance over ground as long as the AUV is within a range of 200 m from the sea floor. The DVL and a pressure sensor (*Paroscientific 8B7000*) used for navigation were operated at 1 Hz. For the navigation at depth the AUV is equipped with a long baseline positioning transponder (LBL, *Hydroid Inc.*). The position of the AUV is determined by communication with at least two short-term moored LBL transponders which need to be calibrated from the ship. During the cruise P403 two bottom-mounted transponders were deployed (Fig. 2.1). The AUV was operated with a speed of 1.5 m/s.

Preprocessing and calibration of AUV-CTD, altimeter and pressure data was done by AUV software. A correction regarding the time-delay between temperature and salinity sensor, adapted from processing of lowered CTD data, as well as a correction regarding the position of the AUV, is applied as reported in the master thesis by *Schaffer (2013)*. Additionally, the data was low-pass filtered (cutoff frequency of 1/6 Hz and interpolated onto a uniform time grid (1 s).

All data were checked for events that might compromise data quality, for instance when the AUV came too close to the bottom and the propeller stopped causing the AUV to ascend. The MR and CTD data were exclusively used from times where the AUV moved with constant speed through the water.

2.3.2 Microstructure Profiler, Mounting and Vibrations

The *MicroRider* (MR) was manufactured by *Rockland Scientific International* (RSI, *MicroRider*) for use on the AUV *Abyss*. It was equipped with two airfoil velocity shear probes (*Siddon, 1971; Osborn, 1974; Lueck et al., 2002*), two fast-responding thermistors (FP07), a pressure sensor (Pa 10L/600Bar from *Keller*), and a three-dimensional accelerometer. The latter was used in data processing to reduce the AUV-induced noise in the velocity shear data (Section 3). The microstructure shear and temperature sensors as well as the acceleration sensors were configured to sample at 512 Hz. The MR pressure sensor sampled at 64 Hz.

The MR consists of two separate pressure cases to equally distribute the weight on each side of the AUV. One pressure case houses the sensor electronics while the other one contains the data storing unit. The power for the MR was supplied by the AUV.

The pressure cases were attached to the AUV using a steel rod underneath the front end (Fig. 2.2a) and additional stabilizing bars to the sides of the AUV (Fig. 2.2b). The MR cannot be mounted in or directly at the AUV nose, as it is the case in some other studies (*Levine and Lueck, 1999; Boyd et al.*), because the AUV nose is part of the launch and recovery system. The sensors were located 280 mm behind the AUV nose at a distance of 350 mm away from the AUV hull. The steel rod, connecting both pressure cases ('main rod' Fig. 2.2b) was mounted 740 mm behind the AUV nose. As the AUV is tapered, it has a larger diameter at the

2 Data and Instruments

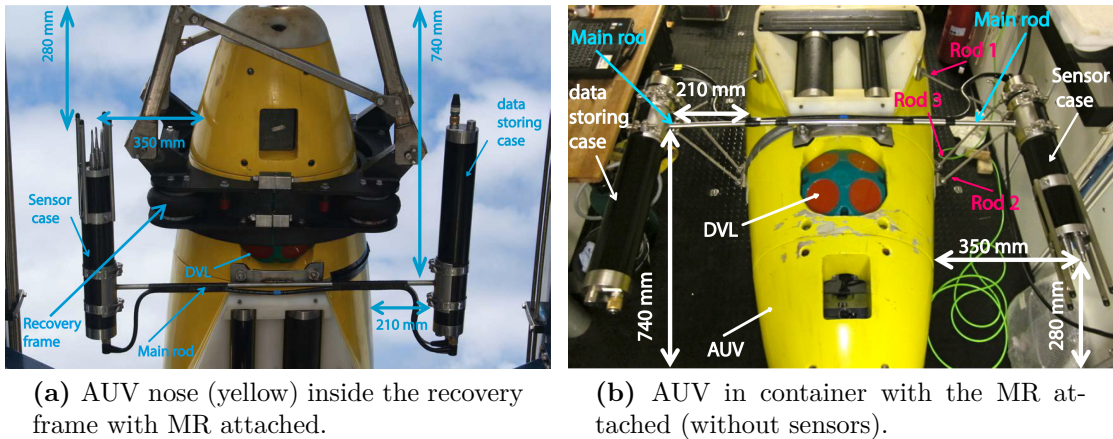


Figure 2.2: AUV on deck with only the main steel rod underneath the AUV front end (a) and inside the container with all steel rods connected as used for Dives 8 and 9 (b).

mounting position such that the distance of the pressure cases to the AUV hull here was 210 mm only.

Figure 2.2 shows the AUV during recovery with the MR attached. The AUV is pulled up and the nose is fixed inside the round, black recovery frame. Once the AUV nose is fixed, the outside, quadratic frame (Fig. 2.3c) is folded backwards into the horizontal and the AUV is back on deck.

During the first dive, only one steel rod, the main rod, was used to mount the MR (Fig. 2.2a). The mounting was modified during the cruise to further reduce

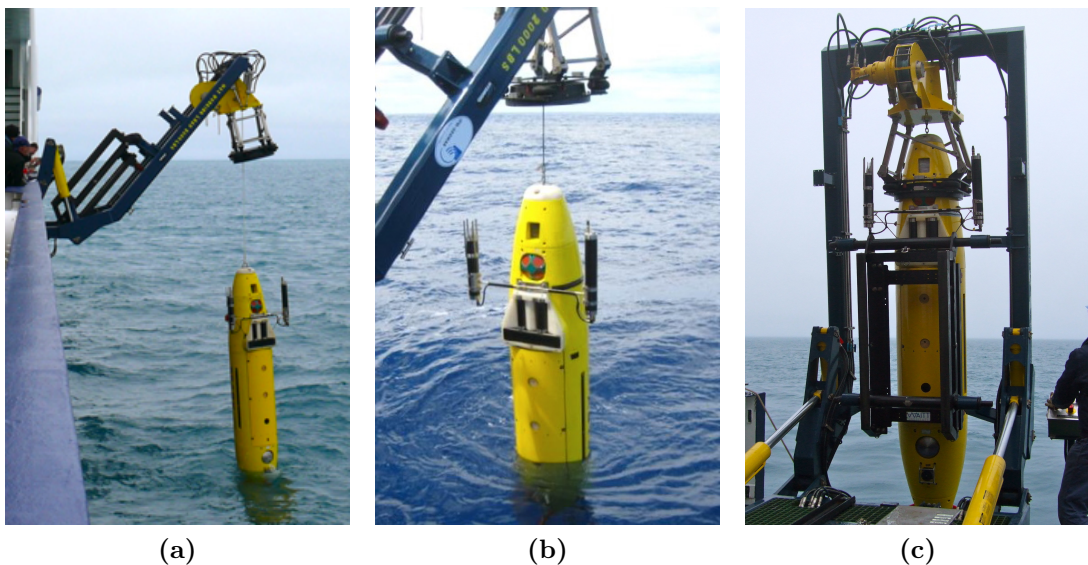


Figure 2.3: During recovery the AUV is pulled up into the recovery frame (a,b). The AUV nose is fixed in the black frame with the MR outside of the frame (c).

vibrations. During Dive 7, two additional smaller steel rods were used at each side of the AUV. Finally, during Dives 8 and 9, another steel rod was added at each side. In Figure 2.2b, the configuration used for Dives 8 and 9 including all mounting rods is shown (main rod and three additional rods at each side).

Compared to free falling profilers, AUVs are known to be a noisy platform for microstructure measurements. The AUV's motor magnet, propeller and rudder actuator constitute the main sources of platform vibrations (*Levine and Lueck, 1999*). Spectra of the accelerometer signal of the MR aboard AUV *Abyss* showed two wavenumber bands of enhanced vibrations situated at 2.3 cpm – 10 cpm and above 15 cpm (Fig. 2.4, cpm – cycles per meter). The rotation frequency of the AUV rotor was about 210 rotations per minute (rpm). The corresponding wavenumber of 2.3 cpm can

be estimated by dividing the propeller rotation frequency of 210 rpm by the speed of the AUV through the water which was approximately 1.5 m/s. Maxima in the accelerometer spectra at the first and second harmonic were clearly pronounced in the low wavenumber noise band. A rather broad peak was found in the y-component at 4.6 cpm during Dive 8, while all three components showed a comparably small peak at 9.3 cpm during Dive 7. The mean displacement due to the vibrations was smaller than 1 mm (not shown). Efforts to improve the mounting during the cruise led to a reduction of vibrations in the lower noise wavenumber band but enhanced them between 15 and 30 cpm. It is thus assumed that the high wavenumber noise band was induced by the mounting of the MR. Further improvement regarding the mounting will lead to further reduction of the instrumental vibrations and thus to a lower noise level (Section 3).

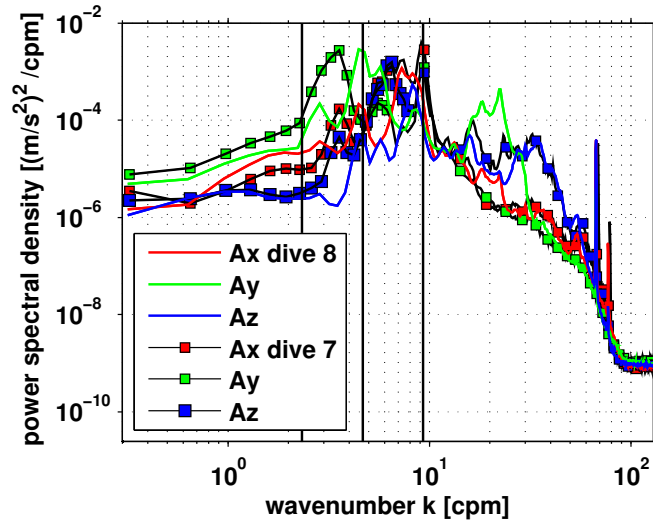


Figure 2.4: Average acceleration spectra from segments with high dissipation from Dives 7 and 8. Black, vertical lines mark harmonics of the rotor frequency at 2.3 cpm, 4.6 cpm, and 9.3 cpm, for an AUV speed of 1.5 m/s. Ax points in the direction of travel, Ay is directed to the port side and Az is directed upward.

2.3.3 Processing and Calibration of Shear Sensor Data

Shear probes measure velocity fluctuations perpendicular to their movement through the water. The raw output signal is converted to horizontal shear of vertical velocity $\delta w/\delta x$ following *Lueck* (2005), according to:

$$\frac{\delta w}{\delta x} = \frac{V_s}{2\sqrt{2} \cdot G \cdot S(T, \rho) \cdot U^2}, \quad (2.1)$$

with the raw output voltage V_s , the gain G of the MR and sensitivity $S(T, \rho)$ of the shear probe. U is the speed of the sensor through the water, w is the vertical velocity component, and x is the horizontal coordinate (along AUV track).

The sensitivity $S(T, \rho)$ of the shear probes used is linearly dependent on both the temperature T and the density ρ of the surrounding water (*Lueck*, 2005). The shear probes are calibrated in water with a density of 997 kg/m^3 by the manufacturer. Here in this study the shear probes were used in denser water. For scaling the shear probes sensitivity a constant seawater density of 1030 kg/m^3 was assumed. Accordingly the sensitivity was corrected for the density dependence by multiplication with 1.03 ($1030/997 = 1.3$).

In addition the sensitivity increases with increasing temperature by approximately $1\%/^\circ \text{C}$ (personal communication, *R. Lueck*). The shear probes have been calibrated at a certain temperature given in the calibration report in the range of 20°C to 25°C . Here the in-situ temperature observed by the AUV-CTD was used for the correction, resulting in about 20% lower values for the sensitivity at 2000 m than near the sea surface. Another effect which has to be taken into account is the spatial smoothing inherent to the shear probe measurements. Structures comparable to or smaller than the size of the probe are affected by spatial averaging. The resulting velocity shear wavenumber spectra are consequently biased low at high wavenumbers. This effect is corrected according to *Macoun and Lueck* (2004) and *Oakey* (1982), using 50 cpm as the half-power wavenumber of the probe.

2.3.4 AUV Missions

Altogether, 9 AUV dives were conducted (Table 2.3). The first six dives delivered no microstructure data due to technical problems inside the MR but the AUV-CTD and altimeter worked without problems. During Dives 7, 8, and 9 the MR worked successfully (dive tracks in Fig. 2.1). Dive 8 was the longest and lasted for 19 h. The AUV crossed the sill six times in along-channel direction. Most of the dives were carried out such that the AUV would cross the sill in a stair case-like mode. The AUV follows a preset track at preset, constant pressure levels (to minimize vibrations caused by up- and downward movement). The AUV changes its depth at a preset position, e.g. it goes up by 100 m and subsequently continues on that pressure level. This has to be programmed based on topographic informations prior to the dive.

The AUV can also be programmed to actually follow the topography at a con-

2.4 AUV Speed, Flow Velocity and Calibration

Dive	Duration		Dive mode	Deployment [UTC]		Recovery [UTC]	
				Date	Time	Date	Time
1	4 h	55 min	stair case	17/08/2010	12:58	17/08/2010	17:53
2		55 min	stair case	18/08/2010	09:52	18/08/2010	10:47
3	4 h	46 min	stair case	18/08/2010	17:40	18/08/2010	22:26
4	3 h		–	19/08/2010	15:50	19/08/2010	18:50
5	13 h	42 min	stair case	19/08/2010	21:20	20/08/2010	11:02
6	2 h	58 min	–	21/08/2010	12:15	21/08/2010	15:13
7	4 h	55 min	stair case	21/08/2010	12:15	21/08/2010	15:13
8	19 h	12 min	stair case	21/08/2010	12:15	21/08/2010	15:13
9	4 h	35 min	topography following	21/08/2010	12:15	21/08/2010	15:13

Table 2.3: Overview of the durations and dive modes as well as deployment and recovery dates for all AUV dives.

stant altitude. Then, the bottom tracking and altitude measurements control the diving depth instantaneously, which might cause permanent depth adjustments depending on the bottom roughness. During Dive 9, the AUV was programmed to actually follow the topography at a constant altitude above the sea floor of 80 m in the first part and 50 m in the second part of the dive.

2.4 AUV Speed, Flow Velocity and Calibration

Precise knowledge of the speed of the AUV through the water is crucial for the estimation of the dissipation rate (Section 3). Unfortunately it cannot directly be measured by the AUV. Instead it was inferred from the rotation frequency of the AUV propeller and was calibrated by in-situ current observations. This was accomplished comparing the mooring-based velocity observations against the flow velocity v_{flow} estimated by the difference of the AUV speed through the water v_{tw} and over ground v_{og} as described below.

The AUV internally determines its speed over ground v_{og} from the DVL, as long as the AUV is within the range of 200 m altitude above the bottom. When outside of that range, the AUV determines its speed using the rotation frequency f_r i.e. the number of rotations of the propeller (# revolutions/s). The rotation frequency is converted to speed by multiplication with an constant conversion factor c_f with the unit [cm/revolution]. The speed determined from the rotations represents the speed through the water in cm/s:

$$v_{\text{tw}}(c_f, f_r) = c_f \cdot f_r \left[\frac{\text{cm}}{\# \text{ revolutions}} \cdot \frac{\# \text{ revolutions}}{\text{s}} \right]. \quad (2.2)$$

2 Data and Instruments

The conversion factor c_f is usually not calibrated and preset on an empirically basis before each dive. After each dive c_f is determined by AUV software using the combined information of the speed over ground v_{og} and the number of rotations of the propeller without taking the flow velocity of the water into account. During the cruise P403, c_f was preset to 43 cm/revolution while the AUV software determined an average of 46 cm/revolution for all dives conducted during the cruise. The AUV was programmed to maintain a constant speed over ground, which led to permanent adjustment of the AUV speed through the water as the water velocity in the sampled area was not zero. In order to determine the actual speed of the AUV through the water, the water velocity has to be taken into account.

The AUV records the rotation frequency f_r of the propeller together with the estimated speed over ground. This offers the possibility to determine the flow velocity v_{flow} by subtracting the speed over ground from the speed through the water

$$v_{flow}(c_f, f_r) = v_{tw}(c_f, f_r) - v_{og}. \quad (2.3)$$

As the AUV records the speed over ground in the direction of travel, i.e. in the coordinate system of the AUV, the estimated v_{flow} is also only valid in the coordinate system of the AUV. Using the AUV's heading v_{flow} can be converted to earth-coordinates. During Dive 8 (Table 2.3, Fig. 2.1) the AUV was profiling back and forth along the channel, changing its heading from northward to southward and vice versa. The coordinate system of the AUV was thus pointing alternately to the north and south. For comparison with the along-channel velocities observed by the moored instruments, v_{flow} was converted using the AUV heading such that positive flow was directed northward and negative flow was directed southward. Tracks which deviate from the along-channel direction were not considered.

As accurate knowledge of the AUV speed through the water $v_{flow}(c_f, f_r)$ is crucial during the estimation of the dissipation rate and it depends only on the propeller rotation frequency f_r in combination with the conversion factor c_f , the factor was calibrated by in-situ velocity observations. This was accomplished by comparing the water velocity v_{flow} determined from the AUV as described above against the flow velocity recorded from the moored ADCPs and the RCM as described below. The averaged flow velocity from 10-minute intervals from the AUV data were compared to the averaged flow velocity from 10-minute intervals from the ADCPs and the RCM data, for all times when the AUV passed the respective instrument. For the calculation of the AUV-based $v_{flow}(c_f, f_r)$ for each interval, the conversion factor c_f was varied in the range of 40 cm/revolution to 47 cm/rotation. Using the resulting $v_{flow}(c_f, f_r)$ and the mooring-based flow velocity $v_{mooring}$ the root mean square (rms) of the velocity deviations was computed resulting in one Δv for each

2.4 AUV Speed, Flow Velocity and Calibration

of the three moored, velocity observing instruments:

$$\Delta v_{\text{ADCP}_{\text{UM}}}(c_f, f_r) = \sqrt{\frac{1}{6} \sum_{i=1}^6 (v_{i\text{ADCP}_{\text{UM}}} - v_{i\text{flow}}(c_f))^2}, \quad (2.4)$$

$$\Delta v_{\text{ADCP}_{\text{DM}}}(c_f, f_r) = \sqrt{\frac{1}{6} \sum_{i=1}^6 (v_{i\text{ADCP}_{\text{DM}}} - v_{i\text{flow}}(c_f))^2}, \quad (2.5)$$

$$\Delta v_{\text{RCM}}(c_f, f_r) = \sqrt{\frac{1}{6} \sum_{i=1}^6 (v_{i\text{RCM}} - v_{i\text{flow}}(c_f))^2}. \quad (2.6)$$

Subsequent averaging of $\Delta v_{\text{ADCP}_{\text{UM}}}(c_f, f_r)$ and $\Delta v_{\text{ADCP}_{\text{DM}}}(c_f, f_r)$ resulted in two final velocity differences Δv_{ADCP} and Δv_{RCM} . This two $\Delta v(c_f, f_r)$ showed a minimum at $c_f = 43.75$ cm/revolution, indicating the conversion factor best reproducing the observed flow velocities which was subsequently used for estimating the AUV speed through the water (Fig. 2.5).

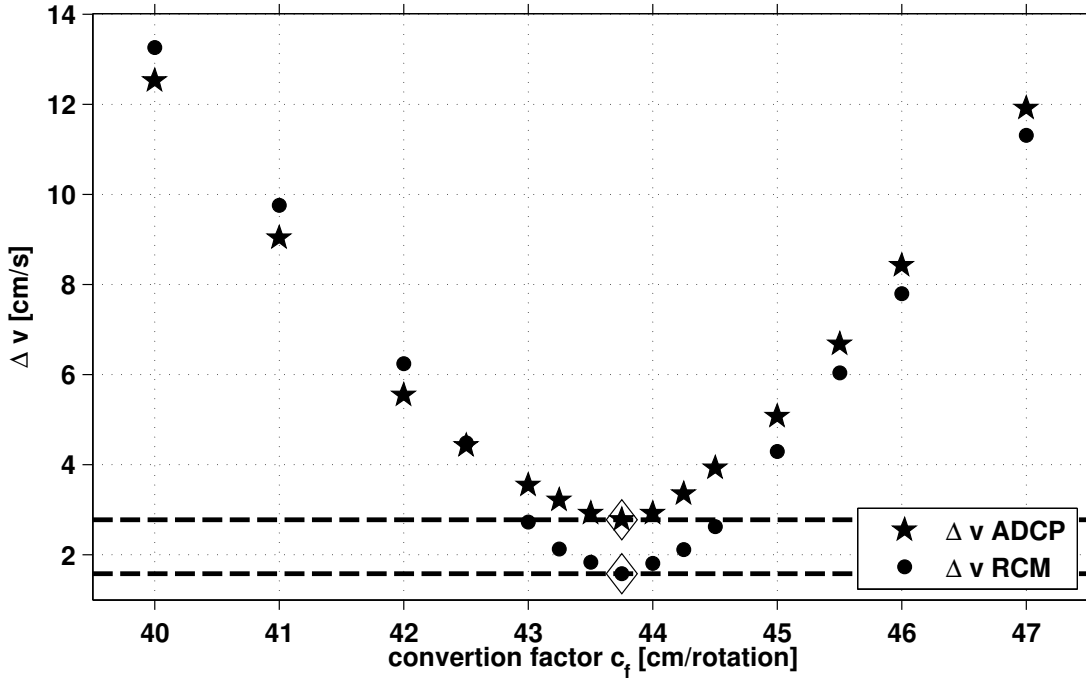


Figure 2.5: Velocity differences Δv_{ADCP} and Δv_{RCM} estimated by varying the conversion factor c_f . The best agreement was achieved for $c_f = 43.75$ cm/rotation. The diamonds denote the minima of the two distributions.

3 Processing Dissipation Rates obtained aboard AUV *Abyss*

The *MicroRider* (MR), the key instrument of this study, was customized for the operation on AUV *Abyss* because of space constraints on the AUV (Section 2.3). The processing of velocity shear microstructure data for this new and unique instrument-platform combination of deep diving AUV and MR was developed over the course of this thesis. The data base provided by the study of *St. Laurent and Thurnherr* (2007) offers a good opportunity to compare the results obtained from the new instrument combination (Section 4).

Microstructure probes have already been successfully used aboard a range of AUVs but this has been limited to the upper ocean (*Levine and Lueck, 1999; Lueck et al., 2002; Thorpe et al., 2003; Goodman et al., 2006; Steele et al.*). The detection limits of these studies were similar to the one of the AUV-MR system described in this thesis. In the following, the general method of inferring dissipation rates from velocity shear microstructure and the specific challenges arising from the operation of the MR on AUV *Abyss* are introduced. Two methods of inferring dissipation rates are compared and the subsequent noise and errors are discussed.

3.1 Inferring Dissipation Rates from Velocity Shear Microstructure

The dissipation rate of turbulent kinetic energy (ϵ) may be computed from velocity shear data by integration of shear spectra (Φ) under the assumption of isotropic turbulence (*Taylor, 1935; Oakey, 1982*):

$$\epsilon = 7.5 \nu \left\langle \left(\frac{\delta w}{\delta x} \right)^2 \right\rangle = 7.5 \nu \int_0^\infty \Phi dk, \quad (3.1)$$

with ν being the kinematic viscosity, k the wavenumber, and $\langle (\delta w / \delta x)^2 \rangle$ representing the variance of the fluctuations of the velocity perpendicular to the direction of travel. Following *Gargett et al. (1984)* and *Yamazaki and Osborn (1990)*, isotropy may be assumed if $\epsilon > 200 \cdot \nu N^2$, with N being the buoyancy frequency. Using $N^2 < 2.3 \cdot 10^{-6} \text{ 1/s}^2$ and $\nu = 1.6 \cdot 10^{-6} \text{ m}^2/\text{s}$ as determined from CTD profiles, a conservative estimate for isotropy conditions is $\epsilon > 8 \cdot 10^{-10} \text{ W/kg}$ which is on the order of the noise level (Section 3.3). Thus, isotropy can be assumed for dissipation rates reported throughout this thesis.

3 Processing Dissipation Rates obtained aboard AUV Abyss

It is commonly assumed that a velocity shear spectrum Φ has the shape of the universal Nasmyth spectrum determined by *Nasmyth* (1970) and reported by *Oakey* (1982). As described in Section 2.3.2, accelerometer data of the MR showed elevated vibrations originating from the AUV and the mounting of the MR. The wavenumber range of these vibrations are collocated within the wavenumber band (k band) occupied by turbulent fluctuations. Thus, their contributions to shear variance have to be eliminated prior to the integration of the shear spectra. Here, two different procedures were used to achieve this requirement introduced below. Facing the same problem as described above, *Goodman et al.* (2006) developed a filter to remove microstructure shear contributions due to vibrations originating from a shallow-water REMUS AUV, that is now standardly implemented into microstructure data processing even for free-falling microstructure profilers (*Fer et al.*, 2014). The filter removes portions of the shear spectrum Φ that are coherent with the three dimensional acceleration signals recorded simultaneously to the shear signal, resulting in a filtered spectrum (ϕ_f). The untreated spectrum is referred to as raw spectrum (ϕ_r) hereafter.

The microstructure shear time series were divided into 6 s long segments for spectral analysis. A fast Fourier transform (FFT) segment length of 2 s was chosen with 50 % overlap. Thus, each estimate of the dissipation rate is based on spectral estimates from five 2 s long ensembles that were detrended and Hanning windowed prior to spectral decomposition (*Blackman and Tukey*, 1958; *Harris*, 1978). The relatively long interval of 6 s is necessary for an optimal use of the Goodman filter (*Goodman et al.*, 2006).

Two examples of typical shear spectra, one corresponding to elevated and one corresponding to low dissipation rates of turbulent kinetic energy, are presented (Fig. 3.1). In the high turbulence case (Fig. 3.1a), the filtered and raw spectrum compare reasonably well for wavenumbers larger than 10 cpm (cpm - cycles per meter). However, in the low turbulence case (Fig. 3.1b), the difference between ϕ_f and ϕ_r of up to two orders of magnitude for the same k band ($k > 10$ cpm) is distinct, indicating elevated contributions from the vibrations of the instrument package. In both cases, power spectral densities for the k band between 10 and 15 cpm are least affected by vibrations, independent from the turbulence level (Fig. 3.1). On the contrary, spectral densities for the k band between 3 and 10 cpm are most strongly affected by the instrumental vibrations. In this k band, elevated differences between ϕ_f and ϕ_r even prevail in the elevated turbulence case.

The vibrations induced from the instrument package showed comparable spectral energy levels for both turbulence environments (Fig. 3.1) as well as in the average accelerometer spectra (Fig. 2.4). This indicates the vibrations to be independent from the turbulent environment at least for the range of turbulence encountered over the course of this study.

3.1 Inferring Dissipation Rates from Velocity Shear Microstructure

Visual inspection of shear spectra from the different dives and regions indicated that the spectral shape of Φ_f compares well to the shape of the universal Nasmyth spectrum for wavenumbers larger than 10 cpm when the signal is above the shear noise level (about $1 \cdot 10^{-6} 1/(s^2 \text{ cpm})$). For smaller wavenumbers ($k < 10 \text{ cpm}$), spectral densities of the filtered spectrum are attenuated too strongly by the Goodman filter. In particular, this is most pronounced for $k < 2 \text{ cpm}$, where acceleration spectra show only weak instrumental vibrations (Figs. 2.4 and 3.1). The reason for this behavior could not be fully assessed. In part, the attenuation could be due to movement of the instrument package induced by turbulent motions of the ocean on length scales that will lead to coherence between the acceleration and the shear signals in this k range (Goodman *et al.*, 2006). Using Φ_f would thus underestimate the turbulent shear contributions in this k range.

In order to avoid both, the use of the attenuated wavenumber band ($k < 2 \text{ cpm}$) and the wavenumber band of particularly elevated instrumental vibrations (2 cpm to 10 cpm), the low noise k band (10 cpm to 15 cpm) is used as origin for estimating dissipation rates of turbulent kinetic energy. Two different methods are introduced to compute the dissipation rate detailed below.

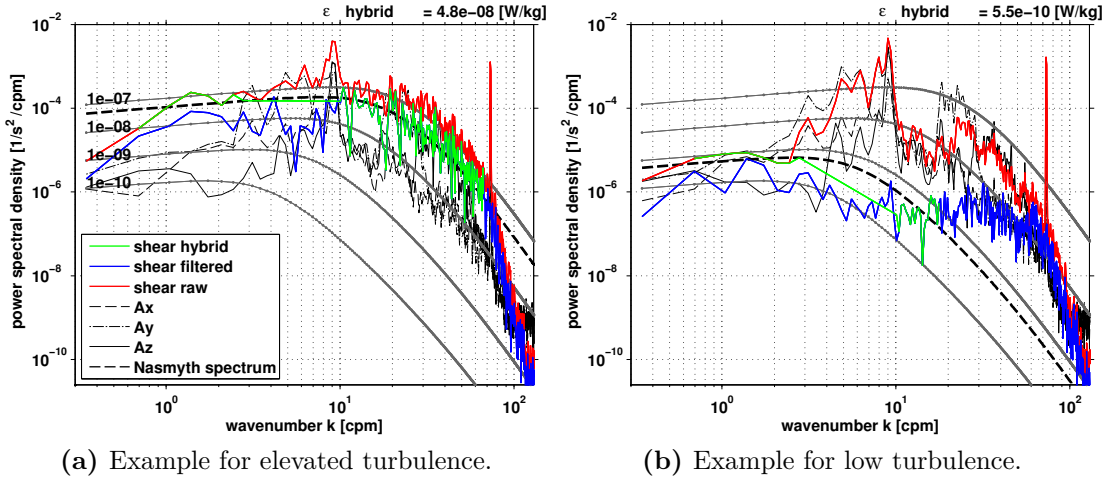


Figure 3.1: Example velocity shear spectra (colored lines) for one segment of elevated turbulence (a) and one segment of low turbulence environment (b). Spectra of the 3-dimensional acceleration are also shown (Ax- the direction of travel, Ay-directed to port, Az-directed upward). The dissipation rate estimate for each segment is given in the upper right corner of each panel. The corresponding Nasmyth spectrum is indicated by the thick black, dashed line. The gray lines with dots indicate the Nasmyth spectra for $\epsilon = [10^{-10}, 10^{-9}, 10^{-8}, 10^{-7}] \text{ W/kg}$.

3.2 Two Methods to compute the Dissipation Rate

The two methods use the filtered spectrum Φ_f in the low noise k band between 10 cpm and 15 cpm. As the influence of the AUV-induced vibrations decreases with increasing energy of the shear signal (Fig. 3.1), a larger k range can be used for the integration with increasing velocity shear energy. This is achieved by computing the dissipation rate iteratively using the filtered spectrum starting in the low-noise k band (10 cpm and 15 cpm) and shifting the upper integration limit (k_4) to higher wavenumbers according to the spectral energy level. The maximum upper limit of the high k range is limited to $k_4 < 68$ cpm due to the pronounced peak in the spectrum which was present in almost every segment (Fig. 3.1). The integration of the filtered spectrum results in the shear power (P_{shear}) for the wavenumber range $k_3 < k < k_4$,

$$P_{\text{shear}} = \int_{k_3}^{k_4} \Phi_f dk. \quad (3.2)$$

P_{shear} is used to estimate the corresponding Nasmyth spectrum Φ_N using a normalized version of the formulation reported by *Wolk et al.* (2002) while considering the transfer function for probe attenuation due to spatial smoothing inherent to the shear probe measurements. This effect is corrected according to *Macoun and Lueck* (2004) and *Oakey* (1982), using 50 cpm as the half-power wavenumber of the probe. Finally, dissipation rates of turbulent kinetic energy are obtained by integration of the Nasmyth spectrum over all wavenumbers.

The hybrid method, which is the second method to compute the Dissipation Rate, uses the same data and the same integration limits for $k > k_3$ and additionally the raw spectrum Φ_r for the lower k range ($k_1 = 0.4$ cpm $< k < k_2 = 2.5$ cpm). Between k_2 and k_3 , where significant noise contamination is found, the shear spectrum is interpolated. This part of the hybrid spectrum is referred to as the interpolated spectrum Φ_I and appears as a straight line between k_2 and k_3 (Fig. 3.1). In order to reduce the sensitivity of Φ_I to the value at k_3 the mean of the filtered spectrum Φ_f within 10 to 14 cpm is used at k_3 . Besides the different integration limits the integration of the hybrid spectrum is identical to the integration of the filtered spectrum and results in the shear power P_{shear} .

$$P_{\text{shear}} = \int_{k_1}^{k_4} \Phi_H dk, \quad \text{with } \Phi_H = \begin{cases} \Phi_r & (k_1 < k < k_2) \\ \Phi_I & (k_2 < k < k_3) \\ \Phi_f & (k_3 < k < k_4) \end{cases} \quad (3.3)$$

The dissipation rates of turbulent kinetic energy from the hybrid spectrum are determined analogously to those from the filtered spectrum by estimating the corresponding Nasmyth spectrum and integration of the Nasmyth spectrum over all wavenumbers.

Comparing both estimates, the dissipation rates computed using the first method

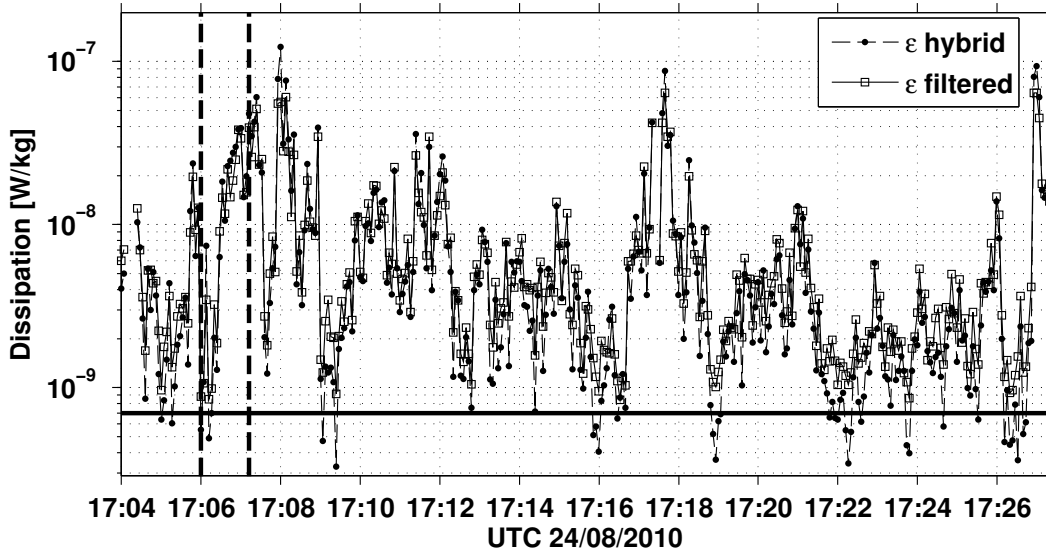


Figure 3.2: Dissipation rate segment from Dive 8 determined from the hybrid spectrum and from the filtered spectrum (for $k > 10$ cpm). The black, dashed, vertical lines indicate the two examples shown in Figure 3.1. The black, horizontal line indicates the noise level for Dive 8. The resolution is 6 s corresponding to 9 m.

were $2 \cdot 10^{-9}$ W/kg higher than those computed using the hybrid method. This discrepancy is mainly associated with a reduction of the noise level inherent to the hybrid method. In a low-turbulent environment ($\epsilon < 1 \cdot 10^{-9}$ W/kg), limited shear variance resides in the high k band ($k > 10$ cpm) and the inclusion of the low k band between k_1 and k_2 contributes to reduce noise in the dissipation rate estimates. In this thesis, dissipation rates determined from the hybrid spectrum Φ_H will be used as those estimates rely on a larger bandwidth constrained by observations and the shape of the hybrid spectra shows reasonable agreement with the corresponding Nasmyth spectra. Spatial structures of the resulting dissipation rate distribution are robust among the two methods (Fig. 3.2).

The resulting dissipation rate time series has a resolution of 6 s corresponding to 9 m along-track resolution (speed of the AUV approximately 1.5 m/s). As two Airfoil probes were deployed simultaneously the mean of both sensors is used.

3.3 Noise and Error Estimate

The dissipation rate time-series of Dives 7 to 9 showed intervals of low and uniform dissipation rates. In these intervals, shear spectra no longer follow the Nasmyth spectrum for $k > 4$ cpm and are noise dominated (Fig. 3.1b). As the processing algorithm always uses the k range between 10 cpm and 15 cpm, fitted Nasmyth spectra cannot be much lower than those Φ_f intersecting the shear noise in that k -range (between 10 cpm and 15 cpm). Thus, using the hybrid spectra much lower dissipation rates cannot be estimated and it is expected to find potentially lower

3 Processing Dissipation Rates obtained aboard AUV Abyss

values biased high. This is illustrated by the histogram of the dissipation rates for Dive 8 (Fig. 3.3) which show an accumulation at low dissipation rates. This interpretation is supported by the microstructure data of *St. Laurent and Thurnherr* (2007) who also observed dissipation rates in the eastern channel of the Lucky Strike segment in the bottom boundary layer. Their dissipation rates fall substantially below the lowest estimates based on the hybrid spectrum (Fig. 3.3). Thus, the most frequently observed dissipation rate was chosen as the noise level ϵ_n for the hybrid method (mode of the logarithm of the dissipation rates).

The noise level was estimated for each dive separately to be $\epsilon_n = 7 \cdot 10^{-10}$ W/kg for Dive 8 and $\epsilon_n = 2.5 \cdot 10^{-9}$ W/kg for Dives 7 and 9. The difference between Dives 7 and 8 originates from an improvement in the mounting of the MR, while the difference between Dives 8 and 9 originates most likely from different dive modes. Dives 7 and 8 were carried out in the staircase mode (Section 2.3.4), while the AUV followed the topography at a constant altitude during Dive 9. This dive mode is accompanied by increased vertical movements of the AUV and therefore by a higher level of vibrations. In data visualization the different noise levels are account for by setting all values below the noise level to a tenth of the noise level for each dive separately (Section 4).

The error of a single dissipation rate estimate is determined from the error of each

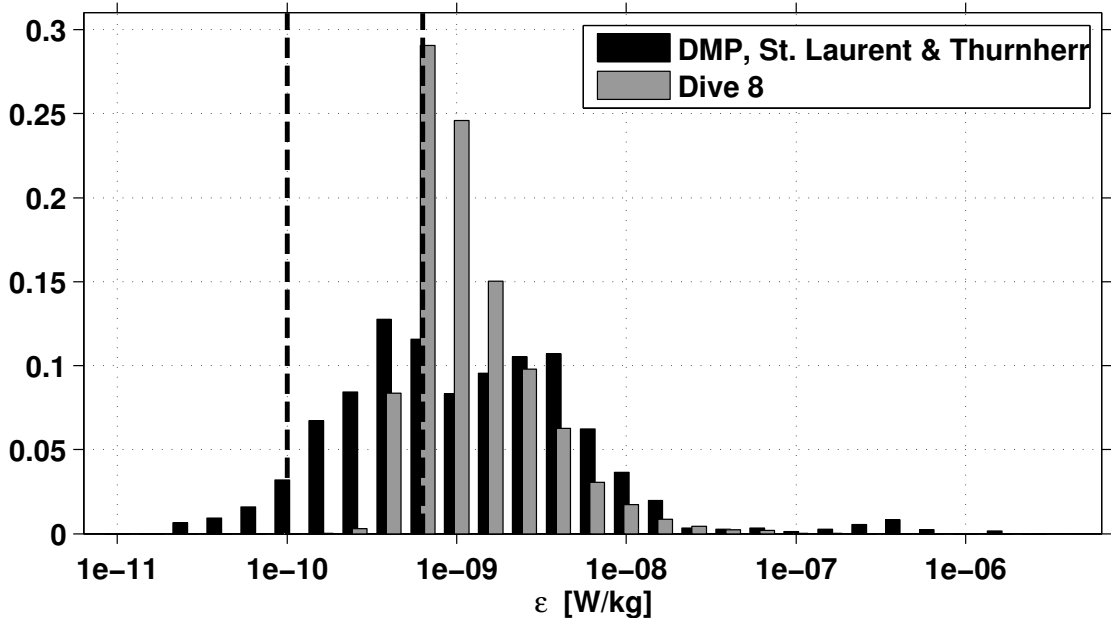


Figure 3.3: Histogram of the dissipation rates in logarithmic space of Dive 8 (gray) and the deepest 150 m from the deep microstructure profiler (DMP) profiles (black) normalized by the number of measurements. Vertical black, dashed lines mark the noise level at $\epsilon_n = 7 \cdot 10^{-10}$ W/kg for Dive 8 and $\epsilon_n = 1 \cdot 10^{-10}$ W/kg for the DMP.

parameter in Equation 2.1 and from the error arising from the spectral analysis in computing the dissipation rate. Here, the error of the output voltage V_s , the MR Gain G , the sensor sensitivity S and the AUV speed through the water are unknown. The error of the AUV speed can be estimated to be on the order of a few cm/s. This estimation is based on the in-situ calibration of the conversion factor c_f , which revealed a difference in the flow velocity determined from the moorings and from the AUV of a few cm/s only (Section 2.4). Estimates of the dissipation rate which are commonly averaged over 1 s intervals for free-falling instruments usually have an uncertainty of about 50 % but the single dissipation rate estimates are subject to variations on a few orders of magnitude on short spatial and temporal scales and thus the uncertainty of a single estimate is often less important (Thorpe, 2005). Here, on the one hand averaging was performed over 3 independent intervals of 2 s length which might reduce the uncertainty but on the other hand, the error of the speed of the AUV through the water might introduce a larger uncertainty as the dissipation rate depends on the speed through the water to the power of 4 (Equation 2.1 and 3.1). The estimation of an error for the single dissipation rate values thus is itself uncertain and was not attempted. A direct measurement of the speed through the water and sensor calibration at different temperatures (Section 2.3.3) is expected reduce the uncertainty. The error of the spatially and temporally averaged dissipation rate (Section 4.1.2) can be estimated with the bootstrap method (Efron, 1979) and will be given in the respective sections where the averaged dissipation rates are discussed.

4 Turbulence, Density and Flow Distribution along the Channel

One of the main questions addressed in this theses is the cross sill structure of the dissipation of turbulent kinetic energy along the channel, across the sill. With the unique instrument combination of deep diving AUV and MR in conjunction with the method of inferring the dissipation rates derived in the course of this thesis, reported in Section 3, the cross sill structure of the dissipation rate can now be studied. The results are reported below in high resolution as well as averaged in depth-latitude-dependent boxes. A comparison with the results by *St. Laurent and Thurnherr (2007)* is performed. In order to relate the findings regarding the distribution of the mixing to the flow throughout the channel the average velocity and density field in the channel are studied. Based on the average dissipation rates and the stratification vertical diffusivities and the density flux are estimated.

Furthermore, small scale density fine-structure anomalies are studied which also provide evidence for strong mixing in stratified waters. The different subranges of turbulence are studied based on temperature gradient spectra. Finally, one example segment of high dissipation rates detected simultaneously with a density anomaly is examined in more detail.

4.1 Dissipation Rate along the Channel

The distribution of the dissipation rate of turbulent kinetic energy – being one of the central aspects of this thesis – is first reported in high resolution. The method of inferring the dissipations rates was introduced in Section 3. Secondly, the average dissipation rates over defined depth-latitude-boxes are discussed as they allow for an easier identification of the pattern of the dissipation rate.

4.1.1 High Resolution Dissipation of Turbulent Kinetic Energy

The horizontal, along-channel distribution of the dissipation rate of turbulent kinetic energy inferred from Dives 7, 8, and 9 revealed elevated dissipation rates in the area 1 – 4 km downstream of the sill, where dissipation rates above $1 \cdot 10^{-7}$ W/kg were found (Figs. 4.1, 4.2, and 4.3). Elsewhere, dissipation rates were generally below $5 \cdot 10^{-9}$ W/kg. The dissipation rates reported here have a horizontal resolution of 9 m corresponding to 6 s (AUV speed 1.5 m/s).

The AUV was profiling along the channel center but also at the channel edges in shallower depths, as the channel walls were very steep (Section 1.3.2). Although

4 Turbulence, Density and Flow Distribution along the Channel

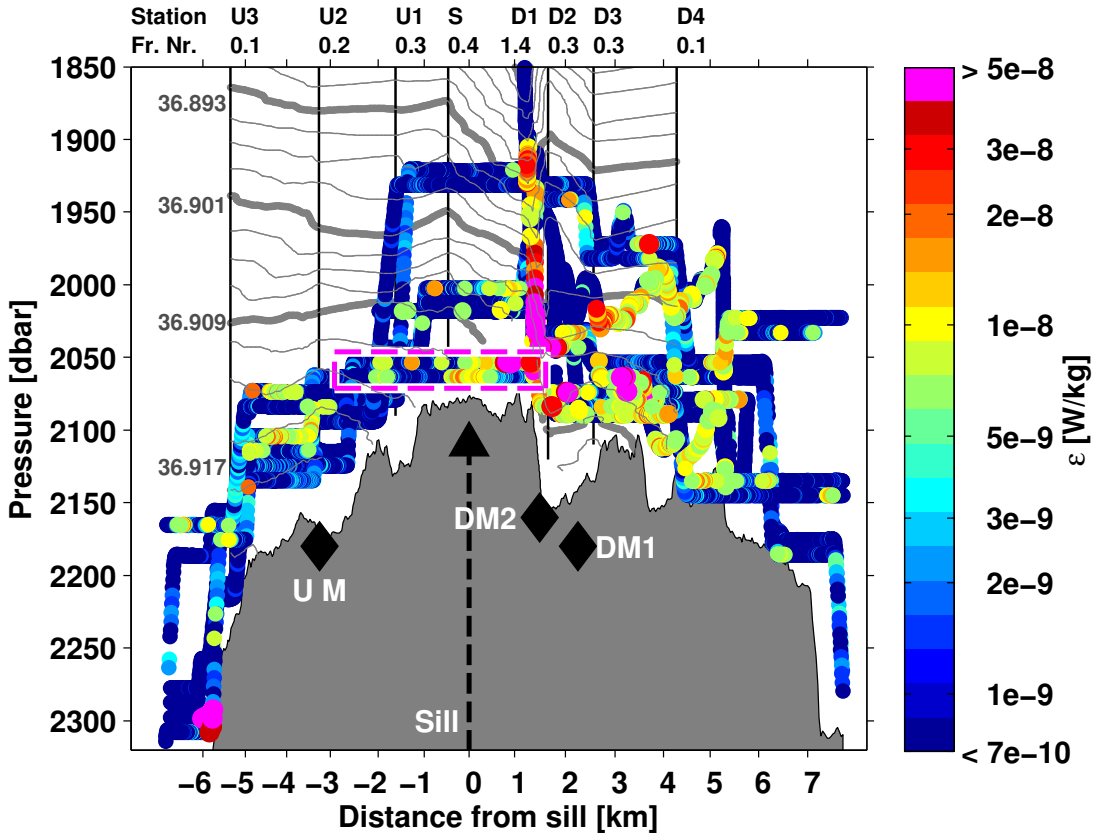


Figure 4.1: Meridional distribution of the dissipation rate [W/kg] along the channel as function of pressure. Areas which were sampled twice by the AUV are shown vertically displaced by 10 dbar. Diamonds show the positions of the moorings DM1, DM2 and UM. Contours show σ_2 from CTD profiles (spacing $\Delta\sigma_2 = 0.002 \text{ kg/m}^3$). Thin vertical lines mark the location of CTD/LADCP stations, their acronyms and associated Froude numbers stated above the plot. The topography corresponds to that along the track of the AUV in the middle of the channel. The magenta dashed box indicates a segment of constant pressure which is discussed in Section 4.4.3.

it appears as if the AUV was sampling about 200 m above the bottom in Figure 4.1 (using the topography along the center of the channel as reference bottom) the AUV stayed in the range from 40 m to 170 m altitude most of the time as can be seen in the latitude-altitude Section (Fig. 4.2). High dissipation rates in the area 0 – 2 km downstream of the sill were found between 50 m and 150 m altitude. Further downstream (2 – 4 km), high dissipation rates were found between 40 m and 120 m altitude with the tendency of higher values towards the sea floor. Thus, elevated dissipation rates were concentrated in the bottom boundary layer as already reported by *St. Laurent and Thurnherr* (2007) but here, with the AUV-based system, a clear asymmetry of the distribution with respect to the position of the sill could be shown (Fig. 4.1). This pattern is expected for overflow induced mixing (e.g. *Alford et al.* (2013)) which is consistent with the average along-channel velocities reported by *St. Laurent and Thurnherr* (2007). The ve-

4.1 Dissipation Rate along the Channel

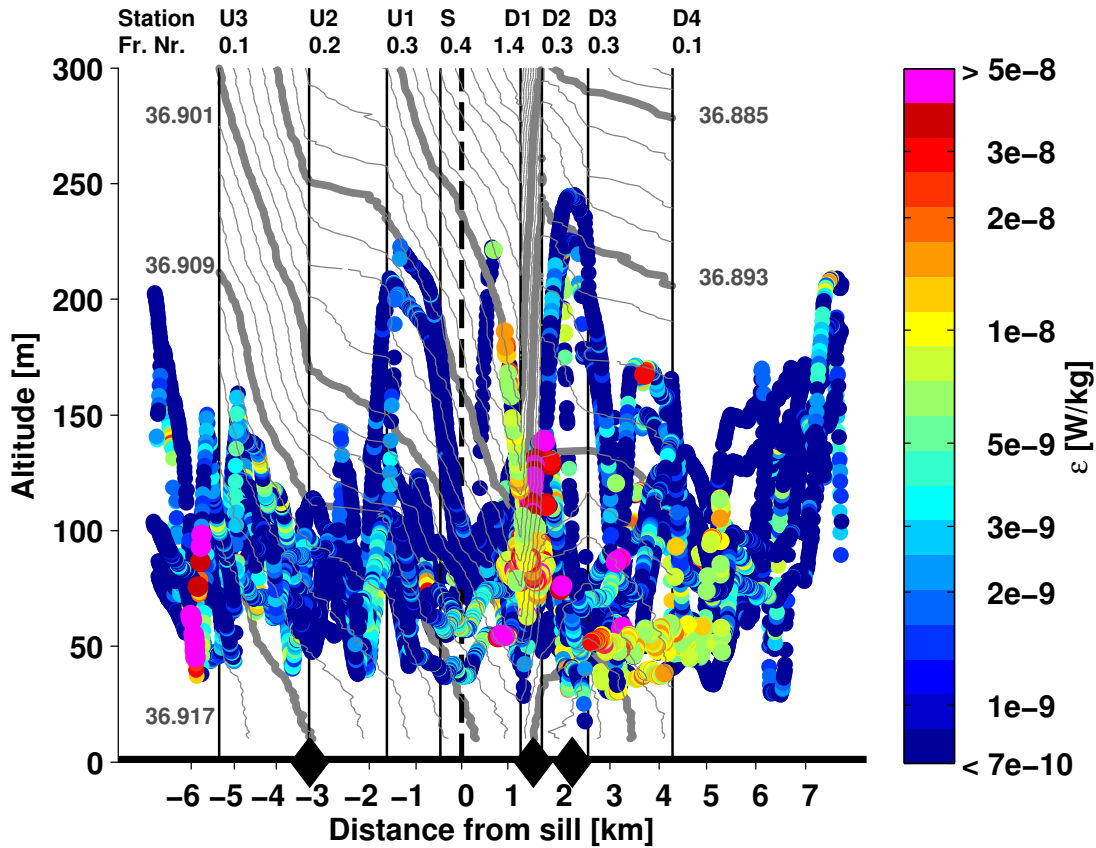


Figure 4.2: Meridional distribution of the dissipation rate [W/kg] along the channel as function of altitude. Areas which were sampled twice by the AUV are shown vertically displaced by 20 m. Diamonds show the positions of the moorings DM1, DM2 and UM. Contours show σ_2 from CTD profiles (spacing $\Delta\sigma_2 = 0.002 \text{ kg/m}^3$). Thin vertical lines mark the location of CTD/LADCP stations, their acronyms and associated Froude numbers stated above the plot.

locity field encountered during the measurement campaign underlying this thesis is analyzed in Section 4.2.

The across-channel distribution of the dissipation rate did not show such a clear pattern. If at all, only a slight tendency towards higher values in the center of the channel compared to the channel edges may be indicated. In general, the dissipation rate was highly variable in space and time.

Elevated dissipation rates were also found in a very confined region 6 km upstream of the sill. Here, patches of elevated turbulence having peak values of $2 \cdot 10^{-7} \text{ W/kg}$ and $7 \cdot 10^{-8} \text{ W/kg}$ were sampled close to the sea floor in the center of the channel during the first and second passage of the AUV, respectively. The AUV had been heading towards the north while remaining at a level of constant pressure, thus approaching the upward-sloping bottom. Less than two minutes before the AUV started to ascend, the high dissipation rates were detected. This might

4 Turbulence, Density and Flow Distribution along the Channel

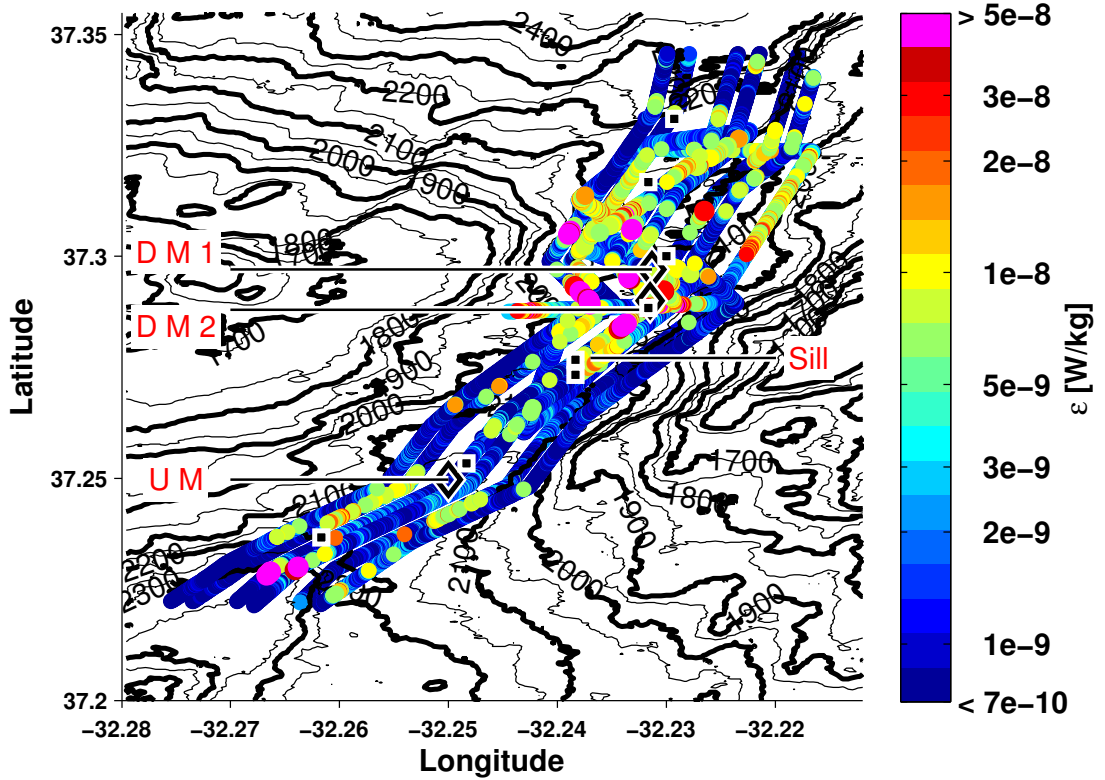


Figure 4.3: Map of the dissipation rate [W/kg]. Tracks sampled twice are shown zonally displaced. Diamonds mark the positions of moorings. The black squares mark the positions of the DMP profiles of St. Laurent and Thurnherr (2007). The sill is located at 37.28° N. Contour spacing of topography is 50 m (thin line) and 100 m (thick line). The magenta dashed box indicates a segment of constant pressure which is discussed in Section 4.4.3.

represent an example of turbulence generated by internal waves being reflected at the bottom with critical topography slope angles. This critical reflection occurs when the topography slope angle to the horizontal $\tan \theta$ equals the internal wave characteristics s (Legg and Adcroft, 2003; Schafstall et al., 2010). The internal wave characteristic s was estimated following Legg and Adcroft (2003):

$$s = \sqrt{\frac{\omega^2 - f^2}{N^2 - \omega^2}}, \quad (4.1)$$

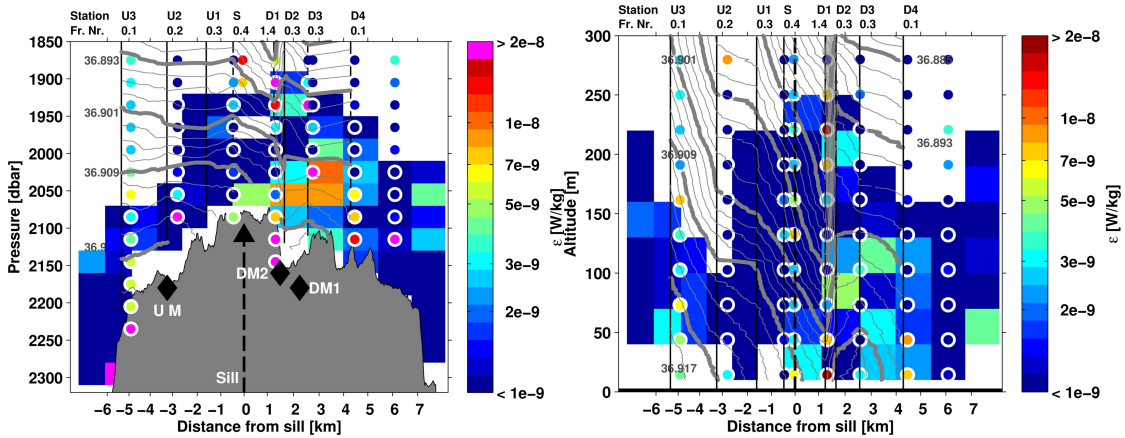
using the semi-diurnal M_2 tide frequency for the wave frequency ω , the Coriolis frequency f , and the buoyancy frequency N . The ratio of the topography slope $\tan \theta_c$ and the internal wave characteristics s at this location was estimated to be close to unity. Near critical reflection of internal waves thus is reasonable to occur at this location and cause the elevated turbulence in this region upstream of the sill.

4.1.2 Average Dissipation Rate

The high resolution dissipation rates reported in the preceding paragraphs were highly variable in space and time. For easier identification of the distribution of the mixing, the dissipation rates were averaged over depth-latitude-boxes along the channel. The data base available here might not be sufficient to represent the variability of the mixing in the channel but averaging over the available data might still help to identify the mixing patten encountered in the course of this study.

Averaging was performed over 12 latitudinal boxes of 30 dbar height i.e. 30 m altitude above the sea floor (Fig. 4.4). For averaging individual dissipation rate estimates below two times the noise level (Section 3.3) were replaced by zero following *Gregg* (1989). This is done to avoid the average dissipation rates near the noise level to be biased high (in contrast to *Tippenhauer et al.* (2015) where the noise was not replaced). It is emphasized that the number of individual values used for the average in each box differs from four to a few hundred values as each position was not sampled equally often.

High dissipation rates were found downstream of the sill within 1 to 4 km. Average values of $> 6 \cdot 10^{-9}$ W/kg extended from 50 m to 140 m above the sea floor.



(a) Box-averaged dissipation rate as a function of pressure.

(b) Box-averaged dissipation rate as a function of altitude.

Figure 4.4: Along-channel distribution of the box-averaged dissipation rate (colored boxes) together with vertical profiles of ϵ obtained with the DMP from *St. Laurent and Thurnherr* (2007). DMP data are shown as colored dots with white surroundings. Both data sets were vertically averaged in 30 m bins. Diamonds show the positions of the moorings DM1, DM2 and UM. Contours show density from CTD profiles (spacing $\Delta\sigma_2 = 0.002 \text{ kg/m}^3$). The stations are given at the top of each panel together with Froude Numbers. Vertical lines mark the latitude of each station. a: Topography as in Figure 4.1. Note that the vertical DMP profiler was subject to advection by currents in the channel, which does not allow a precise location of the position of the profiler. This causes some of the profiles to appear extended beyond the sea floor.

Upstream of the sill the dissipation rate was generally below $3 \cdot 10^{-9}$ W/kg, except for the one location with critical topography slope near 37.23° N close to the sea floor (Section 4.1.1).

The statistical uncertainty of the average dissipation rate for each box was determined using the bootstrap method and 1000 ensembles (*Efron, 1979*). Using this method includes the assumption that the available data set captures the natural variability of the dissipation rate. Although this might not be the case for the underlying data set this assumption was already used in averaging the dissipation rates and is further used for estimating the statistical uncertainty. The result of the bootstrap method is an upper and lower limit of the uncertainty of the logarithmic dissipation rate which can only be interpreted when referenced to the corresponding dissipation rate. This is accomplished using the ‘relative uncertainty’ estimated by dividing the upper limit by the lower limit and tacking the square root (Figs. in appendix A.2a and A.2b). The relative uncertainty was below 2 for most boxes with values up to 2.3 directly downstream of the sill where the variability of the dissipation rate was high. In regions where the dissipation rates were close to the noise level, they were replaced by zero such that the relative error factor becomes infinite for some boxes by dividing by zero (i.e. boxes colored red in Figs. in appendix A.2a and A.2b).

Despite the asymmetric distribution of the dissipation rates across the sill, the observed range obtained here roughly agreed with the data obtained by the Deep Microstructure Profiler (DMP) inside the same channel by *St. Laurent and Thurnherr (2007)* in 2006 (Fig. 4.4). It should be noted, that the data set by (*St. Laurent and Thurnherr, 2007*) consist of individual profiles at each location. Variations in the dissipation rate should be expected in a turbulent region such that it can be stated that the dissipation rates derived from both platforms were in good agreement. This agreement shows that AUV base microstructure observations are suitable for the deep ocean even in narrow channels with rough topography.

Summarizing the results, an asymmetric distribution of the dissipation rates with respect to the location of the sill was found answering one of the main question of this thesis. Such a dissipation rate distribution was expected for the overflow across the sill, which was observed by *St. Laurent and Thurnherr (2007)*. Thus, the velocity observations by *St. Laurent and Thurnherr (2007)* together with the dissipation rate distribution obtained in this thesis, indicate overflow induced mixing downstream of the sill. The flow field inside the channel encountered during the AUV-based dissipation rate observations is studied throughout the next Section.

4.2 Average Velocity and Density Field

The dissipation rates were shown to be distributed asymmetrically with respect to the position of the sill in the previous paragraphs. Such a distribution is expected in a regime with unidirectional overflow across the sill (e.g. *Alford et al. (2013)*)

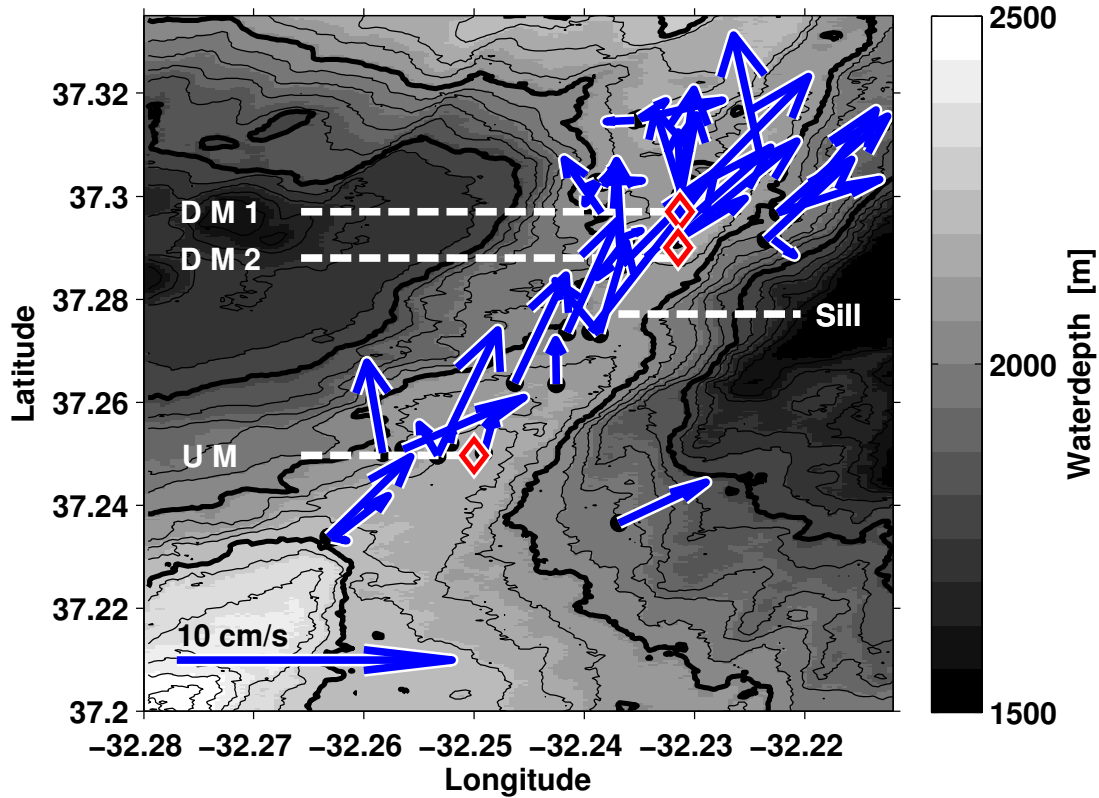


Figure 4.5: Depth-averaged LADCP-derived velocities in the eastern channel of the Lucky Strike segment. A reference arrow of 10 cm/s is placed in the lower left corner. Black dots mark station locations. Diamonds mark mooring positions. Contour line spacing 50 m. Thick contour lines refer to 1800 m, 2050 m and 2250 m.

which was found in the previous study by *St. Laurent and Thurnherr* (2007) in the same channel investigated here. In the following the average flow inside the channel is examined which was encountered at the same time as the microstructure observations were conducted. Firstly, the horizontal distribution of the flow field is studied using the depth averaged lowered observations and the average velocities derived from the moored instruments. Secondly, the vertical along- and across-channel distribution of the velocity and density field is investigated.

4.2.1 Horizontal Distribution of the Flow inside the Channel

The depth averaged LADCP-derived velocities revealed northeastward (along-channel) flow between 1800 m and the bottom at almost every station (Fig. 4.5). Highest velocities were found in the center of the channel downstream of the sill. Where the depth averaged flow speed exceeded 4 cm/s, the directions were between 20° west and 55° east. The mean flow speed below 1800 m determined from all profiles from the eastern channel was 4.7 cm/s in northward direction (16° east).

4 Turbulence, Density and Flow Distribution along the Channel

The 42 profiles collected in the channel were obtained during arbitrary phases of the tide and were distributed as follows: 16 profiles were located upstream of the sill, most of them in the channel center (Fig. 4.5, Station U3 to U1 Table 2.1). The two profiles directly downstream of the sill (station D0) were located slightly off the channel axis to the western edge. The remaining 24 individual stations further downstream were distributed between the channels walls. Thus 38 % of the stations were located upstream and 62 % were located downstream of the sill. The upstream station distribution only allows to study the along channel evolution of the flow, while the downstream distribution of the stations also allows to study across-channel sections.

As mentioned before, most of the stations showed north-eastward along channel flow. The few stations with west- to south-ward velocities were located at the north-western end of the channel where the channel widens towards the northern basin (stations, i.e. 10 % of stations). Only 2 stations showed south-east-ward velocities (Station 39 at D1E and Station 43 at U3, see Table 2.1).

The along-channel flow observed below 1800 m from LADCP measurements was confirmed from mooring-based ADCP observations which showed predominately northward velocities (Table 4.1). To estimate the along-channel component the meridional and zonal velocity components from lowered and moored observations were rotated in along-channel direction using the median of the flow direction observed at each mooring as the angle of rotation respectively (Table 4.1).

The moored ADCP timeseries showed higher flow speeds downstream of the sill, compared to upstream (Table 4.1 and 4.2). Mean values correspond to the depth interval of 2026 to 2066 dbar at the downstream mooring DM1, 1986 to 2026 dbar at the downstream mooring DM2 and 2039 to 2079 dbar at the upstream mooring UM, respectively (this corresponds to height above the sea floor of 74 to 114 m at DM1, 94 to 134 m at DM2 and 86 to 126 m at UM).

The average, unidirectional flow inside the channel, thus was consistent with overflow induced mixing downstream of the sill. What processes lead to mixing down-

Mooring	Meridional velocity [$\frac{cm}{s}$]		Zonal velocity [$\frac{cm}{s}$]		Along channel direction [$^{\circ}$]
	mean	std	mean	std	
UM	3.2	2.5	1.8	2.1	30
DM1	4.4	2.6	3.8	3.0	41
DM2	5.8	2.8	6.3	2.3	47

Table 4.1: Meridional and zonal velocity components with standard deviations (std) from moored ADCPs together with flow directions, which are equal to the angles of rotation.

stream of the sill, whether topographic lee waves, shear instabilities or a hydraulic jump, is investigated in the following.

4.2.2 Vertical along-Channel Flow and Density Distribution

In order to identify the physical process controlling the mixing downstream of the sill, the vertical along-channel distribution of flow throughout the channel is discussed below. For determining the average flow field individual LADCP-derived velocity profiles were averaged with respect to their location according to the grouped stations U3 to D4 (Table 2.1 and Figure 2.1). To interpolate between average profiles of the group-stations a quasi terrain following interpolating technique was used (*Kanzow and Zenk, 2014*). Froude numbers to characterize the flow regime were computed from the same averaged profiles following Equation 1.5 and are given at the top of the figures respectively.

The station-wise averaged along-channel velocity component showed highest flow speeds at the downstream station D1 exceeding 18 cm/s (Fig. 4.6). Froude Numbers were found to be elevated at the station D1 and dropped in both, upstream and downstream direction (top Fig. 4.6). According to *Thorpe (2010)*, a Froude Number of 1.4 is close to the critical value where an undular or a weak hydraulic jump may occur (Section 1.4).

The flow was directed along the channel not only at the station D1 but at all group stations below 1600 m. Thus the average unidirectional flow along the channel observed by *St. Laurent and Thurnherr (2007)* was confirmed. Furthermore, the Froude Numbers indicate the existence of an hydraulic jump downstream of the sill, at least a transient, undular or weak hydraulic jump (Section 1.4).

The average density distribution which was computed analogously to the velocity distribution also showed indications for an hydraulic jump. Downstream of the sill, isopycnals were displaced downward following the topography below 2000 m depth,

Mooring	Along channel velocity [$\frac{\text{cm}}{\text{s}}$]			Cross channel velocity [$\frac{\text{cm}}{\text{s}}$]		Flow speed velocity [$\frac{\text{cm}}{\text{s}}$]			DOF
	mean	std	sem	mean	std	mean	std	sem	
UM	3.7	2.8	0.4	0.0	1.7	4.4	2.2	0.3	59
DM1	5.8	3.4	0.6	0.0	2.0	6.2	3.2	0.6	33
DM2	8.6	3.0	0.6	0.0	3.0	8.8	2.9	0.6	25

Table 4.2: Along- and across-channel velocity components as well as the flow speed with standard deviations (std) and the standard error of the mean (sem) from moored ADCPs. The corresponding degrees of freedom (DOF) used for the estimation of the sem were computed using the time-lag of zero autocorrelation. Data were low-pass filtered with a cutoff frequency of 1/6 1/min.

4 Turbulence, Density and Flow Distribution along the Channel

but exhibited an upward displacement above 2000 m depth starting at about 1 km downstream of the sill. Deviations from horizontal density contours were observed up to 1500 m water depth. Far upstream of the sill isopycnals were oriented nearly horizontally above the sill depth, while closer to the bottom, they slightly bended upwards in downstream direction and then intersected the topography, still upstream of the sill.

The distribution of the density and Froude Numbers together were very much consistent with a hydraulic jump. At this point it is unclear, whether the hydraulic jump is a transient feature. Further analysis regarding this question is reported in Section 5.3. Upward radiating internal waves induced by a hydraulic jump as described by e.g. *Legg and Huijts* (2006) might induce the deviation from horizontal isopycnals observed here up to a depth of 1500 m.

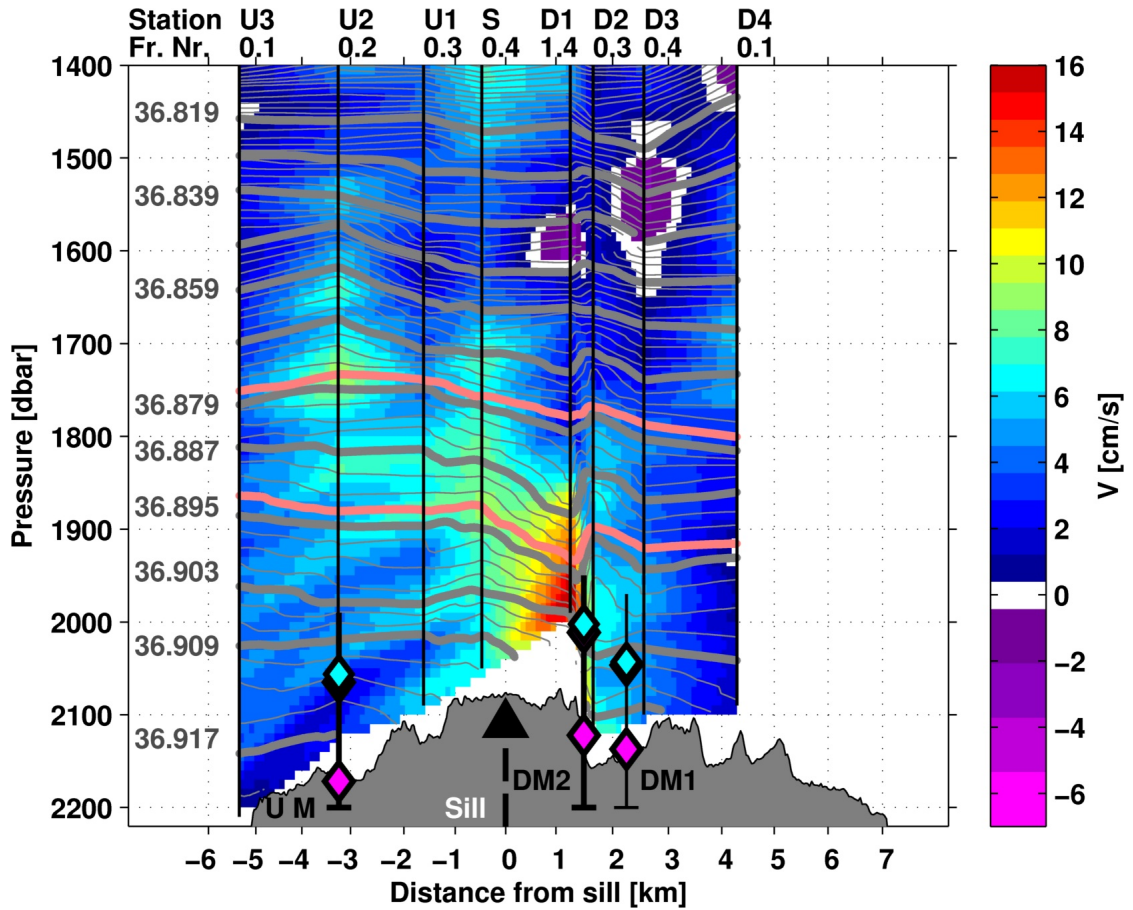


Figure 4.6: Station averaged along-channel LADCP derived velocity. The stations are given at the top of each panel together with Froude Numbers. Vertical lines mark the latitude of each station. At the Stations D2 and D3 only the central stations have been used (Table 2.1 and Fig. 2.1). The color refer to along-channel velocity but Froude Numbers were computed from absolute flow speeds. Contour lines denote potential density (spacing $\Delta\sigma_2 = 0.002 \text{ kg/m}^3$) with colored contours indicating the isopycnals used for Froude Number computation (Section 1.4). Topography as in Fig. 4.1.

4.2 Average Velocity and Density Field

The average across-channel velocity component (zonal velocity) was generally below 2 cm/s throughout the channel (Fig. 4.7). The deviation from the along-channel direction with weak westward flow at station D3 could be attributed to the bottom elevation around 37.305° N, which reaches up to 2000 m (Fig. 4.5), or to the north-westward orientation of the western channel boundary (the Lucky Strike volcano). The flow above ~ 1800 m showed higher westward velocities with a maximum of 7 cm/s at Station D1 which might already be situated above the ridge flank topography confining the flow below into along-channel direction. The weak across-channel velocity component again confirmed that the flow is directed along the channel. Therefore, the across-channel component will not be discussed any further throughout this thesis.

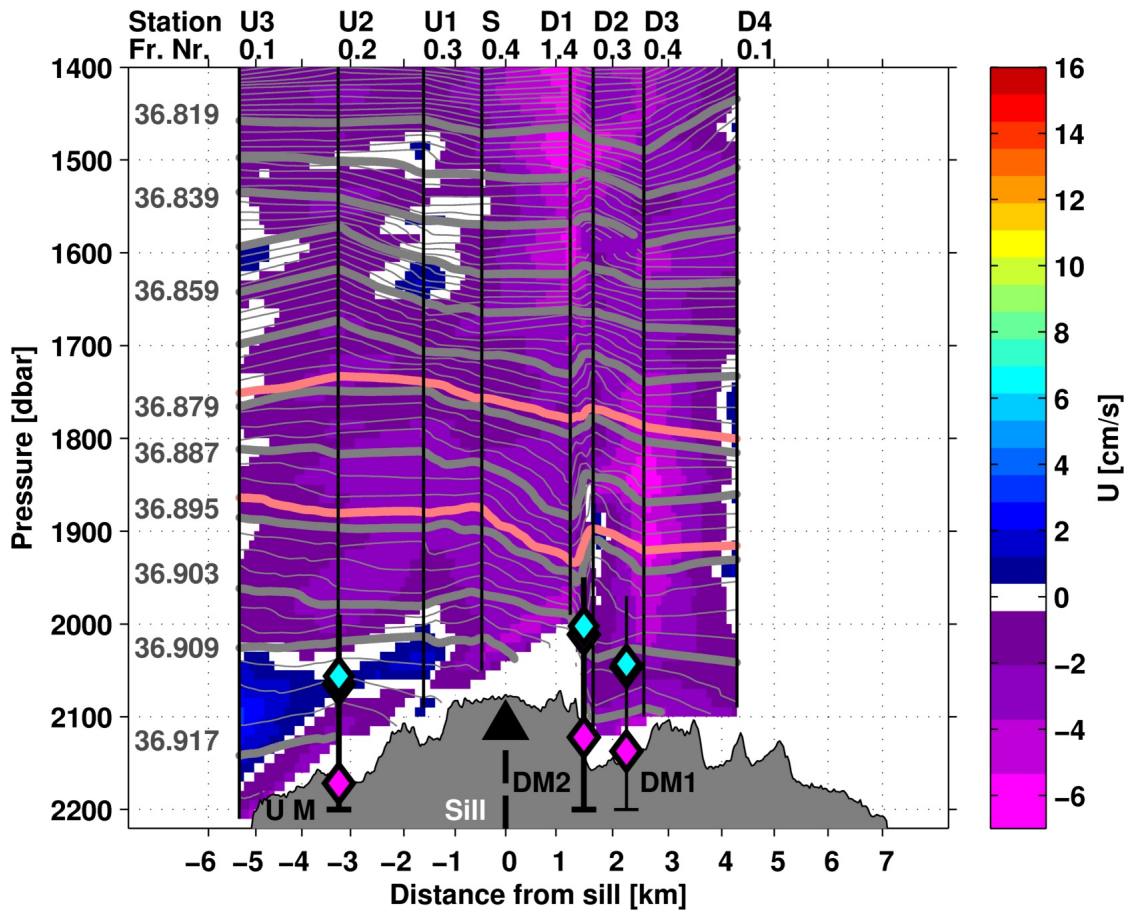


Figure 4.7: Station averaged across-channel LADCP derived velocity. The stations are given at the top of each panel together with Froude Numbers. Vertical lines mark the latitude of each station. At the Stations D2 and D3 only the central stations have been used (Table 2.1 and Fig. 2.1). The color refer to across-channel velocity but Froude Numbers were computed from absolute flow speeds. Contour lines denote potential density (spacing $\Delta\sigma_2 = 0.002 \text{ kg/m}^3$) with colored contours indicating the isopycnals used for Froude Number computation (Section 1.4). Topography as in Fig. 4.1.

Vertical Shear of along-Channel Velocity

The distribution of the flow velocity along the channel with its strong maximum just downstream of the sill revealed strong shear close to the sill (Fig. 4.6) which might potentially lead to shear instabilities. Shear instabilities are likely to occur if the ratio of buoyancy frequency N and vertical shear of horizontal velocity $\delta U/\delta z$, expressed as the Richardson number $R_i = N^2/(\delta U/\delta z)^2$, falls below $1/4$ (Thorpe, 2005). Richardson numbers were computed over 50 m layers from all individual profiles along the channel (Fig. 4.8). The layer thickness of 50 m was chosen to compute the Richardson Number over stable stratified layers. The vertical length scale of stable stratification was estimated based on the Ozmidov scale of about

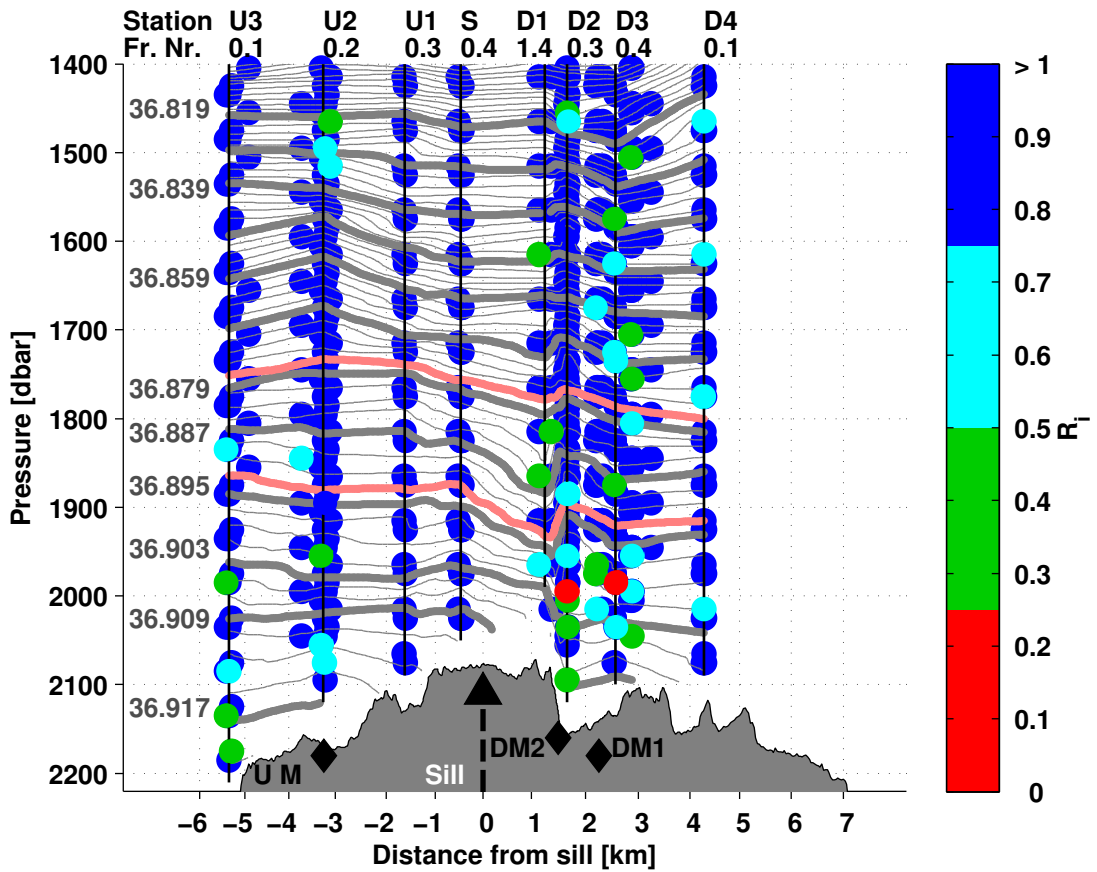


Figure 4.8: Richardson numbers along the channel from station averaged velocity and stratification. The stations are given at the top of each panel together with Froude Numbers. At the Stations D2 and D3 only the central stations have been used (Table 2.1 and Fig. 2.1). Vertical lines mark the latitude of each station. Contour lines denote potential density (spacing $\Delta\sigma_2 = 0.002 \text{ kg/m}^3$) with colored contours indicating the isopycnals used for Froude Number computation (Section 1.4). Topography as in Fig. 4.1.

30 m indicating the maximum overturn size (*Ozmidov* (1965)). For details regarding the overturn size see Section 4.4.3. Critical numbers of less than $1/4$ were found twice in the area just downstream of the sill close to the sea floor. Values below unity were found rather frequently in the range of 1 to 4 km downstream of the sill close the bottom, but also at shallower depth. Upstream of the sill low R_i were found below 1800 m at station U3 and U2 as well as between 1400 m and 1500 m depth at station D2.

While low Richardson numbers downstream of the sill are probably caused by strong shear induced by the overflow it is unclear what caused the low Richardson numbers at shallower depths. Upward propagating internal waves possibly generated by overflow related processes at the sill could be a possible explanation (*Legg and Huijts*, 2006).

As the R_i was below the critical value of $1/4$ only twice in all the observations available here, shear instabilities can probably not explain the strong mixing downstream of the sill. This further supports the evidence of the mixing being caused by a hydraulic jump.

4.2.3 Vertical across-Channel Section of the along-Channel Flow and Density Distribution

In the previous paragraphs the along-channel flow was shown to have a strong maximum downstream of the sill. Elevated Froude Numbers as well as isopycnal displacement (Fig. 4.6) strongly indicated the presence of a hydraulic jump. In the along-channel sections showing these features, only the central stations of the group stations were used (station list see Table 2.1) such that it might be interesting to look at the across-channel structure of the along-channel flow. Downstream of the sill, the stations of lowered observations were distributed such, that two across-channel sections could be analyzed. The first across-channel section was located 1.6 km downstream of the sill with a distance of about 0.17 km to the mooring position DM2 at a mean latitude of 37.292°N , while the second across section was located 2.6 km downstream of the sill with a distance of 0.33 km to the mooring location DM1 at a mean latitude of 37.3°N (Fig. 2.1). Both sections consisted of a western, a central and an eastern station at the latitude of the group stations D2 and D3, respectively (station list Table 2.1).

At the location of the first across-channel section the along-channel velocity showed a maximum in the center of the channel between 1800 m and 1900 m and near the bottom (Fig. 4.9a). The near bottom flow was concentrated more on the eastern side of the channel, while the western side showed a weak tendency towards southward flow. Above 1800 m the flow was weaker with northward direction at the western and center station and southward flow at the eastern station.

The densest water was found in the center of the channel at station D2c. Between the bottom and 1900 m depth the water was slightly lighter on the eastern valley wall compared to center and the western channel edge. The upward displacement of the isopycnals in the center of the channel above 2000 m most probably was

4 Turbulence, Density and Flow Distribution along the Channel

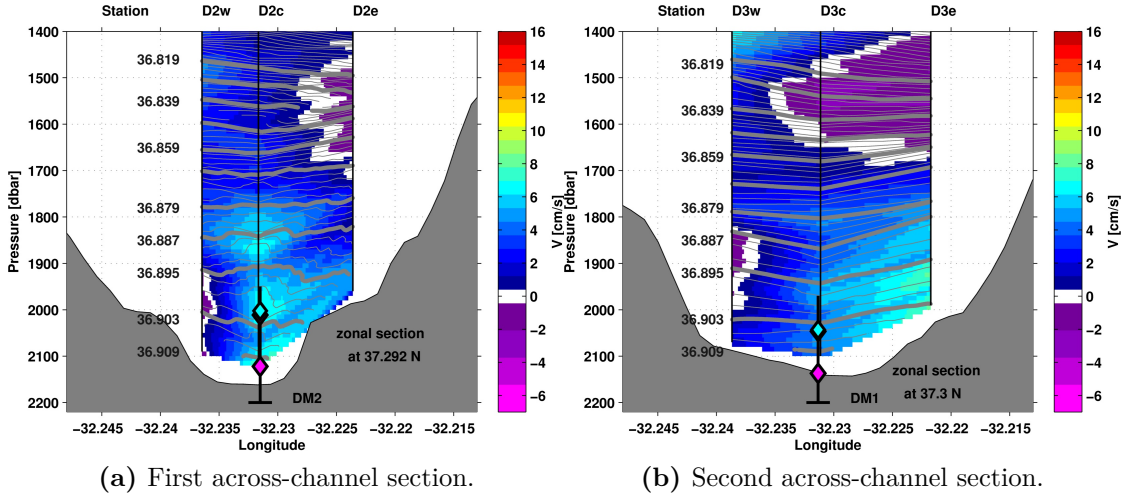


Figure 4.9: Station averaged along-channel LADCP derived velocity at the first (a) and second (b) across-channel section. The station numbers are given at the top of each panel. Vertical lines mark the latitude of each station. Contour lines denote potential density (spacing $\Delta\sigma_2 = 0.002 \text{ kg/m}^3$).

related to the hydraulic jump which was observed at this location in the along-channel section of the along-channel flow and density distribution (Fig. 4.6).

The second across-channel section at the mean latitude of 37.3° N , just downstream of the hydraulic jump, showed elevated northward flow below 1800 m in the center and at the eastern station, while weak southward flow was found at the western station (Fig. 4.9b). Above 1800 m northward velocities were below 3.2 cm/s at the western station except above 1500 m. Weak southward flow was found in the center and at the eastern station.

In the second across-channel section the densest water was again found in the channel center. In contrast to the first across-section (Fig. 4.9a) this was true up to a depth of 1800 m, and the upward displacement of isopycnals observed at the first across-section was not observed here.

The two across-channel sections thus showed indications for a hydraulic jump being confined zonally to the center of the channel and meridionally to the first across-channel section, as the upward displacement of isopycnals was absent at the second across-channel section.

4.2.4 Summary

In the previous paragraphs the average flow in the eastern channel of the LS segment was found to be directed towards the northeast (i.e. along the channel), with highest flow speeds observed at the first downstream station D1. Both, flow and density distribution indicated the presence of a small hydraulic jump (Sec-

tion 1.4), which is supported by near critical Froude numbers just downstream of the sill (Section 4.2.2). Hydraulic jumps have previously been observed in the deep ocean by e.g. *Polzin et al.* (1996) and *Alford et al.* (2013). Further analysis regarding the hydraulic jump at the LS segment and its possible variability are reported in Section 5.3.1.

Richardson numbers were found to be below the critical value for shear instabilities of $1/4$ only at two stations downstream of the sill and no strong evidence of instabilities in the time mean flow was found. This further supports the interpretation of a hydraulic jump inducing the mixing downstream of the sill. Upward energy propagation as observed by *Legg and Huijts* (2006) could be responsible for the near critical Richardson numbers higher in the water column.

The across-channel distribution showed the core of the along channel flow to be situated in the channel center at the downstream station D2 with the upward isopycnal displacement related to the hydraulic jump. In the second across-channel section at station D3 further downstream, no hydraulic jump related displacement was observed, which is consistent with the along-channel section.

4.3 Averaged Diffusivity

The mixing observed at the Lucky Strike segment presented in Section 4.1 was expressed by the dissipation rate which represents the energy dissipated into heat by molecular diffusion. If mixing occurs energy is not only dissipated into heat but also transferred from kinetic to potential energy by diapycnal mixing. In order to express diapycnal mixing a turbulent eddy diffusivity K can be defined in analogy to molecular diffusion as mentioned in the introduction (Section 1.1). It can be used to estimate tracer fluxes by multiplication with the respective gradient. The diffusivity K can be estimated from the dissipation rate of turbulent kinetic energy ϵ using the Osborn model $K = \Gamma \cdot \epsilon / N^2$ (Equation 1.2) where N is the buoyancy frequency and the parameter Γ is related to the mixing efficiency usually assumed to equal 0.2 (*Osborn*, 1980). In the following two paragraphs, the diffusivity is derived from the observed dissipation rate (Section 4.1.2) using the Osborn model and compared to a diffusivity estimate from advection-diffusion balance in a box at the sill based on hydrographic observations.

4.3.1 Turbulent Diffusivity Distribution along the Channel

The turbulent eddy diffusivity K was estimated using the Osborn model (Equation 1.2, *Osborn* (1980)) based on the box averaged dissipation rates reported in Section 4.1.2. The buoyancy frequency was estimated from lowered CTD measurements from the group-averaged stations U3 – U1, S, and D1 – D4 with the same topography following interpolation used before (*Kanzow and Zenk*, 2014). The AUV sampled a larger latitudinal range than covered by lowered measurements such that the buoyancy frequency had to be somehow extrapolated. For the missing range south of station U3, north of station D4, and close to the sea floor, the

4 Turbulence, Density and Flow Distribution along the Channel

buoyancy frequency was assumed to be constant i.e. the value observed next to the missing range was used (Fig. 4.10a).

The measurement error of the CTD data was small (Section 2.1) in comparison to the uncertainty induced by the variability of the stratification encountered at same locations (Section 5) and hence the measurement error was neglected. The uncertainty of the diffusivity was estimated with the uncertainty of the box-averaged dissipation rates (Section 4.1.2) and the error of the average N^2 . The latter was estimated by analyzing the ratio of N^2 determined from ‘extreme profiles’ at each stations (Fig. A.4b. Details regarding ‘extreme profiles’ are given in Section 5). This ratio will be referred to as the ‘ N^2 ratio’ below. The resulting histogram of the N^2 ratio indicated the lower and upper limit of the 95% confidence level at 0.6 and 2, respectively, for the N^2 ratio (Fig. A.5). The error of the box-averaged dissipation rates was determined to range between 1.2 and 1.7 in the latitudinal range where CTD data were available. This leads to a factor of 2.4 – 3.4 in total for the uncertainty of the diffusivity.

Elevated diffusivities were found close to the bottom up- and downstream of the sill. The upstream maximum of $\sim 1 \cdot 10^{-2} \text{ m}^2/\text{s}$ was located at station U3 at the bottom where the topography slope angle was close to the internal wave characteristic s with respect to the M_2 tide favoring critical reflection at the bottom (Section 4.1.1). Furthermore, the stratification was comparably weak below 1800 m upstream of the sill (buoyancy frequency along the channel in Fig. A.4). At station D1, the diffusivity was lowest at the bottom because the buoyancy frequency

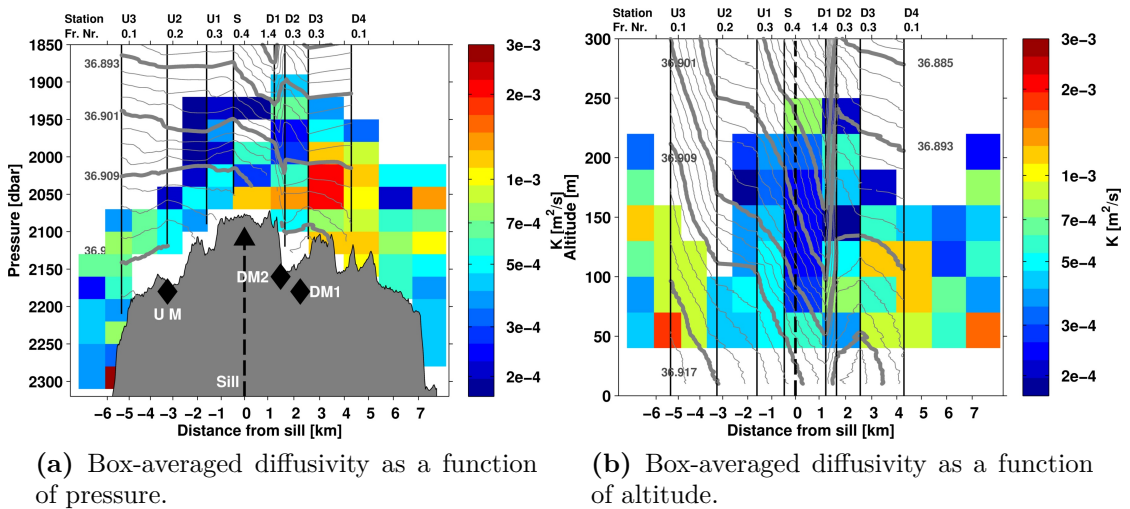


Figure 4.10: Along-channel distribution of turbulent diffusivity (colored boxes). Diamonds show the positions of the moorings DM1, DM2 and UM. Contours show density from CTD profiles (spacing $\Delta\sigma_2 = 0.002 \text{ kg/m}^3$). The stations are given at the top of each panel together with Froude Numbers. Vertical lines mark the latitude of each station. a: Topography as in Figure 4.1.

was comparably large. Downstream of the sill diffusivities up to $\sim 2 \cdot 10^{-3} \text{ m}^2/\text{s}$ were found.

In the altitude dependent projection (Fig. 4.10b), the diffusivity was comparably large ($\sim 7 \cdot 10^{-4} \text{ m}^2/\text{s}$) upstream of the sill in the lower 150 m above the sea floor although the dissipation rates were low (Fig. 4.4), resulting from the low buoyancy frequency. Downstream of the sill, the diffusivities reached values of 1 to $2 \cdot 10^{-3} \text{ m}^2/\text{s}$ within 150 m above the sea floor.

Comparing the results to the findings of *St. Laurent and Thurnherr* (2007) the turbulent diffusivities were in good agreement at the sill and downstream of it. Upstream of the sill *St. Laurent and Thurnherr* (2007) found values above $1 \cdot 10^{-3} \text{ m}^2/\text{s}$, while only $(2 - 7) \cdot 10^{-4} \text{ m}^2/\text{s}$ was observed in this study. Thus, one of the central questions addressed in this thesis can now be answered. The dissipation rates and also the diffusivities were distributed asymmetrically with respect to the position of the sill, while this was unclear from the study by *St. Laurent and Thurnherr* (2007). The elevated mixing upstream of the sill observed by *St. Laurent and Thurnherr* (2007) was found to be weaker than the downstream mixing in this study and potential mechanisms inducing the elevated upstream mixing have been identified (near critical reflection of the M_2 tide at the bottom and weak stratification). Thus, the high dissipation rates and diffusivities downstream of the sill observed in the course of this thesis were consistent with overflow induced mixing.

4.3.2 Advection Diffusion Balance

For comparison with the observed diffusivity for density reported above, the diffusivity for temperature was estimated using an advection diffusion balance similarly as performed by *Ferron et al.* (1998). The diffusivity for temperature is assumed to equal the diffusivity for density (Section 4.4.2 and *Zhang and Moum* (2010)).

In the advection diffusion balance in steady state mixing downstream of the sill causes the temperature to increase, while cold water is constantly advected such that the average temperature is constant ($d\theta/dt = 0$). Using this assumption a box was defined (Fig. 4.11) where the advection diffusion balance applies and the following Equation can be established based on observed temperatures:

$$\bar{u} \bar{\theta} H X + H X K_y \partial_y \theta = A w \theta_A + A K_z \partial_z \theta, \quad (4.2)$$

where \bar{u} is the average velocity, $\bar{\theta}$ the average temperature, H and X the height and width of the box, K_y is the diffusivity for temperature into the box, ∂_y represents $\partial/\partial y$ and respectively $\partial_z = \partial/\partial z$, w is the upward velocity across the surface A with the temperature θ_A and K_z is the vertical diffusivity for temperature across the isotherm defining the surface A , the edge of the box (Fig. 4.11). The first term on each side of Equation 4.2 describes the advective flux, horizontally on the left hand side and vertically on the right hand side (Fig. 4.11). The second term on each side describes the horizontal (left) and vertical diffusion (right). If the

4 Turbulence, Density and Flow Distribution along the Channel

diffusion into the box is neglected ($H X K_y \partial_y \theta = 0$) and continuity of the volume is assumed:

$$\bar{u} H X = A w, \quad (4.3)$$

equation 4.2 reduces to:

$$\begin{aligned} \bar{u} H X (\bar{\theta} - \theta_A) &= A K_z \partial_z \theta, \\ \Leftrightarrow K_z &= \frac{\bar{u} H X (\bar{\theta} - \theta_A)}{A \partial_z \theta} \end{aligned} \quad (4.4)$$

where K_z can be estimated. The isotherm θ_A defining the edge of the box was chosen to be the bottom most temperature observed in the average profile at the most downstream station D4. The inflow was chosen to be defined by station S slightly upstream of the sill because the first downstream station was too shallow to capture the bottom most inflow/overflow as it was located at the edge of the channel (Fig. 4.10 e.g. isopycnal 36.909 disappeared at station D1 but was found again at station D2, see station map in Fig. 2.1). The average temperature and velocity below the isopycnal θ_A defining the upper edge of the box, were taken for $\bar{\theta}$ and \bar{u} , respectively. The surface A was set to equal $A = X \cdot Y$ where Y is the length of the box. The temperature gradient was estimated to be $1 \cdot 10^{-3} \text{ K/m}$ from lowered observations. The channel width was set to $X = 3000 \text{ m}$. Based on these assumptions the vertical diffusivity for temperature K_z across the surface θ_A can be estimated to be about $3 \cdot 10^{-2} \text{ m}^2/\text{s}$, which, on average, is at least one order of magnitude larger than the diffusivity for density estimated based on the dissipation rates and the buoyancy frequency (Section 4.3.1).

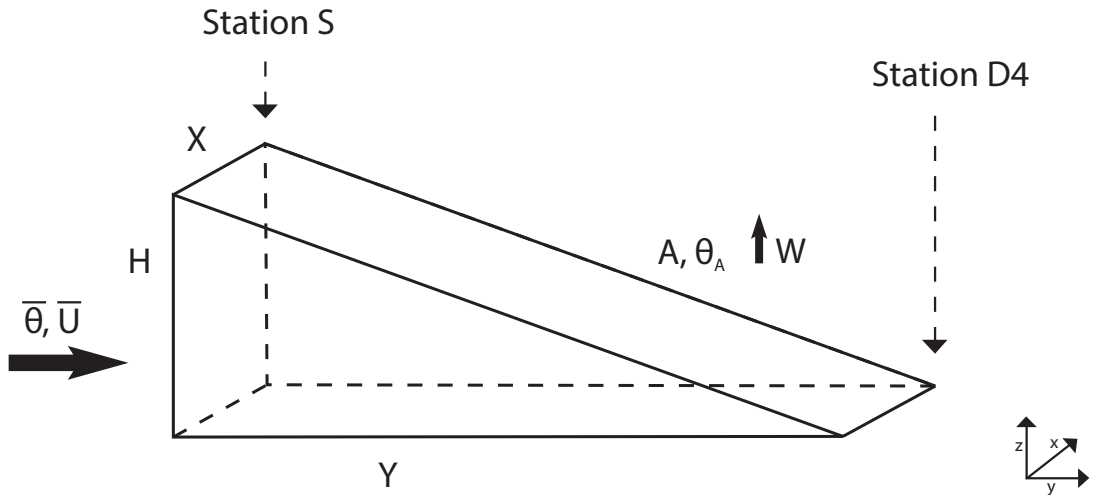


Figure 4.11: Sketch of the box and the respective variables defined for the advection diffusion balance. See text for variable definition. Reference frame in lower right corner.

4.4 Density and Temperature fine-Structure

One source of uncertainty is the diffusive flux into the box (second term in Equation 4.2) which was neglected in Equation 4.4. This term was estimated using the four profiles available at station S by the deviations from the mean of each profile multiplied by the influx surface $H \cdot X$ (Fig. 4.11):

$$H X K_y \partial_y \theta = H X \frac{1}{4} \sum_{i=1}^4 (u_i - \bar{u}) (\theta_i - \bar{\theta}). \quad (4.5)$$

Based on the four profiles available at station S the diffusive flux into the box contributes a diffusivity of $0.2 \text{ m}^2/\text{s}$. As this diffusivity is one order of magnitude larger than the vertical diffusivity K_z estimated to be about $3 \cdot 10^{-2} \text{ m}^2/\text{s}$, this term cannot be neglected.

This simple assumption of an advection diffusion balance in steady state did not provide useful results. Reasons could be:

- temporal variability in the density, velocity, and in the dissipation rates, which possibly were not captured by the observations,
- dense water leaving the channel on the eastern edge (Fig. 4.9b) which was not observed at the station D4 (see map in Fig. 2.1),
- the rough topography possibly inducing spatial variability,
- the assumption of steady state, which might not be feasible.

If the water volume in the box is warming or cooling, further terms describing the heat storage need to be taken into account in Equation 4.2. The mooring-based temperature time-series analyzed in Section 5.1.2 might indicate a warming downstream of the sill and possibly even a cooling upstream. The temporal variability of the flow and the dissipation rates is discussed in Section 5. No further attempts regarding the advection diffusion balance are made throughout this thesis.

4.4 Density and Temperature fine-Structure

So far, the distributions of the dissipation rate, the velocity and the density along the channel have been studied as well as the average dissipation rate and the diffusivity. Strong indications for the presence of a hydraulic jump downstream of the sill were found which is expected to be associated with strong mixing consistent with the distribution of the dissipation rate. Although the measurements have a resolution of a few meters, all considerations were focused on length scales on the order of 100 m. In the following much smaller scales of density and temperature variability on the order of 1 m are studied. These quantities both are expected to be elevated in a region of strong mixing in stratified waters and thus can provide

further evidence for mixing. Furthermore, the density and temperature observations are independent from velocity shear observations and can therefore confirm the velocity shear-based results.

Small scale density variability on the order of a few meters can be studied using the on-board CTD of the AUV which was sampling the density simultaneously to the microstructure observations along the AUV track. Even smaller scales can be studied using the fast temperature microstructure data which were collected together with the velocity microstructure data by the MR. With this high-resolution temperature data the scales of motions in the ocean ranging from small internal waves to the subranges of turbulence can be examined using temperature gradient spectra. Motions on large length-scales are dominated by the internal wave field ('internal-wave' subrange), while the strength of turbulence and the temperature gradient dominate the 'inertial-convective' subrange at the lowest turbulence wavenumbers (*Klymak and Moum, 2007a,b*). At smaller scales the water viscosity becomes more important in the 'inertial-diffusive' subrange (this subrange was referred to as 'viscous-convective' in *Tippenhauer et al. (2015)* but the term 'inertial-diffusive' following *Klymak and Moum (2007b)* will be used below). The different subranges can be distinguished by their isothermal slopes (*Batchelor, 1959; Klymak and Moum, 2007a,b; Zhang and Moum, 2010*). Both, the horizontal density variability and the horizontal temperature variability are reported below. Finally, the differences emerging from AUV-derived small scale density and temperature variability encountered during different occupations of the same sampling track, are discussed at the example of one segment.

4.4.1 Horizontal Density Anomalies

As small scale density variability is expected in turbulent waters experiencing a density gradient. Elevated density variability provides further evidence for the occurrence of turbulence. The CTD aboard the AUV allowed to investigate the along-track density structure in conjunction with the turbulence measurements. In order to identify areas of elevated small scale density variability, detrended density transects from segments along constant depth levels were studied. The spatial and temporal density variability ($\Delta\sigma_2$) was found to be distributed similar as the dissipation rate (Fig. 4.12). The density variability was low upstream of the sill but increased in the downstream direction with the most elevated variability being located 1 to 4 km downstream of the sill, in the same area where elevated dissipation rates were observed (compare Figs. 4.12), 4.1, 4.2 and 4.3). The density variability decreased further downstream but remained at higher levels than upstream of the sill. Although the spatial pattern were robust showing high density gradients downstream of the sill, the temporal variability was large. Areas where a pronounced density gradient was observed in one AUV passing, the gradients were small in the next passing a few hours later as is further discussed in Section 4.4.3. Overall the agreement of the pattern of elevated density variability and elevated dissipation rates confirmed not only the mixing pattern identified in previous sec-

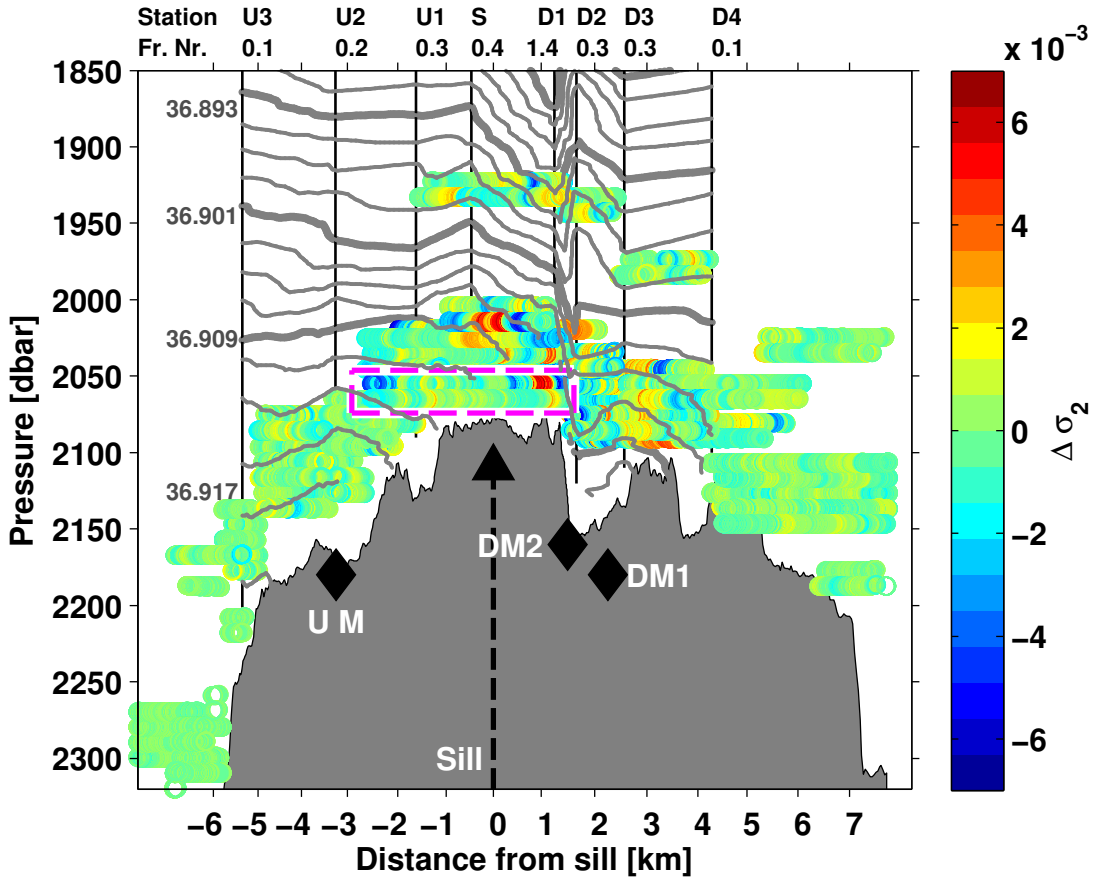


Figure 4.12: Meridional distribution of the density anomalies from Dives 1 to 4 for segments along constant pressure. Areas which were sampled twice by the AUV are shown vertically displaced by 10 to 30 dbar. The contour lines show density from lowered CTD ($\Delta\sigma_2 = 0.002 \text{ kg/m}^3$). The thin vertical lines mark CTD/LADCP stations, their acronyms and associated Froude numbers stated above the plot. Diamonds show the positions of the moorings DM1, DM2 and UM. Topography as in Fig. 4.1. The magenta dashed box indicates the segment discussed in Section 4.4.3.

tions, but also the AUV-based turbulence measurements in general. As the AUV-based density measurements can be seen as independent from AUV induced vibrations this nicely illustrates that the AUV-MR system in combination with the method of inferring dissipation rates developed in the course of this thesis provides robust turbulence observations.

4.4.2 Horizontal Temperature Variability and Scales of Turbulence

Density variability and also small scale temperature variability are expected to be associated to elevated turbulence if turbulence acts on water exhibiting a temperature gradient. Motions in the ocean causing temperature variability on length

4 Turbulence, Density and Flow Distribution along the Channel

scales larger than those associated to turbulence are usually dominated by internal waves. The different mechanisms (internal waves or turbulence) causing temperature variability are referred to as subranges and can be identified studying temperature (gradient) spectra. Using the temperature gradient spectra instead of the temperature spectra allows for easier visual discrimination between different subranges. Here, horizontal temperature gradient spectra are studied. Due to the internal wave aspect ratio with the horizontal length scales of internal waves being much larger than the vertical length scales, larger spacial scales of the turbulent subrange are resolved using horizontal instead of vertical spectra (*Klymak and Moum, 2007a*).

In the following, horizontal temperature gradient spectra are studied focusing on three subjects.

- It is investigated whether elevated turbulence is associated with elevated small-scale temperature variance.
- The different subranges are investigated, i.e. the ‘internal wave’, the ‘inertial-convective’, and the ‘inertial-diffusive’ subrange which are dominated by different physical processes and can be identified by their slopes of the temperature spectra or spectra of vertical isopycnal displacement (*Batchelor, 1959; Klymak and Moum, 2007a,b; Zhang and Moum, 2010*).
- After identifying the different subranges it is tested whether the variance of the temperature gradient spectra in the inertial-convective subrange scales as ϵ^2 as is expected from theory (*Zhang and Moum, 2010*).

The displacement spectra (ζ) can be converted to temperature spectra and vice versa by multiplication with the square of the temperature gradient $(dT/dz)^2$ (*Klymak and Moum, 2007a*). The gradient spectra can be computed from the spectra of the respective variable by multiplication with $(2\pi k)^2$ where $k = \hat{k}/2\pi$ is the wavenumber in cycles per meter (cpm) and $\hat{k} = 2\pi f/u$ is the wavenumber in radians per meter, f is the frequency and u is the velocity of the water relative to the sampling device (*Klymak and Moum, 2007a*).

The internal-wave subrange describes the large-scale motions dominated by internal waves. The spectra fall off to smaller length scales, i.e. larger wavenumbers k as k^0 at low wavenumbers and k^{-1} towards larger wavenumbers with a broad wavenumber range with a slope of $k^{-0.5}$ (*Klymak and Moum, 2007a*). Below the internal-wave subrange, the inertial-convective subrange describes the motions being dominated by large scale-turbulent motions and the temperature gradient. In this subrange the temperature gradient spectra (Φ_{IC}) have a slope proportional to $k^{1/3}$ (*Klymak and Moum, 2007b*):

$$\Phi_{IC} = 2\pi\chi C_T\epsilon^{-1/3} (2\pi k)^{1/3} \quad [\text{cpm}^{-1}], \quad (4.6)$$

where k is the horizontal wavenumber in cycles per meter, $C_T \approx 0.4$ (*Sreenivasan, 1996; Klymak and Moum, 2007b*), χ the dissipation of temperature variance, and

4.4 Density and Temperature fine-Structure

ϵ is the dissipation rate. Turbulent motions with smaller length scales are described as the inertial-diffusive subrange where the viscosity of sea water is important. This subrange has a slope of k^1 (*Klymak and Moum, 2007b*):

$$\Phi_{\text{ID}} = 2\pi\chi q\nu^{1/2}\epsilon^{-1/2}(2\pi k) \quad [\text{cpm}^{-1}], \quad (4.7)$$

where q is an empirical constant.

From high resolution temperature data, horizontal wavenumber spectra were computed along constant pressure. The temperature signal was detrended prior to computing the spectra. Varying numbers of data segments (with 50% overlap) were used to reduce the noise in the high wavenumber range without reducing the resolution at low wavenumbers. Prior to Fourier decomposition a 1/2-cosine taper was applied to the first and last 10% of each segment. The Fourier coefficients were normalized and squared. From the temperature spectra the horizontal temperature gradient spectra were computed by multiplication with $(2\pi k)^2$ (*Dengler and Quadfasel, 2002; Klymak and Moum, 2007a*).

Two 4000 m long segments along constant pressure were used in order to resolve low wavenumbers (k) supposedly dominated by the internal wave regime (Fig. 4.13a). For the more energetic of the two spectra, the internal wave subrange with an expected slope of k^{-1} to k^0 appears to be present at wavelengths below 250 m. The inertial-convective turbulent subrange with an expected slope of $k^{1/3}$ can be identified between wavelengths of 250 m to 1 m. The inertial-diffusive subrange with a slope of k^1 was not fully resolved due to the limited sensor response time and the relatively fast profiling speed. In the less energetic of the two spectra, the internal wave k dependence was less visible (Fig. 4.13a). Also the distinction between the inertial-convective and the inertial-diffusive subranges was less clear.

Temperature gradient spectra were also computed from 500 m long segments along constant pressure in order to discuss the relationship between dissipation rate and temperature gradient variance in the inertial-convective subrange. During Dive 8, in total 128 segments with a length of 500 m were sampled. The resulting 128 spectra were averaged in four groups according to the segment mean dissipation rate (without noise correction). On average, the spectra energy level was elevated at elevated average dissipation rates (Fig. 4.13b). The inertial-convective and inertial-diffusive subranges extend roughly from 250 m to 1 m and from 1 m to about 0.5 m, respectively. Again, the theoretical slope of the inertial-diffusive subrange was not fully resolved.

In the inertial-convective subrange the variance of the temperature gradient spectra is expected to scale as $\epsilon^{2/3}$ under the assumption that variations in stratification

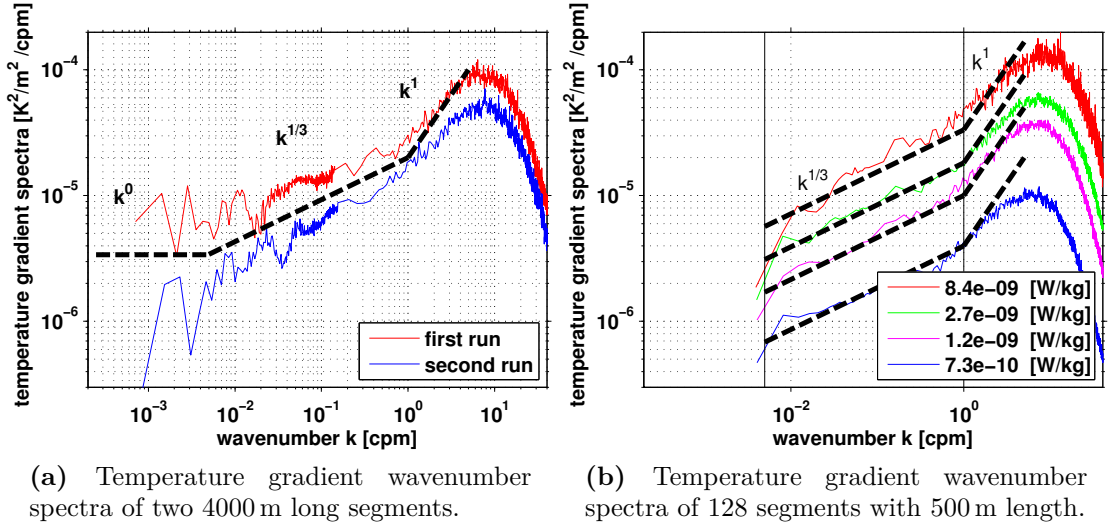


Figure 4.13: Temperature gradient wavenumber spectra along constant pressure. When computing the spectra, varying numbers of data segments (with 50% overlap) were used to reduce the noise in the high wavenumber range without reducing the resolution for low wavenumbers (this causes the change in resolution between 10^{-2} and 10^0 cpm). The 500 m long segments are averaged in 4 groups according to the mean dissipation of each segment. The mean dissipation of each group is given in the legend. The black, dashed lines (both panels) have slopes of k^0 , $k^{1/3}$ and k^1 and indicate the approximate wavenumber range of the internal wave, the inertial convective and the inertial-diffusive subranges, respectively.

can be neglected and the eddy diffusivity for heat (*Zhang and Moum, 2010*),

$$K_T = \frac{\chi_T}{2T_z^2}, \quad (4.8)$$

is equal to the eddy diffusivity for density,

$$K_\rho = \frac{\Gamma\epsilon}{N^2}, \quad (4.9)$$

where T_z is the local vertical temperature gradient dT/dz , N the buoyancy frequency, and $\Gamma = 0.2$ is related to the mixing efficiency (*Osborn, 1980*). Under these assumptions $K_T = K_\rho$, Equations 4.7 can be expressed as (*Zhang and Moum, 2010*),

$$\Phi_{\text{IC}} = 2\Gamma C_T \frac{(dT/dz)^2}{N^2} \epsilon^{2/3} k^{1/3}, \quad (4.10)$$

scaling as $\epsilon^{2/3}$.

The temperature gradient wavenumber spectra from the 128 segments were integrated over the inertial-convective subrange from 250 m to 1 m (Fig. 4.14). The corresponding mean dissipation rate of each segment was computed from individual dissipation rate estimates without any correction regarding the noise, although the

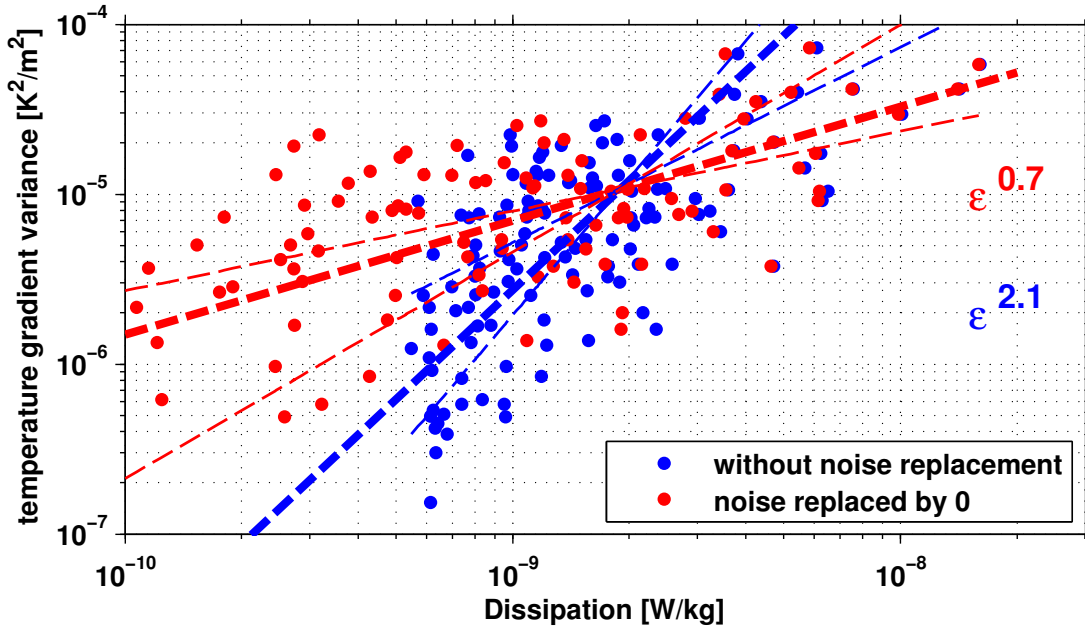


Figure 4.14: Temperature gradient variance integrated over the inertial convective subrange (250 m to 1 m) for each spectrum based on 500 m long segments as function of the segment mean ϵ with measurement noise (blue dots) and with individual ϵ values below two times the noise level ϵ_n replaced by zero (red dots). The slope of the bold, dashed line was found by major axis regression and is given at the right side. The thin dashed lines denote the slope error (see text for explanation).

mean dissipation rate was dominated by noise within most of the 500 m segments (Section 3). Thus, the averages were biased high. To avoid this bias averaging was also performed after replacing all individual dissipation rate estimates below two times the noise level by zero (*Gregg, 1989*). For each of the two mean dissipation rate versions the best exponential fit was estimated by major axis regression for logarithmic variables following *Laws (1997)*. As error for this estimate, a range for the slope was estimated by linearly fitting the dissipation-axis against the temperature-gradient-axis and vice versa. The resulting slopes represent the minimum and maximum slope occurring by neglecting the measurement error of the axis used for the regression, respectively.

A slope of 2.1 (range 1.2 to 2.7) was found for the noise biased mean dissipation rates (Fig. 4.14). For the mean dissipation rate where the noise was replaced by zero, a slope of 0.7 (0.5 to 1.3) was found. The dissipation rate dependence of the temperature gradient variance of the version without noise replacement is too steep but after replacing the noise, the slope is consistent with an $\epsilon^{2/3}$ dependence. Note that variations in stratification have been neglected (Equation 4.10).

Studying the temperature gradient spectra revealed the theoretically expected slope of $k^{1/3}$ and k^1 in the inertial-convective and inertial-diffusive subranges, respectively. The inertial-convective subrange of turbulence, was shown to extend

to wavelengths as large as a few hundred meters in the deep and narrow channel of the Lucky Strike segment. For the upper ocean this has been demonstrated by *Klymak and Moum* (2007b). In this thesis, only weak indications were found for the internal wave subrange with a slope of k^{-1} to k^0 which might be attributed to the proximity to the sea floor and the narrow channel where only waves with relatively short wavelengths can propagate. The consistency of the temperature gradient wavenumber spectra with the $\epsilon^{2/3}$ dependence in the inertial-convective subrange as expected from *Zhang and Moum* (2010) could be further utilized. In future horizontal microstructure surveys, this relationship could be used to infer dissipation rates from the temperature gradient spectra directly (provided that variations in stratification are small compared to changes in ϵ). This would be of particular interest in low-turbulence environments where platform induced noise might inhibit the use of shear based measurements. By using the relation expressed in Equation 4.10, it would be sufficient to observationally resolve the internal-convective subrange of temperature microstructure to infer the dissipation rate. The issue of resolving the high wavenumbers of the temperature microstructure spectra due to the limited sensor response time would be avoided.

4.4.3 One Example of the Variability of Turbulence, Density and Temperature

The two 4000 m long segments analyzed above were the longest segments sampled along constant pressure during this study. They revealed differences in their energy level in the temperature gradient spectra (Fig. 4.13a) with the one segment exhibiting higher energy levels over the whole wavenumber range than the other segment. Furthermore, the different subranges identified by their different slopes scaling with k^{-1} to k^0 , $k^{1/3}$, and k^1 were more pronounced in the more energetic spectrum. These differences might be linked to differences in the turbulence level due to spatial and temporal variability or to the presence or absence of internal waves. As the segments were 4000 m long and only one spectrum over this range was estimated, averaging is inherent in this analysis. In order to address the question what might induce the differences observed in the temperature gradient spectra, the two segments were further analyzed using their density and turbulence time-series.

Both segment were observed during Dive 8. The same track was covered twice within 12 h (magenta dashed box in Figs. 4.1 and 4.3) such that the first run represents the first segment and the second run represents the second segment. The AUV crossed the sill at constant pressure from south to north from about 2.2 km upstream of the sill to 1.5 km downstream of it along the channel axis. During the first run, a patch of particularly elevated dissipation rates having a horizontal extent of 500 m was detected at the northern end of the segment about 800 m downstream of the sill (Fig. 4.15 upper panel). Although patches of similar horizontal extent were observed quite frequently (e.g., Fig. 4.3), the patch here was much more energetic exhibiting peak dissipation rates of $1 \cdot 10^{-7}$ W/kg. During

4.4 Density and Temperature fine-Structure

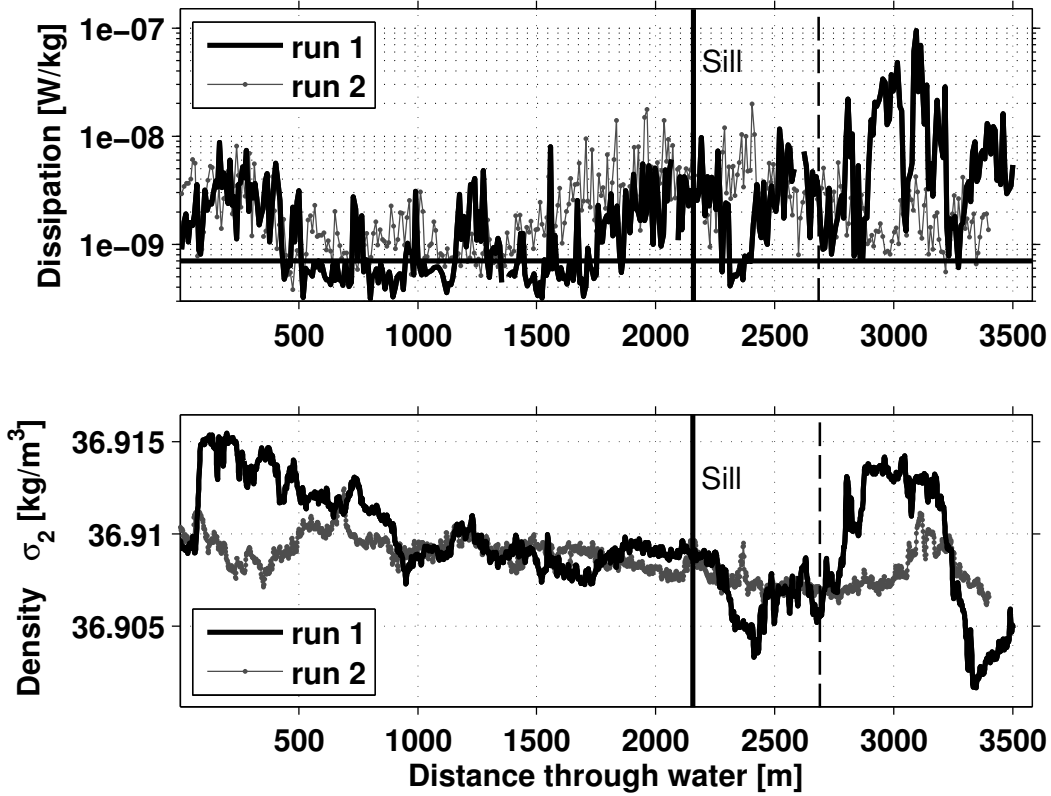


Figure 4.15: Dissipation of turbulent kinetic energy (upper panel) and potential density referenced to 2000 dbar (lower panel), as function of distance, acquired by the AUV at constant pressure in the middle of the channel (magenta box in Figs. 4.1 and 4.3). The vertical, black line marks the location of the sill. The thin dashed line marks the beginning of the turbulent patch. The horizontal, black line in upper panel indicates the noise level for Dive 8.

the second run, turbulent dissipation rates as low as $3 \cdot 10^{-9}$ W/kg were observed at the same location.

The patch of elevated turbulence observed during the first run was accompanied by elevated density and a sharp density step at the end of the patch. Within a horizontal distance of 300 m, σ_2 decreased by 0.013 kg/m^3 . During the second run, a reduced horizontal density step of 0.005 kg/m^3 was encountered at the same location. If the horizontal density step of 0.005 kg/m^3 is regarded as a background level, then the difference 0.008 kg/m^3 between the first and second run might be attributed to a turbulent overturn. To test this hypothesis, the horizontal density decrease was related to a vertical displacement of isopycnals using the mean density profile from station D2 (Fig. 4.16 lower panel). Station D2 was used as it was the second nearest station. The nearest station was station D1, but it was too shallow as it was conducted at the western edge of the channel. A maximum vertical displacement of $L_{\max} = 100 \text{ m}$ was found. This can be related to the Thorpe scale giving the mean vertical displacement in a turbulent overturn $L_T = 58 \text{ m}$

4 Turbulence, Density and Flow Distribution along the Channel

using $L_T = L_{\max} \cdot \sqrt{3}$ for a single overturn (Lorke and Wüest, 2002). This Thorpe scale is twice as large as the Ozmidov scale L_O of the largest possible overturns (Ozmidov, 1965). The Ozmidov scale was estimated to be in the range of 10 m to 30 m estimated by $L_O = \sqrt{\epsilon/N^3}$ using $\epsilon = 1 \cdot 10^{-7}$ W/kg and $N = 0.5 \cdot 10^{-3}$ to $N = 1 \cdot 10^{-3}$ 1/s. The relation of the Thorpe scale L_T and the Ozmidov scale L_O was found empirically to be $L_O/L_T \approx 0.8 - 0.93$ (Dillon, 1982; Peters et al., 1988; Ferron et al., 1998; Thorpe, 2005), while it was derived from measurements in the Strait of Gibraltar to scatter in the range of $0.25 < L_T < 4 \cdot L_O$ with a linear relation $L_T \approx L_O$ (Wesson and Gregg, 1994; Thorpe, 2005). The relation of the Thorpe and Ozmidov scale estimated here was in the range of $L_O/L_T \approx 0.17$ to 0.52 which is much smaller than the first and at the edge of the second relation reported above. It is thus considered as unlikely that the density anomaly was due to density overturning occurring in the turbulent patch. This argument is also supported

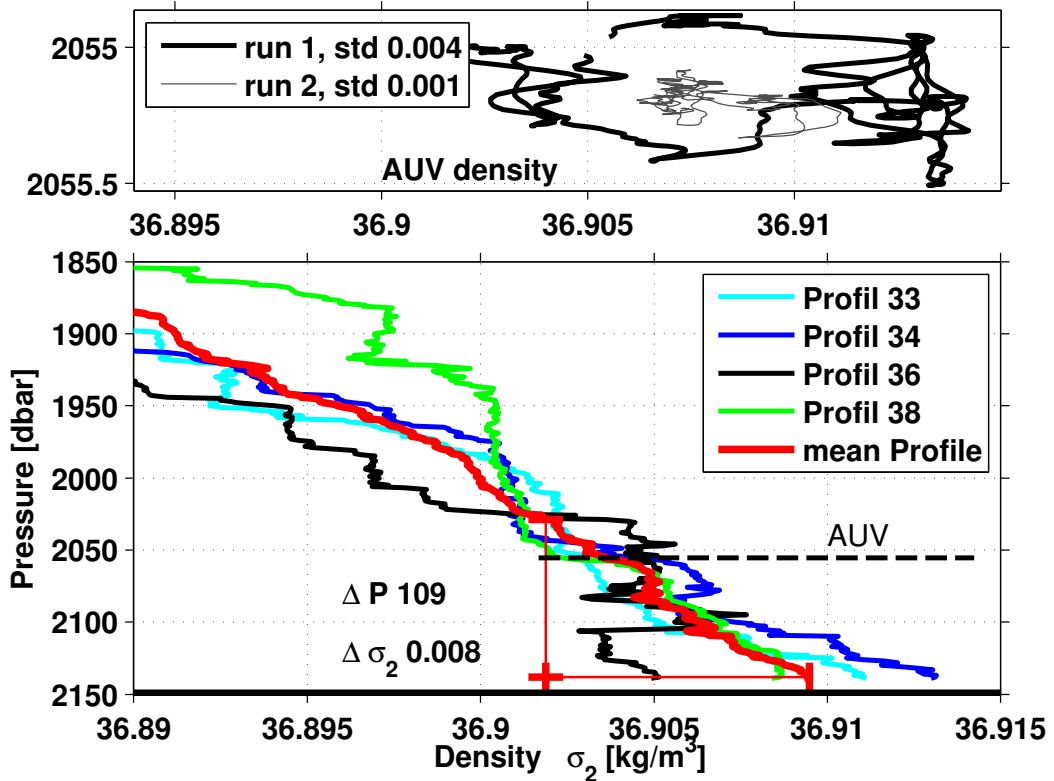


Figure 4.16: Upper panel: Potential density from the AUV CTD versus pressure for the segment shown in Fig. 4.14. The first run is shown in black (bold), the second run in grey. The legend shows standard deviation in kg/m^3 . Lower panel: Lowered CTD profiles of station 33, 34, 36, and 38 (D2w and D2c) from the region of elevated dissipation rates located downstream of the sill. The red profile shows the mean of the individual profiles. Based on that mean profile, the density difference of 0.008 kg/m^3 corresponds to a vertical displacement of about 100 m. Black dashed line indicates AUV depth and density range encountered during the patch.

by the large horizontal extent (about 500 m) of the density anomaly that should be significantly reduced in the case of a turbulent overturn. Thorpe scales were also computed for overturns observed in individual CTD profiles (Fig. 4.16 lower panel). Most of them were consistent with the Ozmidov scale. Only one CTD profile showed a Thorpe scale of 47 m, again twice as large as the Ozmidov scale. The question emerges which process might be responsible for the vertical displacement of the near-bottom waters that probably was inconsistent with a turbulent overturn. An explanation for the high-density, high-turbulent patch (Fig. 4.15) could be a horizontally sampled hydraulic jump which is likely to exist in the same area where the patch was observed. It is unclear how turbulence and density would be distributed inside a hydraulic jump on a constant pressure level. The study by *Legg and Huijts* (2006) shows a density distribution (their Fig. 7) which could, if sampled horizontally, result in a distribution comparable to the one obtained here (Fig. 4.15). Unfortunately no velocity record is available at the time and location of the patch, the hydraulic jump hypothesis cannot be supported by in-situ velocity measurements.

However, the differences encountered during both passings indicate temporal variability of the density and turbulence field. Temporal variability induced by tides has been observed in the rift valley of the MAR by *Keller et al.* (1975) and could explain the above described differences. A tidal analysis was conducted which is reported in Section 5.

4.5 Summary and Discussion

With the new AUV-MR system the horizontal distribution of the dissipation rate and the diffusivity along the deep ocean channel over complex topography was derived in the context of this thesis. From the measurements presented here a clear pattern of the along-channel distribution of the dissipation rate emerged, with highest dissipation rates being present in a segment 1 to 4 km downstream of the sill, and lower values both upstream and downstream of it. The same asymmetry was found in small-scale density variability confirming the distribution of the mixing from an independent measurement parameter. The question how the dissipation rate is distributed along the channel, across the sill, which as a result of a sparse data set remained open from the study of *St. Laurent and Thurnherr* (2007) thus was answered here. Indications for single mixing events upstream of the sill were found also in this study and were consistent with near critical reflection of the barotropic M_2 tide at the steep bottom. At least, some of the elevated mixing found by *St. Laurent and Thurnherr* (2007) upstream of the sill might be explained by the same mechanisms.

Elevated mixing downstream of the sill as shown in this thesis is consistent with a mean overflow across the sill (*Alford et al.*, 2013) which was observed by *St. Laurent and Thurnherr* (2007) and was confirmed here. A sketch of the observed flow conditions in the eastern channel of the Lucky Strike segment was developed to demonstrate the processes (Fig. 4.17).

4 Turbulence, Density and Flow Distribution along the Channel

The mean overflow across the sill fuels the mixing downstream. A hydraulic jump was observed in the study by *St. Laurent and Thurnherr (2007)* as well as in this thesis. Froude Numbers were in the range indicating a small hydraulic jump i.e. an ‘undular’ or ‘weak’ hydraulic jump. If the jump would be an undular hydraulic jump it would be transient i.e. disintegrate due to upstream propagation of intern waves (Section 1.4). Furthermore, enhanced variability would be expected downstream of the jump due to the undular waves of the jump (Section 1.4). At this point it is unclear whether the hydraulic jump is a permanent feature. This is further discussed in Section 5.

Temporal variability of a hydraulic jump might also be induced by variability of the along-channel velocity magnitude. The analysis of temperature gradient spectra in conjunction with the density and dissipation measurements in Section 4.4.3 indicated temporal variability which might be induced by tides. A strong influence of semi-diurnal tides was reported by *Keller et al. (1975)* for a sill south of the LS segment. Tidal analysis of the data set underlying this thesis is conducted in the following Section.

The density distribution downstream of the hydraulic jump is dependent on the jump amplitude and can not be further determined here. It is unclear whether isopycnals oscillate due to waves of an undular jump, whether isopycnals bend downward due to the downward sloping bottom (as indicated in the sketch in Fig. 4.17) or whether they should be at a constant depth level downstream of the hydraulic jump. As the distance between station D3 and D4 was quite large (> 1 km) and no further downstream station was obtained, possible oscillations of isopycnals cannot be verified.

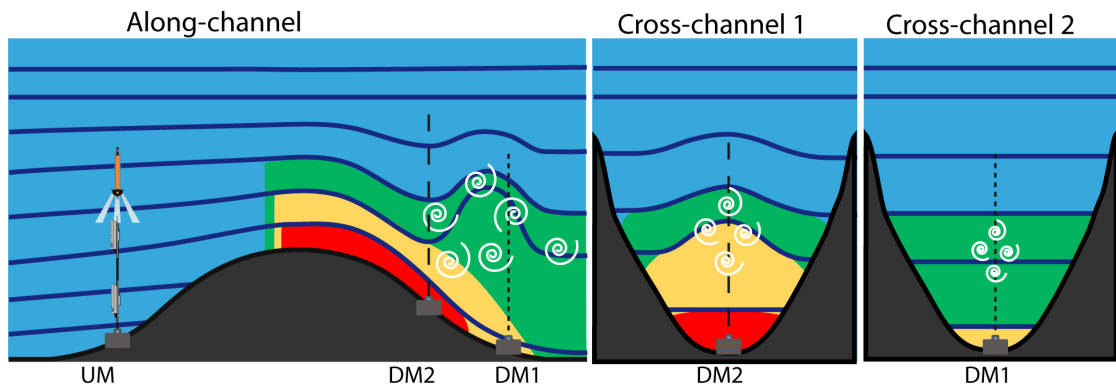


Figure 4.17: Sketch of the along-channel (left) and across-channel (middle and right) flow and density distribution. The location of the cross channel sections are indicated in the along-channel section by the mooring positions. The flow is indicated by background colors, while contour-lines indicate isopycnals. The white spirals indicate mixing. Also indicated are the mooring positions in the along and across-channel section as well as their instrumentation. They were all equipped like indicated at the upstream mooring (one ADCP and two MicroCats). Note that the jump amplitude is overdone and that the sizes of all features are not to scale.

The small scale analysis of the temperature variability showed the turbulent subrange to extend to length scales of a few hundred meters which was also observed by *Klymak and Moum* (2007b). Their study was conducted in the upper ocean near the Hawaiian Ridge with an average stratification of $4.5 \cdot 10^{-3}$ 1/s, while the results presented here apply to a narrow channel with weaker stratification of about $0.5 \cdot 10^{-3}$ to $1 \cdot 10^{-3}$ 1/s. The consistency of the temperature gradient wavenumber spectra in the inertial-convective subrange of turbulence with the $\epsilon^{2/3}$ dependence could be of interest for future studies. If the inertial-convective subrange of turbulence is fully resolved, the diffusivity for temperature can be assumed to equal the diffusivity for density and changes in the stratification can be neglected. This relationship could be used to infer the dissipation rate in low turbulence environments where the AUV induced noise inhibits the use of velocity shear based measurements. Despite this option, the mounting of the MR could be improved such that the AUV induced noise would be reduced.

In this Section it was demonstrated that AUV based velocity shear observations are suitable for the deep ocean above rough topography in constricted channels. This widens the measurement range for horizontal profiling to areas where free-falling and lowered measurements are inefficient and partly lack the possibility to sample at exact, pre-defined positions which might be crucial for understanding flow-topography interaction. The importance of the bottom topography for mixing has recently been shown by *Alford et al.* (2013) in the Pacific Ocean. Resolving and understanding the spatially variable deep-ocean mixing is essential as it provides buoyancy to deep-ocean waters causing upwelling as part of the meridional overturning circulation. With AUV-based microstructure mapping the understanding of such processes could be advanced in future studies. The observations presented here can serve as test case for numerical modeling efforts of topography-induced, deep-ocean mixing in the presence of a time mean flow.

5 Tidal Influence on the Flow, the Density, and the Dissipation Rate Distribution

The mixing pattern in the eastern channel of the Lucky Strike segment and a potential driving mechanism, namely the overflow induced hydraulic jump, have been identified in Section 4. Both seemed to be fueled by the mean flow. Besides the mean flow of about 8 cm/s along the channel, variability on timescales of a few hours was found (Section 4.4), which might be induced by tides. Tidal variability has indeed been observed by *Keller et al. (1975)* at a sill south of the LS segment, as mentioned in the introduction (Section 1.3). For the data set of this study, the large standard deviation of the moored ADCP velocity time-series (Table 4.2) also suggested large variability superimposed on the mean flow.

In this section short term variability which might be induced by tides is investigated. Based on velocity and temperature time-series from moored instruments the variability is analyzed and the influence of tides throughout the channel is examined. On the basis of the results from the tidal analysis the variability on different time-scales up to the time-scales of turbulence is studied. It is furthermore investigated whether high-frequency variability, which is attributed to turbulence, is elevated during certain phases of the tide.

In the second part of this section the evolution of the flow on short time-scales of a few hours is studied at one location.

In the third part the findings regarding the tidal influence on the flow and density field are applied to distinguish between different phases of the tide. Two flow regimes are defined, one describing phases of high flow speeds, referred to as ‘flood tide’, and the other one describing phases of low flow speeds, referred to as ‘ebb-tide’. Finally an analysis of the dissipation rate with respect to the tidal phase is attempted.

5.1 Tides and short term Variability

The average distribution of the velocity field as discussed in Section 4.2 revealed a mean flow in along-channel direction, while the relatively high standard deviations of the mooring-based velocity observations (Table 4.1 and 4.2) indicated large variability. Furthermore, individual LADCP profiles at repeated stations showed considerable differences between different occupations (Fig. 4.5). As tidal variability was observed in the area of the Lucky Strike segment in previous studies

(Keller *et al.*, 1975; Thurnherr *et al.*, 2008), tidal analysis of the data set underlying this thesis was performed. In the following the moored ADCP derived velocity time-series are analyzed and the tidal signal is characterized. The results are then applied to the temperature time-series of moored instruments.

5.1.1 Tidal Variability in along-Channel Velocity

Semi-diurnal variability has been reported to dominate the tidal variability at the LS segment and at a sill south of it (Keller *et al.*, 1975; Thurnherr *et al.*, 2008). The velocity time-series studied in this thesis showed pronounced semi-diurnal variability especially at the upstream mooring UM (upper panel Fig. 5.1), but also at both the downstream moorings DM1 and DM2 semi-diurnal variability could be identified (middle and lower panel Fig. 5.1). As an independent reference for the observed time-series, barotropic semi-diurnal tides were extracted from the TPXO global model of ocean tides, which is based on satellite data from

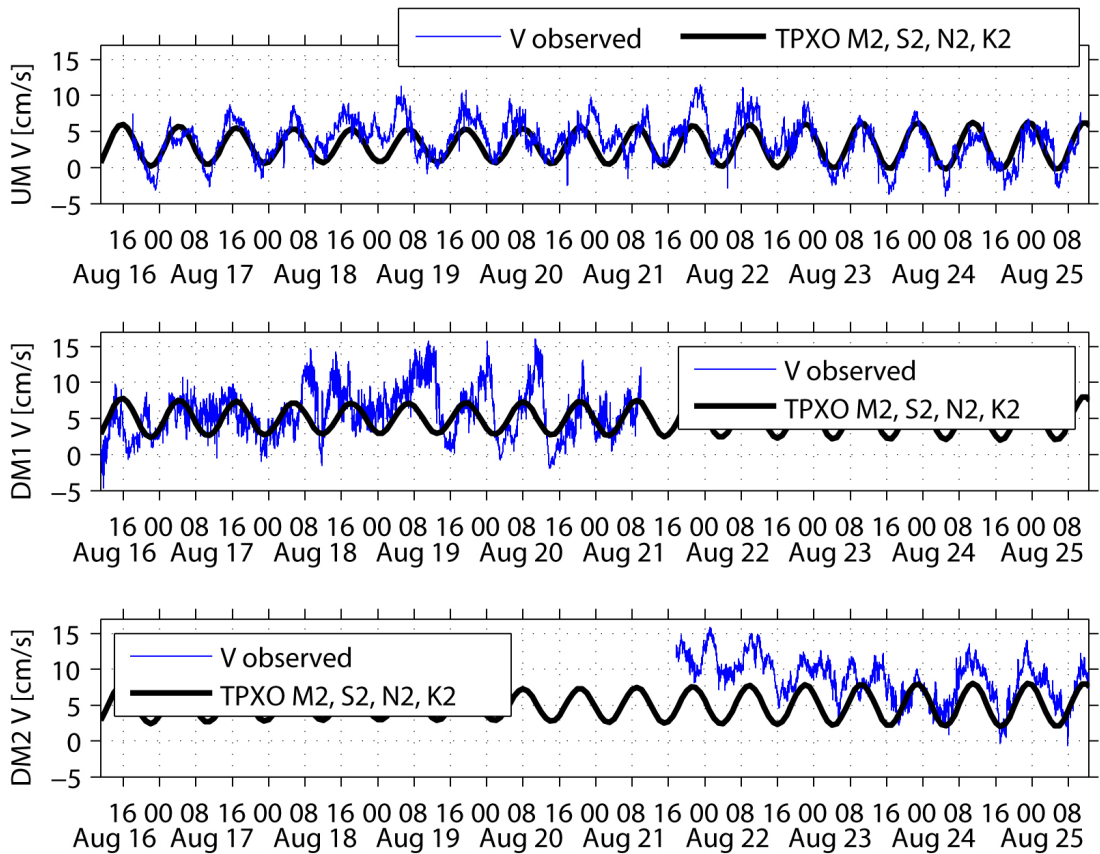


Figure 5.1: Along-channel velocity from upstream (upper panel UM) and downstream moored ADCPs (mid panel DM1, lower panel DM2). Time-series were six minutes low-pass filtered. Black lines mark the barotropic M_2 -, S_2 -, N_2 -, and K_2 -tide amplitude and phase from TPXO model (Egbert and Erofeeva, 2002). An offset was added for better visual comparison.

5.1 Tides and short term Variability

Mooring	Tide	Frequency [cpd]	Amplitude [m]	Greenwich Phase [°]	SNR
UM	M_2	1.93	2.60 ± 1.21	344.43 ± 27.39	4.6
DM1	K_1	1.00	1.41 ± 0.67	20.86 ± 30.72	4.4
	M_2	1.93	1.79 ± 1.21	44.37 ± 46.03	2.2
	M_3	2.90	0.86 ± 0.32	265.72 ± 24.65	7.2
DM2	M_2	1.93	2.21 ± 0.59	12.04 ± 18.70	14
	M_4	3.86	1.08 ± 0.45	226.98 ± 27.10	5.8

Table 5.1: Tidal constituents found with the program T-Tide (*Pawlowicz et al.*, 2002) for all mooring based along-channel velocity observations. Tidal constituents found: M_2 -principal lunar semi-diurnal, K_1 -lunar diurnal, M_3 -lunar terdiurnal and M_4 -shallow water overtides of principal lunar.

TOPEX/Poseidon and Jason (*Egbert and Erofeeva*, 2002). All semi-diurnal tides available in the TPXO model version TPXO 7.2 were considered. These were the M_2 -principal lunar, the S_2 -principal solar, the N_2 -larger lunar elliptic and the K_2 -lunisolar tide. Due to the relatively short duration of observations of only eight days available here, it was not possible to study the comparably weak variability at longer timescales such as tides with diurnal or longer periods. For comparison with the observed time-series two cases of the barotropic tide from TPXO 7.2 were used. Firstly, the M_2 -tide only and secondly, the sum of the M_2 -, S_2 -, N_2 -, and K_2 -tidal constituents were considered, i.e. all available semi-diurnal tides in the TPXO model.

To increase the confidence in the barotropic tides from the TPXO model used as reference, tidal constituents were additionally fitted to the six minutes low-pass filtered velocity time series and compared to the model output (time-series Fig. 5.1, fits Fig. 5.2). Two different fitting methods were used: firstly the program T-Tide (*Pawlowicz et al.*, 2002) and secondly a simple sine-wave-fit with the M_2 -frequency based on the matlab routine `fminsearch` (personal communication *Marcus Dengler*, *GEOMAR*). The tidal constituents found with the program T-Tide are displayed in Table 5.1. Only significant tidal constituents are reported (with signal to noise ratio $\text{SNR} > 1$).

The T-Tide fit for the velocity time-series observed at the UM mooring found only the M_2 -tide to be significant. This fit and the sine-wave-fit were in good agreement both, in amplitude and phase with each other and with both versions of the barotropic tide (top panel Fig. 5.2). At the downstream mooring location DM1, the T-Tide program found three tidal constituents with the lowest SNR for the M_2 -tide (Table 5.1). The comparison of the different fits showed that they did not match as good as at the upstream location (middle panel Fig. 5.2). At the DM2 mooring location both fits and the TPXO barotropic tides were again in good agreement. The T-Tide fit found only the M_4 (the ‘shallow water overtide of the principal lunar tide’) and the M_2 -tide with a $\text{SNR} > 1$ (Table 5.1).

5 Tidal Influence on the Flow, the Density, and the Dissipation Rate Distribution

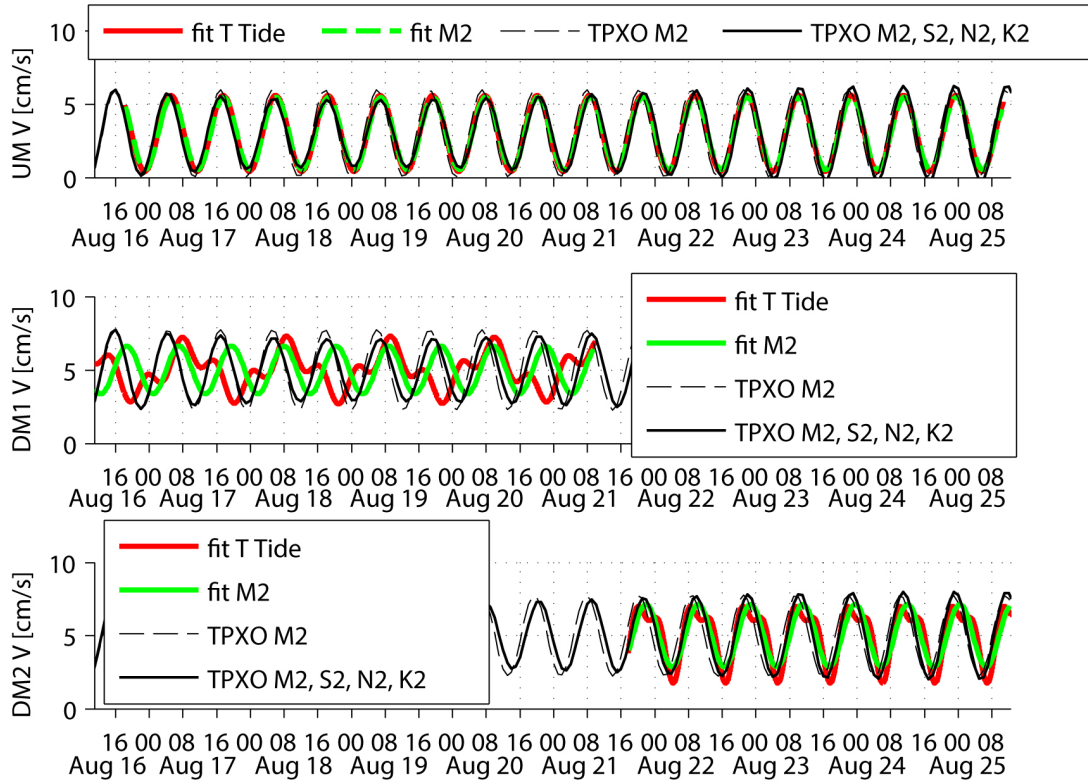


Figure 5.2: Tidal fits to the along-channel velocity from the program T-tide (red) and from the simple sine-wave-fit (green) as well as the barotropic tides extracted from TPXO model (black, dashed - M_2 from TPXO model, black, solid - M_2 , S_2 , N_2 , and K_2 from TPXO model (Egbert and Erofeeva, 2002). To the barotropic tides an offset of 3 cm/s at UM and 5 cm/s at both DM moorings was added, respectively.

Comparing both versions of the TPXO barotropic tides, the M_2 -, S_2 -, N_2 -, and K_2 -tide showed a weak neap-spring-cycle in contrast to the TPXO barotropic M_2 -tide. To examine which version of the TPXO barotropic tides fits the observations best, correlations between the TPXO barotropic tides and the along-channel velocity have been computed for both versions (Table 5.2). As the correlation was higher for the TPXO barotropic M_2 -, S_2 -, N_2 -, and K_2 -tide, only this version of the TPXO barotropic tide is used in the following. The two other fits from the program T-Tide and from the simple sine-wave-fit are not shown in the following figures as they 1) either were in good agreement with the TPXO barotropic tide and thus are redundant or 2) they did not match the observed velocity time-series as good as the barotropic tides.

Up to now, the TPXO barotropic tides were extracted from the TPXO model for the different mooring locations separately. As they were all in phase and the amplitude differed by less than 1% only, the TPXO barotropic tide will be considered uniform throughout the channel in the following.

Comparison of the observed bin-averaged along-channel velocities and the TPXO barotropic tide, showed reasonable agreement at the UM mooring, especially at the beginning and end of the deployment (upper panel Fig. 5.1). The two flanks of the tidal cycle were mostly in good agreement, while during the observed maxima and minima, the observed flow velocity often overshoot those of the TPXO barotropic tide (i.e. first 2 and last 4 tidal cycles of the deployment period). During intervals when the fitted flanks did not agree with the observed signal, the minima or maxima agreed better with the TPXO barotropic tide such that at least one part of each tidal cycle was explained quite well by the TPXO barotropic tide.

From August 19 to August 22 the observations overshoot the barotropic tide in every maximum. In the first part (until August 20) the maximum flow speed was reached before the maximum of the barotropic tide. The ebb-tide flank was often in better agreement with the barotropic tide than the rest of the cycle. In the second part (August 20 to August 22) the maximum flow speed was reached after the maximum of the TPXO barotropic tide and the flood-tide flank was in better agreement with the TPXO barotropic tide than the decreasing flank for some cycles. Despite the discrepancies, semi-diurnal variability was observed to dominate the variability at the UM mooring.

The two other time series observed downstream of the sill were unfortunately shorter. The downstream mooring was deployed 2.3 km downstream of the sill (DM1), but was moved after nearly 5 d further to the south and redeployed about 1.5 km downstream of the sill (DM2). Changing the mooring position has the drawback of a shorter time-series, but also the advantage of conducting measurements at different locations close to the sill. The first deployment period DM1 (mid panel Fig. 5.1) showed much more irregular variability than the second deployment period DM2 closer to the sill (lower panel Fig. 5.1). In addition, the resulting fits from the different fitting methods for the time-series from the DM2 mooring were in better agreement than those for the location of the DM1 mooring (mid panel Fig. 5.2).

The correlation of the TPXO barotropic tide and the velocity time-series was highest at the UM mooring regardless of the cutoff used for the low-pass filter (six minutes or one hour). This indicated the variability not matching the TPXO barotropic tides to be situated at longer timescales than one hour. Correlation was also found at the location DM2 as expected, while no significantⁱ correlation was found at the location DM1, 800 m further downstream. The fit obtained by the program T-Tide for the DM1 mooring indicated only a weak influence of the M_2 -tide but did not represent the observations, neither did the simple sine-fit. This indicated, that the flow regime at the location of the first deployment DM1 was more turbulent than at the location of the second deployment DM2 closer to the sill and would explain the large discrepancy to the fits.

ⁱThe significance was tested using a t-test at a 95 % confidence level. The degrees of freedom were determined by the zero-crossing of the auto-correlation (*Emery and Thomson, 2004*).

5 Tidal Influence on the Flow, the Density, and the Dissipation Rate Distribution

Correlation of along channel velocity at mooring		Correlation coef. with M_2	Correlation coef. with M_2, S_2, N_2, K_2
UM	6 min low-pass	0.63 (0.40)	0.70 (0.49)
UM	1 h low-pass	0.65 (0.42)	0.73 (0.53)
DM1	6 min low-pass	0.07 (0.00)	0.23 (0.05)
DM1	1 h low-pass	0.08 (0.01)	0.25 (0.06)
DM2	6 min low-pass	0.38 (0.14)	0.54 (0.29)
DM2	1 h low-pass	0.41 (0.17)	0.57 (0.32)

Table 5.2: Correlation coefficients R (and fraction of explained variance R^2 in parentheses) of along-channel velocity (Fig. 5.1) at each mooring location with the barotropic M_2 tide and the barotropic $M_2, S_2, N_2,$ and K_2 constituents from the TPXO model (Egbert and Erofeeva, 2002). Correlations were computed for six minutes low-pass filtered and one hour low-pass filtered data. Bold values are significant at a 95 % confidence level.

The observed variability at the DM1 mooring changed its characteristic 1.5 d after the deployment. The observed flow speed did not exceed a flow speed of 10 cm/s during the first part of the deployment and a semi-diurnal signal was hardly visible. From August 18 onwards, higher velocities were present. The mean flow speed increased from 4.5 cm/s during the first part to 6.5 cm/s during the second part with peak velocities of 16 cm/s. A semi-diurnal signal can be identified from August 19 onward for the following 3 to 4 cycles with a phase lag of about 4 h compared to the TPXO barotropic tide. The shape of the signal was asymmetric, like a sawtooth. The slope of the decreasing flank was much steeper than the increasing flank and it appears as if the M_2 -tide triggered the sawtooth signal. The maximum flow speed was reached about 6 h after the maximum of the TPXO barotropic tide, while the minima were reached much faster within 1 to 3 h. For the last hours before the recovery the peak flow speeds were again smaller and the signal shape was similar to the first hours of the deployment.

Combining these findings regarding the tidal influence on the flow field with the results from the analysis of the mean flow, a hydraulic jump downstream of the sill might be established only during phases of large flow velocities. The location of a hydraulic jump might also vary. If supercritical flow would be established even at the location DM1 (2.6 km downstream of the sill), the rapid decrease of the flow speed associated with the sawtooth signal, could be linked to the flow regime changing back to sub-critical flow. This situation might be consistent with an upstream propagating hydraulic jump. To verify this hypothesis, a time-series of Froude Numbers would be needed. Unfortunately, Froude Numbers computed from the mooring derived velocities were not representative for the bottom layer (not shown) as the mooring-derived velocity measurements covered a depth range of only 40 m and the near bottom flow was highly baroclinic. The hypothesis of

an upstream propagating hydraulic jump can thus not be supported here. The sawtooth phenomenon will be discussed in more detail in Section 5.2.

A sawtooth signal was not observed at the DM2 mooring. The flanks of the signal were much more symmetric than at the DM1 mooring and the barotropic tide was in much better agreement with the observed signal (Figs 5.2 and 5.1). Highest flow speeds were observed in the first two peaks and the velocities decreased over the first two days. Amplitudes were largest during the last two cycles which also showed the most pronounced semi-diurnal signal.

As already mentioned the T-Tide program found a strong contribution of the M_2 -Tide at the DM2 location (Table 5.1) and significant correlationⁱⁱ was found between observed velocities and the TPXO barotropic tides (Table 5.2). The non-periodic variability superimposed on the M_2 -tidal signal appeared to be weaker at DM2 closer to the sill compared to DM1 further downstream.

In conclusion, the along channel velocity determined from moored instruments showed pronounced semi-diurnal variability, which was correlated with the TPXO barotropic tides at the mooring UM and DM2. At the mooring DM1 the TPXO barotropic tide was not significantly correlated with the observed velocities, which is considered to be a local effect related to a hydraulic jump. Besides this local effects at DM1, the flow throughout the channel was thus mainly dominated by semi-diurnal tides, but variability on time-scales of hours to days was superimposed. The short-term variability was much more pronounced downstream compared to upstream and even more pronounced 2.3 km downstream compared to 1.5 km downstream of the of the sill. This might be related to processes downstream of a hydraulic jump and is further discussed at the end of this chapter (Section 5.5).

5.1.2 Tidal Variability in Temperature Time-Series

As tides were found to influence the velocity field, they might also have an impact on the temperature distribution, if the velocity vectors are not aligned with isotherms. Furthermore, isopycnal displacement associated with a hydraulic jump should also be associated with a displacement of isotherms (the contribution of salinity variability is neglected here). In the following the temperature variability and their time-scale are examined with respect to the tidal cycle. For this analysis the time-series of the two CTD recorders are studied, which were deployed in each mooring (one at about 20 m, and the other at 130 m above the sea floor (Section 2.2)). Indeed the temperature records also showed pronounced variability, but the semi-diurnal signature was not as clear as in the velocity records. The analysis concentrated on the one hour low pass filtered potential temperature (θ_2) referenced to 2000 dbar (Fig. 5.3). Average temperatures and standard deviations from the one hour low-pass filtered time-series are reported in Table 5.3.

ⁱⁱSignificant correlation at a 95 % confidence level.

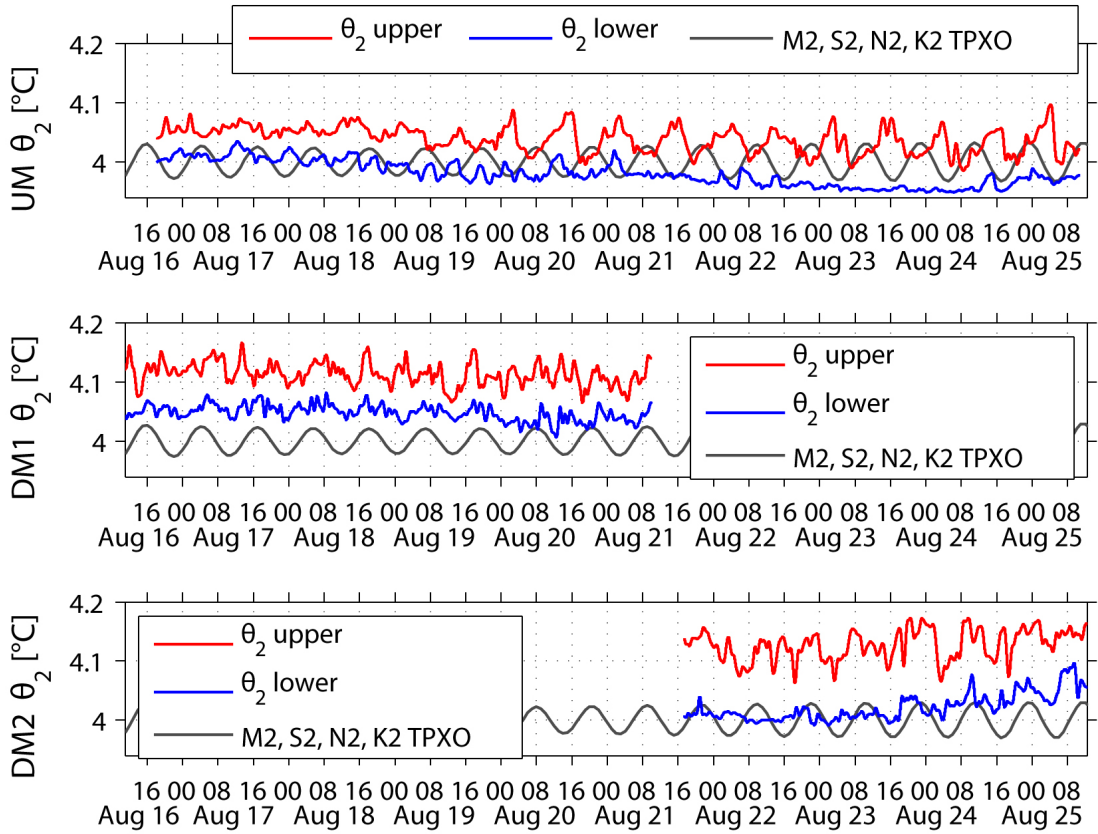


Figure 5.3: Potential temperature time-series from upstream (upper panel UM) and downstream moored CTDs (mid panel DM1, lower panel DM2). Each mooring was equipped with two CTD recorders, one at about 80 m to 110 m (red) and the other at one about 20 m above the bottom (blue). Data were one hour low-pass filtered. In gray the M_2 -, S_2 -, N_2 -, and K_2 -tide from TPXO model (scaled with a factor of 100 and an offset of 4).

Besides the semi-diurnal variability the temperature records showed variability on shorter as well as on longer time scales. Different characteristics were observed among different mooring positions and between the upper and lower CTD recorders deployed in one mooring. The upper CTD recorded higher variability than the lower CTD at all locations (Fig. 5.3).

If the temperature variability was related to the velocity field and to the tides, correlation with the TPXO barotropic tide would be expected, thus correlations were computed. The temperature recorded from the lower CTD at the location DM1 showed a weak correlation with the TPXO barotropic tide (Table 5.4). With increasing barotropic-tide velocity the temperature slightly increased. This was not visible at the upper CTD at the mooring DM1 and the correlation with the barotropic tide was significant only with the one hour low-passed filtered time-series.

At the DM2 mooring the two recorded temperatures also showed different pat-

Mooring		θ_2 upper CTD [$^{\circ}\text{C}$]	θ_2 lower CTD [$^{\circ}\text{C}$]
UM	mean	4.039	3.980
	std	0.022	0.021
DM1	mean	4.113	4.048
	std	0.019	0.013
DM2	mean	4.127	4.022
	std	0.025	0.023

Table 5.3: Potential temperature θ_2 referenced to 2000 dbar for each deployed CTD recorder. Average and standard deviation (std) of the one hour low-pass filtered time series are indicated (Fig. 5.3). Upper CTD deployed at about 130 m, lower CTD at about 20 m above the sea floor.

terns. The upper CTD recorded higher amplitudes than the lower CTD which showed a temperature increase towards the end of the deployment period. This temperature increase might have caused the failure of the advection-diffusion balance attempted in Section 4.3.2. The correlation between the temperatures and the TPXO barotropic tide was higher for the time-series recorded at the upper CTD compared to the correlation with the temperature record from the lower CTD (Table 5.4).

At the UM mooring the two temperature time-series showed similar behavior during the first 4 d. Then, the variability and amplitude observed at the upper CTD increased and was larger than the variability and amplitude observed at the lower CTD. Only some peaks were found simultaneously in both records. The correlation with the TPXO barotropic tides was comparably large for the temperature record from the upper CTD recorder, while there was no significant correlation with the temperature record from the lower CTD recorder.

The temperature and TPXO barotropic tides were positively correlated at the downstream moorings, whereas they were negatively correlated at the upstream mooring (Table 5.4). To verify the positive or negative sign of the simple cross-correlation, a lag correlation was performed between the time-series of each upper CTD recorder and the TPXO barotropic tide (Fig. 5.4). The highest correlation

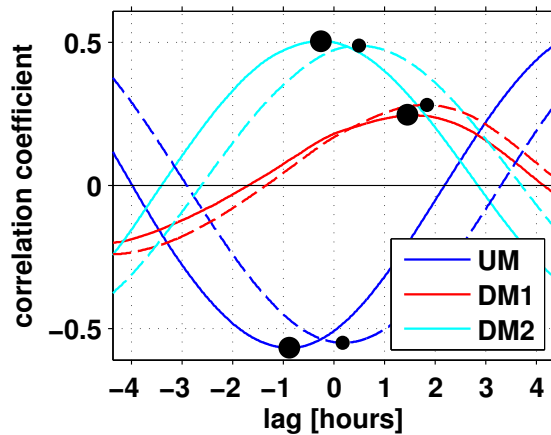


Figure 5.4: Lag correlation of the θ_2 record of the upper CTD at each mooring with the M_2 -, S_2 -, N_2 -, K_2 -tide (solid) and with the M_2 -tide (dashed).

5 Tidal Influence on the Flow, the Density, and the Dissipation Rate Distribution

Correlation of potential temperature θ_2 at mooring		Correlation coef. with M_2	Correlation coef. with M_2, S_2, N_2, K_2
UM	6 min low-pass, upper CTD	-0.55 (0.30)	-0.51 (0.26)
	6 min low-pass, lower CTD	-0.17 (0.03)	-0.14 (0.02)
UM	1 h low-pass, upper CTD	-0.55 (0.30)	-0.52 (0.27)
	1 h low-pass, lower CTD	-0.17 (0.03)	-0.14 (0.02)
DM1	6 min low-pass, upper CTD	0.17 (0.03)	0.18 (0.03)
	6 min low-pass, lower CTD	0.27 (0.07)	0.33 (0.11)
DM1	1 h low-pass, upper CTD	0.19 (0.04)	0.20 (0.04)
	1 h low-pass, lower CTD	0.32 (0.1)	0.39 (0.15)
DM2	6 min low-pass, upper CTD	0.47 (0.22)	0.50 (0.25)
	6 min low-pass, lower CTD	0.37 (0.14)	0.26 (0.07)
DM2	1 h low-pass, upper CTD	0.49 (0.25)	0.51 (0.26)
	1 h low-pass, lower CTD	0.40 (0.16)	0.29 (0.08)

Table 5.4: Correlation coefficients R (and fraction of explained variance R^2 in parentheses) of potential temperature θ_2 at each mooring location and for each deployed CTD (Fig. 5.3) with the barotropic M_2 tide and the barotropic M_2 -, S_2 -, N_2 -, and K_2 constituents from TPXO model (Egbert and Erofeeva, 2002). Correlations were computed for six minutes low-pass filtered and one hour low-pass filtered data. Bold values are significant at a 95% confidence level.

for the TPXO barotropic M_2 -, S_2 -, N_2 -, and K_2 -tide with the temperature record from the upper CTD at the UM mooring was negative, at a lag of 52 min (with M_2 -tide 11 min). The minimum temperature was reached 52 min before the M_2 -, S_2 -, N_2 -, and K_2 -tide reached the maximum flow velocity (11 min after the M_2 -tide maximum velocity).

The temperature recorded at the upper CTD at mooring DM2, which also showed relatively high correlation with the barotropic tides, showed the largest correlation at a lag of 15 min with positive correlation (31 min with the M_2 -tide). The lowest correlation was found for the temperature record from the upper CTD at the DM1 mooring with the M_2 -, S_2 -, N_2 -, and K_2 -tide. The correlation was positive and largest for a lag of 1.5 h (1 h 50 min for the M_2 -tide).

Concluding the previous analysis, correlation was found for the temperature records from moored instruments with the TPXO barotropic tides throughout the channel. The correlation was weak and positive i.e. in phase, at the DM1 mooring further away from the sill. At the DM2 mooring downstream but closer to the sill, the correlation was also positive. The maximum temperatures were reached around the same time as the maximum flow velocity of the TPXO barotropic tides. In contrast, the correlation of the temperature record observed at the UM mooring with the TPXO barotropic tides was negative i.e. opposite in phase. The minimum temperatures were reached slightly before the maximum flow velocity of the

TPXO barotropic tides. This suggested that cold water was lifted to shallower depth with higher flow velocities upstream of the sill, while warmer water reached the downstream moorings together with higher flow velocities. The weaker correlation at the far downstream mooring DM1 compared to the mooring DM2 might indicate a larger influence of turbulence at the DM1 location as already suggested by the velocity analysis in Section 5.1.1. A larger influence of turbulence during phases of high along-channel flow would be consistent with a hydraulic jump only being established during phases of high along-channel flow. If the jump would be located downstream of the mooring DM2 but upstream of the location DM1, larger turbulence would be expected at the mooring DM1. To further understand the temperature variability, the frequency dependency is studied in the next paragraph.

Frequency Dependence of Temperature Variability

The temperatures in the eastern Lucky Strike channel were shown to be influenced by the semi-diurnal tidal variability in the previous paragraph. The observation of colder or warmer water at a constant depth level indicated up- or downward movement of isopycnals, which might be related to tidally forced internal waves. To further understand the variability and the different characteristics at the different mooring locations, the frequency dependence of the temperature variability was studied using isothermal slope spectra. Isothermal slope spectra, i.e. the spectra of vertical displacement of isopycnals related to the background internal wave field are described for the open ocean by the Garrett-Munk internal wave energy spectrum (GM, *Garrett and Munk* (1972, 1975); *Cairns and Williams* (1976)). The comparison of the observed energy distribution to the GM spectrum might help to interpret the temperature variability and to identify the relative contribution of internal waves and turbulence. It should be noted that it is not clear how representative the GM spectrum is inside such small deep ocean canyons as the GM spectrum was deduced from open ocean measurements and thus represents the open ocean background internal wave energy field. However, there is no background internal wave energy spectrum available for deep ocean channels.

To get the isothermal slope from the temperature time-series, the unfiltered, detrended θ_2 time-series were divided by a vertical temperature gradient of $1 \cdot 10^{-3} \text{ }^\circ\text{C/m}$. This vertical temperature gradient was determined from the lowest 100 m average lowered CTD profiles from station U2, D2 and D3 by assuming a linear temperature decrease with increasing depth ($0.1 \text{ }^\circ\text{C}/100 \text{ m}$). Spectra were computed using an increasing number of data segments (with 50 % overlap) to reduce the noise in the high frequency range without reducing the resolution for low frequencies (as done for the horizontal gradient spectra in Section 4.4.1). Prior to Fourier decomposition a 1/2-cosine taper was applied to the first and last 10 % of each segment. The Fourier coefficients were normalized and squared (personal communication *Marcus Dengler, GEOMAR*).

The dominant signal at all locations was close to the M_2 tide frequency (Fig. 5.5), while inertial frequencies showed only little energy compared to the GM internal

wave spectrum. Lower energy at near inertial frequencies compared to the background spectrum for the open ocean might be attributed to the narrow channel or the proximity to the sea floor limiting internal wave propagation. The near inertial band was reported to be largely suppressed close to the bottom by *Thurnherr et al.* (2005) in a deep canyon on the MAR flank.

The slope towards higher frequencies (f) showed some differences between the different θ_2 records. The observations from the lower CTD recorder at the location UM showed less energy at the inertial and the M_2 frequency compared to the GM spectrum but for $f > 4$ cycles per day (cpd) it was in good agreement with the GM spectrum. The upper record from the UM mooring showed the over all highest

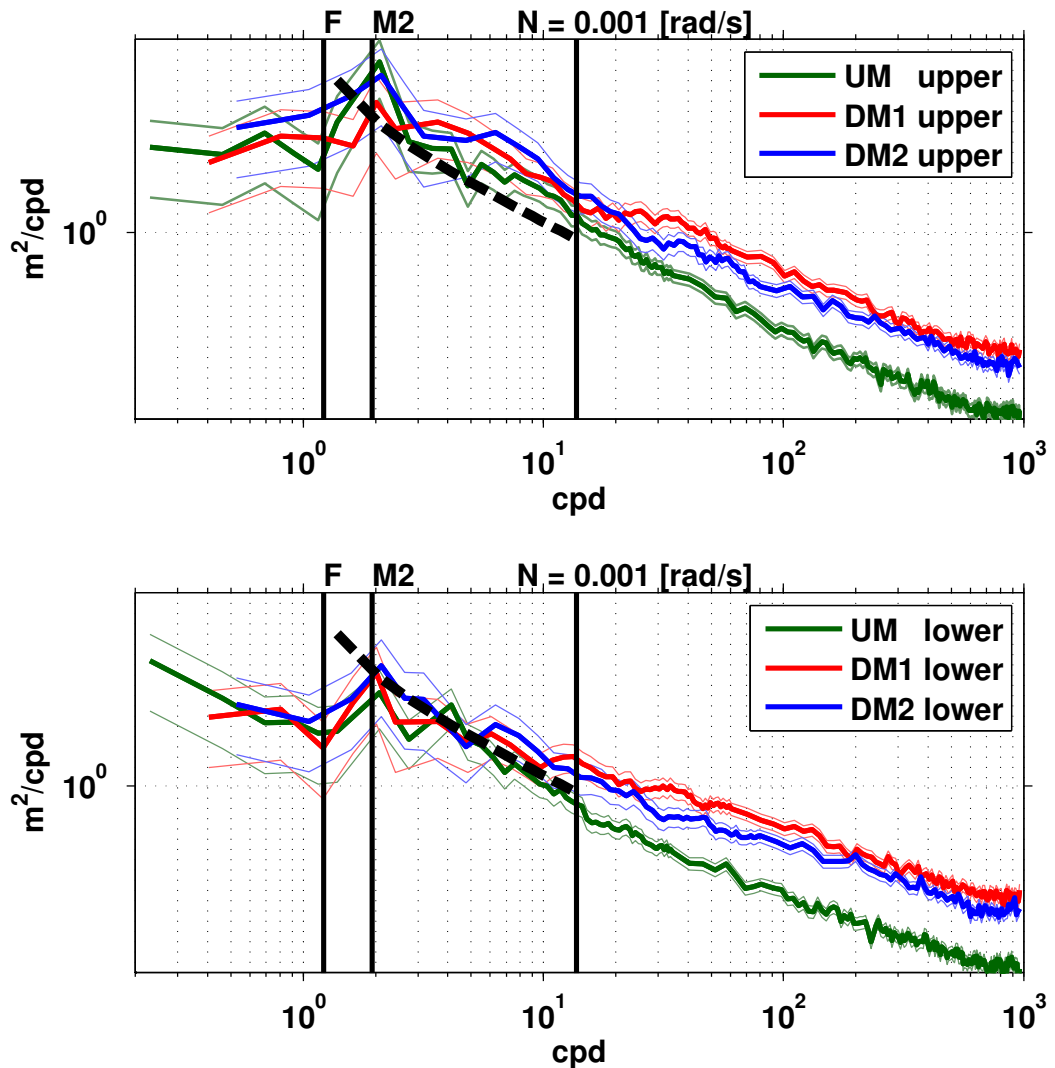


Figure 5.5: Spectrum of isothermal displacement with 95% confidence limits at mooring UM, DM1, and DM2 from the upper (upper panel) and lower CTD recorder (lower panel), respectively. Vertical lines indicate the inertial frequency F , the semi-diurnal tidal frequency M_2 and the buoyancy frequency N . The dashed, black line represents the GM internal wave energy spectrum.

energy at the M_2 frequency. For larger f it showed slightly elevated energy at 3 cpd. For the f -range larger than 4 cpd the energy was elevated compared to the GM spectrum in the upper UM record.

At the mooring DM1 the lower θ_2 record showed about the same energy level at the M_2 frequency compared to the GM spectrum. For larger f the energy dropped below the GM level but for $f > 4$ cpd the energy increased and remained above the GM level for larger f . The upper θ_2 record showed slightly higher energy at the M_2 frequency compared to the GM spectrum and elevated energy for $f > 2$ cpd. For $f > 12$ cpd the energy was highest in this θ_2 record compared to all other time-series.

The isothermal slope spectrum from the lower CTD at location DM2 showed only slightly higher energy at the M_2 frequency compared to the GM spectrum, about the same energy for $1.5 < f < 4$ cpd and higher energy for $f > 4$ cpd. The upper temperature record showed high energy at the M_2 frequency, the energy remained above the GM-level for $f > 1$ cpd and showed the over all largest energy for $4 < f < 11$ cpd.

In summary, the spectral analysis of isothermal slopes indicates elevated internal wave energy compared to the GM spectrum close to the M_2 tidal frequency. This further confirms the importance of the M_2 tide as a source of variability. Towards larger frequencies, only slightly elevated energy was found at the UM mooring, while internal wave energy was elevated at both DM moorings. On time scales shorter than the buoyancy frequency elevated energy was found at both DM mooring locations compared to upstream. This is probably related to higher turbulence downstream compared to upstream of the sill. The asymmetric distribution of turbulence across the sill has been shown by microstructure velocity shear observations reported in Section 4.1.

High Frequency Temperature Variability in Tidal Cycle

The spectral analysis of the temperature variability in the previous paragraph indicated turbulence downstream of the sill in agreement with the results from Section 4. If turbulence is associated with a hydraulic jump, which in-turn might be associated only to high along-channel flow (Section 5.1.1), turbulence might be also varying within the tidal cycle. Turbulence, i.e. high frequency (temperature) variability might thus be associated with a certain phase of the tide. This was further investigated by applying a high-pass filter with a cutoff at 30 min to the original time-series. From the high-pass filtered θ_2 time-series, the standard deviation (std) was computed over segments of 3 h with 50 % overlap between segments (Fig. 5.7). The time-interval of 3 h was chosen to resolve the M_2 -tidal cycle. As expected from the spectral analysis, both UM time-series showed only little high frequency variability (upper panel Fig. 5.7). At the mooring DM1 high variability seemed to be roughly accompanied by high along-channel velocities indicated by the TPXO barotropic tide (middle panel Fig. 5.7). At the DM2 mooring, closer to the sill this was less clear (lower panel Fig. 5.7).

5 Tidal Influence on the Flow, the Density, and the Dissipation Rate Distribution

Correlation of std of low-pass filtered θ_2 at mooring		Correlation coef. with 3 h low-pass filtered along-channel velocity
UM	upper CTD	0.09 (0.01)
	lower CTD	0.49 (0.24)
DM1	upper CTD	0.65 (0.42)
	lower CTD	0.36 (0.13)
DM2	upper CTD	-0.13 (0.02)
	lower CTD	-0.39 (0.15)

Table 5.5: Correlation coefficients R (and fraction of explained variance R^2 in parentheses) of the standard deviation (std) over 3 h with 50 % overlap of the 30 min high-pass filtered potential temperature θ_2 time-series from each mooring location from each deployed CTD (Fig. 5.7) with the 3 h low-pass filtered observed along-channel velocity. Bold values are significant at a 95 % confidence level.

Although the agreement with the TPXO barotropic tides was not striking, alternating periods of high and low high-frequency variability were observed especially at the downstream moorings. To identify a possible relation to the tidally varying flow a lag-correlation was performed between the std of the high pass-filtered θ_2 time-series and the observed 3 h low-pass filtered along-channel velocity with a maximum lag of 6 h (lag correlation in Fig. 5.6. Correlation coefficients of zero lag are given in Table 5.5).

The correlation was largest at a lag of zero for the upper θ_2 record from the DM1 mooring and the lower θ_2 record from the UM mooring, indicating larger high-frequency variability during phases of larger along-channel flow.

At the DM2 mooring, closer to the sill, the correlation was significant only at the lower θ_2 record with negative correlation over a range of zero to 4.5 h lag. At a lag of 1.5 h the correlation was slightly larger than the zero-lag correlation. This indicated that large high-frequency variability was observed during and

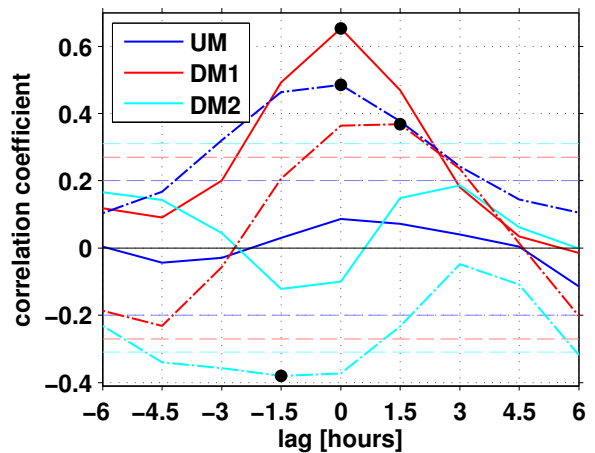


Figure 5.6: Lag correlation of the std over 3 h with 50 % overlap of the 30 min high-pass filtered potential temperature θ_2 time-series from each mooring location and from each deployed CTD (Fig. 5.7) with the 3 h low-pass filtered observed along-channel velocity (solid line – upper CTD, dashed line – lower CTD). Black dots indicate the maxima which are significant at a 95 % confidence level. Corresponding confidence levels are indicated with dashed lines.

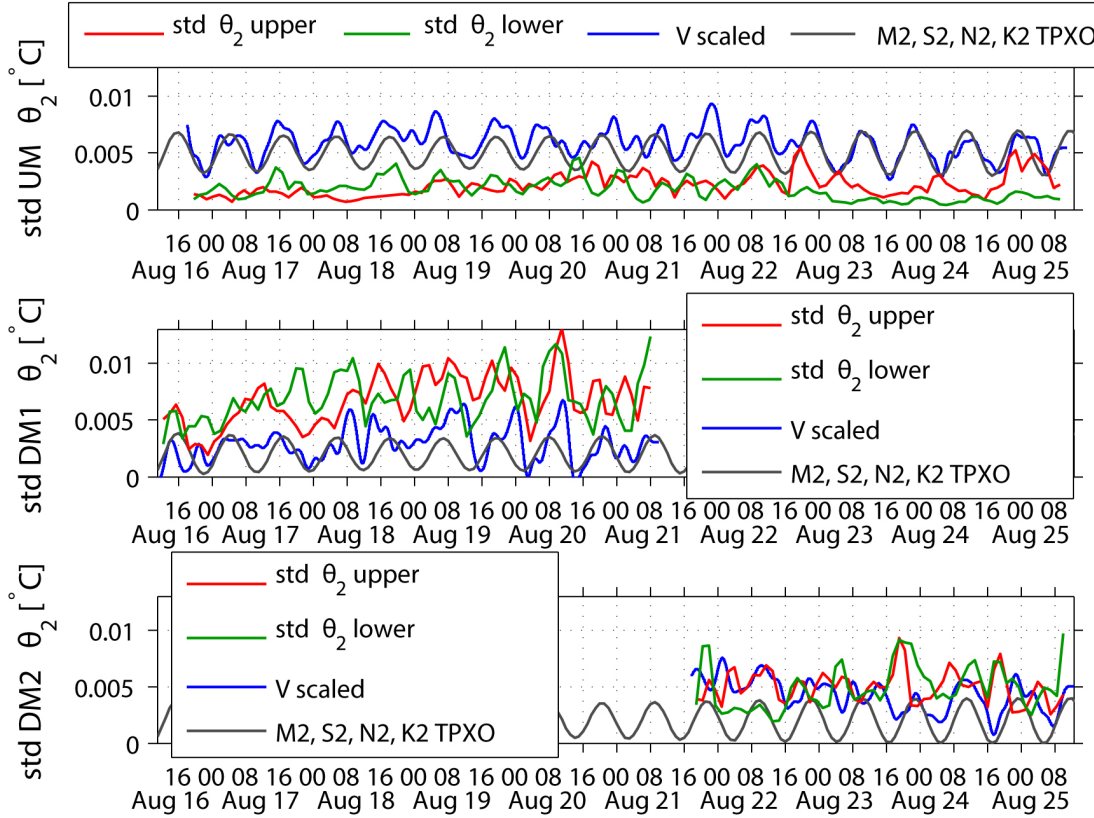


Figure 5.7: Standard deviation (std) over 3 h with 50% overlap of the 30 min high-pass filtered θ_2 time-series of each CTD recorder from moorings UM (upper panel), DM1 (middle panel) and DM2 (lower panel). The blue and the gray line mark the 3 h low-pass filtered along-channel velocity and the M_2 -, S_2 -, N_2 -, and K_2 -tide from TPXO model respectively. Y-axes does only apply for temperature standard deviations.

after phases of weak along-channel velocities and vice versa. If the DM2 mooring would be located in the temporarily supercritical flow regime, low temperature variability would be expected in the layer of large flow velocities as internal wave propagation would be suppressed or prohibited in the supercritical layer depending on the Froude Number (Section 1.4). The presence of significant correlation in the time-series of the lower CTD recorder might indicate that the upper recorder was not, or less often, located in the supercritical layer.

The elevated high-frequency variability observed at the upper recorder at the DM1 mooring further downstream during phases of large along-channel flow might be related to an undular hydraulic jump or to turbulence. The waves of the undular hydraulic jump would oscillate at the upper boundary of the lower layer (Section 1.4 and *Thorpe (2010)*), which would explain the larger correlation at the upper compared to the lower recorder. As the stratification is continuous in the real ocean the concept of a ‘upper boundary’ is limited, but oscillating waves can still induce such a signal.

At the lower recorder at the UM mooring elevated high-frequency variability was

observed during elevated along-channel flow, but the absolute variability was quite low compared to that observed at the downstream moorings (Fig. 5.7). The high-frequency variability observed at the upper CTD recorder showed no correlation with the along-channel flow. While it is unclear how the elevated variability at the lower recorder might be interpreted, there might just not be that much high frequency variability at the upper recorder.

5.1.3 Summary

The semi-diurnal variability of the along-channel flow was shown to be correlated with the TPXO barotropic tides at the mooring UM and DM2, while it was not significantly correlated with the TPXO barotropic tides at the mooring DM1. Furthermore, the displacement of isotherms was shown to be correlated with the TPXO barotropic tides at the UM and the DM2 mooring. The spectral energy in the range of semi-diurnal frequencies was elevated at this two positions with respect to the GM spectrum. High velocities and high temperatures indicating downward displacement were in phase at the downstream mooring DM2. Whether this might be related to a hydraulic jump is discussed in Section 5.5. At the upstream mooring they were opposite in phase indicating upward displacement during phases of high flow velocities.

The isothermal displacement at the DM1 mooring was only weakly correlated with the barotropic tides and the displacement of isotherms showed about the same energy level as the GM spectrum at semi-diurnal frequencies.

Variability on shorter time-scales was found to be elevated at both downstream moorings, which was probably linked to elevated turbulence downstream of the sill (Section 4).

The elevated high-frequency variability was correlated with the observed along-channel velocities at the DM1 mooring. A hydraulic jump located upstream of the mooring DM1 might induce this variability via turbulence or downstream propagating waves associated to an undular hydraulic jump (Section 1.4).

Closer to the sill at the DM2 mooring low levels of high-frequency variability were observed to be correlated with large along-channel flow. This might be related to the supercritical flow upstream of a hydraulic jump, where wave propagation is reduced or prohibited (Section 1.4 and *Thorpe (2010)*). This would indicate the hydraulic jump to be located between the two downstream moorings. A sketch of the processes described here together with the results reported in the following Sections is discussed at the end of the chapter (Section 5.5).

5.2 Evolution of the Flow and Density Field on short Time Scales

In the preceding paragraphs a strong influence of the semi-diurnal tides on the along-channel flow was shown based on the analysis of the velocity and temperature time-series from the moored instruments. As these time-series cover only the lower ~ 100 m water depth no conclusions can be made so far for the waters above 100 m altitude from the sea floor. The short term evolution and variability over the lower 800 m water column can be investigated based on one longterm station occupied for seven hours at station D1 located 1.2 km downstream of the sill, where continuous profiling was performed between 1300 dbar and the bottom (yoyo-station). At this location high flow speeds and elevated Froude Numbers were found in the average along-channel flow field (Section 4.2). In addition, continuous profiling was performed while steaming at about 0.7 – 0.9 km along the channel (tow-yo-station), which allows to study the evolution of the density field not only at one location but also along the channel at a high temporal resolution. Three tow-yos were performed with start-point at station U2 and end-point downstream of the sill near station D2c and D3c, respectively.

In the following paragraphs the flow and density field obtained from the yoyo and tow-yo stations are studied and compared to the flow speeds observed during the same time from the moored instruments. Differences observed at the different locations and during different phases of the tide are analyzed.

5.2.1 Evolution of the Flow and Density Field at one Location just downstream of the Sill

At station D1 just downstream of the sill high flow speeds and elevated Froude Numbers were observed as discussed in Section 4.2. As semi-diurnal variability was shown to dominate the variability inside the channel up- and downstream of the sill based on moored velocity observations (Section 5.1), semi-diurnal variability is also expected at station D1 just downstream of the sill. This was investigated based on one yoyo-station occupied on August 19 parallel to the detection of the first of the three sawtooth signals in the along-channel velocities at the DM1 mooring (Fig. 5.1). The yoyo-station showed high along-channel velocities below 1800 m during the first 3.5 h of the observations with maximum velocities of 23 cm/s between 10 and 11 UTC (Fig. 5.8). This was much larger than the maximum velocity recorded by the moorings (13.5 cm/s at the DM1, 15.1 cm/s at DM2 closer to the sill and 10.6 cm/s at the UM mooring). Above 1800 m weaker, predominately northward velocities were observed during the first 3.5 h with larger temporal variability compared to the layer below 1800 m sometimes switching to weak southward flow. Froude Numbers were computed following Equation 1.5 for the layer below the isopycnal $\sigma_2 = 36.893$ (green line in Fig. 5.8) and the average density of the layer between the isopycnals $\sigma_2 = 36.893$ and $\sigma_2 = 36.877$ (the later indicated as red line in Fig. 5.8), the same layers as described in Section 1.4

5 Tidal Influence on the Flow, the Density, and the Dissipation Rate Distribution

and used in Section 4.2.2. Froude Numbers were found to range between 0.6 and 1.7 (top of Fig. 5.8). During phases of high Froude Numbers a hydraulic jump is likely to occur downstream of this location, in the region where the Froude Numbers drop below the critical level (see Section 1.4 and *Thorpe (2010)*).

During the phase of high flow speeds and high Froude Numbers isopycnals were observed at a constant depth (Fig. 5.8). This might be linked to reduced upstream propagation of waves in flows with near critical Froude Numbers (*Thorpe, 2010*) indicating supercritical flow (Fig. 5.8, 7:30 to 11 UTC). As the yoyo-station was located at station D1 upstream of the hydraulic jump, which was shown likely to be located between stations D1 and D3 (Section 4.2), reduced upstream propagation of internal waves would be likely to occur at this location.

The same yoyo-cast was analyzed by *Thurnherr (2011)*, who presented a new method of inferring vertical velocities from LADCP data. Apparently the large horizontal velocities observed between 7:30 and 11 UTC on August 19 (Figs. 5.8

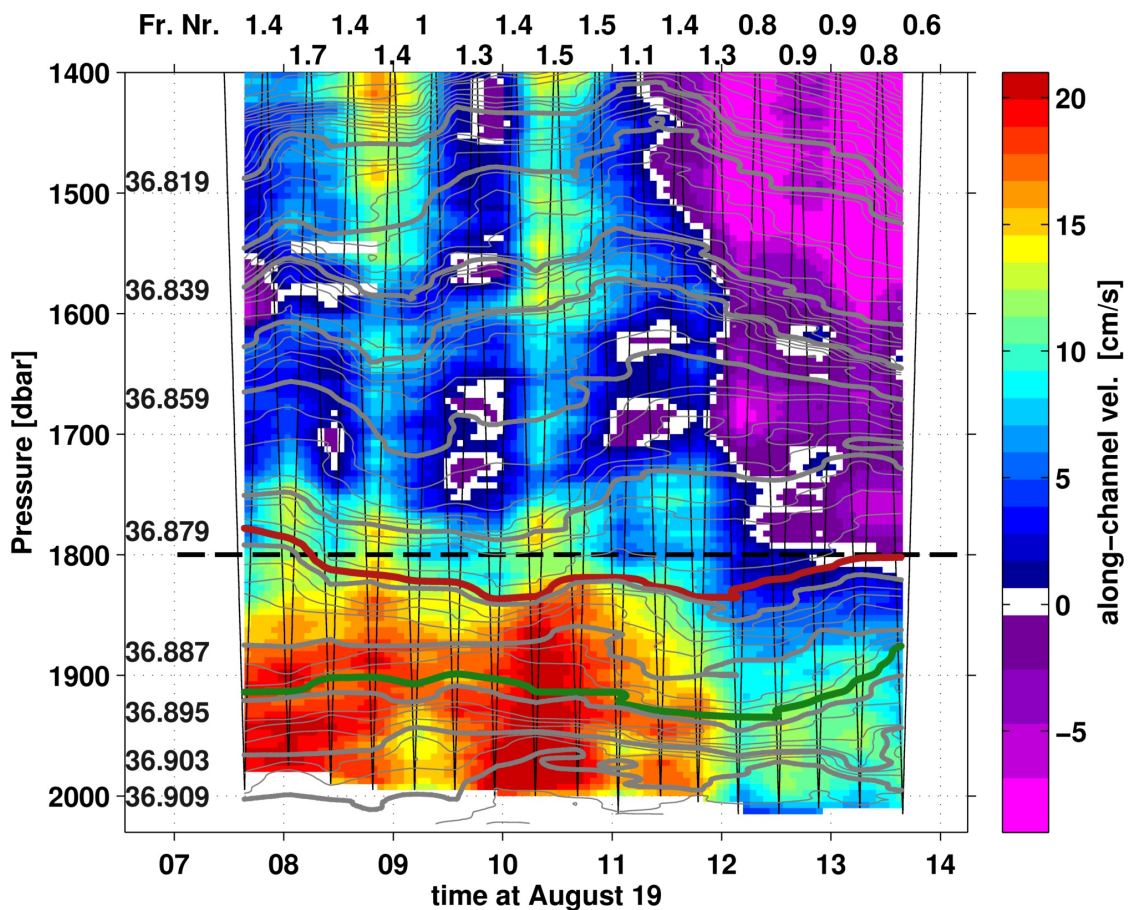


Figure 5.8: Along-channel velocity at the yoyo-station at D1. Density denoted by contour lines and density labels at the left hand side (spacing $\Delta\sigma_2 = 0.002 \text{ kg/m}^3$). Froude Numbers are given at the top. Vertical black lines indicate the time of the individual up- and downcasts.

5.2 Evolution of the Flow and Density Field on short Time Scales

and A.3a) were accompanied by downward velocities of up to 3 cm/s (Fig. A.3b). According to *Thurnherr* (2011) this is consistent with a dense gravity current flowing down the lee slope of the sill. After 11 UTC, the along-channel flow speed decreased to 3–13 cm/s below 1800 m and southward flow was found above 1800 m. Below 1850 m, vertical velocities were still directed downwards (*Thurnherr*, 2011) and the isopycnals were found lower in the water column compared to the 3.5 h before (green line in Fig. 5.8). After 12 UTC isopycnals sloped upwards between 1700 m and the bottom, which was consistent with upward velocities (Fig. A.3b by *Thurnherr* (2011)). A propagating wave might induce such down- and upward movement in the lower layer and might also affect the along-channel flow (*Thorpe*, 2010). The possibility of propagating signals is studied in more detail in Section 6.

Besides the possibility of propagating signals the question emerges how the decrease of the flow observed during the yoyo-cast might be related to the tidal phase. Comparing the yoyo-cast derived along-channel velocities to the simultaneously observed mooring-derived along-channel velocities, it was found that the cast was carried out during maximum velocities observed at the mooring DM1 during the first sawtooth signal (Fig. 5.9). The large velocities and the steep decreasing flanks in the mooring based velocity time-series between 8 and 13 UTC on August 19 and between 17 and 2 UTC on August 19 and 20 were referred to as sawtooth signals (Section 5.1.1). For comparison with the mooring-based velocity, the LACDP-derived velocity is averaged between 1400 dbar and the bottom. The vertical average showed a similar trend as the velocity observed at the DM1 mooring. Both time-series increased to about 12 cm/s, showed a slight decrease, increased again to about 13 cm/s and decreased to velocities of 1 cm/s or -3 cm/s (i.e. southward velocities). Both decreases occurred first in the lowered observations, which were located just downstream of the sill, but upstream of the mooring DM1. At the upstream mooring UM the velocity maximum was reached before it was reached at the yoyo-station or at the downstream mooring (Fig. 5.9). This temporal offset is studied in more detail in Section 6.

The comparison of the velocity time-series revealed that the observed velocity signals did not match the TPXO barotropic tide (Fig. 5.9), although the velocities showed semi-diurnal variability. The decrease in the along-channel flow observed at all three locations (UM, D1, and DM1) was out of phase with each other and with the TPXO barotropic tide. Nevertheless, weak flow velocities were observed simultaneously at the locations UM and D1 after 12 UTC corresponding to the minimum of the TPXO barotropic tide (Fig. 5.9) and also at the mooring DM1 after 14 UTC. The large flow velocities and near-critical Froude Numbers observed in the yoyo-cast (Froude Numbers given at the top of Fig. 5.8) thus were followed by a phase of weak north- or even southward flow accompanied by low Froude Numbers indicating sub-critical flow. A hydraulic jump, which was found likely to exist downstream of the sill (Fig. 5.8 and in Section 4.2) was thus likely to be absent during the phase of weak along-channel flow observed at the end of the yoyo-cast

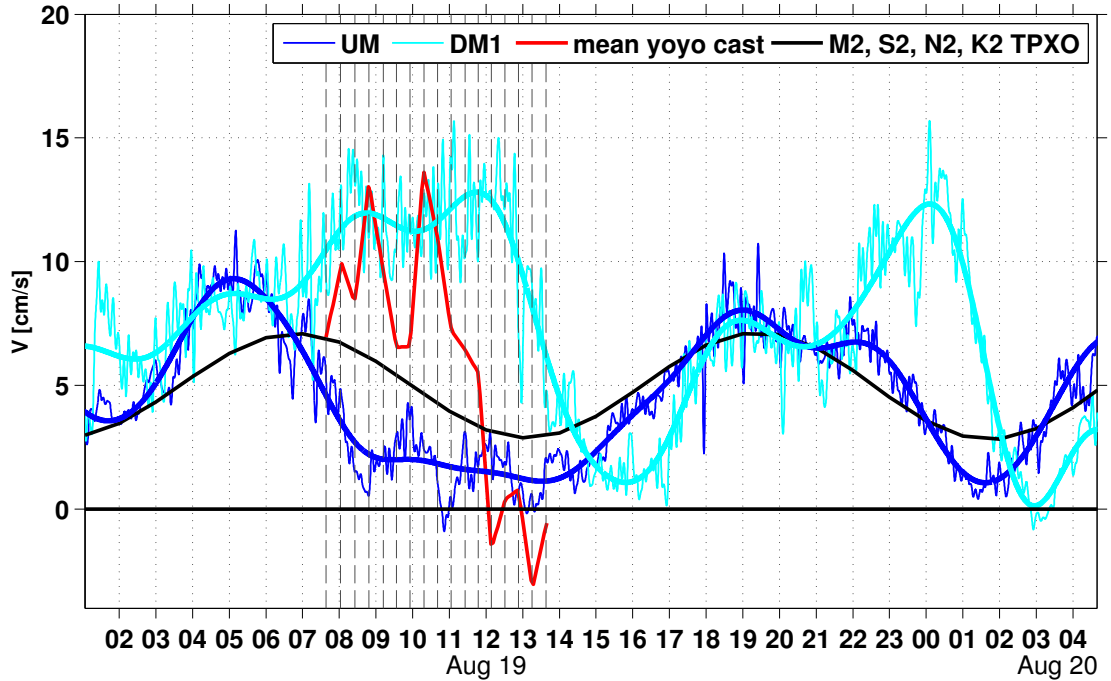


Figure 5.9: Along-channel velocity at the UM and DM2 mooring (thin lines 6 min, thick lines 1 h low-pass filtered) observed during the time when the yoyo-cast was carried out together with the vertical average of the LADCP-derived velocities. Vertical black lines indicate times of the individual casts (when the instrument was at the bottom). Also shown the barotropic tide from TPXO model (*Egbert and Erofeeva, 2002*).

(Fig. 5.8). This further supports the interpretation of the hydraulic jump being no permanent feature. The hydraulic jump might only be found during phases of large along-channel flow as was already suggested by the results discussed in Section 5.1.1.

Although the interpretation of a hydraulic jump causing mixing is consistent with the downstream maximum of the mixing found in Section 4.1, the strong shear between the layer of large along-channel flow and the waters above might also contribute to the mixing by shear instabilities. The possibility of the occurrence of shear instabilities was already estimated in Section 4.2.2 for all single-profile lowered velocity observations and was estimated here for the yoyo-cast (Fig. 5.8). Shear instabilities are likely to occur if the Richardson Numbers ($R_i = N^2/(\delta U/\delta z)^2$) fall below 1/4 (*Thorpe, 2005*). Richardson Numbers were computed as describe in Section 4.2.2. The Richardson Numbers were well above unity in all yoyo-profiles (Fig. 5.10) indicating shear instabilities to be unlikely to occur at this location even at strong along-channel velocities. Thus shear instabilities probably do not contribute significantly to the mixing at the Lucky Strike segment.

5.2 Evolution of the Flow and Density Field on short Time Scales

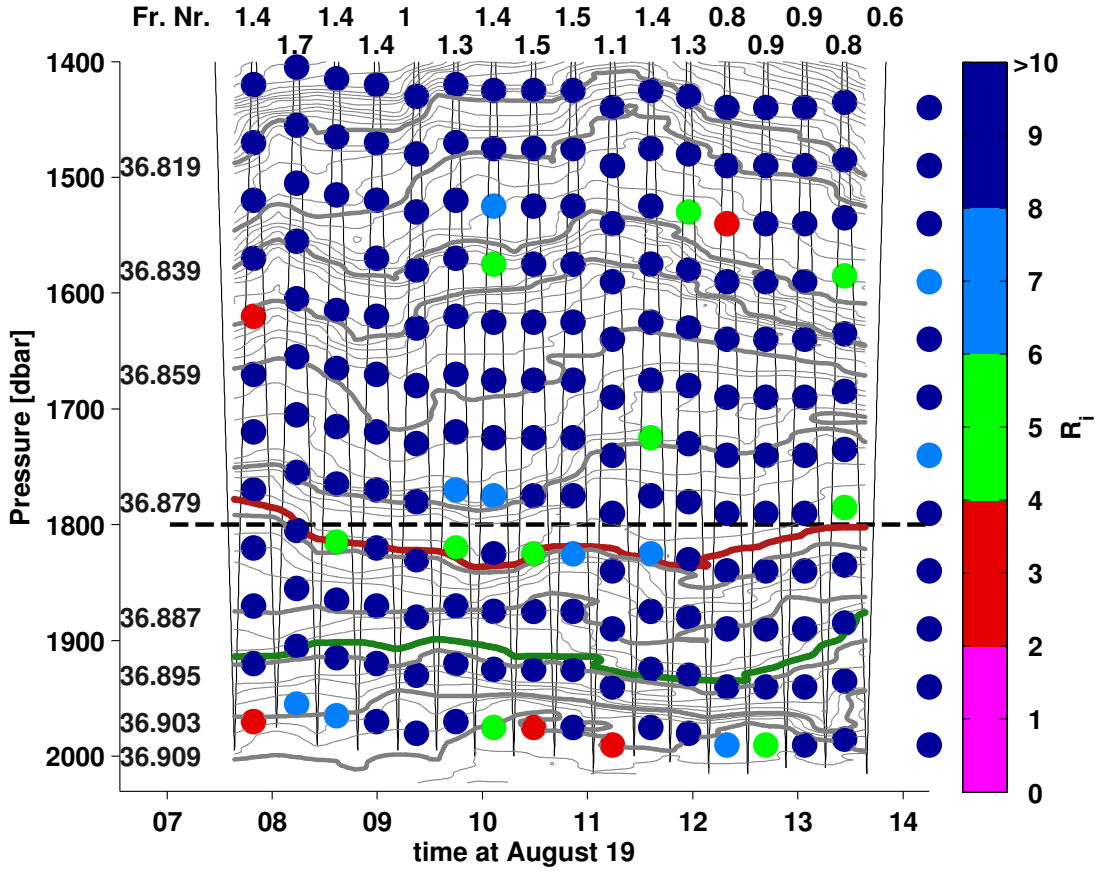


Figure 5.10: Richardson Numbers for the yoyo-cast at D1 with density contours and density labels at the right (spacing $\Delta\sigma_2 = 0.002 \text{ kg/m}^3$). Froude Numbers are given at the top. Vertical black lines indicate the time of the individual up- and downcasts.

Concluding this paragraph Richardson Numbers indicated that the elevated mixing downstream of the sill reported in Section 4.1 was probably not related to shear instabilities but caused by a hydraulic jump.

Up- and downward movement of isopycnals consistent with the observed elevated vertical velocities (*Thurnherr, 2011*), indicated the propagation of internal waves to be weakened or suppressed during phases of large along-channel flow, i.e. in supercritical flow.

Large along-channel velocities were found in the overflow layer below 1800 m. Froude Numbers were in a range indicating a small hydraulic jump downstream of the yoyo-cast location. As the flow velocity decreased and the Froude Numbers dropped below the critical level (see Section 1.4 and *Thorpe (2010)*), the hydraulic jump cannot be stationary. Thus, a transient, undular or weak hydraulic jump located downstream of station D1 might be the most likely scenario. Further analyses regarding the temporal variability of the along-channel flow is discussed in Section 5.3.

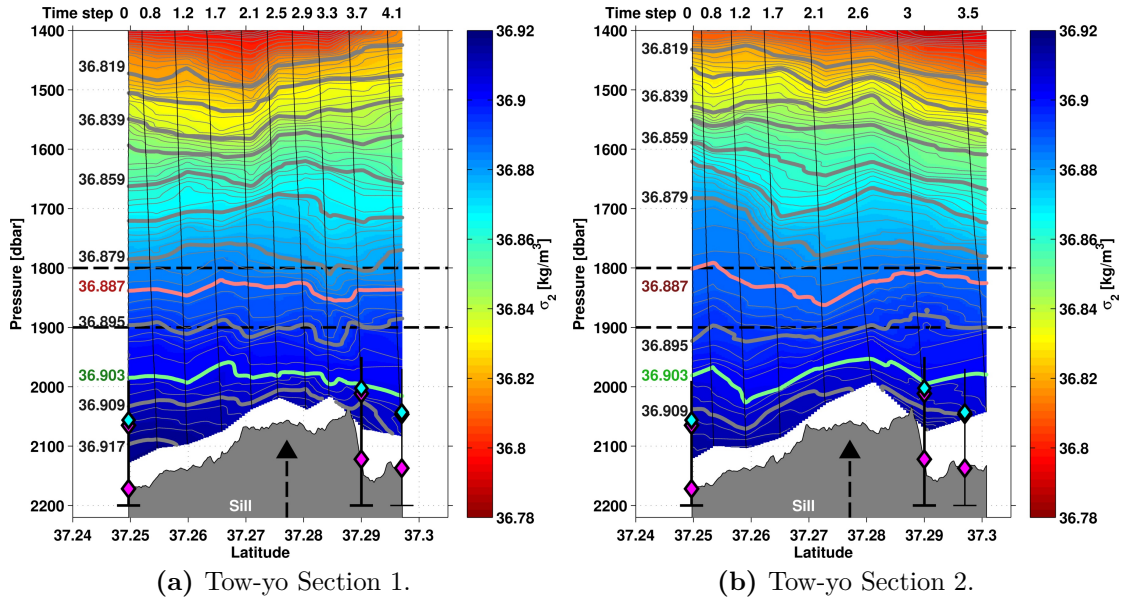


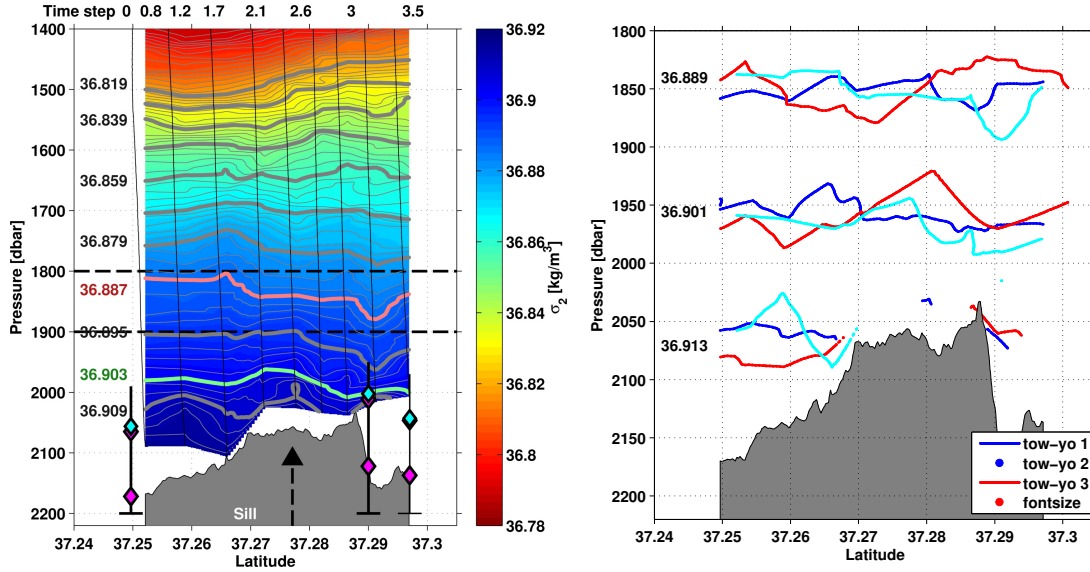
Figure 5.11: Density distribution (spacing $\Delta\sigma_2 = 0.002 \text{ kg/m}^3$) obtained from tow-yo Sections one (panel a) and two (panel b). Vertical black lines indicate locations of the individual downcasts. Density contours labeled at the left.

5.2.2 Temporal Variability in along-Channel Density Field

The along-channel flow and density field was shown to vary in the (semi-diurnal) tidal cycle based on moored (Section 5.1) and lowered observations (Section 5.2.1). It was argued that the temporal variability might cause the hydraulic jump to be a transient feature, i.e. to exist only during phases of large along channel flow. A hydraulic jump was observed in the average along-channel flow (Section 4.2). Based on three consecutively occupied tow-yo sections along the channel, the temporal variability of the density field was studied as it might clarify the presence of hydraulic jumps during different phases of the tide. Only density could be analyzed, as the velocity data derived with the LADCP system were biased due to the ships movement and thus the movement of the instrument over ground (personal communication *Andreas Thurnherr, Lamont-Doherty Earth Observatory*). The density was interpolated between individual casts using the same quasi-terrain following interpolation technique as before (*Kanzow and Zenk, 2014*).

The three tow-yo sections were obtained successively along the same track. They were conducted such that different phases of the tide were captured. Comparing the first and the second tow-yo (Figs. 5.11a and 5.11b), denser water was found at the bottom at the beginning (south i.e. left in Figs. 5.11 and 5.12) of the first

5.2 Evolution of the Flow and Density Field on short Time Scales



(a) Tow-yo Section three. Vertical black lines indicate locations of the individual downcasts.

(b) Three selected density contours from all three tow-yos.

Figure 5.12: Density distribution (spacing $\Delta\sigma_2 = 0.002 \text{ kg/m}^3$) obtained from tow-yo Section three (a) and three selected density contours of all three tow-yos (b). Density contours labeled at the left].

section compared to the beginning of the second section. For easier comparison between different tow-yos, two arbitrary contours were colored, the $\sigma_2 = 36.903$ colored green and the $\sigma_2 = 36.887$ colored red. At the sill at around 37.27°N the red density contour was found deeper in the water column in the second tow-yo than in the first tow-yo. Downstream of the sill, above 1900 m, the same density contours were found higher in the water column in the second tow-yo compared to the first. Below 2000 m the same contours were found slightly deeper during tow-yo two than during tow-yo one. The same was found comparing tow-yo section two and three (Fig. 5.12a), while tow-yo one and three were relatively similar. At the northern end of tow-yo one and three a hydraulic jump might be identified as density contours (e.g. $\sigma_2 = 36.887$) bend sharply, first down- and then upward (from south to north).

For direct comparison five isopycnals from all three tow-yos are shown together (Fig. 5.12b). The displacements described above are clearly visible indicating denser water in shallower water depth during the tow-yos one and three compared to tow-yo two upstream of the sill, while the situation was reversed downstream. There, light water was found deeper in the water column during the tow-yos one and three than during tow-yo two. Thus, the density distribution during tow-yo one and three was similar while it was different during tow-yo two.

In order to classify the three tow-yo sections into the tidal phase, the along-channel velocities observed from the moorings UM and DM2 during the same time were

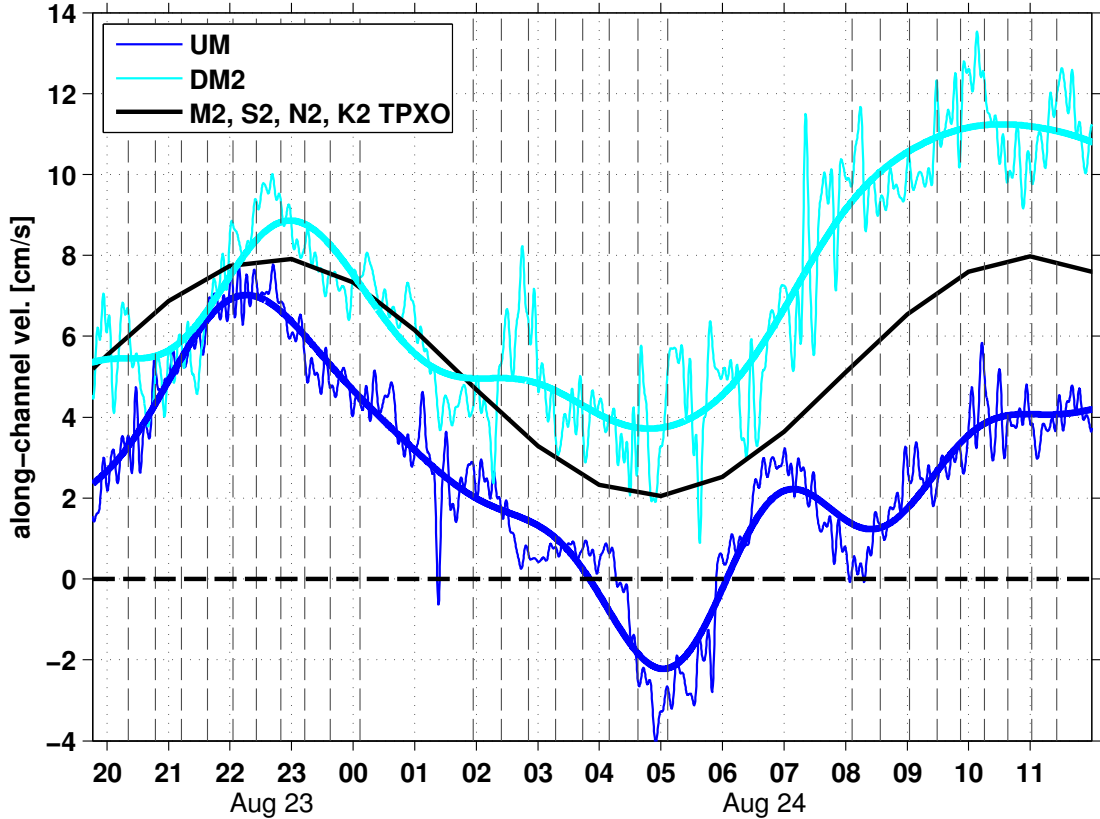


Figure 5.13: Along-channel velocity at the UM and DM2 mooring observed during the time when the three tow-yo-Stations were carried out. Also shown is the barotropic tide from TPXO model (Egbert and Erofeeva, 2002). Vertical black lines indicate times of the individual casts, when the instrument was at the bottom.

studied. At the DM2 mooring velocities of about 10 cm/s were observed during the first tow-yo, velocities of 4 to 5 cm/s were observed during the second tow-yo, and more than 13 cm/s were observed during the tow-yo three (Fig. 5.13). The velocities observed at both moorings showed good agreement regarding the phase of the tide and they were in good agreement with the TPXO barotropic tidal phase (Egbert and Erofeeva, 2002). Tow-yos one and three thus were conducted during phases of high along-channel flows, while tow-yo two was conducted during a phase of lower velocities.

Combining these results denser water was found higher in the water column during phases of high along-channel flow compared to phases of weaker along-channel flow. This was in good agreement with the temperature record from the upstream mooring which showed high correlation with the TPXO barotropic tide relating colder and thus denser water to phases of high along-channel flows (Section 5.1.2). Thus, upstream of the sill density contours were displaced upward during phases of large along-channel flow. Downstream of the sill the opposite was observed. Lighter water was found deeper in the water column during phases of high along-

5.3 Tidal Variability of the Flow and Density Field

channel flow compared to phases of weaker along-channel flow. Downstream of the sill, density contours thus were displaced downward during phases of large along-channel flow. This was consistent with a layer of supercritical flow, where the flow depth is smaller compared to sub-critical flow (i.e. the extend of the lower layer is smaller, Section 1.4).

In this paragraph it was shown that denser water was found higher in the water column during phases of large along channel flow compared to weaker along-channel flow. Whether denser water crosses the sill during high-velocity phases could not be clarified as no measurements were carried out at the sill during phases of weak along-channel flow. Indications for the presence of a hydraulic jump were found during phases of large along-channel flow, while there were indications for the absence of a hydraulic jump during phases of weak along-channel flow. This supports the previous findings (Sections 5.1 and 5.2.1) indicating the hydraulic jump to be a transient feature.

If the hydraulic jump is a transient feature, the associated mixing is expected to vary within the tidal cycle, which is studied in Section 5.4. First, all lowered measurements conducted inside the Lucky Strike channel are revised with respect to the tidal cycle in the following paragraph.

5.3 Tidal Variability of the Flow and Density Field

The analysis of the average flow and density field revealed indications for a hydraulic jump downstream of the sill, consistent with the asymmetric distribution of the mixing (Section 4). Mooring-based velocity and temperature time-series indicated semi-diurnal variability to be superimposed onto the mean flow, suggesting the hydraulic jump to be a transient feature. Repeated profiling just downstream of the sill revealed a phase of strong along-channel flow accompanied by elevated Froude Numbers, which was followed by a phase of strong decrease of the flow velocity accompanied by low Froude Numbers. Thus Froude Numbers indicated supercritical flow during the first phase and sub-critical-flow during the second phase of the observations (Section 5.2.1). This supported the hydraulic jump to be non permanent. Furthermore, the density field observed during continuous profiling while steaming along the channel suggested the hydraulic jump to be found only during phases of high along-channel flow (Section 5.2). In order to identify differences in the along-channel distribution of the velocity and density fields during different tidal phases and to further support the hypothesis of a hydraulic jump being established only during phases of high along-channel flow, all lowered observations conducted in the context of this study were sorted according to the tidal phase (Fig. 5.14, tide dependent sorting of profiles in Table A.1). As profiles were taken during arbitrary phases of the tide, not every tidal-phase was resolved at each position and only two flow regimes are distinguished. In this study the mean northward flow was approximately as large as the tidal amplitude superim-

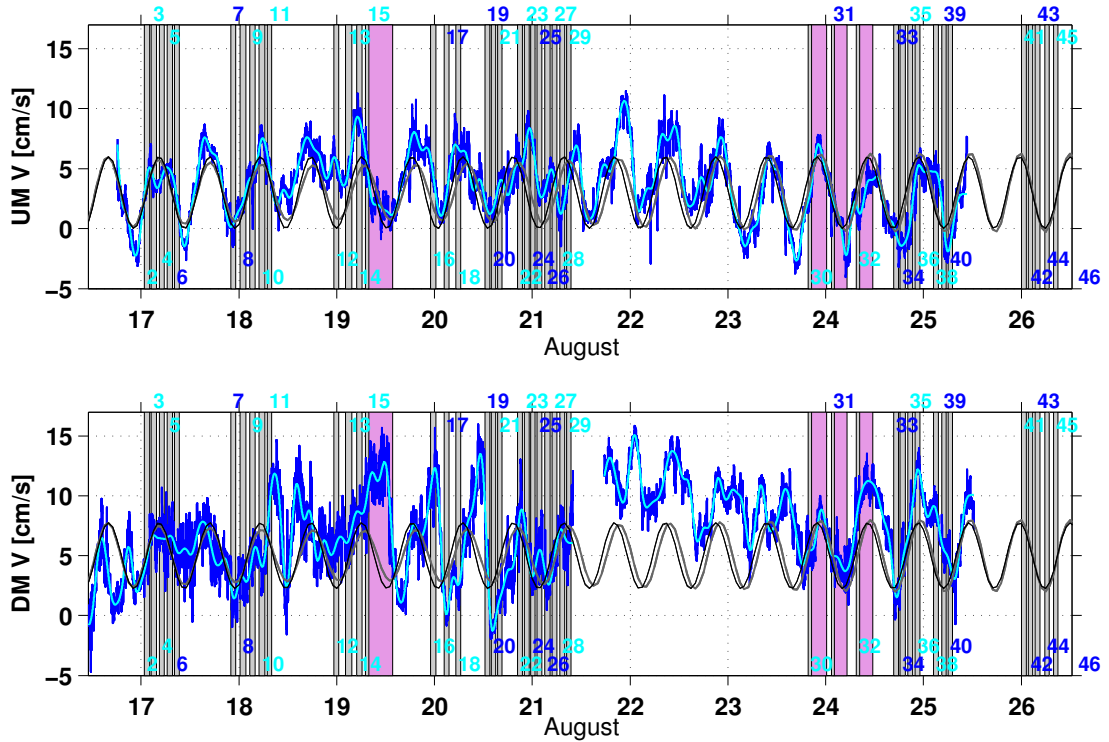


Figure 5.14: Along-channel velocity (blue) and 3 h low-pass filtered along channel velocity (cyan) at the upstream (upper panel) and downstream mooring (lower panel). TPXO barotropic M_2 tide and M_2 -, S_2 -, N_2 -, and K_2 -tide (Egbert and Erofeeva, 2002) are indicated in black and gray. Vertical gray bars mark time-frame of each profile with the numbers indicating the profile number color-coded according to the tide-dependent grouping (cyan-flood, blue-ebb). Magenta vertical bars, indicate the time-frame of the yoyo and tow-yo longterm station discussed in Section 5.2. Tide dependent sorting of profiles is also given in Table A.1.

posed to the mean flow (Section 5.1) such that the direction of the flow hardly changes sign. Subsequently, the term ‘flood’ will be used to describe phases of high flow velocities and ‘ebb’ will be used to describe phases of low flow velocities throughout this thesis. The lowered measurements were sorted according to the flow speed observed at the mooring closest to each profile location (Fig. 5.14). In the following the average along-channel flow and density distributions (Section 4.2) are revised as well as the LADCP-derived depth averaged velocities. Differences in the distributions of the flow and density field originating from different tidal flow regimes are examined.

5.3.1 Along-channel Flow and Density Distribution

The along-channel flow map projection discussed in Section 4.2 (Fig. 4.5) can now be split up into ‘flood’ and ‘ebb’ conditions. In Figures 5.15 and 5.16 the same data discussed in Section 4.2 was now color-coded according to the two tidal phases

5.3 Tidal Variability of the Flow and Density Field

‘flood-tide’ and ‘ebb-tide’. Additionally to sorting the velocity observations in two tidal phases, the depth averaging was performed in two layers. One layer covered the depth range from 1800 m to the sill depth (2060 m, Fig. 5.15) and the other one covered the depth range below the sill depth down to the bottom (Fig. 5.16). With these two layers it can be examined whether along-channel flow is observed also below the sill depth or whether blocking of the along-channel flow occurs.

Above the sill depth the flow was directed along the channel at the majority of the stations recorded during flood-tide (Fig. 5.15). Shallower stations at the edges of the channel deviated from this direction. The velocities observed upstream of the sill showed larger deviation from the along-channel direction during ebb-tide than during flood-tide. Near the sill, where the channel is particularly narrow the alignment with the along-channel direction was largest. Downstream of the sill, where the channel widens towards the northern basin, the flow directions were less confined. In the middle of the channel the flow was directed along the channel during flood- and ebb-tide unlike at the channel edges. At the north-western channel-sidewall from the latitude of the sill to the northern end of the channel, velocities showed variable directions including southward return flow.

At the majority of the stations, the flow was slightly bottom intensified (compare Figs. 5.15 and 5.16) Note that less values determine the average below the sill depth than above. Below the sill depth southward flow was present at the north-western sidewall of the channel during ebb-tide, while the flow was directed along the channel to the north-east at the eastern side of the channel during both phases of the tide. Upstream of the sill, southward flow was present at ebb-tide at station U3, but also during flood-tide at one station at the location U2. All other stations showed along-channel flow during flood-tide.

In both depth intervals the characteristics of flood-tide and ebb-tide were similar. By definition higher velocities were present during flood-tide with along-channel direction throughout the channel. During ebb-tide smaller flow speeds with more variable directions including southward return flow were found. Bottom intensified along-channel flow was found mainly during flood-tide downstream but also upstream of the sill. Along-channel flow was observed also below the sill depth possibly indicating dense water from below the sill depth to cross the sill during phases of large along channel flow.

The same tide-dependent sorting of stations as applied to the map projection (Figs. 4.5, 5.15, and 5.16) was applied to the along-channel section of velocity and density such that the mean state, discussed in Section 4.2.2 can now be studied with respect to the tidal phase. At each of the group-stations (U3-U1, S, and D1-D4) profiles were sorted according to the phase of the tide (Fig. 5.14) and averaging was performed for the profiles acquired during flood- (Fig. 5.17) and during ebb-tide (Fig. 5.18) separately at each of the group-stations (tide dependent sorting of profiles in Table A.1). At station D1, only two profiles were available, both recorded during flood-tide and the station D1 thus was omitted in the ebb-tide section. As not every station was sampled equally often, the group-station tide-

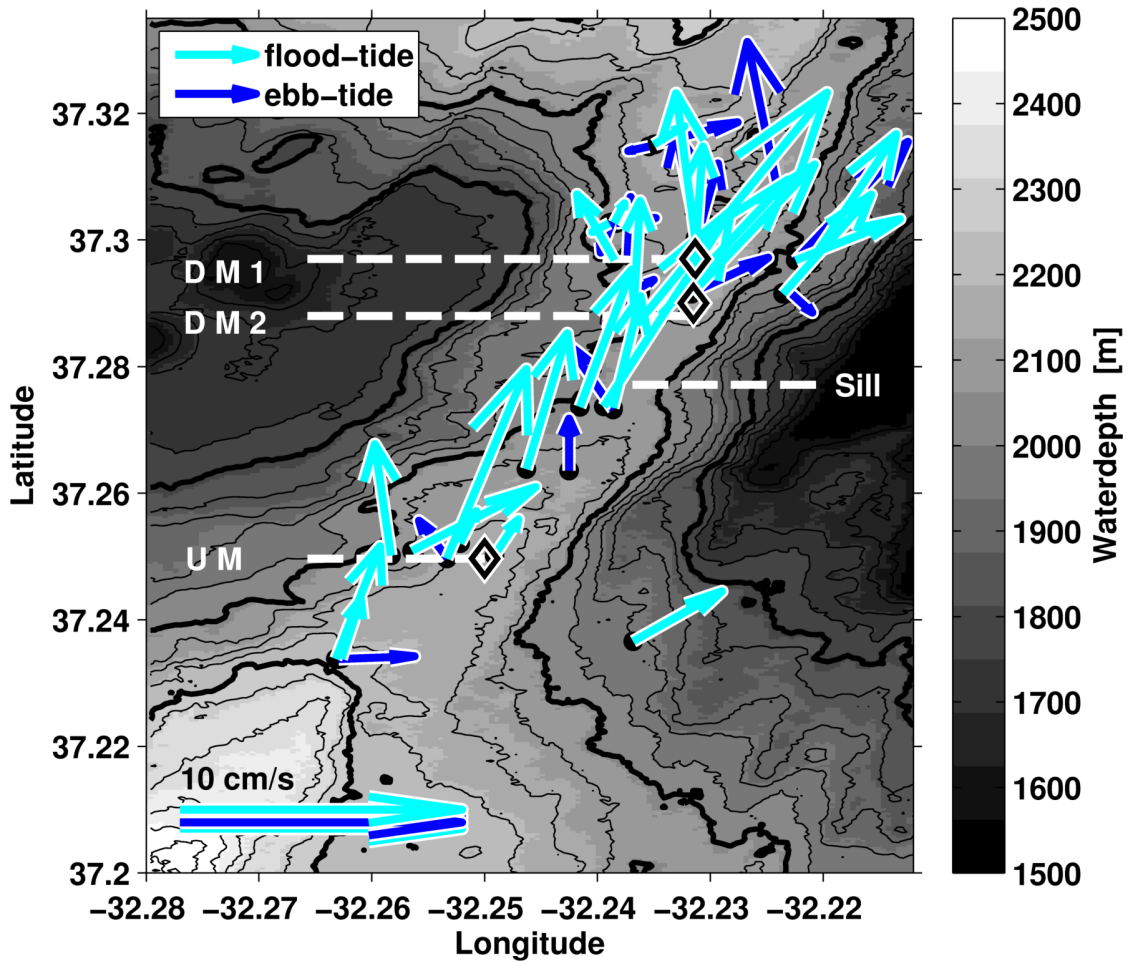


Figure 5.15: Depth averaged LADCP derived velocities averaged between 1800 m depth and the sill depth (2060 m). Reference arrows of 10 cm/s in lower left corner. Black dots mark station locations. Diamonds mark mooring positions. Contour line spacing 50 m. Thick contour lines refer to 1800 m, 2050 m and 2250 m.

dependent averages are based on varying numbers of profiles at each station.

During flood-tide northward flow was present throughout the channel (Fig. 5.17). Compared to the average of all stations without tide-dependent sorting (Fig. 4.6), by definition stronger flow was observed at all stations besides the D1 station, where both profiles were recorded during flood-tide. Downstream of the sill, the topography following current was more pronounced (Fig. 5.17) compared to the average-state (Fig. 4.6). Higher velocities were also observed higher in the water column at station D2 and at the bottom at station D3 compared to the average (Fig. 4.6).

The Froude Numbers computed for the flood-tide average profiles following Equation 1.5 were again largest at the station D1 and dropped sharply in both, up-

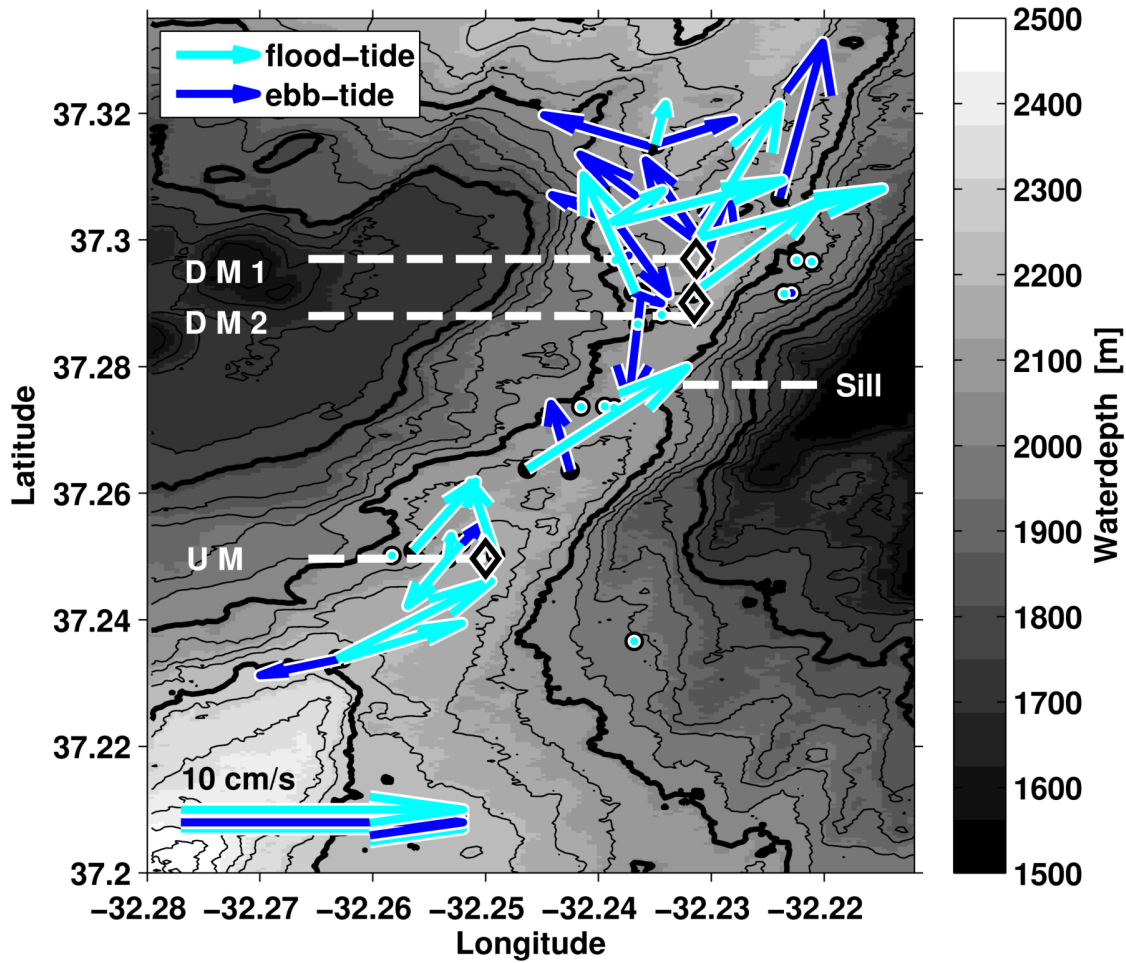


Figure 5.16: Depth averaged LADCP derived velocities from the sill depth (2060 m) to the bottom. Reference arrow of 10 cm/s in lower left corner. Black dots mark station locations. Diamonds mark mooring positions. Contour line spacing 50 m. Thick contour lines refer to 1800 m, 2050 m and 2250 m.

and downstream direction. At the stations U1-D3, and D2 Froude Numbers were slightly larger during flood-tide than during the average-state. The density distribution again supported the interpretation of the existence of a hydraulic jump during flood-tide. Isopycnals below $\sigma_2 = 36.893$ were following the bottom topography downstream of the sill, while above isopycnals were displaced upward just downstream of the velocity maximum at the sill. This upward displacement was more pronounced compared to the average-state (Fig. 4.6) and visible up to 1400 m depth, possibly indicating upward propagation of internal waves as found in the model study by *Legg and Huijts* (2006). Upstream of the sill density contours were slightly less horizontal and the same contours were found a little higher in the water column compared to the average-state. This supported the previous findings of dense water being found higher in the water column during phases of higher

5 Tidal Influence on the Flow, the Density, and the Dissipation Rate Distribution

flow velocities, which was indicated by the temperature variability observed at the moored CTDs (Section 5.1.2) as well as by the tow-yo observations (Section 5.2).

The distribution of both, the density and Froude Numbers indicated a hydraulic jump to be located between stations D1 and D3 during phases of high along-channel flow. The Froude Numbers were in the range of an undular or weak hydraulic jump (Section 1.4 and *Thorpe (2010)*). The higher Froude Numbers close to the sill and the larger displacement of isopycnals during flood-tide might indicate the hydraulic jump to vary in strength within the tidal cycle. A variation in the strength of the hydraulic jump would probably also cause variations in the location of the jump.

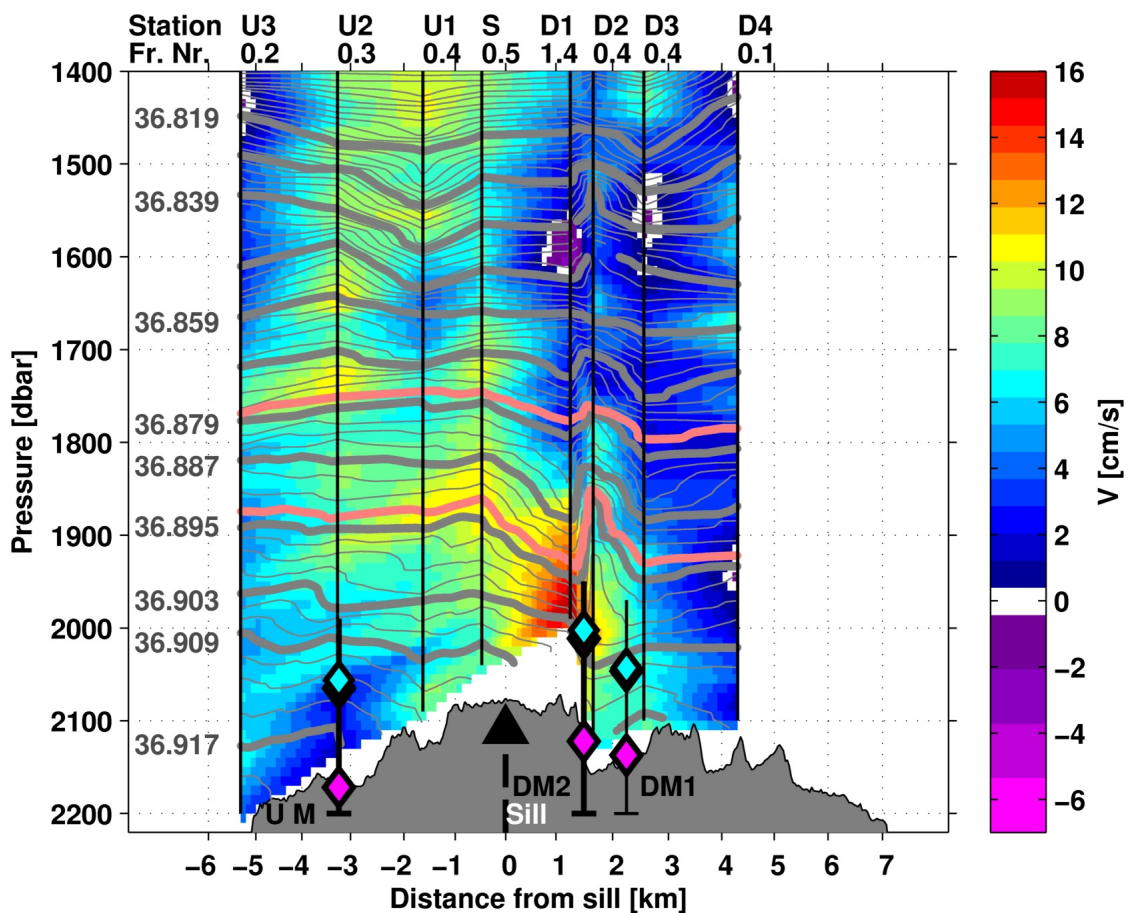


Figure 5.17: Along-channel LADCP derived velocity for flood-tide. Station names are given at the top with the respective Froude Numbers below each station name. Vertical lines mark the latitude of each station. Note that colors refer to along-channel velocity but Froude Numbers were calculated with flow speed. Contour lines denote potential density (spacing $\Delta\sigma_2 = 0.002 \text{ kg/m}^3$). Station numbers used: U3 (10, 14), U2(30, 32, 41), U1(3), S(4, 16, 18), D1(5, 15), D2(38), D3(23, 29), D4(12).

5.3 Tidal Variability of the Flow and Density Field

During ebb-state much smaller velocities were found compared to both, the flood-state (Fig. 5.18) and the average-state (Fig. 4.6). At station D2 weak southward flow was present below 1900 m while at station D3 weak northward flow was found (Fig. 5.17). Upstream of the sill weak northward flow mostly below 5 cm/s was observed. Only south of station U2, where the bottom slopes down towards the southern basin, southward flow was present.

At stations U1, S, D2, and D3, where Froude Numbers of 0.4 to 0.5 were observed during flood-state only 0.2 to 0.4 were found during ebb-state. The observed velocities indicated a sub-critical flow regime throughout the channel.

Density contours were nearly horizontal downstream of the sill between 1800 m

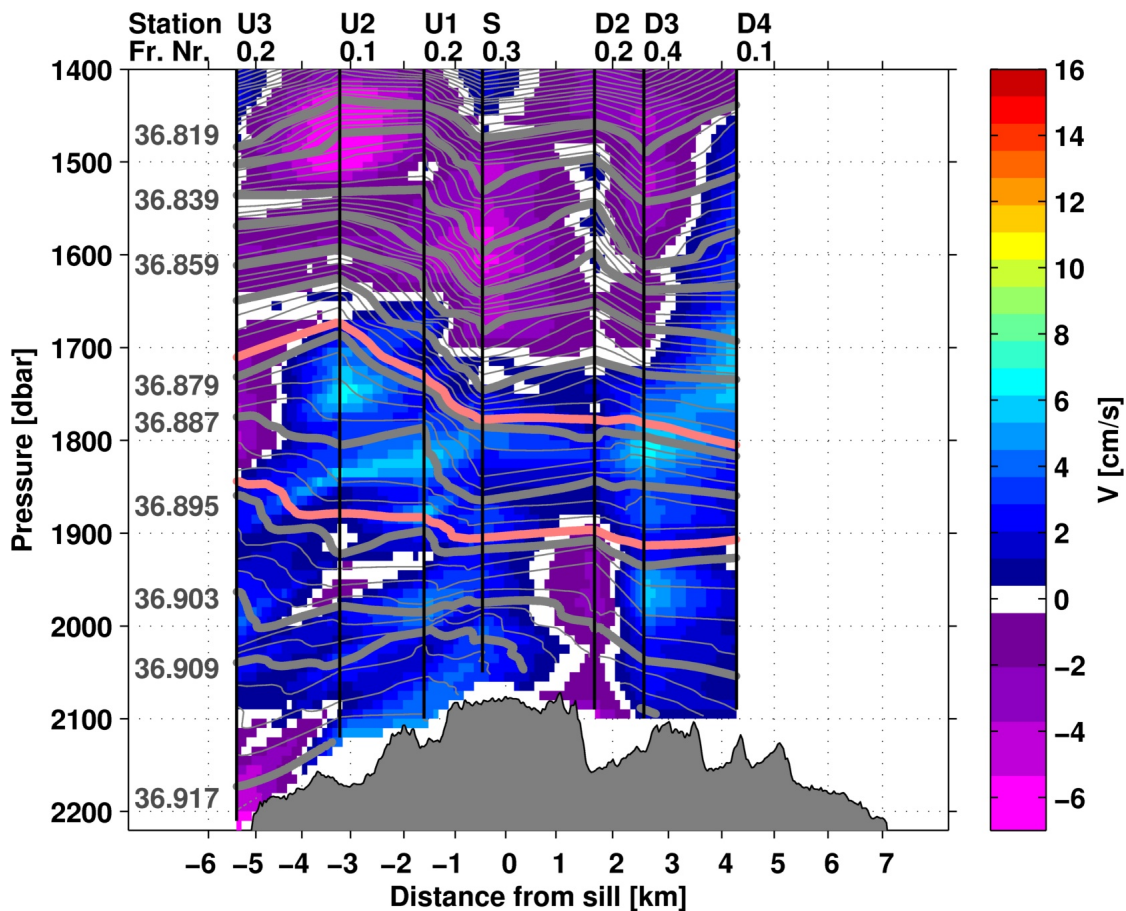


Figure 5.18: Along-channel LADCP derived velocity for ebb-tide. Station names are given at the top with the respective Froude Numbers below each station name. Vertical lines mark the latitude of each station. Note that colors refer to along-channel velocity components but Froude Numbers were calculated with the flow speeds. Contour lines denote potential density (spacing $\Delta\sigma_2 = 0.002 \text{ kg/m}^3$). Station numbers used at U3(43), U2(31), U1(42), S(17), D1(no station available), D2(34), D3(20, 26), D4(7, 44).

5 Tidal Influence on the Flow, the Density, and the Dissipation Rate Distribution

and 2000 m depth, in the same depth range where the upward displacement was observed during flood-state. Below, isopycnals followed the topography also during ebb-state but the slope was less steep. Upstream of the sill, density contours were more irregular than during flood- or the average-state.

The tide-dependent sorting of lowered measurements revealed substantial differences in the flow and density distribution between flood- and ebb-state. High flow velocities and elevated Froude Numbers were found during flood-tide, which indicated the presence of a hydraulic jump during high-velocity conditions. This was kind of masked in the average state. The upward displacement of isopycnals downstream of the sill (downstream of the velocity maximum) supported this interpretation (compare Section 1.4). In contrast, during ebb-state, weak flow velocities accompanied by small Froude Numbers and horizontal density contours were observed, indicating sub-critical along-channel flow. Thus, the hydraulic jump seems to be established only during periods of elevated tidal flow velocities. Two mechanisms could prevent a hydraulic jump during ebb-tide. Firstly, during weak along-channel flow, supercritical flow might not be established. Alternatively, an undular hydraulic jump might decay in any case due to upstream propagation of waves (Section 1.4), even without a tidally varying flow field.

As the cross-channel flow was found to be very weak (Fig. 4.7 in Section 4.2.3), this component will not be discussed with respect to the tidal-phase. Instead, the along-channel flow and density distribution in across-channel direction are analyzed with respect to the tidal-phase in the following paragraph.

5.3.2 Across-Channel Distribution of Flow and Density

The across-channel distribution of the velocity and density field reported in Section 4.2.3, indicated the hydraulic jump to be confined to the center of the channel. As the along-channel flow and density distribution revealed substantial differences between flood- and ebb-state (Section 5.3.1), the across-channel distribution is also expected to vary within the tidal cycle. This is examined in the following.

The central station of the first across-channel section was located within a range of 0.17 km from the mooring position DM2 at 37.292° N, 1.6 km downstream of the sill. At this location the upward displacement of isopycnals in the center of the channel was observed in the average across-channel section (Fig. 4.9a), which was interpreted to be associated to the hydraulic jump.

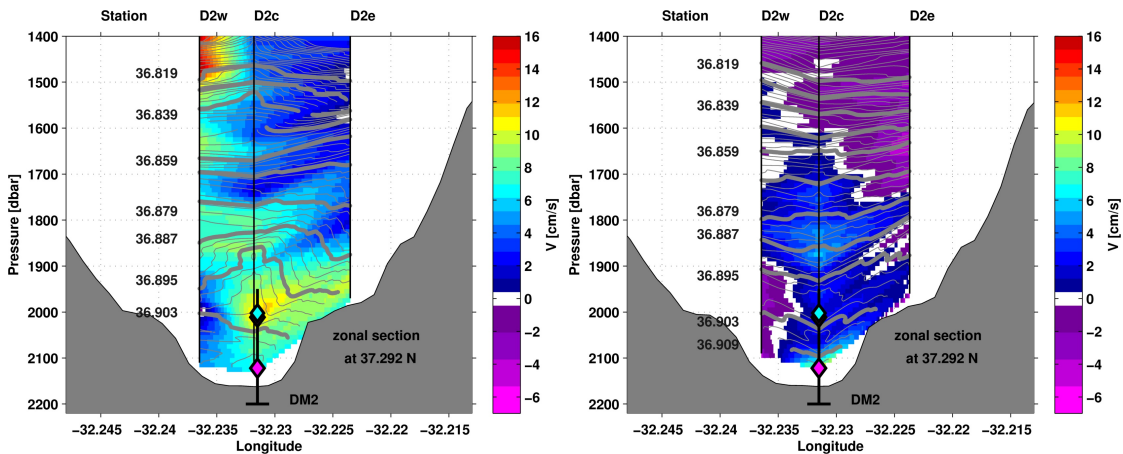
The tide dependent evaluation of the across-channel sections revealed a maximum along-channel flow of 12 cm/s during flood-tide at the center-station at 2000 m depth, where only about 7 cm/s were observed for the average-state (Fig. 5.19a). At the eastern edge of the channel 5 cm/s to 10 cm/s were observed during flood-tide compared to less than 5 cm/s for the average-state (Fig. 4.9a). At the western edge the flow was still above 5 cm/s during flood-tide while it was about 0 cm/s in the average-state.

5.3 Tidal Variability of the Flow and Density Field

As in the average-state, the densest water was found in the center of the channel during flood-tide. The 36.903 isopycnal was sloping down from west to east. Above 2000 m, where the high flow velocities were observed, dense water was displaced upwards in the center of the channel (compare Fig. 4.9a). This across-channel section located at station D2 (consisting of the western-, center-, and eastern-station) is the same station, where the upward displacement was observed in the along-channel section of the along-channel flow (Fig. 5.17). Thus, the upward displacement of isopycnals found in the across-channel section in the center of the channel is interpreted to be related to the hydraulic jump analogue to the interpretation described in Section 4.2.3. The upward displacement of about 60 m was larger during flood-tide compared to the average-state, where it was only about 20 m. As indicated by the average-state across-channel section, the upward displacement was zonally confined to the center of the channel also during flood-tide (Fig. 5.19a).

During ebb-state (Fig. 5.19b) along-channel velocities were below 6 cm/s and isopycnals were slightly displaced downwards in the center of the channel. Thus, no hydraulic jump is evident. As only two profiles were recorded at this position, the ebb- and flood-state are determined from a single profile. The structure between profiles should be viewed with caution as the interpolated flow and density fields are determined by measurements only in the center and at both edges.

The second across-channel section was located about 2.6 km downstream of the sill at the stations D3 at a latitude of 37.3° N close to the mooring location DM1 (Fig. 5.20). The distance of the center station from the mooring DM1 was 0.3 km.

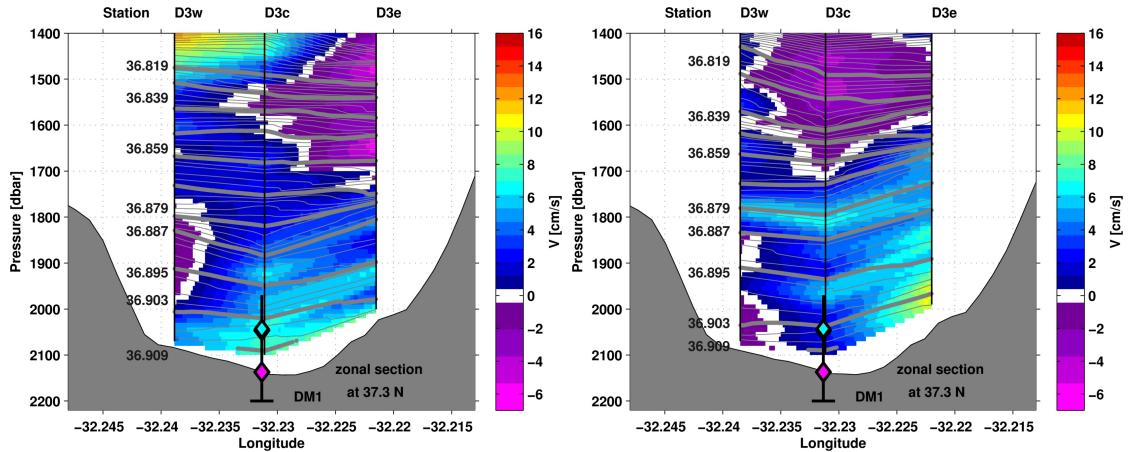


(a) Flood-tide (Stations used: D2w(36), D2c(38), D2e(35)).

(b) Ebb-tide (Stations used: D2w(33, 40), D2c(34), D2e(39)).

Figure 5.19: Along-channel LADCP derived velocity for flood- (a) and ebb-tide (b) at the first across-channel section close to the DM2 mooring. Stations are given at the top of each panel. Vertical lines mark the latitude of each station. Contour lines denote potential density (spacing $\Delta\sigma_2 = 0.002 \text{ kg/m}^3$).

5 Tidal Influence on the Flow, the Density, and the Dissipation Rate Distribution



(a) Flood-tide (Stations used: D3w(22, 28), D3c(23, 29), D3e(21)).

(b) Ebb-tide (Stations used: D3w(19, 25), D3c(20, 26), D3e(24)).

Figure 5.20: Along-channel LADCP derived velocity for flood- (a) and ebb-tide (b) at the second across-channel section close to the DM1 mooring. Stations are given at the top of each panel. Vertical lines mark the latitude of each station. Contour lines denote potential density (spacing $\Delta\sigma_2 = 0.002 \text{ kg/m}^3$).

During flood-tide along-channel velocities from 4 cm/s to 6 cm/s below 1900 m were found in the center and at the eastern edge of the channel increasing to 8 cm/s at the bottom (Fig. 5.20a). For the average-state velocities were below 7 cm/s at the western edge and below 5 cm/s in the center of the channel. Weak southward velocities were found at the western edge between 1800 m and 2000 m during flood-state as well as in the average-state. During ebb state elevated along-channel velocities with a maximum of 11 cm/s were concentrated at the eastern edge of the channel, while there was weak southward flow of less than 2 cm/s at the western edge of the channel (Fig. 5.20b).

Density contours showed only small differences between flood-, ebb-, and the average-state. Isopycnals were found deeper in the water column in the center compared to both edges of the channel below 1800 m for all cases. No upward displacement of isopycnals was observed, which indicated the hydraulic jump to be located upstream of station D3, which was consistent with the along-channel sections of the along-channel flow and density distribution (Figs. 4.6 and 5.17).

In conclusion, the across-channel sections of the along-channel flow and density distribution showed clear differences between tidal phases at the first across-channel section closer to the sill, while only the location and strength of the maximum along-channel flow seemed to be influenced by the tidal-phase at the second across-channel section further downstream.

The differences observed between tidal phases at the first across-channel section close to the sill support the hypothesis of a hydraulic jump to be found only during phases of large along-channel flow and to be confined to the center of the channel.

5.3.3 Summary

The flow throughout the channel showed better alignment to the along-channel direction during phases of large flow velocities compared to phases of weaker flow velocities and denser water was indicated to cross the sill during high flow velocity conditions.

Supercritical flow at the first downstream station and the existence of a hydraulic jump downstream of the sill were indicated during phases of high along-channel flow. During phases of lower along-channel flow, the flow regime was found to be sub-critical throughout the channel. No clear differences between phases of high and low along-channel flow were found at the location of the second across-channel section. The later was taken close to the mooring DM1, which time-series did not allow a clear differentiation of tidal phases. Possible mechanisms which might explain such a pattern are discussed in Section 5.5.

5.4 Dissipation in tidally varying Flow

In the previous paragraphs the tidal variability of the along-channel flow and density distribution was studied. Strong influence of the semi-diurnal tides was observed indicating a hydraulic jump to be established only during phases of large along-channel flow. As a hydraulic jump is expected to be accompanied by elevated turbulence (Section 1.4) it would be very interesting to study the dissipation rate with respect to the tidal cycle. The analysis of the concurrently obtained AUV-based dissipation rates and the mooring-based velocity observations might improve the understanding of the processes driving the mixing. This is attempted below using the microstructure shear data obtained in the course of this study. The differences observed in the dissipation rate at the segment occupied twice on a constant pressure level reported in Section 4.4.3 might be related to a different flow regime. As a reference for the flow regime, the flow velocity observed at the downstream mooring DM2 was used.

Unfortunately, Dive 7 and 9 lasted for less than 5 h and cannot provide information on temporal differences at one location as each location was sampled only once. Dive 8 lasted for 19 h, covering 1.5 tidal cycles. The AUV sampled along three different tracks, each track covered twice during the 1.5 tidal cycles, allowing comparison of two measurements for each track. Two of the three tracks however were sampled twice during similar flow regimes.

To directly compare the observed flow with the dissipation rate, the along-channel velocity observed at the downstream mooring was interpolated onto the AUV track. In this way the observed dissipation rate can be compared with the flow velocity at corresponding times and positions of the AUV. Note that the flow velocity refers to that observed downstream of the sill although it is shown in a latitudinal projection (Figs. 5.21, 5.22, and 5.23). The maximum distance of the AUV to the downstream mooring was 8400 m. An additional map projection of the dissipation

rates and the along-channel flow velocity is shown in the appendix (Figs. A.6, A.7, and A.8). For the dissipation rates and the flow velocities 10 min averages were computed without overlap between intervals (corresponding to 900 m). Dissipation rates below the noise level ϵ_n were replaced by zero prior to averaging (noise level see Section 3.3). The variability encountered in each of the 10 min segments (i.e. the statistical error) was estimated using the bootstrap method based on 1000 ensemblesⁱⁱⁱ (Efron, 1979). This estimate represents the error of the average for each segment resulting from the variability of the dissipation rate. The measurement error was neglected. The error of the average velocities was estimated by the error of the mean at a 95 % confidence level represented by twice the standard deviation divided by the square-root of the sample size minus one ($2 \cdot \text{std}/\sqrt{n-1}$) of each 10 min segment again by neglecting the measurement error which was estimated to be below 0.6 cm/s (Section 2.2).

The AUV crossed the sill six times on three different tracks one being located in the center (Figs. 5.21 and 5.24b), one on the western edge (Figs. 5.22 and 5.24a), and one on the eastern edge of the channel (Figs. 5.23 and 5.24c). The tracks were sampled in the following order: 1) in the center, 2) at the western edge, 3) at the eastern edge, 4) at the western edge, 5) in the center, and 6) at the eastern edge of the channel.

As mentioned before elevated dissipation rates were observed in the range 1 to 4 km downstream of the sill. The dissipation rate estimates obtained during the two runs in the center of the channel were significantly different from each other at some locations upstream of the sill, just downstream of the sill, and 4 to 6 km downstream of the sill. Upstream of the sill besides the first two values, the differences were small and interchanging with slightly lower dissipation rates during the first run. The difference of the first two values can be attributed to the confined area of elevated mixing supposedly induced by reflection of the M_2 -tide under a critical angle to the topographic slope (Section 4.1.1). The area of elevated dissipation rates was encountered at slightly different latitudes during both runs inducing the shift in the 10 min average values. Just downstream of the sill the dissipation rate was a factor of 2 to 3 larger during the first compared to the second run. This was the location where the turbulent patch was observed (Section 4.4.3). In the range 4 to 6 km downstream of the sill the dissipation rate was larger by up to a factor of 4.6 comparing the first to the second run (Fig. 5.21).

The first run was conducted during a phase of weak along-channel flow approaching the minimum flow speed when the AUV was just downstream of the sill (Fig. 5.21 lower panel). Both tracks were sampled from south to north. During the second run, the flow speed was higher with about 6 cm/s but small compared to maximum observed along-channel flows of 15 cm/s during the next tidal cycle. The velocities were significantly different from each other in every 10 min segment but the last value.

During the time when the MR observed higher dissipation rates during the first

ⁱⁱⁱConfidence interval 95 %.

5.4 Dissipation in tidally varying Flow

run in the center of the channel 4 to 6 km downstream of the sill, lower flow velocities were observed at the DM2 mooring compared to the time of the second run. From the two tracks, thus a tendency towards higher dissipation rates during times of weaker along-channel flow was indicated. A possible explanation for this tendency might be a propagating hydraulic jump, which would be triggered by low flow velocities. The elevated dissipation rates observed during a phase

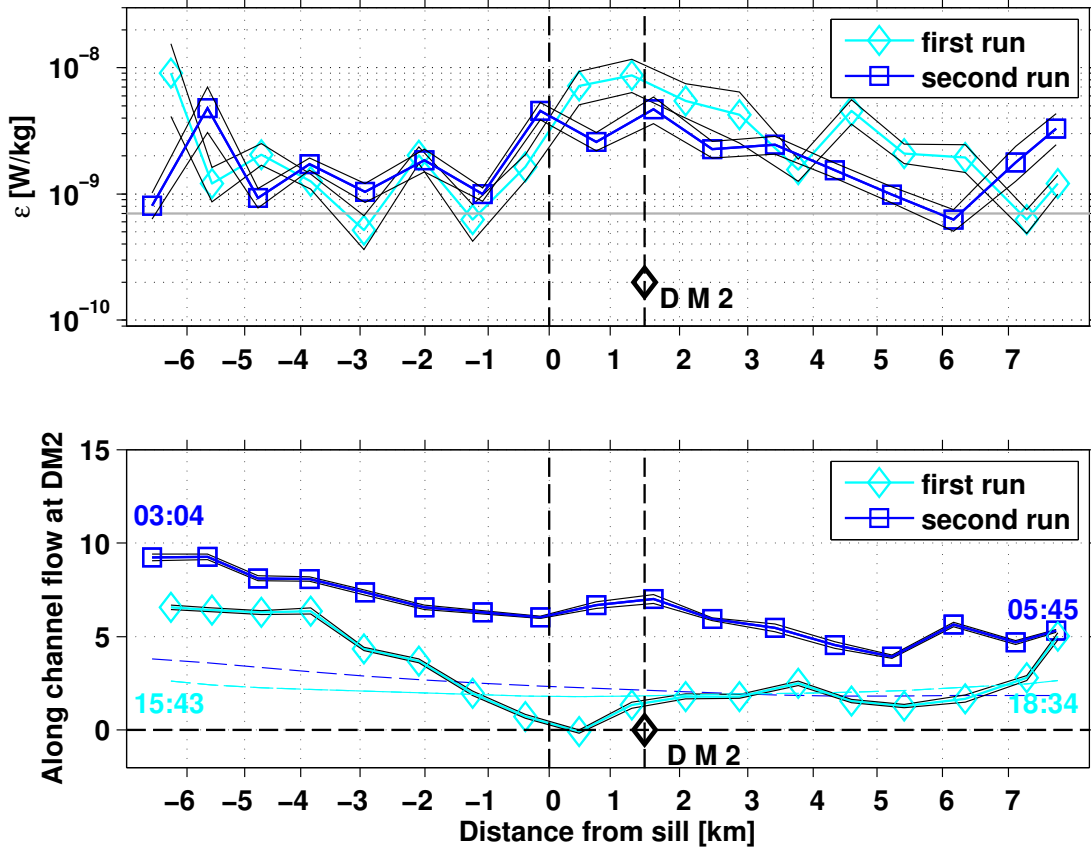


Figure 5.21: Ten minute average dissipation rates observed on the same track in the center of the channel (upper panel) and 10 min averaged flow velocity (lower panel) observed at mooring DM2, interpolated onto the same coordinates as AUV measurements. Hence the flow speed refers to that observed downstream of the sill during the time as the AUV was sampling at the indicated positions. The barotropic tide extracted from the TPXO model (*Egbert and Erofeeva, 2002*) was also interpolated onto the AUV position and is shown with an offset of 5 cm/s in dashed colored lines respectively (lower panel). Vertical dashed lines indicate the location of the sill and the mooring DM2 (diamond), respectively. The time [UTC] is given at the start and end of each track. Gray solid line marks the dissipation rate noise level (upper panel). Black lines in the upper panel indicate 95% confidence level estimated using the bootstrap method based on 1000 ensembles (*Efron, 1979*), in the lower panel they represent the error of the mean at a 95% confidence level ($2 \cdot \text{std}/\sqrt{n-1}$) of each 10 min segment.

5 Tidal Influence on the Flow, the Density, and the Dissipation Rate Distribution

of weaker along-channel flow correspond to the turbulent patch discussed in Section 4.4.3. There it was shown that a turbulent overturn can probably not explain the density anomaly, which was observed simultaneously to the high mixing rates and suggested that a hydraulic jump was sampled. Whether the hypothesis of a propagating hydraulic jump can be supported is examined in Section 6. The elevated mixing rates further downstream, however, cannot be explained with the scenario of an upstream propagating hydraulic jump during weak along-channel flow. Hence, the source of the elevated mixing downstream is unknown. It might be either related to flow-topography interactions as it was located close to a small sea-mount like elevation (Figs. A.6 and A.1) or to a southward return flow possibly encountered during ebb-tide phases. The aim of studying the elevated mixing, which is expected downstream of energetic overflows, cannot be assessed from this two tracks as the flow was weak during both runs.

The two runs conducted at the western edge of the channel were carried out during medium flow speeds between 5 cm/s and 12 cm/s observed at the downstream mooring DM2 (Figs. 5.22 and 5.24a). The first run was conducted during increasing and the second during more or less constant flow speeds although the TPXO barotropic tides (*Egbert and Erofeeva, 2002*) indicated a phase of decreasing flow speeds (both tracks were sampled from north to south). Dissipation rates upstream of the sill were minimum a factor of 3 larger, at the sill even by a factor of 8 during the first run, but downstream of the sill they were lower by a factor 2 (Figs. 5.22 and 5.24a). It might be speculated that the larger dissipation rates observed during the first run upstream of the sill were associated to the possibly upstream propagating hydraulic jump (turbulent patch Section 4.4.3) observed during the first run in the center of the channel. If the two signals are related using the distance and time of the observations, the signal would have traveled 4 km upstream from the turbulent patch with a speed of about 25 cm/s (map projection on Fig. A.7). Further estimates regarding reasonable propagation speeds are discussed in Section 6. It has to be noted that the elevated dissipation rates on the western edge further upstream were found deeper in the water column than the turbulent patch observed in the center of the channel. Thus downward propagation would be required to relate the two signals (compare Figs. 5.24a and 5.24b). The second run at the western edge was conducted during decreasing flow velocities, which implied the presence of larger flow velocity conditions before the AUV was sampling that location. One might speculate that the larger dissipation rates observed downstream of the sill during the second run were related to energetic overflow with a possible hydraulic jump a few hours earlier (Fig. 5.24a). From the two tracks sampled at the western edge thus a slight indication for larger dissipation rates during larger along-channel flow might be drawn.

The two runs along the eastern edge of the channel were conducted in opposing directions, the first was sampled from south to north and the second vice versa. During the first run the along-channel flow was high with about 10 to 14 cm/s,

5.4 Dissipation in tidally varying Flow

whereas it was low during the second run with 2 to 6 cm/s only (Figs. 5.23, 5.24c, and A.8). The dissipation rates observed by the AUV were weak and partly below the noise level (Section 3) especially close to the sill. This was probably related to the shallow sampling depth of the AUV on the track at the eastern edge of the channel (Fig. 5.24c). Close to the sill, the AUV was probably too high in the water column or too far east, outside of the energetic overflow and mixing regime.

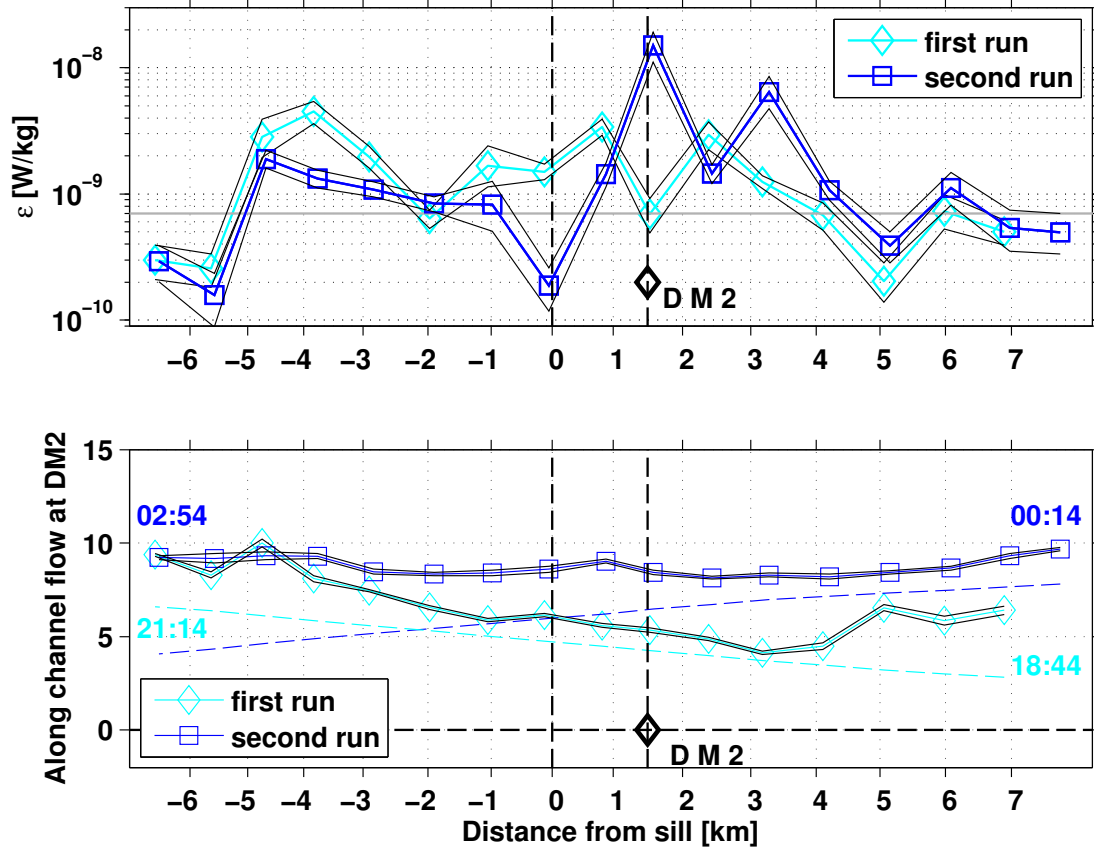


Figure 5.22: Ten minute average dissipation rates observed on the same track at the western edge of the channel (upper panel) and 10 min averaged flow velocity (lower panel) observed at mooring DM2, interpolated onto the same coordinates as AUV measurements. Hence the flow speed refers to that observed downstream of the sill during the time as the AUV was sampling at the indicated positions. The barotropic tide extracted from the TPXO model (*Egbert and Erofeeva, 2002*) was also interpolated onto the AUV position and is shown with an offset of 5 cm/s in dashed colored lines respectively (lower panel). Vertical dashed lines indicate the location of the sill and the mooring DM2 (diamond), respectively. The time [UTC] is given at the start and end of each track. Gray solid line marks the dissipation rate noise level (upper panel). Black lines in upper panel indicate 95% confidence level estimated using the bootstrap method based on 1000 ensembles (*Efron, 1979*), in the lower panel they represent the error of the mean at a 95% confidence level ($2 \cdot \text{std}/\sqrt{n-1}$) of each 10 minute segment.

5 Tidal Influence on the Flow, the Density, and the Dissipation Rate Distribution

Up- and downstream of the sill the dissipation rates were slightly larger during the first run compared to the second run (by a factor of 2 to 2.5 upstream and by a factor of 4 to 5 downstream of the sill). This might be again a weak indication for larger dissipation rates during phases of larger along-channel flow.

From the three different tracks along the channel sampled twice by the AUV

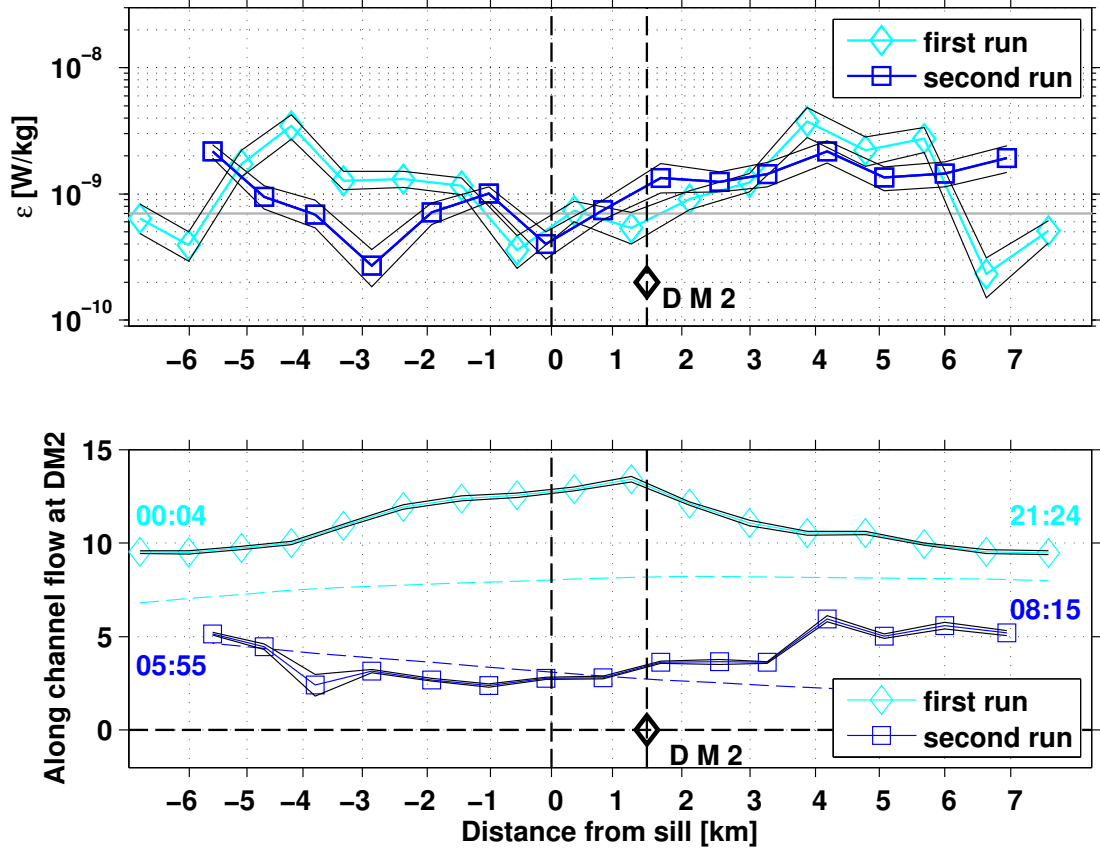


Figure 5.23: Ten minute average dissipation rates observed on the same track at the eastern edge of the channel (upper panel) and 10 min averaged flow velocity (lower panel) observed at mooring DM2, interpolated onto the same coordinates as AUV measurements. Hence the flow speed refers to that observed downstream of the sill during the time as the AUV was sampling at the indicated positions. The barotropic tide extracted from the TPXO model (*Egbert and Erofeeva, 2002*) was also interpolated onto the AUV position and is shown with an offset of 5 cm/s in dashed colored lines respectively (lower panel). Vertical dashed lines indicate the location of the sill and the mooring DM2 (diamond), respectively. The time [UTC] is given at the start and end of each track. Gray solid line marks the dissipation rate noise level (upper panel). Black lines in upper panel indicate 95% confidence level estimated using the bootstrap method based on 1000 ensembles (*Efron, 1979*), in the lower panel they represent the error of the mean at a 95% confidence level ($2 \cdot \text{std}/\sqrt{n-1}$) of each 10 min segment.

could change tremendously. Considering the comparably few data available here to study the evolution of the dissipation rate in the tidal cycle and the expected large natural variability in dissipation rates, only a weak indication for larger mixing being present during phases of larger along-channel flow can be reported.

5.5 Summary and Discussion

In this chapter the mean northward flow in the eastern channel of the Lucky Strike segment described in Chapter 4 was shown to vary within the semi-diurnal tidal cycle (Section 5.1.1). This was also reported for a channel south of the Lucky Strike segment by *Keller et al.* (1975). In this thesis furthermore, the temperature and density were shown to vary within the semi-diurnal tidal cycle, which was manifested in up- and downward displacement of isopycnals. The displacement was in phase with the tidal flow downstream of the sill indicating downward displacement i.e. less dense water being observed during phases of higher flow velocities (Section 5.1.2). Upstream of the sill, the displacement was opposite in phase indicating upward displacement i.e. denser water being observed during phases of higher flow velocities (Section 5.1.2). This might indicate that denser water can cross the sill during phases of higher along-channel flow compared to phases of weaker along channel flow. As along-channel flow was observed even below the sill depth during phases of large along-channel flow (Section 5.3.1), water from below the sill depth can possibly also cross the sill.

During phases of high along-channel flow a hydraulic jump was shown to occur, while there were no indications for the occurrence of a hydraulic jump during ebb-tide (Section 5.3.1). The hydraulic jump possibly caused isopycnal displacement also in shallower water depth a few hundred meter above the bottom due to upward radiating internal waves (Section 5.3.1). In across-channel direction the hydraulic jump was shown to be confined to the center of the channel (Fig. 5.19a). Downstream of the hydraulic jump the density and mixing distribution depends on the type of the jump. In the case of an undular jump, the downstream propagating waves would lead to vertically oscillating isopycnals and pulses of mixing (Section 1.4 and *Thorpe* (2010)), which probably would also be confined to the center of the channel. In the case of a weak hydraulic jump, no or only weak isopycnal oscillation would be expected. Turbulence would occur mainly close to the hydraulic jump.

The two flow velocity conditions of large and weak along-channel flow, the corresponding distributions of isopycnals as well as the distribution of the mixing are indicated in two sketches (for flood-tide in Fig. 5.25 and for ebb-tide in 5.27). It has to be noted that the two sketches are based on the observed velocity and density distributions obtained for both flow velocity conditions, while the distribution of the mixing could be determined only for the average state from observations due to limited temporal coverage of the velocity shear data (Section 5.4). The differences discussed below regarding the distribution of the mixing are thus largely

based on the findings of *Chow* (1959) and the model study by *Thorpe* (2010). The Froude Numbers derived in this thesis suggested the hydraulic jump to be an undular or weak hydraulic jump (based on findings of *Thorpe* (2010)). An undular hydraulic jump would decay due to upstream propagation of internal waves (left in Fig. 5.26), while a weak hydraulic jump (right in Fig. 5.26) would be stable (*Thorpe*, 2010). As the hydraulic jump seemed to occur only during phases of high flow velocity it was not possible to examine whether it would vanish due to upstream propagating internal waves or due to decreasing along-channel flow. In the case of a weak hydraulic jump no upstream propagation would occur and the jump would be stable, if the flow velocity would remain sufficiently high (*Thorpe*, 2010). In theory it would be possible to estimate the amplitude or size of a hydraulic jump by computing the Froude Number of the given flow as well as the critical Froude Number Fr_c , which determines the lower limit for a stable hydraulic jump for the given flow (Section 1.4 and *Thorpe* (2010)). But, as Fr_c depends on the exact shape of the density and velocity profiles up and downstream of the hydraulic jump, as has been shown by *Thorpe* (2010), this could be assessed in a model study only.

In summary, a hydraulic jump was found only during phases of high along-channel flow and it was confined to the center of the channel. The size of the jump presumably was that of an undular or weak hydraulic jump (Figs. 5.25 and 5.26).

As the distribution of mixing associated to a hydraulic jump depends on the amplitude of the hydraulic jump, it is expected to vary within the tidal cycle as the hydraulic jump amplitude is expected to vary in the tidal cycle. In Section 5.4 the observed mixing rates were studied with respect to the tidal phase, but no clear classification could be found due to limited temporal data coverage. Only a slight

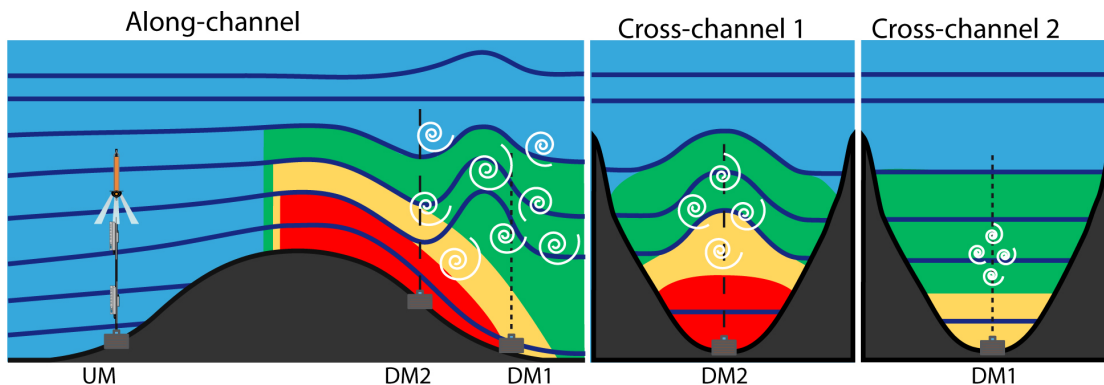


Figure 5.25: Sketch of the along-channel (left) and across-channel (middle and right) flow and density distribution during flood-tide. The cross channel sections are located at the two downstream mooring positions. The flow velocity is indicated by background colors (red - high, blue - weak flow), while contour-lines indicate isopycnals. The white spirals indicate mixing. All moorings were equipped as indicated at the upstream mooring (down-locking ADCP and two MicroCats below). Note that the sizes of all features are not to scale.

tendency of larger dissipation rates associated with larger along-channel flow was found.

Instead some indications regarding the type, amplitude and location of the hydraulic jump might be drawn from the mooring based temperature and velocity time-series and their correlations with the TPXO barotropic tide. Investigating the isothermal displacement (Section 5.1.2) had revealed downward displacement downstream of the sill during phases of larger flow velocities. This is consistent with a reduced flow depth associated to supercritical flow upstream of a hydraulic jump (Section 1.4) and would suggest the two downstream moorings to be located temporarily in the layer of supercritical flow. The correlation of the TPXO barotropic tide and the mooring-based temperature time-series was higher at DM2, located 1.5 km downstream of the sill ($R = 0.5$, Table 5.4) compared to the correlation at DM1, located 2.3 km downstream of the sill ($R = 0.2$ to 0.3 , Table 5.4). This might indicate the mooring closer to the sill to be located in the supercritical flow more often than the mooring further downstream. This would indicate the transition from supercritical to sub-critical flow, i.e. the initial upward displacement of isopycnals associated to the hydraulic jump, to be located between the two downstream moorings during most of the flood-tide phases (Figs. 5.25 and 5.26). This means that the mooring further downstream would be located in the turbulent region downstream of the hydraulic jump during most of the flood-tide phases (Figs. 5.25 and 5.26). During flood-tide phases of particularly high along-channel flow the supercritical layer might extend further downstream and even the DM1 mooring could be located in supercritical flow (not shown in the sketches). During such phases isopycnals would be displaced downward also at the mooring DM1. For the time-period analyzed in this thesis the hydraulic jump seemed to be located between the two downstream moorings during most of the flood-tide phases. This is supported by the along-channel density distribution (Figs. 4.6 and 5.17),

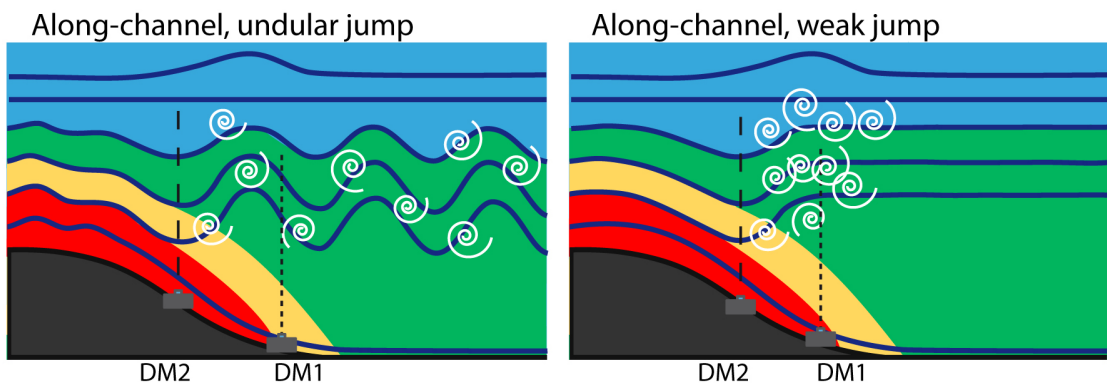


Figure 5.26: Sketch of the along-channel flow and density distribution during flood-tide for an undular (left) and a weak hydraulic jump (right). The flow velocity is indicated by background colors (red - high, blue - weak flow), while contour-lines indicate isopycnals. The white spirals indicate mixing. The two moorings are indicated without instrumentation. Note that the sizes of all features are not to scale.

which suggested the DM2 mooring to be located in the supercritical flow, while the DM1 mooring seemed to be located in sub-critical flow (Sections 4.2.2 and 5.3.1). Further support for the hypothesis of the hydraulic jump being located between the two downstream moorings can be drawn from the analysis of the high-frequency temperature variability (Section 5.1.2). If the hydraulic jump would be located between the two downstream moorings weak high-frequency temperature variability would be expected at the DM2 mooring closer to the sill (temporarily located in supercritical flow) and high-frequency temperature variability would be expected at the DM1 mooring further downstream (temporarily located in sub-critical flow downstream of the hydraulic jump). The correlation ($R = 0.65$, Table 5.6) of the high-frequency temperature variability with phases of large along-channel velocity observed at the DM1 mooring supports this hypothesis.

During weak flow velocity conditions uniform sub-critical flow along the channel down the lee slope of the sill is expected as sketched in Fig. 5.27. Weak southward return flow might occur (not shown in the sketch). No hydraulic jump and no upward displacement of isopycnals are expected. Unfortunately, it was not possible to clearly classify the mixing into tidal phases due to limited temporal data coverage (Section 5.4). As differences in the distribution of the mixing are thus unknown, the mixing is sketched similar during weak and large flow velocity conditions.

To summarize: During high flow velocity conditions supercritical flow downstream of the sill is expected, followed by a hydraulic jump and sub-critical flow further downstream (left panel Fig. 5.25). The hydraulic jump is associated to an upward displacement of isopycnals, which possibly also affects isopycnals in shall-

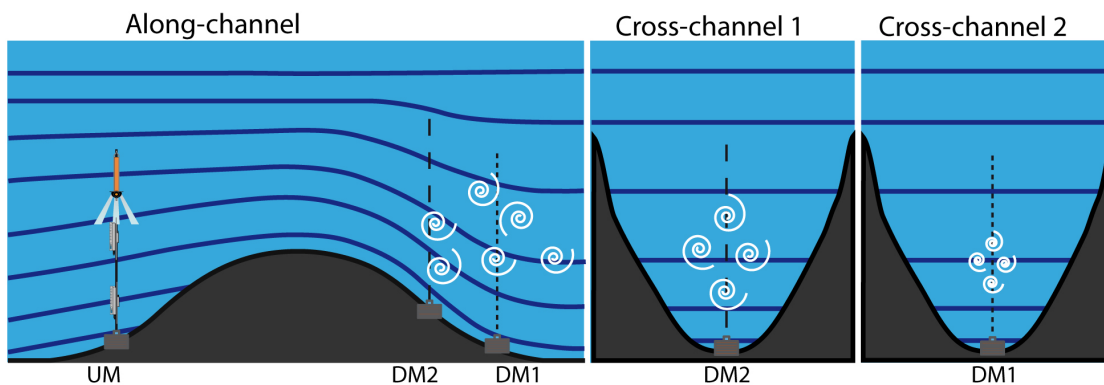


Figure 5.27: Sketch of the along-channel (left) and across-channel (middle and right) flow and density distribution during weak along-channel flow conditions. The cross channel sections are located at the two downstream mooring positions. The flow velocity is indicated by background colors (red - high, blue - weak flow), while contour-lines indicate isopycnals. The white spirals indicate mixing. All moorings were equipped as indicated at the upstream mooring (down-locking ADCP and two MicroCats below). Note that the sizes of all features are not to scale.

lower water depth a few hundred meter above the bottom due to upward radiating internal waves (left panel Fig. 5.25). Furthermore, the hydraulic jump is associated with mixing at the location of the upward displacement of isopycnals and further downstream (Figs. 5.25 and 5.26). The shape of the isopycnals and the distribution of the mixing further downstream depend heavily on the amplitude of the jump (Fig. 5.26 and Section 1.4). In case of an undular jump, isopycnals are expected to oscillate vertically downstream of the initial upward displacement and only a small fraction of the jumps energy is dissipated locally at the location of the hydraulic jump (left in Fig. 5.26). A large fraction of the energy dissipation would be carried downstream by the undular waves of the jump (Section 1.4 and (Thorpe, 2010)). In case of a weak but stationary hydraulic jump, mixing would occur mainly at the location of the initial upward displacement. The isopycnals would be distributed horizontally at a constant depth downstream of the jump (right in Fig. 5.26). In order to quantify the amount and location of mixing, it is thus important to determine the jump amplitude as, in the case of an undular jump, a considerable amount of mixing might occur further downstream in a region, which was not captured by this study.

The processes controlling mixing as well the influence of the tides in the eastern channel of the Lucky Strike segment can now be identified which answers two of the main questions underlying this thesis (Section 1.2). The mean along-channel flow in combination with the tidal flow induces a transient hydraulic jump downstream of the sill, which is associated to strong mixing. For the time frame covered by this thesis the mean flow was not sufficiently high to maintain a hydraulic jump during ebb-tide phases. In a scenario with a more pronounced mean flow it seems plausible that a hydraulic jump is maintained during all tidal phases and that only the jump amplitude is modulated within the tidal cycle. Longterm variations of the mean flow have been reported by Keller *et al.* (1975) for a channel just south of the LS segment and for a deep ocean channel at the MAR flank near 22° S by Thurnherr *et al.* (2005). Such longterm variations might induce periods of stronger along-channel flow possibly associated with a hydraulic jump during all tidal phases and thus with stronger mixing.

The question introduced by Thurnherr *et al.* (2005) whether the energetic mean along-channel flow or the varying tidal flow is dominating the downstream mixing at sills cannot be answered, as the impact of the tidally varying flow on mixing intensity could not be quantified. As mixing was found to be elevated downstream of the sill compared to upstream also during phases of weak along-channel flow it could be argued that the average along-channel flow controls the mixing pattern. With a zero time mean flow the tidal regime would result in a symmetric distribution of the average mixing across the sill (Legg, 2004; Legg and Huijts, 2006; Legg and Klymak, 2008). For the Lucky Strike segment the long-term persistent along-channel flow reported by several studies (Keller *et al.*, 1975; Thurnherr and Richards, 2001; Thurnherr *et al.*, 2005; Thurnherr, 2006; Thurnherr *et al.*, 2008) probably accounts for weak but persistent mixing downstream of the sill. Longterm

5.5 Summary and Discussion

variations of the mean flow as reported by *Keller et al.* (1975) might induce periods of stronger mixing downstream. For a quantification of the amount and location of energy dissipated by the persistent flow across the sill and the additional energy supplied by tides further observations are needed. A model study constrained by the observations and results of this thesis might also be useful to quantify mixing with respect to the distance from the sill in a tidally varying flow superimposed on a mean flow of longterm varying amplitudes.

6 Signal Propagation

In the previous chapters the average along-channel flow, density and mixing rate distributions have been analyzed (Chapter 4) as well as their variability in the tidal cycle (Chapter 5). A hydraulic jump was found to be periodically forced by the tidal flow downstream of the sill which was associated with strong mixing. In the tidally decreasing flow the hydraulic jump is expected to propagate in upstream direction as has been observed in shallow waters (*Brandt et al.*, 1996, 1997; *Cummins et al.*, 2006; *Cummins and Armi*, 2010) and was shown in model studies by e.g. *Legg and Klymak* (2008).

Indications for propagating signals as internal waves or hydraulic jumps were observed also in this thesis. One example for a propagating hydraulic jump might be found in the patch of dense water and strong turbulence observed about 800 m downstream of the sill (Section 4.4.3). The hydraulic jump was indicated to be located further downstream (1000 to 2000 m) during phases of strong along-channel flow observed with lowered measurements (Section 4.2.2 and 5.3.1). The turbulent patch might thus be a horizontally sampled hydraulic jump which was propagating towards the sill during weak flow velocity conditions (Section 4.4.3).

From a longterm station occupied for seven hours 1.2 km downstream of the sill (yoyo-station) indications for internal waves and possibly also for a propagating hydraulic jump were found (Section 5.2.1). Isopycnals were shown to vertically oscillate consistent with vertical velocities indicating up-and downward moment. Furthermore, the sawtooth signals observed in the mooring-based velocity time-series (Section 5.1.1) might be the result of superposition of internal waves. In the following paragraphs the observed phenomena are studied in more detail. The aim is to jointly characterize the signals observed from different platforms in order to understand their relations.

6.1 Internal Waves

In the following paragraph the time-frame of the yoyo-cast is analyzed in more detail using moored and lowered observations. The aim is to understand the observed features regarding internal wave-like motions during different tidal phases and during different flow regimes, i.e. in supercritical and sub-critical flow (Section 1.4). Furthermore, phenomena of high flow velocities observed at different locations which showed a time lag and were out of phase with the TPXO barotropic tide are analyzed. They might possibly be related to superimposed internal waves or induced by hydraulic jumps.

6 Signal Propagation

During the yoyo-cast (for details see Section 5.2.1) up- and downward movement of isopycnals was observed consistent with vertical velocities reported by *Thurnherr* (2011) indicating the presences of internal waves (Section 5.2.1). The along-channel velocity and density distribution suggested the supposed internal waves to be more pronounced in the layer above 1800 m compared to the layer below where strong, presumably supercritical flow was present (Section 5.2.1, Fig. 5.8, and Fig. 6.1). Supercritical flow was indicated by elevated Froude Numbers (given at the top in Fig. 5.8 and Fig. 6.1) computed following Equation 1.5 (Section 1.4). At the end of the yoyo-cast after about 11 UTC the velocities in the lower layer strongly decreased, while enhanced isopycnal displacement was present also in the layer below 1800 m compared to time of stronger flow velocities (Fig. 5.8). This might point to potential differences of internal wave induced isopycnal displacements during the different flow regimes.

To characterize the supposed differences between phases of super- and sub-critical flow as well as in the upper and lower layer, vertical averaging of the yoyo-cast-derived velocities was performed in two layers, firstly between 1400 m and 1800 m

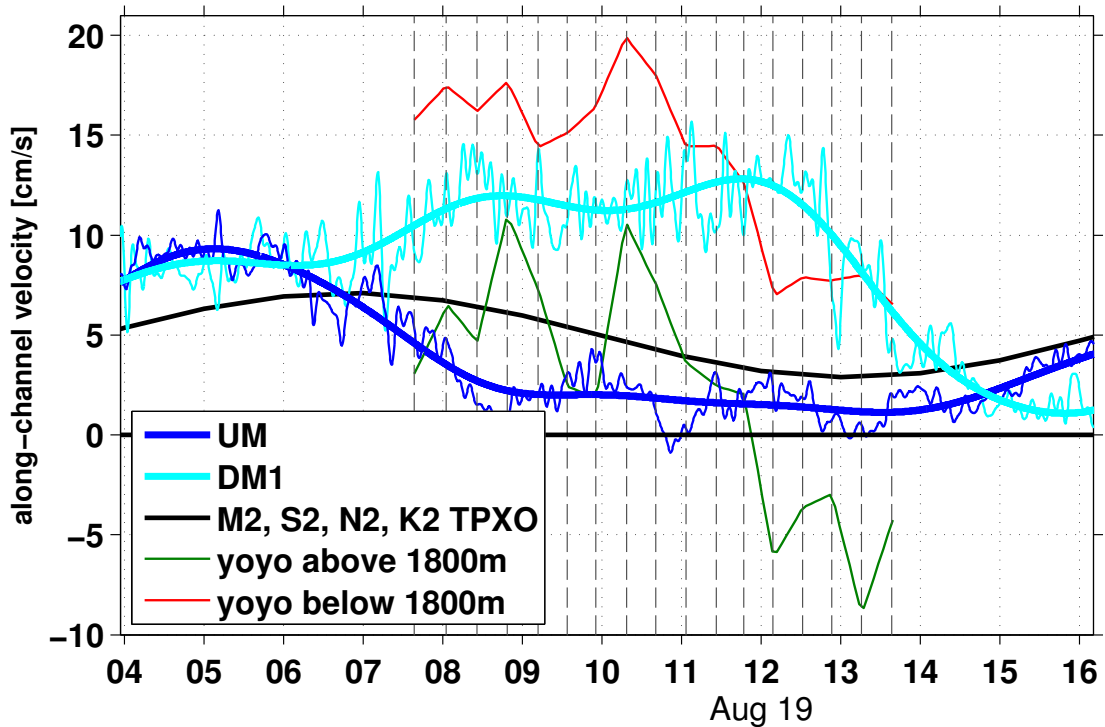


Figure 6.1: Along-channel velocity at the upstream (UM) and downstream (DM1) mooring observed during the time were the yoyo-Station was carried out, together with the barotropic M_2 , S_2 , N_2 , and K_2 tide from TPXO model (*Egbert et al.*, 2014). Also shown are the vertically averaged along-channel velocities from the yoyo-station. They were averaged in two layers. First below 1800 m (red) and second between 1400 m and 1800 m (green). Vertical black lines indicate moments of the individual up- and downcasts when the instrument was at the bottom.

and secondly over the layer below 1800 m (green and red line in Fig. 6.1, respectively). Comparing the two layers much weaker flow with a maximum of about 10 cm/s was found in the upper layer compared to a maximum of almost 20 cm/s in the lower layer. The decrease of the flow velocities began at about the same time in both layers. Additionally, in the upper layer the velocities seemed to be modulated with a period of about 1.5 h. This modulation might be present also in the lower layer but it was less pronounced.

The signal modulating the velocities with a period of 1.5 h was confirmed by the along-channel velocity anomaly computed from the yoyo observations (Fig. 6.2). The average along-channel velocity at each depth level was subtracted from the time series of each depth level (vertical resolution of LADCP data was 10 m). From the velocity anomalies the modulation of the velocities with a period of 1.5 h was visible in the upper layer over the whole time-period of the yoyo-cast. However, the isopycnals did not show periodic up- and downward movement after ~ 11 UTC. Instead, they were deepening above 1700 m depth. The alternating north and

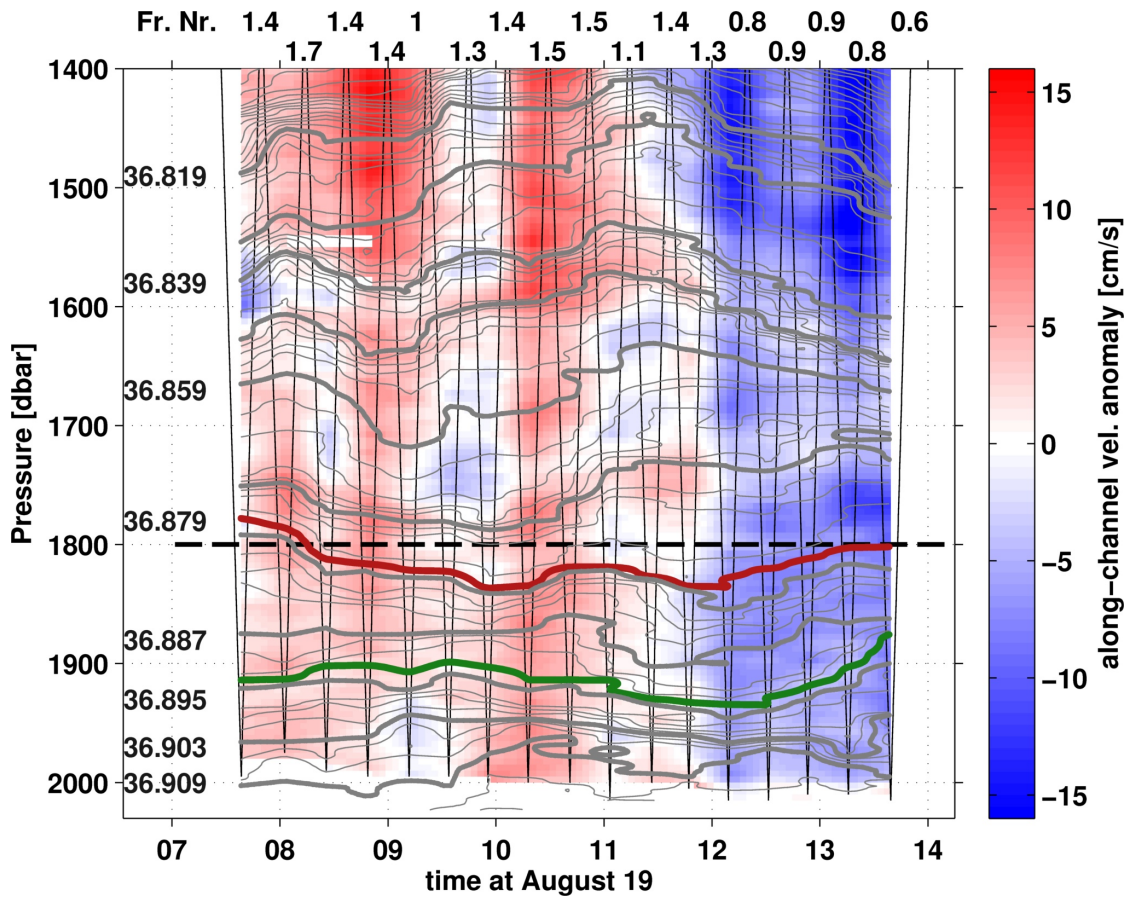


Figure 6.2: Along-channel flow anomaly at the yoyo-Station at D1. Average flow velocity of each depth layer was subtracted. Density contours with labels at the left (spacing $\Delta\sigma_2 = 0.002 \text{ kg/m}^3$). Froude Numbers are given at the top. Vertical black lines indicate the time of the individual up- and downcasts.

6 Signal Propagation

southward velocity anomalies can probably be explained by internal waves with a period of 1.5 h. Analyzing the same yoyo-cast *Thurnherr* (2011) reported internal wave-like motion at about 1600 m depth during the first 4 h of the cast. *Thurnherr* (2011) estimated a buoyancy period of about 1.5 h based on 25 m thick layers. Furthermore, he reported vertical velocities to vary on the same time-scale (Fig. A.3, *Thurnherr* (2011)).

In the lower layer the modulation of the along-channel velocities with a period of 1.5 h might be identified but only rather weak. During the phase of strong along-channel flow this might be attributed to the presumably supercritical flow regime where internal waves are expected to be largely suppressed (Section 1.4 and *Thorpe* (2010)). During the phase of decreasing and weak along-channel flow enhanced isopycnal displacement was present in the lower layer, but still no modulation of the along-channel velocities with a period of 1.5 h could be identified. However, isopycnals in the lower layer were rapidly shoaling consistent with upward velocities reported by (*Thurnherr*, 2011) at the end of the cast. The upward movement in the lower layer after 13 UTC might be related to a hydraulic jump propagating towards the sill. A propagating hydraulic jump would appear when the associated supercritical flow decreases, causing the jump to move upstream. The speed of a propagating hydraulic jump depends on the amount of flow decrease, not on the speed of internal waves (*Çengel and Cimbala*, 2006). The propagation speed of such a feature might be estimated if it is observed at different locations which was not the case here.

It is thus concluded, that internal waves with a buoyancy period of about 1.5 h were present in the upper layer during the phase of large along channel flow, while they were largely suppressed in the lower layer which was probably related to supercritical flow.

After 11 UTC where the flow velocity strongly decreased in the lower layer (Fig. 5.8) a clear southward velocity anomaly was present in both depth layers (Fig. 6.2) suggesting the signal or mechanism which induced this anomaly to affect both depth layers. Comparison with the mooring-based along-channel velocity revealed a temporal offset between the time of decreasing flow speeds at the yoyo-cast location D1 and at the two mooring positions UM and DM1 (Section 5.2.1). The mechanisms causing the strong velocity decrease at D1, which affected both depth layers (Fig. 6.2) might be related to the mechanism inducing the strong velocity decrease at the locations of the moorings. In the following the temporal offset is characterized.

The temporal offset of the strong velocity decrease observed at D1 and at DM1 was about 1.5 to 2 h (Fig. 6.1). Compared to the TPXO barotropic tide the velocity at DM1 was decreasing just shortly before lowest flow velocities would be expected and thus had a temporal offset of almost 6 h compared to the TPXO barotropic tide. At UM the velocities began to decrease about 2 h earlier than expected from the TPXO barotropic and about 7 h earlier than at D1 (Fig. 6.1). The decrease in along-channel flow velocities at the different locations can thus not be explained by the TPXO barotropic tide, neither in phase nor in amplitude. A quasi simul-

taneous decrease at all locations would be expected if they were caused by the tidally decreasing flow. The peak – to – peak amplitude of 3 cm/s of the TPXO barotropic tide cannot explain the amplitude of almost 20 cm/s at the D1 location. The discrepancy in amplitude and phase between different locations along the channel might be caused by a wave superimposed onto the tidal flow. To test this hypothesis the speed was estimated at which a wave would need to propagate to explain the succession of the decrease in flow velocities at the different locations. The temporal offset of the decrease in flow velocity of about 1.5 to 2 h between D1 (red line in Fig. 6.1) and DM1 (cyan line in Fig. 6.1) and their distance of less than 1.2 km would require a signal, which might induce the decrease in flow velocities, to propagate at a speed of 17 to 20 cm/s in northward direction. If the same signal would also be related to the decrease in flow velocities at UM (blue line in Fig. 6.1) the signal would have to travel the 5.5 km distance from UM to DM1 in about 7 h, corresponding to a speed of about 22 cm/s. Both estimated propagation speeds were thus in reasonable agreement, which indicated a possible relation. The strong decrease in flow velocity observed successively at UM, D1 and DM1 might thus have been induced by a wave propagating along the channel at a speed of 17 to 22 cm/s in northward direction.

Another relation of the successive decrease in the flow velocity at UM, D1, and DM1 might be found to the pronounced velocity maxima observed in the following two tidal cycles in mooring-based velocity time-series (Section 5.1.1). The time frame covered by the yoyo-cast corresponded to the time of the first of three ‘sawtooth’ signals observed in mooring-based velocities at DM1 (Fig. 5.1, Section 5.1.1). The steep flank of velocity decrease at DM1, the ‘sawtooth signal’, thus corresponds to the decrease which was observed successively at UM, D1, and DM1, which was found to be consistent with a northward propagating wave with a speed of 17 to 22 cm/s. As the first sawtooth signal was thus probably propagating along the channel, the second and third sawtooth signal might have too. The mooring-based velocities revealed that the second and third sawtooth signals also were accompanied by a preceding maximum in flow velocities at UM much larger than expected from the TPXO barotropic tide (Fig. 5.1). The preceding maximum at UM occurred about 5 and 6 h before the maximum flow velocities at the downstream mooring were observed which is less than the 7 h offset observed for the first sawtooth signal described above. The offset of 5 and 6 h would require a propagation speed of 31 and 25 cm/s from UM to DM1 which is larger than the 17 to 22 cm/s which were found for the first sawtooth signal.

If the three sawtooth signals are viewed as resulting from a wave-train, the wave-train period (τ) would be 11 to 12.3 h which was slightly smaller than the M_2 semi-diurnal tidal period (Fig. 5.1). Using the relation for the phase speed of long gravity waves $c = \omega/k = \lambda/\tau$, with the wave frequency $\omega = 2\pi/\tau$, and the horizontal wavenumber $k = 2\pi/\lambda$, this period range can be related to a wavelength range of $\lambda = 8000 - 9000$ m using a propagation speed of 20 cm/s. This length scale corresponded to the distance between the upstream and downstream stations U3 – D3 or U3 – D4. If the speed range of 17 to 31 cm/s is used, than a wavelength

6 Signal Propagation

range of $\lambda = 7000 - 13000$ m is found. Both wavelength ranges were consistent with the wavelength range of long gravity waves.

The hypothesis of a northward propagating wave-train inducing the sawtooth signals might be supported by additionally considering the vertical wavenumber. The velocity anomaly indicated the sawtooth signal to influence not only the bottom boundary layer but at least the lower 600 m water column (Fig. 6.2). Using the dispersion relation for internal gravity waves a vertical wavenumber can be estimated for the observed ranges of wavelengths and periods. The dispersion relation for internal gravity waves in a rotating fluid following (Gill, 1982)

$$\omega = \sqrt{\frac{f^2 m^2 + N^2 (k^2 + l^2)}{k^2 + l^2 + m^2}}, \quad (6.1)$$

was used with the following parameter or parameter ranges: the Coriolis parameter f for 37.25° N, the buoyancy frequency $N = 1 \cdot 10^{-3}$ 1/s determined from CTD observations, the horizontal wavenumber range in along-channel direction $k = 2\pi/7000$ to $2\pi/13000$ 1/m, the horizontal wavenumber in across-channel direction $l = 0$ 1/m, and the vertical wavenumber $m = 2\pi/1000$ 1/m. Using $m = 2\pi/1000$ 1/m and the above estimated range for the horizontal wavenumber k , the period range $\tau = 2\pi/\omega$ was estimated as $\tau = 10$ to 15 h. This period range was in good agreement with the wave-train period of 11 to 12.3 h determined from the mooring-based velocity time-series (Fig. 5.1). A vertical wavelength of 1000 m was thus reasonable for the supposed wave-train and was consistent with the vertical extend on the signal indicated by the velocity anomaly distribution (Fig. 6.2).

In conclusion, internal waves with a period of 1.5 h (which is close to the buoyancy period) were indicated by isopycnal displacements and vertical velocities in the layer above the supercritical layer, while internal waves were largely suppressed in the supercritical layer (Section 1.4 and Thorpe (2010)). The sawtooth signals possibly were caused by an internal wave of about 7000 to 13000 m wavelength and a period of about 12 h which possibly was superimposed onto the tidal flow. Furthermore a propagating hydraulic jump would be consistent with the flow and density signature observed at the end of the yoyo-cast but no evidence could be found as the profiling stopped before the supposed hydraulic jump had passed the location.

6.2 Vertical Velocities and their High-Frequency Variability

Vertical velocities observed during the yoyo-cast downstream of the sill have been interpreted as a dense gravity current flowing down the lee slope by Thurnherr (2011). Froude Numbers computed in this thesis indicated the flow to be partly supercritical indicating a hydraulic jump downstream of the yoyo-cast location (Fig. 5.8). At the end of yoyo-cast, where Froude Numbers indicated sub-critical

6.2 Vertical Velocities and their High-Frequency Variability

Mooring	Vertical velocity [$\frac{\text{cm}}{\text{s}}$]		Maximum Upward velocity [$\frac{\text{cm}}{\text{s}}$]	Maximum Downward velocity [$\frac{\text{cm}}{\text{s}}$]
	mean	std		
UM	0.17	0.58	2.42	-2.02
DM1	-0.16	0.76	2.47	-3.58
DM2	-0.38	0.79	1.96	-2.63

Table 6.1: Vertical velocity average, standard deviation (std) and maximum upward and downward velocity of 6 min low-pass filtered time-series observed by the moored ADCPs. The error of the time-average was estimated by 0.12 cm/s for the downstream and 0.08 cm/s for the upstream mooring respectively (error estimates see Section 2.2).

flow vertical velocities were directed upwards (Fig. A.3, *Thurnherr* (2011)). This might indicate a hydraulic jump propagating towards the sill (Section 6.1). In comparison to the gravity current flowing down the lee slope a (propagating) hydraulic jump is expected to be associated with vertical velocity anomalies (Section 1.4). Investigating mooring-based vertical velocities thus might offer a possibility to find indications for upstream propagating hydraulic jumps. Furthermore, vertical velocity variability is expected to be elevated in a turbulent region downstream of a hydraulic jump (Section 1.4). Investigating the relation of along-channel and vertical velocities as well as their variabilities might thus provide further indications for the existence and location of a hydraulic jump. It is assessed whether any relation of high-frequency variability or propagating signals as e.g. propagating hydraulic jumps might be found to the magnitude of the along-channel velocity. Vertical movements of the moored instruments which would induce false vertical velocities have been neglected as pitch and roll angles were below 3.5° degrees and variations in pressure were below 1 dbar.

Upstream of the sill average upward velocities of 0.17 cm/s with a maximum of 2.42 cm/s were observed, while downstream of the sill average downward velocities of 0.38 cm/s were found with a maximum of 2.63 cm/s (Table 6.1). The upward velocities upstream of the sill indicated that water from below the sill depth might cross the sill i.e. that blocking of the upstream waters does not necessarily occur at the sill depth (Section 5.5). The downward velocities downstream of the sill were in good agreement with the findings by *Thurnherr* (2011) and were consistent with a gravity current flowing down the lee slope of the sill.

The mooring-based velocity time-series showed strong variability of vertical velocities but without a clear periodicity or relation to the along-channel flow or the TPXO barotropic tides (Fig. 6.3). A lagged correlation between the 3 h low-pass filtered vertical and along-channel velocities was performed using a maximum lag of 6 h. Only weak correlations were found (not shown) which are therefore not further discussed. The strong variability without a clear periodicity especially at the downstream moorings might be associated with turbulence which was found to

6.2 Vertical Velocities and their High-Frequency Variability

Correlation of std of high-pass filtered vertical velocity at mooring	Correlation coef. with 3 h low-pass filtered along-channel velocity
UM	0.49 (0.24)
DM1	0.73 (0.53)
DM2	-0.27 (0.07)

Table 6.2: Correlation coefficients R (and fraction of explained variance R^2 in parentheses) of blocks of 3 h std with 50 % overlap of 30 min high-pass filtered vertical velocity at each mooring location (Fig. 6.5) with the 3 h low-pass filtered observed along-channel velocity. Bold values are significant at a 95 % confidence level.

The correlation was largest at a lag of zero at the UM and at the DM1 mooring (Table 6.2 and Fig. 6.4) indicating strong variability in vertical velocities on time scales faster than internal waves during phases of large along-channel flow. The strong correlation at DM1 (Table 6.2) might be attributed to turbulence or to high frequency waves forced by a hydraulic jump. An undular or weak hydraulic jump (Section 1.4) which was found likely to be located upstream of DM1 (Sections 5.1.2 and 5.5) might induce such high-frequency variability and turbulence.

The origin of the correlation at the UM mooring is unclear. It might possibly be related to turbulence induced by near critical reflection of the semi-diurnal tide at the bottom which was found to be likely to occur at least upstream of the UM mooring (Section 4.1).

At the DM2 mooring the correlation was largest at a lag of 1.5 h but the correlation was negative (Table 6.2 and Fig. 6.4). This indicated that little high-frequency variability was observed after phases of strong along-channel flow. Little variability in vertical velocities would be expected in a supercritical flow regime where propagation of internal waves would be largely suppressed (Section 1.4 and (Thorpe, 2010)).

The absence of a positive correlation at the DM2 mooring indicated no simple, linear relationship of high-frequency variability of the vertical velocity and strong along-channel flow. Nevertheless variability on short time scales was observed (Fig. 6.3). A correlation would be expected only if propagating signals would be

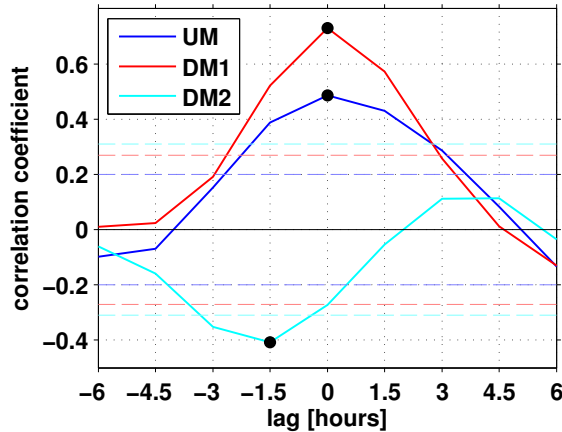


Figure 6.4: Lag correlation of blocks of 3 h std (with 50 % overlap) of 30 min high-pass filtered vertical velocities at each mooring (Fig. 6.5) with the corresponding 3 h low-pass filtered observed along-channel velocity. Black dots indicate the maxima which are significant at a 95 % confidence level. Corresponding confidence levels are indicated as dashed lines.

6 Signal Propagation

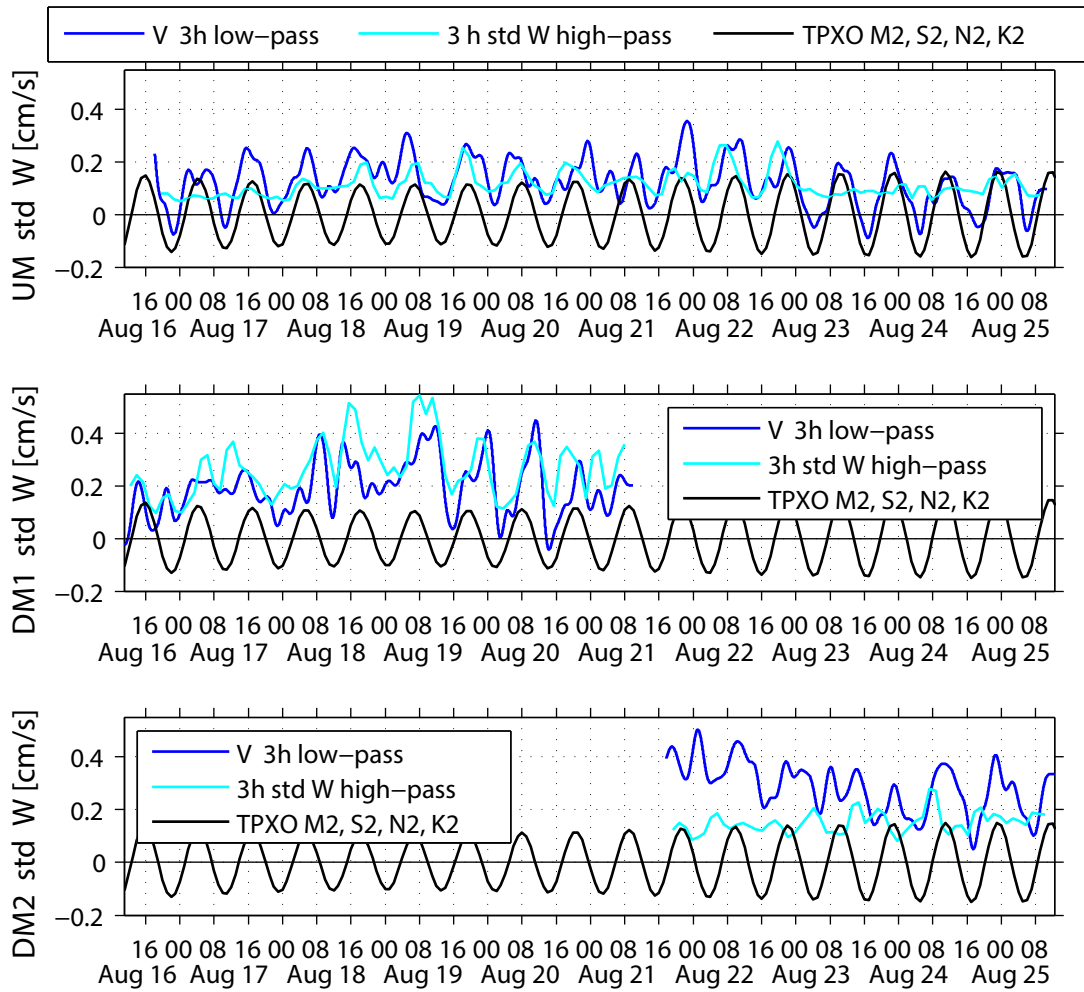


Figure 6.5: Time-series of blocks of 3 h std from 30 min high-pass filtered vertical velocities and 3 h low-pass filtered along-channel velocities from moorings UM (upper panel), DM1 (middle panel), and DM2 (lower panel). Along-channel velocities were scaled such that the y-axes applies only for vertical velocity std. The black line mark the M_2 -, S_2 -, N_2 -, and K_2 -tide from TPXO model.

confined to a clear phase in the tidal cycle. If an undular hydraulic jump is established downstream of DM2, which was found to be a likely scenario based on Froude Number analyses (Section 5.3.1), upstream propagation of internal waves would be possible during all phases of the tide and might only be weaker during high along-channel flow (Section 1.4). Furthermore, if propagating signals would be induced by a decaying hydraulic jump of any amplitude, the time lag of large along-channel flow and the observation of such a signal would depend on the position of the former jump in relation to the mooring where the signal will be observed. It is likely that the hydraulic jump does not always occur at the same location. In this case the correlation may be rather low. To find a correlation of along-channel flow and elevated variability in vertical velocities which might be

6.3 Upstream propagating Hydraulic Jump?

related to upstream propagating hydraulic jumps, the phase lag would have to be constant or at least similar during each tidal cycle. This was not apparent in this rather short time-series and no quantitative results can be drawn regarding propagating jumps. Nevertheless, single events have been found which indicate large upward velocities shortly after a maximum of the along-channel velocity. Such an event is investigated in the next paragraph (Section 6.3).

In conclusion, average upward velocities were found upstream of the sill while average downward velocities were found downstream of the sill. This indicated blocking of the along-channel flow to possibly occur not directly at but below the sill depth. No significant or only weak correlation was found between the vertical and along-channel velocities which possibly can be attributed to strong high-frequency variability. High-frequency variability was found to be correlated with strong along-channel flow at the DM1 mooring which was attributed to turbulence downstream of the sill. It might also be related to forced internal waves due to a hydraulic jump upstream of DM1. Why the high-frequency variability was elevated during phases of strong along-channel flow at UM is unclear. For the absence of a correlation of high-frequency variability and strong along-channel flow at the DM2 mooring two possible explanations were found. Firstly, if the high-frequency variability was associated with propagating hydraulic jumps during phases of relaxing tidal flow or with upstream propagating waves of an undular hydraulic jump, no clear phase relation would be expected. Secondly, if DM2 was temporarily located in the supercritical layer a correlation of weaker high-frequency variability with stronger along-channel flow would be expected.

6.3 Upstream propagating Hydraulic Jump?

An interesting phenomenon which has been observed in shallow waters are propagating hydraulic jumps or bores which are found during relaxing tidal flows (*Brandt et al.*, 1996, 1997; *Cummins et al.*, 2006; *Cummins and Armi*, 2010). They have also been shown in model studies by e.g. *Legg and Klymak* (2008). In the following it is tested whether the turbulent-density patch which was observed about 800 m downstream of the sill (Section 4.4.3) might have been a propagating hydraulic jump.

In a hydraulic jump, propagating or stationary, turbulence is expected to be associated with higher densities and upward velocities as water is displaced upward in the jump. If a hydraulic jump is established downstream of the sill in a phase of large along channel flow, this jump might propagate in upstream direction as the flow decreases. In such a setting, high mixing, denser water and upward velocities would be expected upstream of the position where the hydraulic jump was observed during strong flow velocities. To observe such a phenomenon, results from the different platforms used in this study have to be combined. This will be conducted in the following.

Apparently an undular or a weak hydraulic jump was located downstream of the

6 Signal Propagation

sill during strong flow velocity conditions, most likely between the mooring locations DM1 and DM2 (Section 5.3.1). An upstream propagating jump thus should be detected at the DM2 mooring located closer to the sill, south of DM1. To find a possible relation between the turbulent patch (Section 4.4.3) and the mooring-based along-channel and vertical velocity, the velocities observed during the time where the turbulent patch was observed were reviewed in more detail (Fig. 6.6). The turbulent patch was observed in the first hours of AUV Dive 8. The AUV started this dive at the southern end of the channel shortly before the minimum of the observed along-channel velocities was reached (upper panel Fig. 6.6). The AUV sampled along the channel at the track in the center of the channel (lower panel Fig. 6.6). The turbulent patch (Fig. 4.15) was observed about 800 m downstream of the sill, at the end of a segment sampled along constant pressure (whole segment indicated as orange dots in lower panel of Fig. 6.6). At the DM2 mooring weak along-channel flow of 0–3 cm/s was observed during the sampling time of the segment (marked orange in upper panel 6.6). The two lowered station measurements obtained shortly after the AUV deployment were carried out 1.6 km downstream of the sill close to the mooring position DM2. Station 33 was obtained at distance of about 500 m, while Station 34 was only 150 m away from the mooring DM2. Both profiles were classified as ebb-tide profiles (Section 5.3) and showed no indication for a hydraulic jump in the along- and across-channel distribution of the flow and density field (Sections 5.3.1 and 5.3.2). During the time of the two lowered measurements a period of upward velocities was observed at the mooring DM2 (marked by a black, dashed ellipse in middle panel Fig. 6.6) which thus cannot be related to a stationary hydraulic jump as no jump was present inferred from lowered measurements. As the upward velocities were observed during the minimum in along-channel flow, they could be related to a relaxing background flow field. Indications for a relaxing background field with denser water being found higher in the water column during phases of lower along-channel flow downstream of the sill were found from the tow-yo casts (Section 5.2.2). As the next period of upward velocities (marked by the a black, dashed ellipse in middle panel Fig. 6.6) was observed during stronger along-channel flow of about 8 to 10 cm/s, it can probably not be explained by the same mechanism of a relaxing background field.

Before the AUV observed the turbulent patch (end of first orange segment in Fig. 6.6), a short peak of upward (or less downward) velocities was observed at the mooring DM2 at about 15:30 UTC ('Peak 1', marked by black, solid ellipse in middle panel Fig. 6.6). The turbulent patch was observed at about 17:10 UTC downstream of the sill but 1.1 km upstream of the DM2 mooring. If Peak 1 was propagating in upstream direction with a speed of about 18 cm/s it would have reached the location of the turbulent patch at the time were the patch was observed and might thus be related to the turbulent patch. As the speed of a propagating hydraulic jump depends on the amount of decrease of the along-channel flow velocity as well as the up- and downstream flow conditions (*Çengel and Cimbala, 2006*) the speed cannot be estimated from the available observations in this study.

6.3 Upstream propagating Hydraulic Jump?

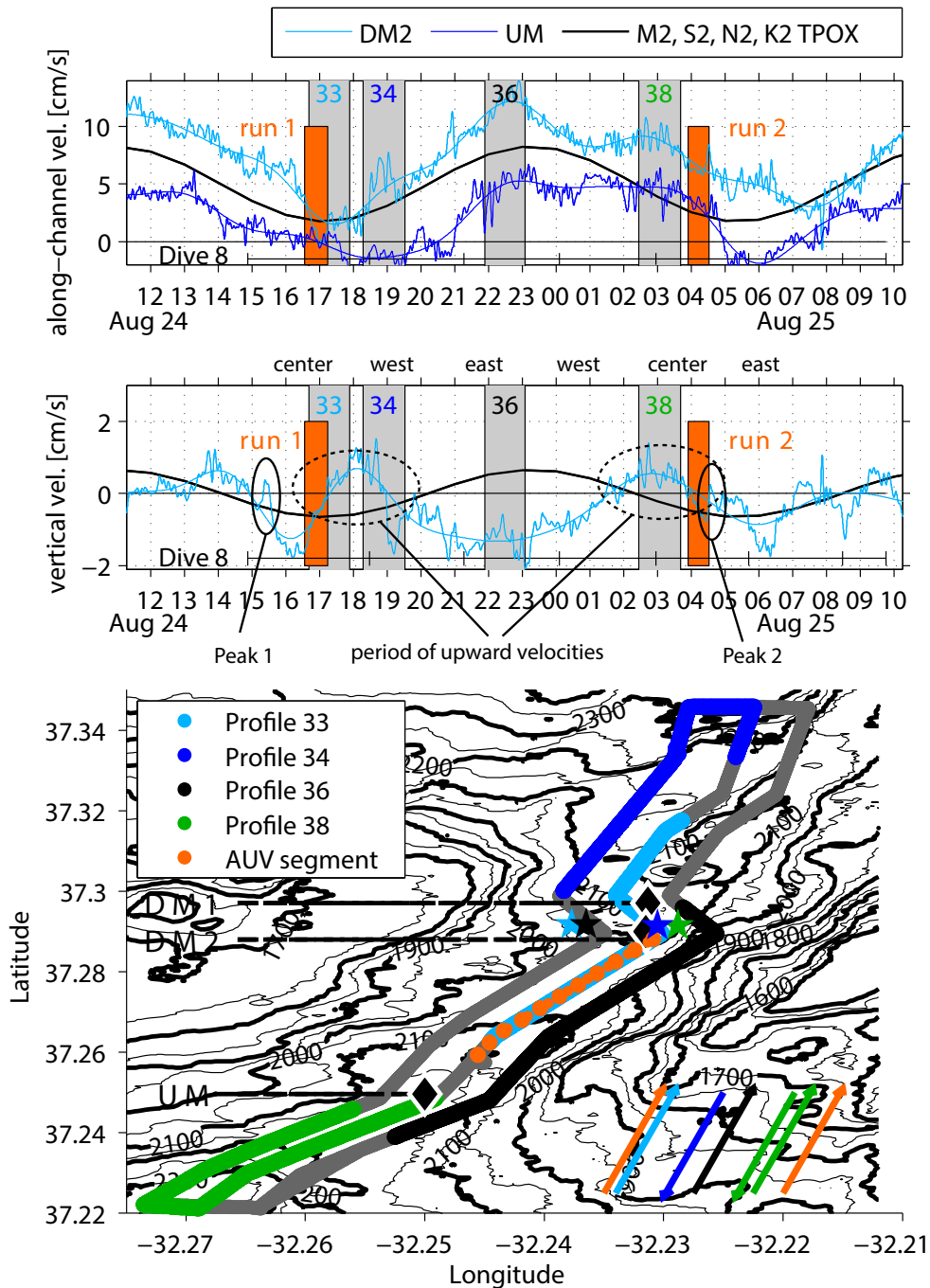


Figure 6.6: Along-channel (upper panel) and vertical velocity (middle panel) 6 min and 3 h low-pass filtered, obtained from moored instruments at DM2 and UM during AUV Dive 8. Gray bars and colored numbers indicating lowered measurements profile time and number. Orange marks the time frame (bars in upper two panels) and position (dots in lower panel) of the AUV run 1 and 2 shown in Figure 4.15. The gray line marks the track of Dive 8 (lower panel) with color indicating the time intervals and stars indicating the position of lowered measurements. Black diamonds indicate mooring position. Errors in lower left corner indicate heading of the AUV during color-coded segments. Vertical black bar in upper two panels marks time frame of the Dive 8 with vertical ticks indicating the end of each track in the ‘center’, at the ‘western’, or at the eastern edge, indicated above the middle panel.

6 Signal Propagation

The speed might e.g. be determined by in-situ measurements of isopycnal displacement.

In shallow water studies propagating hydraulic jumps haven been observed to disintegrate into waves. If the Peak 1 is treated as an upstream propagating internal wave and the propagation speed $c = 18 \text{ cm/s}$ estimated above is assumed to equal the phase speed for long gravity waves $c = \omega/k = \lambda/\tau$ with $\omega = 2\pi/\tau$ and $k = 2\pi/\lambda$, a wavelength can be estimated by assuming a certain frequency. If the buoyancy frequency $N = 1 \cdot 10^{-3} \text{ rad/s}$ is assumed as upper limit for the wave frequency, the lower limit for the wavelength can be estimated by $\lambda = 1100 \text{ m}$. If the length of the turbulent patch, which was about 500 m (Section 4.4.3), is interpreted as the length scale of the wave, then the estimated wavelength of 1100 m is too large. Thus, the approximation with a long gravity waves is probably not reasonable.

The waves resulting from the disintegration of hydraulic jumps in shallow waters have been described as non-linear wave trains (solitons or bores) by e.g. *Brandt et al.* (1996, 1997); *Cummins et al.* (2006); *Cummins and Armi* (2010). For solitons, the propagation speed is proportional to the amplitude of the soliton *Brandt et al.* (1996) and the displacement induced by a soliton is directed to the deeper layer (*Apel et al.*, 2006). Following *Apel et al.* (2006) the propagation speed u of a soliton of the amplitude η propagating along the interface of a thin layer (h_1) underlying an infinitely deep layer ($h_2 \rightarrow \infty$) can be described as

$$u = c + \frac{\alpha\eta}{4}, \quad \text{with} \quad \alpha = -\frac{3c}{2h_1}, \quad \text{and} \quad c = \sqrt{g'h_1}, \quad (6.2)$$

where g' is the reduced gravity. The width Δ of the soliton can be estimated using (*Apel et al.*, 2006)

$$\Delta = \frac{8\beta}{\alpha\eta}, \quad \text{with} \quad \beta = \frac{ch_1 \rho_2}{2 \rho_1}, \quad (6.3)$$

where ρ_2 and ρ_1 are the density of the upper and lower layer, respectively. Using $g' = 1.7 \cdot 10^{-4} \text{ m/s}^2$ and $\rho_2/\rho_1 = 1.0005$ determined from lowered observations, the propagation speed u and the width Δ can be calculated for a certain soliton amplitude η and layer depth h_1 . As it is difficult to estimate the layer depth and the amplitude from the observations available, the speed u and the width Δ were estimated for a range of parameters which might be applicable here. The upward displacement of isopycnals associated with the hydraulic jump downstream of the sill was observed to be in the range of 50 m to 100 m (Fig. 4.6 and 5.17) which was used as range for the soliton amplitude. The thickness of the lower layer was approximately 100 to 150 m (Fig. 4.6 and 5.17). Using this parameter range, the corresponding range of propagation speeds u and widths Δ were estimated (Table 6.3). If the length of 500 m of the turbulent patch is interpreted as the width of the supposed soliton, than the parameter combination of $\eta = 80 \text{ m}$ and $h_1 = 120 \text{ m}$ best reproduce the observed values of the propagation speed $u = 18 \text{ cm/s}$ and the width $\Delta = 500 \text{ m}$ of the supposed soliton. Thus, the Peak 1 and the turbulent patch were consistent with an upstream propagating soliton.

η [m]	50	60	70	80	90	100
$v(\eta, h_1 = 100)$ [cm/s]	15	16	16	17	17	18
$\Delta(\eta, h_1 = 100)$ [m]	534	444	382	334	296	266
$v(h_1 = 110)$ [cm/s]	16	16	17	17	18	18
$\Delta(\eta, h_1 = 110)$ [m]	645	538	462	404	358	322
$v(\eta, h_1 = 120)$ [cm/s]	17	17	17	18	18	19
$\Delta(\eta, h_1 = 120)$ [m]	768	640	548	480	426	384
$v(\eta, h_1 = 130)$ [cm/s]	17	17	18	18	19	19
$\Delta(\eta, h_1 = 130)$ [m]	902	752	644	564	500	450

Table 6.3: Propagation speed u and width Δ of a soliton estimated for the given parameters η – the soliton amplitude and h_1 – the layer depth. Values were computed using Equations 6.2 and 6.3.

During the second run of the AUV in the center of the channel decreasing along-channel flow of 6 to 7 cm/s was observed at the DM2 mooring. Dissipation rates and the density range encountered during the second run were much lower compared to the first run (Section 4.4.3). If there was a propagating hydraulic jump during the first run, there was no comparable phenomenon during the second run. However, there was a similar peak in vertical velocity observed at around 4:30 UTC during the end of the second run which might have led to a similar phenomenon as Peak 1. As the AUV was not sampling the center of the channel again, this could not be verified.

From the estimations above it might be concluded that the turbulent patch and the Peak 1 signal were consistent with an upstream propagating hydraulic jump possibly disintegrating into a soliton propagating at a speed of about 18 cm/s, having an amplitude of about 80 m. A propagating soliton or hydraulic jump might be a possible explanation for the observed phenomenon of the turbulent patch which was shown unlikely to be explained by a turbulent overturn based on the Ozmidov and Thorpe scale estimations from nearby lowered observation (Section 4.4.3, *Ozmidov (1965); Thorpe (2005)*). If the turbulent patch is interpreted as a propagating hydraulic jump or soliton this would be the first observation of such a signal in the deep ocean in water depth of about 2000 m.

6.4 Summary and Discussion

The analyses of along-channel and vertical velocities revealed the presence of internal waves above the layer of supercritical flow having a frequency close to the buoyancy frequency (Section 6.1). In the supercritical layer internal waves were found to be largely suppressed as expected (Section 1.4 and *Thorpe (2010)*). The

6 Signal Propagation

rapid decrease of the flow velocities in the lower layer and the southward velocity anomaly in the upper layer, in combination with the phenomena of the ‘sawtooth’ signals (Section 5.1.1) were shown to be consistent with an internal wave-train superimposed onto the tidal flow propagating from south to north (Section 6.1). This wave-train was estimated to have a wavelength range of about 7000 to 13000 m and a period of about 12 h. After the rapid decrease of the flow velocities referred to as the first sawtooth signal, isopycnals were displaced upward consistent with upward vertical velocities possibly indicating an upstream propagating hydraulic jump (Section 6.1).

High-frequency variability of the vertical velocities at DM1 on time-scales above the buoyancy frequency was shown to be correlated with strong along-channel flow (Section 6.2). This might be attributed to hydraulic jump induced forced internal waves and turbulence. This further supported the DM1 mooring to be located downstream of the hydraulic jump. As no zero-lag correlation was found at DM2 closer to the sill, the DM2 mooring probably was located temporarily in the supercritical flow upstream of the hydraulic jump where less variability would be expected (Section 1.4 and *Thorpe* (2010)).

The considerations regarding the propagation of the confined peak of upward vertical velocities referred to as Peak 1 during a phase of weak along-channel flow in combination with the turbulent patch (Section 4.4.3) were consistent with an upstream propagating hydraulic jump possibly disintegrating into a soliton (Section 6.3). If this feature is interpreted as an upstream propagating hydraulic jump or soliton this would provide a possibility to induce mixing closer to the sill, upstream of the location where the hydraulic jump was observed during strong flow velocity conditions (Sections 4.2.2 and 5.3.1). It is unclear how far such a feature might propagate. This particular feature was observed downstream of the sill and thus cannot explain the elevated mixing rates which were reported upstream of the sill by *St. Laurent and Thurnherr* (2007). For the quantification of processes associated with upstream propagating hydraulic jumps or solitons more spatially and temporally high resolution observations would be needed covering several tidal cycles.

As propagating hydraulic jumps or solitons have been observed only in shallow straits in water above 1000 m depth, this might be the first observation of such a signal in a deep ocean channel in water depth of about 2000 m.

7 Synthesis

Mixing and buoyancy gain in the deep ocean is directly linked to the global ocean energy budget as it fuels the upwelling of deep water masses to close the MOC (Munk, 1966; Bryden and Imawaki, 2001; Kanzow *et al.*, 2007). Several studies showed that elevated mixing which was previously interpreted to occur above rough topography (Polzin *et al.*, 1997) is actually found mainly inside deep ocean channels (Thurnherr and Richards, 2001; Thurnherr *et al.*, 2005; Thurnherr, 2006; St. Laurent and Thurnherr, 2007; Alford *et al.*, 2013). Inside the studied channels mostly unidirectional along-channel flow down the density gradient was found. Elevated mixing was shown to be associated with energetic, often supercritical flow across sills blocking the along-channel flow (Thurnherr *et al.*, 2005; Alford *et al.*, 2013). This suggested the buoyancy flux to depend heavily on the local flow conditions and the bottom topography arrangement. Thurnherr *et al.* (2005) estimate that about 1000 channels exist on slow spreading ridges with $O(10^4)$ sills. If they all show similar flow and hydrographic conditions, elevated mixing might be present in all of them. In this case the buoyancy flux in these channels might be even important for the global ocean energy budget.

St. Laurent and Thurnherr (2007) estimate that water mass conversion occurring in deep ocean channels at the MAR in the greater North Atlantic equals that occurring at the Romanche Fracture Zone, a major deep ocean Fracture Zone connecting the Brazil and the Sierra Leone basin. However, the physical mechanisms leading to mixing in the deep ocean channels at the MAR are currently not fully understood. The study by St. Laurent and Thurnherr (2007) focused on a deep ocean channel with unidirectional flow across a sill where they found indications for a hydraulic jump downstream of the sill but they did not find a downstream maximum in the dissipation rate which is expected for such a setting (Alford *et al.*, 2013). This thesis returned to the question of the distribution of the mixing along the channel as it is the key to understanding the driving mechanisms of the mixing in such deep ocean channels.

The channel investigated in this thesis was the eastern channel of the Lucky Strike segment located in the subtropical north-Atlantic near 37° N, the same channel as investigated by St. Laurent and Thurnherr (2007). To be able to resolve the mixing along the channels a new platform-instrument combination of deep diving AUV and microstructure probe was used. A new processing software for the new instrument combination was developed for inferring the dissipation rate of turbulent kinetic energy from velocity shear observations (Section 3).

In contrast to the study by St. Laurent and Thurnherr (2007), the dissipation of turbulent kinetic energy was found to be distributed asymmetrically along the

7 Synthesis

channel, across the sill, with the maximum being located 1 to 4 km downstream of the sill (Section 4.1). Single events of elevated mixing were found also upstream. They were consistent with near critical reflection of the semi-diurnal tide at the bottom topography leading to strong mixing (Section 4.1.1).

The average flow in the eastern channel of the Lucky Strike segment was found to be directed along the channel to the north as expected from former studies (*Keller et al.*, 1975; *Fehn et al.*, 1977; *Thurnherr and Richards*, 2001; *Thurnherr et al.*, 2002; *Thurnherr*, 2006; *St. Laurent and Thurnherr*, 2007; *Thurnherr et al.*, 2008). This supported the hypothesis of a long term persistent rift valley circulation of along valley flow which was introduced by *Keller et al.* (1975) and further characterized by *Thurnherr et al.* (2002, 2008). The along-valley flow was observed to be partly blocked by sills and the flow across these sills was found to be accompanied by strong density gradients (Section 1.3, *Thurnherr et al.* (2002, 2008)). This thesis confirmed the indications for a hydraulic jump downstream of such a sill reported by *St. Laurent and Thurnherr* (2007) which induces strong mixing downstream (Section 4.2). A sketch illustrating the distribution of the flow, the density, and the mixing was developed shown in Figure 4.17.

In this thesis it was shown that the average northward along-channel flow was superimposed by strong semi-diurnal tidal variability causing the flow to be periodically enhanced (Section 5.1). Semi-diurnal tidal variability south of the Lucky Strike segment was already reported by *Keller et al.* (1975). In this thesis the tidal variability was shown to periodically force supercritical flow down the lee slope of the sill inducing a transient hydraulic jump during phases of strong flow velocities (Section 5.3.1). Sketches illustrating the two cases of strong and weak along-channel flow were developed shown in Figures 5.25 and 5.27. The hydraulic jump's amplitude was most likely in the range of an undular or a weak hydraulic jump (Section 1.4). In the case of an undular hydraulic jump, only little of the jump's energy is dissipated locally while a large fraction is radiated downstream by the undular waves (Section 1.4 and *Thorpe* (2010)). This downstream radiation might induce turbulence further downstream, possibly outside of the range sampled in the course of this study. Furthermore, upstream propagation of internal waves would be possible in the case of an undular hydraulic jump which would be suppressed in the case of a weak hydraulic jump where the critical Froude Number F_c would be exceeded (Section 1.4). In the case of a weak hydraulic jump a larger fraction of the jumps energy would be dissipated at the location of the jump compared to the case of an undular jump. A sketch illustrating the case of an undular and a weak hydraulic jump is shown in Figure 5.26. As internal waves were found to be largely suppressed in the layer of supercritical flow in one tidal cycle, the hydraulic jump probably was a weak hydraulic jump, at least during that particular tidal cycle (Section 6.1).

The hydraulic jump was found likely to be located between the two downstream moorings DM1 and DM2. This interpretation was based on the analyses of the variability found in mooring-based along-channel and vertical velocities as well as in temperature time-series (Sections 5.1.1, 5.1.2, and 6.2). The analyses indi-

cated the DM2 mooring to be located in the area where the flow was temporarily supercritical, i.e. upstream of the hydraulic jump, while it indicated the DM1 mooring to be located in the turbulent area downstream of the hydraulic jump. The exact location of the hydraulic jump in different tidal cycles is expected to vary as the magnitude of maximum flow was found to vary between different tidal cycles (Section 5.1.1, *Çengel and Cimbala (2006)*). Furthermore, the location of the jump might vary in one tidal cycle when the magnitude of the flow varies. In the case of decreasing flow the hydraulic jump is expected to propagate upstream as was observed in shallow water and model studies (*Brandt et al., 1996, 1997; Cummins et al., 2006; Legg and Klymak, 2008; Cummins and Armi, 2010*). In this thesis one event was found consistent with an upstream propagating hydraulic jump possibly disintegrating into a soliton (Section 6.3). This would provide a mechanism to induce mixing events closer to the sill or even upstream of the sill and might be the first observation of a propagating hydraulic jump or soliton in the deep ocean in water depth of about 2000 m. Despite this possibility to induce mixing also upstream of the sill, the mixing was shown to be distributed asymmetrically across the sill indicating the downstream mixing to exceed that induced by possibly upstream propagating signals (Section 4.1). Nevertheless, an upstream propagating hydraulic jump might be an explanation for the elevated mixing observed by *St. Laurent and Thurnherr (2007)* upstream of the sill. As their survey consisted of only a few profiles, they might, by chance, have captured an upstream propagating signal. More spatially and temporally high resolution observations covering several tidal cycles would be needed for the quantification of such processes possibly inducing mixing upstream of the sill.

Although the downstream mixing rates were shown to exceed the upstream mixing it was not possible to quantify the evolution of the mixing in the tidal cycle due to little temporal coverage of the microstructure velocity shear observations (Sections 4.1 and 5.4). The dissipation rates showed a downstream maximum also during periods of comparably weak along-channel flow. From this observation it might be speculated that already relatively weak flow across the sills causes a downstream mixing maximum. As shear instabilities were shown to be unlikely to occur, the question remains what physical process would induce this mixing during phases without a hydraulic jump. In order to answer this question simultaneous observations of the flow regime and the mixing distribution would be needed. Furthermore, indications for stronger mixing were observed during periods of stronger flow velocities (Section 5.4). This might indicate the mixing to be periodically amplified by the tidal flow. In this case, the mixing inside deep ocean channels downstream of sills would exhibit the same variability as the tidal flow itself. The amount and location of mixing would depend heavily on the topographic conditions, the amplitude of the mean flow, the tidally induced variability and the presence and strength of hydraulic jumps. High resolution model studies with realistic topographic and flow conditions found in deep ocean channels in conjunction with further observations are needed for quantification of this processes.

7 Synthesis

The quantification of these processes is needed to enable modelers to find a good parametrization for mixing in the deep ocean for e.g. climate models.

As this thesis was focusing mainly on the physical processes controlling the mixing, no new estimations regarding the amount of water mass conversion were attempted. As the magnitude of the diffusivities as well as the density gradient estimated in this thesis were in good agreement with those estimated by *St. Laurent and Thurnherr* (2007) (Section 4.3.1) the same buoyancy flux is expected. *St. Laurent and Thurnherr* (2007) estimated the buoyancy flux occurring in a 2° stretch of MAR rift valley in the area of the Lucky Strike segment to equal a tenth of the buoyancy flux occurring at RFZ.

Returning to the scientific-technological tasks that were addressed in this thesis (see introduction Section 1.2) it can be reported that

- a new processing software for the MR-AUV system was successfully developed. It uses a filter to reduce the noise induced by the AUV vibrations. The processing software was optimized for the use on AUV *Abyss* but is expected to be easily adaptable for the processing of data sets obtained by other similar AUVs.
- AUV based microstructure measurements are suitable for dissipation rate observations in the deep ocean in the vicinity of complex topography. This widens the measurement range for horizontally profiling techniques to areas where free-falling and lowered measurements are inefficient, time-consuming and (partly) lack the possibility to sample exactly at pre-defined positions which might be crucial for understanding flow-topography interaction.

The main scientific questions addressed by this thesis (repeat in italic letter) can now be answered.

- *Is the mixing distributed uniformly along the channel with respect to the position of the sill?*

No. The mixing is distributed non-uniformly along the channel with respect to the position of the sill. The downstream average dissipation rates were found to exceed the upstream values by at least one order of magnitude. This pattern was found to be consistent with the average flow along the channel across the sill.

- *What underlying physical processes control the mixing inside the deep ocean channel?*

Supercritical flow and the transition to sub-critical flow – the hydraulic jump – were identified as the main source for the elevated mixing downstream of the sill. Shear instabilities were found to be unlikely to occur.

- *Do tides influence the flow, density and mixing distribution throughout the channel?*

Yes. The semi-diurnal tides were found to strongly modulate the along-channel flow velocities. The average along-channel flow of about 8 cm/s varied between weak return flow of less than 5 cm/s up to more than 20 cm/s in along-channel direction. This variability was found to strongly affect the processes leading to mixing. Supercritical flow and the associated hydraulic jump were found only during strong flow velocity conditions. This affected the density distribution as a hydraulic jump is associated to upward displacement of isopycnals which was absent during weak flow velocity conditions. It is expected that also the distribution and magnitude of the mixing are affected by the tidal variability but this could not be shown due to limited temporal data coverage of the dissipation rate observations.

- *Is there evidence for internal waves and/or hydraulic jumps?*

Yes. Hydraulic jumps were observed during strong flow velocity conditions. Internal waves were found to be largely suppressed in the supercritical flow regime. Above the layer of supercritical and during phases of sub-critical flow indications for internal waves were found. There were indications for internal waves close to the buoyancy frequency as well as on longer time scales up to the semi-diurnal tidal frequency. On time-scales of inertial waves only low energies were found which was attributed to the narrow channel and the proximity to the sea floor.

- *Is there evidence for upstream propagating signals which could induce mixing at the sill or further upstream?*

Yes. There were indications for upstream propagating hydraulic jumps during phases of decreasing along-channel flow. One event was observed which was consistent with an upstream propagating hydraulic jump or a soliton inducing strong mixing close to the sill, upstream of the location where the hydraulic jump was found during strong flow velocity conditions. This might be the first observations of a soliton in the deep ocean.

The results summarized above were obtained in the eastern channel of the Lucky Strike segment and are thus only validated there. However, as several studies

7 Synthesis

reported comparable flow, density and mixing distributions in a comparable topographic environment (*Ledwell et al.*, 2000; *Thurnherr and Speer*, 2003; *Thurnherr et al.*, 2005; *MacKinnon et al.*, 2008) the fundamental physical mechanisms identified in this thesis are expected to be applicable to many other channels with a blocking sill showing similar flow and density distributions.

To address the open questions such as

- the dependence of the amount and location of turbulent mixing on the flow and topography conditions,
- the characterization of upstream propagating hydraulic jumps as well as their contribution to mixing, or
- the origin of the longterm variability found in deep ocean channels (e.g. *Thurnherr et al.* (2005)),

more research is needed. For a detailed understanding of the sill related processes, high resolution model studies are needed. Such studies would benefit from further high-resolution measurement campaigns especially involving AUV(s). These studies should be designed to cover several tidal cycles to be able to investigate turbulent mixing in dependence on the tidal phase. To characterize the longterm variability future studies need to cover even longer time-scales of several months or years. The study currently conducted in a rift flank canyon on the MAR near 22° S by *Andreas M. Thurnherr* and others at the *Lamont-Doherty Earth Observatory* will provide further exiting insight into these questions.

A Additional material

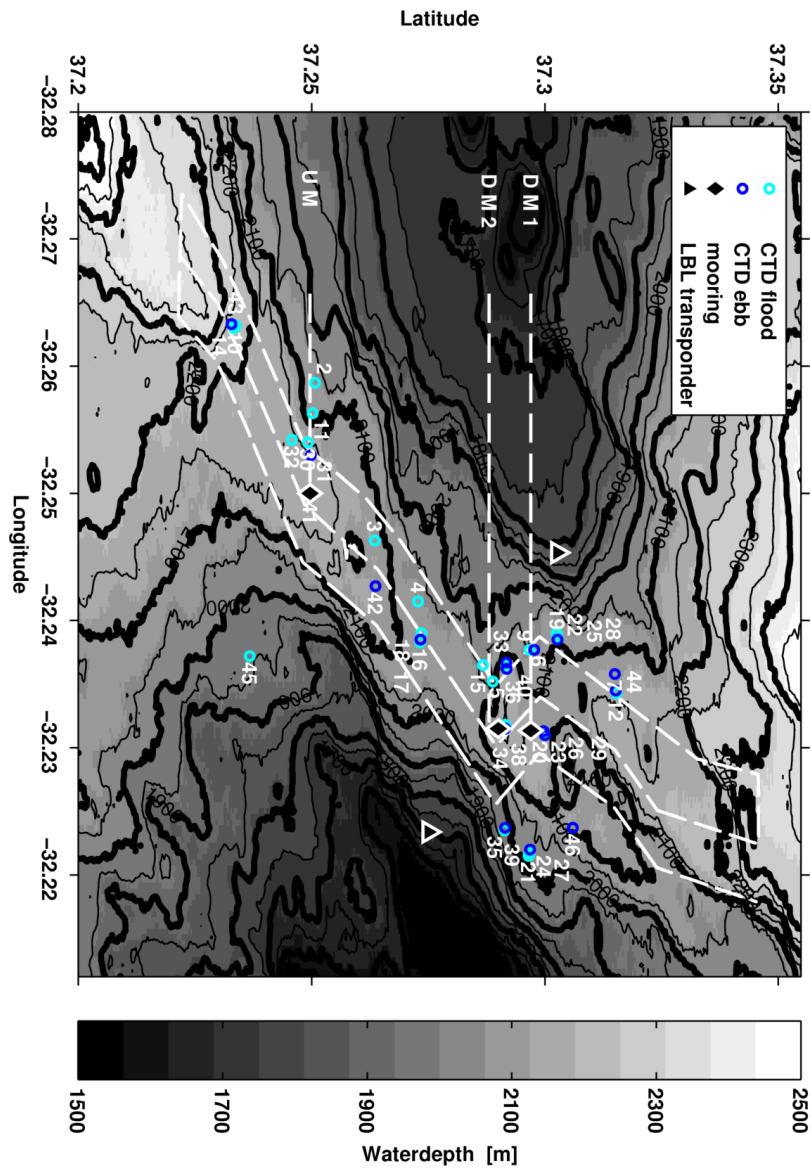


Figure A.1: Topography of the eastern channel of the Lucky Strike segment. Locations and station numbers of all shipboard, lowered CTD/LADCP measurements color coded according to the tidal-phase dependent sorting described in Section 5.1. White dashed line indicates the AUV Track of Dive 8.

A Additional material

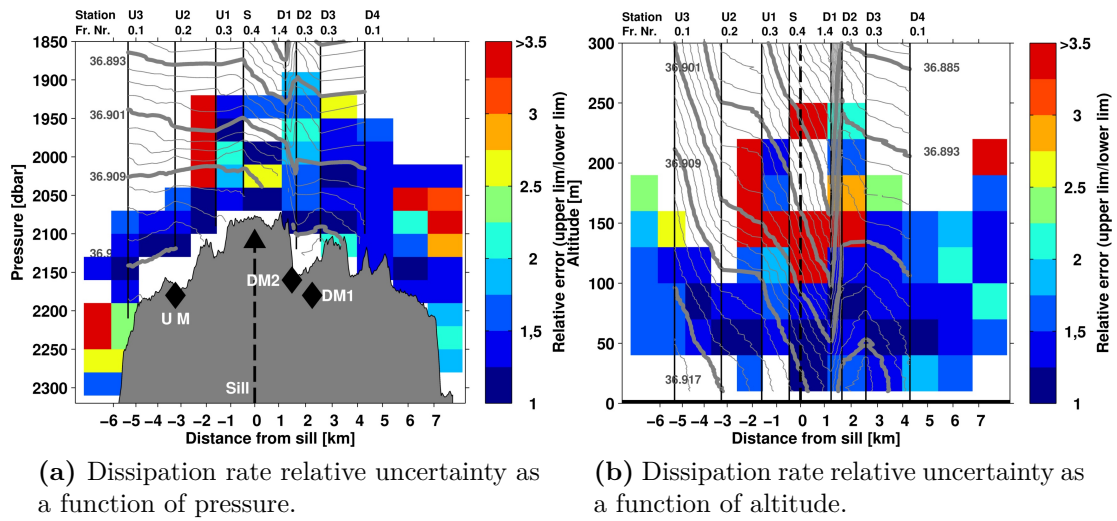


Figure A.2: The uncertainty was estimated from individual ϵ estimates using the bootstrap method with 1000 ensembles (*Efron, 1979*). The stations are given at the top of each panel together with the respective Froude Number estimated for the average flow state. Vertical lines mark the latitude of each station. Contour lines denote potential density (spacing $\Delta\sigma_2 = 0.002 \text{ kg/m}^3$).

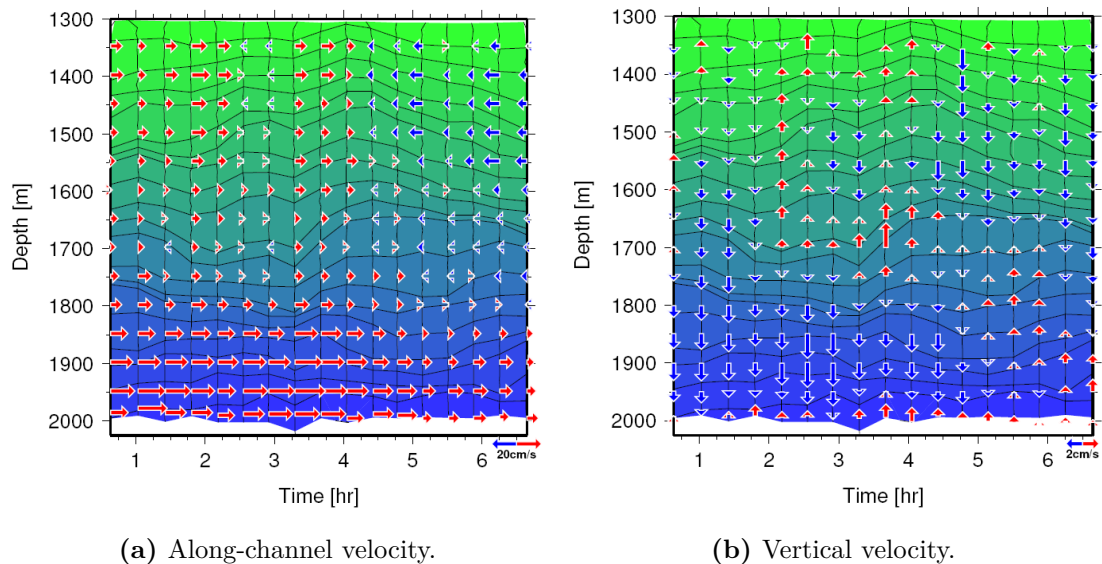
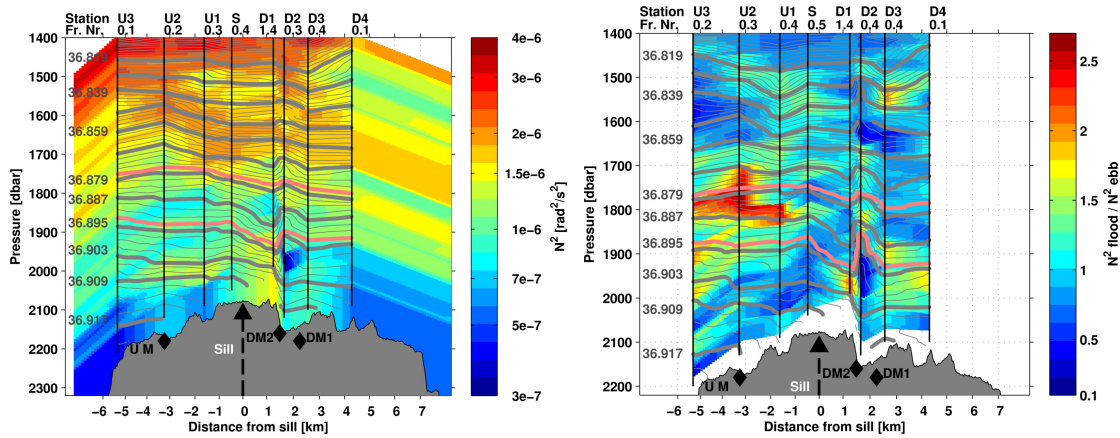


Figure A.3: Potential density (shading and contours) and LADCP-derived velocities (arrows) from the CTD/LADCP yo-yo cast by *Thurnherr (2011)*. Panel a: along-channel velocities, panel b: vertical velocities. Note the different velocity scales for the two panels.



(a) Buoyancy frequency along the channel from station averaged lowered CTD profiles computed over 50 m thick layers.

(b) Buoyancy frequency during flood state divided by buoyancy frequency during ebb state from station averaged lowered CTD profiles computed over 50 m thick layers.

Figure A.4: Both panels: The respective stations are given at the top of each panel together with the Froude Numbers estimated for the average flow state. Vertical lines mark the latitude of each station. Contour lines denote potential density with a spacing of $\Delta\sigma_2 = 0.002 \text{ kg/m}^3$.

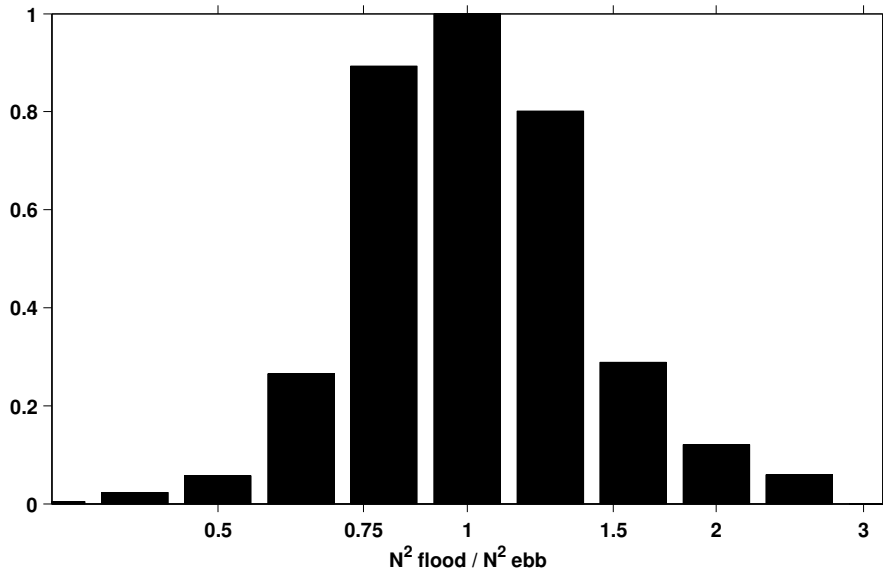


Figure A.5: Histogram of the buoyancy frequency during flood state divided by buoyancy frequency during ebb state from station averaged lowered CTD profiles computed over 50 m thick layers. X -axis is shown logarithmic.

A Additional material

Group	Latitude [° N]	Longitude [° W]	Station #		Comment
			flood	ebb	
U3	37.233	32.263	10, 14	43	Upstream 3
U2	37.249	32.254	2, 11, 30, 32, 41	31	Upstream 2
- e	37.237	32.237	45		east
U1	37.264	32.245	3,	42	Upstream 1
S	37.273	32.239	4, 16, 18	17	Sill
D1	37.288	32.236	5, 15		Downstream 1
D2	37.293	32.233			Downstream 2
- w	37.294	32.237	36	33, 40	west
- c	37.292	32.232	38	34	center
- e	37.291	32.224	35	39	east
D3	37.300	32.231			Downstream 3
- w	37.303	32.239	9, 22, 28	6, 19, 25	west
- c	37.230	32.231	23, 29	20, 26	center
- e	37.299	32.222	21, 27	24, 46	east
D4	37.315	32.235	12,	7, 44	Downstream 4
western channel			47 - 51		

Table A.1: Group- and individual-stations names and positions of shipboard low-ered CTD and LADCP measurements.

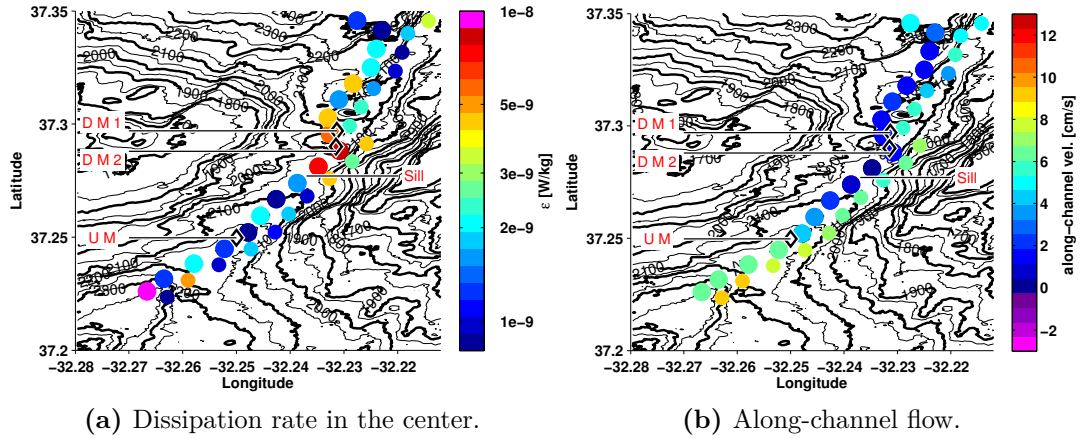


Figure A.6: Dissipation rate 10 min average observed on the same track in the center of the channel (a) and 10 min averaged flow velocity (b) observed at mooring DM2, interpolated onto the same coordinates as AUV measurements. Hence the color-indicated flow speed was observed downstream of the sill during the time as the AUV was sampling at the indicated positions. The first track is plotted at the sampling location while the second track is plotted with smaller dots displaced to the east by 0.005° . Diamonds show the positions of the moorings DM1, DM2, and UM.

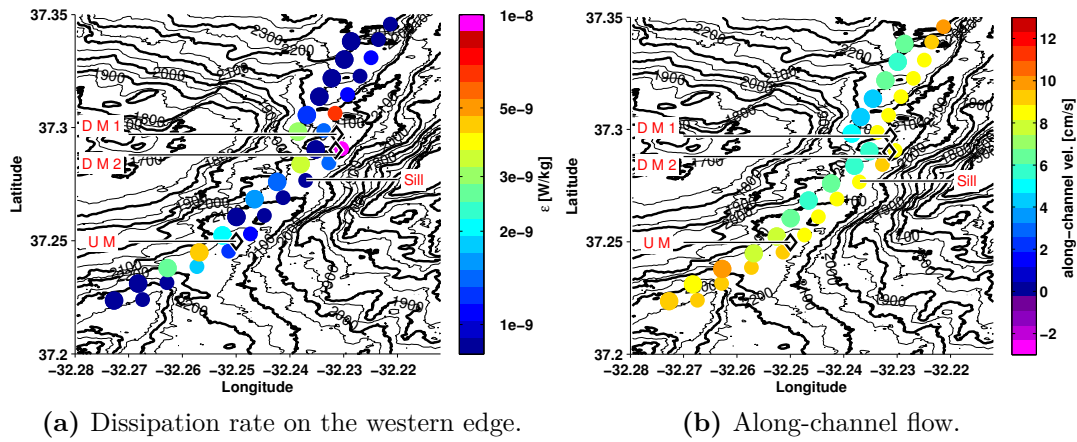


Figure A.7: Dissipation rate 10 min average observed on the same track at the western edge of the channel (a) and 10 min averaged flow velocity (b) observed at mooring DM2, interpolated onto the same coordinates as AUV measurements. Hence the color-indicated flow speed was observed downstream of the sill during the time as the AUV was sampling at the indicated positions. The first track is plotted at the sampling location while the second track is plotted with smaller dots displaced to the east by 0.005° . Diamonds show the positions of the moorings DM1, DM2, and UM.

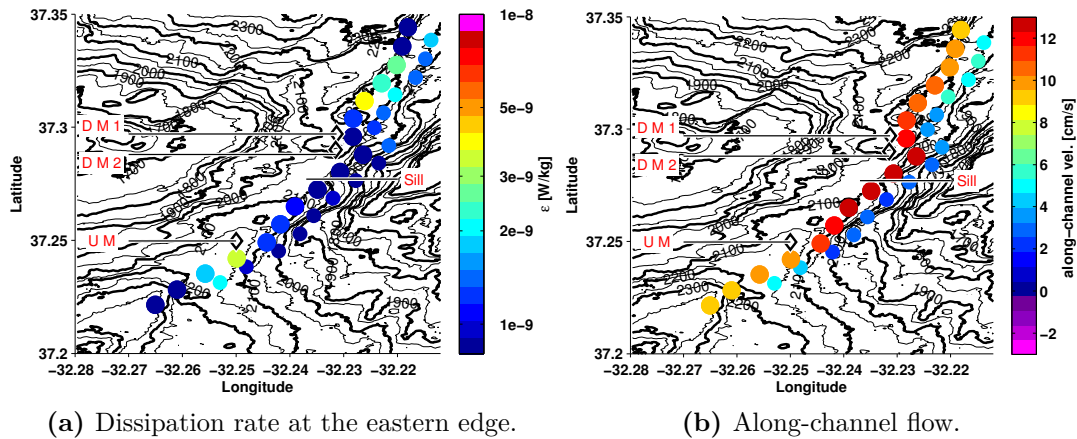


Figure A.8: Dissipation rate 10 min average observed on the same track at the eastern edge of the channel (a) and 10 min averaged flow velocity (b) observed at mooring DM2, interpolated onto the same coordinates as AUV measurements. Hence the color-indicated flow speed was observed downstream of the sill during the time as the AUV was sampling at the indicated positions. The first track is plotted at the sampling location while the second track is plotted with smaller dots displaced to the east by 0.005° . Diamonds show the positions of the moorings DM1, DM2, and UM.

References

- Alford, M. H., J. B. Girton, G. Voet, G. S. Carter, J. B. Mickett, and J. M. Klymak, Turbulent mixing and hydraulic control of abyssal water in the samoan passage, *Geophysical Research Letters*, 40(17), 4668–4674, 2013.
- Apel, J. R., L. A. Ostrovsky, Y. A. Stepanyants, and J. F. Lynch, Internal solitons in the ocean, *Woods Hole Oceanographic Institution, Technical Report*, 2006.
- Batchelor, G. K., Small-scale variation of convected quantities like temperature in turbulent fluid part 1. general discussion and the case of small conductivity, *Journal of Fluid Mechanics*, 5(01), 113–133, 1959.
- Blackman, R. B., and J. W. Tukey, The measurement of power spectra from the point of view of communications engineering — part ii, *Bell System Technical Journal*, 37(2), 485–569, 1958.
- Boyd, T., M. Inall, E. Dumont, and C. Griffiths, Auv observations of mixing in the tidal outflow from a scottish sea loch, in *Autonomous Underwater Vehicles (AUV)*, 2010 IEEE/OES, pp. 1–9.
- Brandt, P., W. Alpers, and J. O. Backhaus, Study of the generation and propagation of internal waves in the strait of gibraltar using a numerical model and synthetic aperture radar images of the european ers 1 satellite, *Journal of Geophysical Research: Oceans*, 101(C6), 14,237–14,252, 1996.
- Brandt, P., A. Rubino, W. Alpers, and J. O. Backhaus, Internal waves in the strait of messina studied by a numerical model and synthetic aperture radar images from the ers 1/2 satellites, *Journal of Physical Oceanography*, 27(5), 648–663, 1997.
- Bryden, H. L., and S. Imawaki, Ocean heat transport, in ocean circulation and climate, *Edited by G. Siedler, J. Church and J. Gould, Academic Press*, pp. 455–474, 2001.
- Bryden, H. L., and A. J. G. Nurser, Effects of strait mixing on ocean stratification, *Journal of Physical Oceanography*, 33(8), 1870–1872, 2003.
- Cairns, J. L., and G. O. Williams, Internal wave observations from a midwater float, 2, *Journal of Geophysical Research*, 81(12), 1943–1950, 1976.
- Chow, V. T., *Open-Channel Hydraulics*, McGraw-Hill, New York, 1959.

References

- Cummins, P. F., and L. Armi, Upstream internal jumps in stratified sill flow: Observations of formation, evolution, and release, *Journal of Physical Oceanography*, 40(6), 1419–1426, 2010.
- Cummins, P. F., L. Armi, and S. Vagle, Upstream internal hydraulic jumps, *Journal of Physical Oceanography*, 36(5), 753–769, 2006.
- Curry, R., B. Dickson, and I. Yashayaev, A change in the freshwater balance of the atlantic ocean over the past four decades, *Nature*, 426(6968), 826–829, 10.1038/nature02206, 2003.
- Dale, A. C., and M. E. Inall, Tidal mixing processes amid small-scale, deep-ocean topography, *Geophysical Research Letters*, 42(2), 2014GL062,755, 2015.
- Datasheet, *RDI Workhours 300 kHz*, <http://www.rdinstruments.com/sen.aspx>.
- Dengler, M., and D. Quadfasel, Equatorial deep jets and abyssal mixing in the indian ocean, *Journal of Physical Oceanography*, 32(4), 1165–1180, 2002.
- Dickson, R. R., and J. Brown, The production of north atlantic deep water: Sources, rates, and pathways, *Journal of Geophysical Research: Oceans*, 99(C6), 12,319–12,341, 1994.
- Dillon, T. M., Vertical overturns: A comparison of thorpe and ozmidov length scales, *Journal of Geophysical Research: Oceans*, 87(C12), 9601–9613, 1982.
- Döös, K., and D. J. Webb, The deacon cell and the other meridional cells of the southern ocean, *Journal of Physical Oceanography*, 24(2), 429–442, 1994.
- Efron, B., Bootstrap methods: Another look at the jackknife, *The Annals of Statistics*, 7(1), 1–26, 1979.
- Egbert, G. D., and S. Y. Erofeeva, Efficient inverse modeling of barotropic ocean tides, *Journal of Atmospheric and Oceanic Technology*, 19(2), 183–204, 2002.
- Egbert, G. D., A. F. Bennett, M. G. Foreman, and L. Erofeeva, The osu topex/poseidon global inverse solution tpxo, <http://volkov.oce.orst.edu/tides/global.html>, Version 7.2, 2014.
- Emery, J., William, and E. Thomson, Richard, *Data Analysis Methods in Physical Oceanography*, Elsevier, 2004.
- Çengel, Y. A., and J. M. Cimbala, *Fluid Mechanics: Fundamentals and Applications*, McGraw-Hill, 2006.
- Fehn, U., M. D. Siegel, G. R. Robinson, H. D. Holland, D. L. Williams, A. J. Erickson, and K. E. Green, Deep-water temperatures in the famous area, *Geological Society of America Bulletin*, 88(4), 488–494, 1977.

- Fer, I., A. K. Peterson, and J. E. Ullgren, Microstructure measurements from an underwater glider in the turbulent faroe bank channel overflow, *Journal of Atmospheric and Oceanic Technology*, 31(5), 1128–1150, 2014.
- Ferron, B., H. Mercier, K. Speer, A. Gargett, and K. Polzin, Mixing in the romanche fracture zone, *Journal of Physical Oceanography*, 28(10), 1929–1945, 1998.
- Gargett, A. E., T. R. Osborn, and P. W. Nasmyth, Local isotropy and the decay of turbulence in a stratified fluid, *Journal of Fluid Mechanics*, 144, 231–280, 1984.
- Garrett, C., and W. Munk, Oceanic mixing by breaking internal waves, *Deep Sea Research and Oceanographic Abstracts*, 19(12), 823–832, 1972.
- Garrett, C., and W. Munk, Space-time scales of internal waves: A progress report, *Journal of Geophysical Research*, 80(3), 291–297, 1975.
- Gill, A., *Atmosphere-Ocean Dynamics, International Geophysics*, vol. 30, Academic Press, 1982.
- Goodman, L., E. R. Levine, and R. G. Lueck, On measuring the terms of the turbulent kinetic energy budget from an auv, *Journal of Atmospheric and Oceanic Technology*, 23(7), 977–990, 2006.
- Gould, W. J., Physical oceanography of the azores front, *Progress in Oceanography*, 14(0), 167–190, 1985.
- Gregg, M. C., Scaling turbulent dissipation in the thermocline, *Journal of Geophysical Research: Oceans*, 94(C7), 9686–9698, 1989.
- Harris, F. J., On the use of windows for harmonic analysis with the discrete fourier transform, *Proceedings of the IEEE*, 66(1), 51–83, 1978.
- Harvey, J., and M. Arhan, The water masses of the central north atlantic in 1983–84, *Journal of Physical Oceanography*, 18(12), 1855–1875, 1988.
- Helfrich, K. R., Time-dependent two-layer hydraulic exchange flows, *Journal of Physical Oceanography*, 25(3), 359–373, 1995.
- Kanzow, T., and W. Zenk, Structure and transport of the iceland scotland overflow plume along the reykjanes ridge in the iceland basin, *Deep Sea Research Part I: Oceanographic Research Papers*, (0), 2014.
- Kanzow, T., et al., Observed flow compensation associated with the moc at 26.5 n in the atlantic, *Science*, 317(5840), 938–941, 2007.
- Keller, G. H., S. H. Anderson, and J. W. Lavelle, Near-bottom currents in the mid-atlantic ridge rift valley, *Canadian Journal of Earth Sciences*, 12(4), 703–710, 1975.

References

- Klymak, J. M., and J. N. Moum, Oceanic isopycnal slope spectra. part i: Internal waves, *Journal of Physical Oceanography*, *37*(5), 1215–1231, 2007a.
- Klymak, J. M., and J. N. Moum, Oceanic isopycnal slope spectra. part ii: Turbulence, *Journal of Physical Oceanography*, *37*(5), 1232–1245, 2007b.
- Käse, R. H., and W. Zenk, Reconstructed mediterranean salt lens trajectories, *Journal of Physical Oceanography*, *17*(1), 158–163, 1987.
- Kuhlbrodt, T., A. Griesel, M. Montoya, A. Levermann, M. Hofmann, and S. Rahmstorf, On the driving processes of the atlantic meridional overturning circulation, *Reviews of Geophysics*, *45*(2), RG2001, 2007.
- Kunze, E., E. Firing, J. M. Hummon, T. K. Chereskin, and A. M. Thurnherr, Global abyssal mixing inferred from lowered adcp shear and ctd strain profiles, *Journal of Physical Oceanography*, *36*(8), 1553–1576, 2006.
- Laws, E. A., *Mathematical methods for oceanographers: An introduction*, 1997.
- Ledwell, J. R., A. J. Watson, and C. S. Law, Evidence for slow mixing across the pycnocline from an open-ocean tracer-release experiment, *Nature*, *364*(6439), 701–703, 10.1038/364701a0, 1993.
- Ledwell, J. R., E. T. Montgomery, K. L. Polzin, L. C. St. Laurent, R. W. Schmitt, and J. M. Toole, Evidence for enhanced mixing over rough topography in the abyssal ocean, *Nature*, *403*(6766), 179–182, 10.1038/35003164, 2000.
- Legg, S., Internal tides generated on a corrugated continental slope. part ii: Along-slope barotropic forcing*, *Journal of Physical Oceanography*, *34*(8), 1824–1838, 2004.
- Legg, S., and A. Adcroft, Internal wave breaking at concave and convex continental slopes*, *Journal of Physical Oceanography*, *33*(11), 2224–2246, 2003.
- Legg, S., and K. M. H. Huijts, Preliminary simulations of internal waves and mixing generated by finite amplitude tidal flow over isolated topography, *Deep Sea Research Part II: Topical Studies in Oceanography*, *53*(1–2), 140–156, 2006.
- Legg, S., and J. Klymak, Internal hydraulic jumps and overturning generated by tidal flow over a tall steep ridge, *Journal of Physical Oceanography*, *38*(9), 1949–1964, 2008.
- Levine, E. R., and R. G. Lueck, Turbulence measurement from an autonomous underwater vehicle, *Journal of Atmospheric and Oceanic Technology*, *16*(11), 1533–1544, 1999.
- Lherminier, P., H. Mercier, T. Huck, C. Gourcuff, F. F. Perez, P. Morin, A. Sarafanov, and A. Falina, The atlantic meridional overturning circulation and the subpolar gyre observed at the a25-ovide section in june 2002 and 2004,

- Deep Sea Research Part I: Oceanographic Research Papers*, 57(11), 1374–1391, 2010.
- Lighthill, M. J., Waves in fluids, *Communications on Pure and Applied Mathematics*, 20(2), 267–293, 1967.
- Lorke, A., and A. Wüest, Probability density of displacement and overturning length scales under diverse stratification, *Journal of Geophysical Research: Oceans*, 107(C12), 3214, 2002.
- Lueck, R., Converting shear probe and thermistors signals to physical units, 2005.
- Lueck, R., F. Wolk, and H. Yamazaki, Oceanic velocity microstructure measurements in the 20th century, *Journal of Oceanography*, 58(1), 153–174, 2002.
- MacKinnon, J. A., T. M. S. Johnston, and R. Pinkel, Strong transport and mixing of deep water through the southwest indian ridge, *Nature Geosci*, 1(11), 755–758, 10.1038/ngeo340, 2008.
- Macoun, P., and R. Lueck, Modeling the spatial response of the airfoil shear probe using different sized probes, *Journal of Atmospheric and Oceanic Technology*, 21(2), 284–297, 2004.
- Mantyla, A. W., and J. L. Reid, Abyssal characteristics of the world ocean waters, *Deep Sea Research Part A. Oceanographic Research Papers*, 30(8), 805–833, 1983.
- Marshall, J., and K. Speer, Closure of the meridional overturning circulation through southern ocean upwelling, *Nature Geosci*, 5(3), 171–180, 10.1038/ngeo1391, 2012.
- Munk, W. H., Abyssal recipes, *Deep-Sea Research*, 13, 707–730, 1966.
- Munk, W. H., and C. Wunsch, Abyssal recipes ii: energetics of tidal and wind mixing, *Deep Sea Research Part I: Oceanographic Research Papers*, 45(12), 1977–2010, 1998.
- Nasmyth, P., Oceanic turbulence. ph.d. thesis, institute of oceanography, university of british columbia, 69 pp, 1970.
- NOAA, National geophysical data center, etopo1 global relief model.
- Oakey, N. S., Determination of the rate of dissipation of turbulent energy from simultaneous temperature and velocity shear microstructure measurements, *Journal of Physical Oceanography*, 12(3), 256–271, 1982.
- Olbers, D., J. Willebrand, and C. Eden, Ocean dynamics, 2012.
- Osborn, T. R., Vertical profiling of velocity microstructure, *Journal of Physical Oceanography*, 4(1), 109–115, 1974.

References

- Osborn, T. R., Estimates of the local rate of vertical diffusion from dissipation measurements, *Journal of Physical Oceanography*, 10(1), 83–89, 1980.
- Ozmidov, R. V., On the turbulent exchange in a stably stratified ocean, *Atmospheric and Oceanic Physics Series*, 8, 853–860, 1965.
- Pawlowicz, R., B. Beardsley, and S. Lentz, Classical tidal harmonic analysis including error estimates in matlab using tide, *Computers and Geosciences*, 28(8), 929–937, 2002.
- Peters, H., M. C. Gregg, and J. M. Toole, On the parameterization of equatorial turbulence, *Journal of Geophysical Research: Oceans*, 93(C2), 1199–1218, 1988.
- Polzin, K. L., K. G. Speer, J. M. Toole, and R. W. Schmitt, Intense mixing of antarctic bottom water in the equatorial atlantic ocean, *Nature*, 380(6569), 54–57, 10.1038/380054a0, 1996.
- Polzin, K. L., J. M. Toole, J. R. Ledwell, and R. W. Schmitt, Spatial variability of turbulent mixing in the abyssal ocean, *Science*, 276(5309), 93–96, 1997.
- Rahmstorf, S., Ocean circulation and climate during the past 120,000 years, *Nature*, 419(6903), 207–214, 10.1038/nature01090, 2002.
- Rahmstorf, S., Thermohaline circulation: The current climate, *Nature*, 421(6924), 699–699, 10.1038/421699a, 2003.
- Schaffer, J., Small-scale variability associated with mixing in the denmark strait overflow plume based on horizontally profiling observations, 2013.
- Schafstall, J., M. Dengler, P. Brandt, and H. Bange, Tidal-induced mixing and diapycnal nutrient fluxes in the mauritanian upwelling region, *Journal of Geophysical Research: Oceans*, 115(C10), C10,014, 2010.
- Siddon, T. E., A miniature turbulence gauge utilizing aerodynamic lift, *Review of Scientific Instruments*, 42(5), 653–656, 1971.
- Sreenivasan, K. R., The passive scalar spectrum and the obukhov–corrsin constant, *Physics of Fluids (1994-present)*, 8(1), 189–196, 1996.
- St. Laurent, L. C., and A. M. Thurnherr, Intense mixing of lower thermocline water on the crest of the mid-atlantic ridge, *Nature*, 448(7154), 680–683, 10.1038/nature06043, 2007.
- St. Laurent, L. C., J. M. Toole, and R. W. Schmitt, Buoyancy forcing by turbulence above rough topography in the abyssal brazil basin*, *Journal of Physical Oceanography*, 31(12), 3476–3495, 2001.
- Steele, E., T. Boyd, M. Inall, E. Dumont, and C. Griffiths, Cooling of the west spitsbergen current: Auv-based turbulence measurements west of svalbard, in *Autonomous Underwater Vehicles (AUV), 2012 IEEE/OES*, pp. 1–7.

- Sy, A., Investigation of large-scale circulation patterns in the central north atlantic: the north atlantic current, the azores current, and the mediterranean water plume in the area of the mid-atlantic ridge, *Deep Sea Research Part A. Oceanographic Research Papers*, 35(3), 383–413, 1988.
- Taylor, G., Statistical theory of turbulence, *Proceedings of the Royal Society of London. Series A*, 151, 421–444, 1935.
- Thorpe, S. A., *The Turbulent Ocean*, vol. 1, Cambridge University Press, 2005.
- Thorpe, S. A., Dissipation in hydraulic transitions in flows through abyssal channels, *Journal of Marine Research*, 65(1), 147–168, 2007.
- Thorpe, S. A., Turbulent hydraulic jumps in a stratified shear flow, *Journal of Fluid Mechanics*, 654, 305–350, 2010.
- Thorpe, S. A., T. R. Osborn, J. F. E. Jackson, A. J. Hall, and R. G. Lueck, Measurements of turbulence in the upper-ocean mixing layer using autosub, *Journal of Physical Oceanography*, 33(1), 122–145, 2003.
- Thurnherr, A. M., *LADCP processioning software inversion method*, <ftp://ftp.ldeo.columbia.edu/pub/ant/LADCP/>.
- Thurnherr, A. M., Diapycnal mixing associated with an overflow in a deep submarine canyon, *Deep Sea Research Part II: Topical Studies in Oceanography*, 53(1–2), 194–206, 2006.
- Thurnherr, A. M., Vertical velocity from ladcp data, *Current, Waves and Turbulence Measurements (CWTM)*, 2011 *IEEE/OES 10th*, pp. 198–204, 2011.
- Thurnherr, A. M., and K. J. Richards, Hydrography and high-temperature heat flux of the rainbow hydrothermal site, *Journal of Geophysical Research: Oceans*, 106(C5), 9411–9426, 2001.
- Thurnherr, A. M., and K. G. Speer, Boundary mixing and topographic blocking on the mid-atlantic ridge in the south atlantic*, *Journal of Physical Oceanography*, 33(4), 848–862, 2003.
- Thurnherr, A. M., K. J. Richards, C. R. German, G. F. Lane-Serff, and K. G. Speer, Flow and mixing in the rift valley of the mid-atlantic ridge, *Journal of Physical Oceanography*, 32(6), 1763–1778, 2002.
- Thurnherr, A. M., L. C. St. Laurent, K. G. Speer, J. M. Toole, and J. R. Ledwell, Mixing associated with sills in a canyon on the midocean ridge flank*, *Journal of Physical Oceanography*, 35(8), 1370–1381, 2005.
- Thurnherr, A. M., G. Reverdin, P. Bouruet-Aubertot, L. C. St. Laurent, A. Vangriesheim, and V. Ballu, Hydrography and flow in the lucky strike segment of the mid-atlantic ridge, *Journal of Marine Research*, 66(3), 347–372, 2008.

References

- Tippenhauer, S., M. Dengler, T. Fischer, and T. Kanzow, Turbulence and finestructure in a deep ocean channel with sill overflow on the mid-atlantic ridge, *Deep Sea Research Part I: Oceanographic Research Papers*, 99, 10–22, 2015.
- Toggweiler, J. R., and B. Samuels, On the ocean’s large-scale circulation near the limit of no vertical mixing, *Journal of Physical Oceanography*, 28(9), 1832–1852, 1998.
- Toole, J. M., R. W. Schmitt, and K. L. Polzin, Estimates of diapycnal mixing in the abyssal ocean, *Science*, 264(5162), 1120–1123, 1994.
- Trenberth, K. E., and J. M. Caron, Estimates of meridional atmosphere and ocean heat transports, *Journal of Climate*, 14(16), 3433–3443, 2001.
- Warren, A., Bruce, *Deep Circulation of the World Ocean*, pp. 6–41, MIT Press, Cambridge, 1981.
- Webb, D. J., and N. Suginohara, Oceanography: Vertical mixing in the ocean, *Nature*, 409(6816), 37–37, 10.1038/35051171, 2001.
- Wesson, J. C., and M. C. Gregg, Mixing at camarinal sill in the strait of gibraltar, *Journal of Geophysical Research: Oceans*, 99(C5), 9847–9878, 1994.
- Whitehead, J. A., Topographic control of oceanic flows in deep passages and straits, *Reviews of Geophysics*, 36(3), 423–440, 1998.
- Wilson, C., K. Speer, J.-L. Charlou, H. Bougault, and G. Klinkhammer, Hydrography above the mid-atlantic ridge and within the lucky strike segment, *Journal of Geophysical Research: Oceans*, 100(C10), 20,555–20,564, 1995.
- Wilson, C., J.-L. Charlou, E. Ludford, G. Klinkhammer, C. Chin, H. Bougault, C. German, K. Speer, and M. Palmer, Hydrothermal anomalies in the lucky strike segment on the mid-atlantic ridge, *Earth and Planetary Science Letters*, 142(3–4), 467–477, 1996.
- Wolk, F., H. Yamazaki, L. Seuront, and R. G. Lueck, A new free-fall profiler for measuring biophysical microstructure, *Journal of Atmospheric and Oceanic Technology*, 19(5), 780–793, 2002.
- Wunsch, C., and R. Ferrari, Vertical mixing, energy, and the general circulation of the oceans, *Annual Review of Fluid Mechanics*, 36(1), 281–314, 2004.
- Yamazaki, H., and T. Osborn, Dissipation estimates for stratified turbulence, *Journal of Geophysical Research: Oceans*, 95(C6), 9739–9744, 1990.
- Zhang, Y., and J. N. Moum, Inertial-convective subrange estimates of thermal variance dissipation rate from moored temperature measurements, *Journal of Atmospheric and Oceanic Technology*, 27(11), 1950–1959, 2010.

List of Figures

1.1	Sketch of the global meridional overturning circulation (MOC) (<i>Rahmstorf, 2002; Kuhlbrodt et al., 2007</i>).	1
1.2	Schematic diagram by <i>Marshall and Speer (2012)</i> of the upper and lower cell of the global MOC.	4
1.3	Flow, density, and dissipation distribution in a ridge-flank channel on the western flank of the MAR in the south Atlantic near 22° S from <i>Thurnherr et al. (2005)</i>	5
1.4	Topography of the North Atlantic (Etopo 1 (<i>NOAA</i>)). The Lucky Strike segment is marked by a white dot.	9
1.5	Map by <i>Wilson et al. (1995)</i> of the French-American Zero-Angle Photon Spectrometer and Rocks (FAZAR) cruise study region. . . .	10
1.6	θ -S diagram from the eastern channel of the Lucky Strike segment.	11
1.7	Topography of the MAR from 33° N to 40° N.	12
1.8	Topography of the rift valley 400 km south of the Azores.	12
1.9	Section of potential density σ_θ for the FAZAR study region by <i>Wilson et al. (1995)</i>	13
1.10	θ -S diagram from World Ocean Database east and west of the MAR together with all profiles obtained in the course of this study.	14
1.11	Topography of the Lucky Strike segment.	15
1.12	Potential density σ_2 obtained in the eastern channel of the LS segment and the density difference from southern to northern basin. . . .	17
1.13	Sketch of a hydraulic jump in uniform flow.	18
1.14	Sketch of hydraulic jumps of different amplitude by <i>Chow (1959)</i>	19
1.15	Sketch of a hydraulic jump in a stratified shear flow.	20
1.16	The dependence of the flow and density profile from the parameter η	21
1.17	The Froude Number Fr_* and Fr_c as funktion of the parameter η	23
2.1	Map of study site and position of measurements.	26
2.2	Picture of the AUV with MR and mounting.	30
2.3	Picture of the AUV with MR and mounting during recovery.	30
2.4	Spectra of acceleration signals.	31
2.5	Velocity differences of mooring derived and AUV derived flow velocities.	35
3.1	Example velocity shear spectra for elevated and low turbulence environments.	39

List of Figures

3.2	Dissipation rate segment determined from the hybrid and from the filtered spectrum.	41
3.3	Histogram of the dissipation rates.	42
4.1	Meridional distribution of the dissipation rate as function of pressure.	46
4.2	Meridional distribution of the dissipation rate as function of altitude.	47
4.3	Map of the dissipation rate.	48
4.4	Along-channel distribution of the box-averaged dissipation rate together with vertical profiles of the dissipation rates obtained by <i>St. Laurent and Thurnherr (2007)</i>	49
4.5	Map of depth-averaged LADCP-derived velocities.	51
4.6	Section of station averaged along-channel LADCP derived velocity.	54
4.7	Section of station averaged across-channel LADCP derived velocity.	55
4.8	Richardson numbers along the channel.	56
4.9	Average cross-channel distribution of along-channel velocity.	58
4.10	Along-channel distribution of turbulent diffusivity.	60
4.11	Sketch for advection diffusion balance.	62
4.12	Meridional distribution of the density anomalies.	65
4.13	Temperature gradient wavenumber spectra.	68
4.14	Temperature gradient variance integrated over the inertial convective subrange.	69
4.15	Dissipation rate and potential density along an AUV track segment.	71
4.16	Potential density derived from the AUV CTD in comparison with nearby lowered CTD observations.	72
4.17	Sketch of the along-channel and across-channel flow and density distribution.	74
5.1	Along-channel velocity from upstream and downstream moored ADCPs.	78
5.2	Tidal fits to the along-channel velocity.	80
5.3	Mooring-based potential temperature time-series.	84
5.4	Lag correlation of the θ_2 time-series with semi-diurnal tides.	85
5.5	Spectrum of isothermal displacement.	88
5.6	Lag correlation of the std of high-pass filtered potential temperature with low-pass filtered observed along-channel velocity.	90
5.7	Standard deviation of high-pass filtered θ_2 time-series.	91
5.8	Along-channel velocity at the yoyo-station.	94
5.9	Mooring-based along-channel velocity during yoyo-Station.	96
5.10	Richardson Numbers for the yoyo-cast.	97
5.11	Density distribution obtained from tow-yo Sections.	98
5.12	Density distribution obtained from tow-yo Sections.	99
5.13	Mooring-derived along-channel velocity during tow-yo Sections.	100
5.14	Mooring-based along-channel velocity, semi-diurnal tide and time of lowered observations.	102

5.15	Depth averaged LADCP derived velocities averaged between 1800 m depth and the sill depth.	104
5.16	Depth averaged LADCP derived velocities from the sill depth (2060 m) to the bottom.	105
5.17	Along-channel LADCP derived velocity for flood-tide.	106
5.18	Along-channel LADCP derived velocity for ebb-tide.	107
5.19	Across-channel section of along-channel LADCP derived velocity at the first across-channel section for flood- and ebb-tide.	109
5.20	Across-channel section of along-channel LADCP derived velocity at the second across-channel section for flood- and ebb-tide.	110
5.21	Dissipation rate and along channel flow 10 min averages.	113
5.22	Dissipation rate and along channel flow 10 min averages.	115
5.23	Dissipation rate and along channel flow 10 min averages.	116
5.24	Dissipation rates 10 min averages respect to pressure.	117
5.25	Sketch of the along-channel and across-channel flow and density distribution during flood-tide.	119
5.26	Sketch of the along-channel flow and density distribution during flood-tide for an undular and a weak hydraulic jump.	120
5.27	Sketch of the along-channel and across-channel flow and density distribution during weak along-channel flow conditions.	121
6.1	Along-channel velocity observed at the upstream and downstream mooring during the time of the yoyo-Station.	126
6.2	Along-channel flow anomaly at the yoyo-Station at D1.	127
6.3	Low-pass filtered mooring-based vertical velocity.	132
6.4	Lag correlation of std of high-pass filtered vertical velocity with low-pass filtered along-channel velocity, both mooring-based.	133
6.5	Time-series of std of high-pass filtered vertical velocity with low-pass filtered along-channel velocity, both mooring-based.	134
6.6	Along-channel and vertical velocity during AUV Dive 8.	137
A.1	Topography of the eastern channel of the Lucky Strike segment and station map.	147
A.2	Dissipation rate relative uncertainty.	148
A.3	Potential density and LADCP-derived velocities from the CTD/LADCP yo-yo cast by <i>Thurnherr</i> (2011).	148
A.4	Buoyancy frequency and buoyancy frequency variability along the channel.	149
A.5	Histogram of the buoyancy frequency variability.	149
A.6	Dissipation rate and along channel flow maps of 10 min averages.	150
A.7	Dissipation rate and along channel flow maps of 10 min averages.	151
A.8	Dissipation rate and along channel flow maps of 10 min averages.	151

List of Tables

2.1	Group- and single-station names and positions of shipboard lowered CTD and LADCP measurements.	27
2.2	Positions and times of mooring deployments.	28
2.3	Overview of the durations and dive modes as well as deployment and recovery dates for all AUV dives.	33
4.1	Mooring-derived meridional and zonal velocity components.	52
4.2	Mooring-derived along- and across-channel velocity components.	53
5.1	Tidal constituents found with the program T-Tide (<i>Pawlowicz et al.</i> , 2002).	79
5.2	Correlation coefficients of along-channel velocity with semi-diurnal barotropic tides.	82
5.3	Mooring-based average and std of potential temperature θ_2	85
5.4	Correlation coefficients of potential temperature with semi-diurnal barotropic tides.	86
5.5	Correlation coefficients of std of high-pass filtered potential temperature with low-pass filtered observed along-channel velocity.	90
6.1	Mooring-based vertical velocity average, std, maximum, and minimum.	131
6.2	Correlation coefficients of std of high-pass filtered vertical velocity with low-pass filtered along-channel velocity, both mooring-based.	133
6.3	Propagation speed and width of a soliton estimated for the given parameters.	139
A.1	Group- and individual-stations names and positions of shipboard lowered CTD and LADCP measurements.	150

Acknowledgments

I would like to thank all the people, who have supported me during this study.

- My advisor *Prof. Dr. Torsten Kanzow* for your dedicated supervision.
- *Prof. Dr. Inga M. Koszalka* for giving the second evaluation.
- *Prof. Dr. Arne Biastoch* for the willingness to give the second evaluation.
- *Dr. Marcus Dengler* and *Dr. Tim Fischer* for the countless discussions and encouraging advices.
- *Dr. Andreas M. Thurnherr* not only for the possibility to stay at LDEO but also for your support, the helpful discussions, advices and your enormous knowledge. I learned a lot from you and really enjoyed my stay!
- *Dr. Rebecca Hummels*, *Dr. Tim Fischer*, *Dr. Johannes Hahn*, *Rainer Zantopp*, *Dr. Michael Brüdgam* and *Dr. Andreas Bick* for proofreading!
- *Dr. Andreas M. Thurnherr* for processing the LADCP data, *Dr. Gerd Krahm* for processing the CTD data, and *Dr. Johannes Hahn* for calibrating the MicroCat data.
- *Marcel Rothenbeck* and the whole AUV-team for your enormous support at sea and land!
- *Uwe Koy* for your help with the MicroRider and the support in technical as well as non-technical questions.
- My colleagues in B11: *Rebecca*, *Donata*, *Manuela*, *Sven*, *Johannes*, *Michael*, *Yao*, *Florian* and *Robert*. Thanks for the great (working)-atmosphere and the many little advices and ideas.
- My new colleagues at AWI, especially *Wilken*, *Markus*, *Jens*, and *Thorben* for your support.
- All my colleagues from (IFM-)GEOMAR especially ALL colleagues from the PO. Thanks for the great time with you!
- I also want to acknowledge the funding by the Deutsche Forschungsgemeinschaft as part of the DFG-Projekt – GZ: KA 3204/2-1 *Vertical near sea floor ocean mixing in the central valley of the Mid-Atlantic Ridge*

All my friends and everyone who supported me in the last years!

SANDRA TIPPENHAUER

Erklärung

Hiermit versichere ich, dass ich die vorliegende Arbeit - abgesehen von der Beratung durch meinen Betreuer - unter Einhaltung der Regeln guter wissenschaftlicher Praxis der Deutschen Forschungsgemeinschaft und nur unter Zuhilfenahme der angegebenen Quellen und Hilfsmittel selbstständig erarbeitet und verfasst habe. Diese Arbeit hat weder ganz, noch zum Teil, an anderer Stelle im Rahmen eines Prüfungsverfahrens vorgelegen, ist nicht veröffentlicht und auch nicht zur Veröffentlichung eingereicht.

Kiel, 2015

Sandra Tippenhauer